Development of composite nanoporous gold stamps and their application in capillary microprinting of polymer melts

Dissertation

by

Ruža Periz

School of Biology/Chemistry, University of Osnabrück

2023

Dissertation to partially fulfill the requirements for the degree of
'Doctor rerum naturalium'

presented by Ruža Periz

to the School of Biology/Chemistry, University of Osnabrück

Reviewer #1: Prof. Dr. Martin Steinhart

Reviewer #2: Prof. Dr. Uwe Beginn

Acknowledgments

First, I would like to express my gratitude to my supervisor **Prof. Dr. Martin Steinhart** for his patience, encouragement and for always making the time to answer my questions and give me constructive feedback. Thank you for your trust and freedom to develop my skills and knowledge in my own way, that allowed me to grow both personally and professionally, and made me feel more confident in my abilities as a result. Your guidance had significant impact on my career, and I will always be grateful for the opportunity and the time I spent working under your supervision.

I would also like to thank **Prof. Dr. Uwe Beginn** for his support and review of my thesis. Many thanks to **Dr. Nadiia Mameka** for the help with electrochemical dealloying experiments and **Dr. Jürgen Markmann** for conducting the sputtering of AgAu films on mSi . Without them this work would not be possible.

During my PhD journey I had the honor to work with great people who made this time fun and joyful. Big thanks to all my current and former colleagues from the department of physical chemistry for their help, scientific discussions, and support. Especially to **Claudia Heß** and **Christine Schulz-Kölbel** for their great assistance in the lab, to **Barbara Gunkel** for all the administrative help and many pleasant conversations, and to **Dr. Helmut Schäfer** for all his help to settle in when I first came to Osnabrück. My special gratitude goes to **Wajiha Akram**, **Dr. Mercedes Runge**, **Dr. Qaiser Ali Khan**, and **Dr. Michael Philippi**. To my dear friend **Markus Geuss** for his help with PFM experiments and many philosophical discussions. And to my dearest friend and α-N, **Dr. Fernando Vazquez Luna** for countless walks, conversations, jokes, and fun. Thank you for being an amazing friend.

I want to thank all my friends for always being there for me, especially to **Dr. Milena Dimitrijević** for inspiring me and motivating me along the way. My heartfelt thanks to **Andrei**, for his love and support.

Finally, I would like to thank my family, my dear sister **Sandra**, for always giving me the extra push when needed and being the best sister and my best friend. And to my parents, **Jovo** and **Jela**, for encouraging my curiosity and always believing in me, my gratitude to you is eternal.

Table of Contents

1   Introduction

As many technologies are focusing on the miniaturization of its products, the ability to pattern at the micro/nano scale over the large areas on material surfaces is critical to the development of next generation technologies in many industries from electronics[1] to energy[2] and medicine[3]. The ability to print polymer microstructures opens new possibilities for the development of innovative and functional materials in various areas such as drug delivery systems[4], tissue engineering[5], microelectromechanical (MEMS) devices[6], surface engineering[7] and many more.

Patterning on the micro/nano scale can be accomplished by various lithography techniques including photolithography[8], dip pen lithography[9], microcontact printing[10], nanoimprint lithography[11] and more. In the need to overcome the limitations of the microcontact printing method developed at Harvard University in the 90s by Whiteside and Kumar[12] porous stamps were developed in 2009 by Xu et al[13]. Porous structure of the stamp served as an ink reservoir that enabled the printing of various inks such as proteins and dendrimers in multiple consecutive cycles without the need for reinking the stamp. Capillary stamping (Figure 1) technique was then introduced in 2018 by Schmidt et al.[14] by developing the mesoporous silica stamp that enabled the printing from organic solutions in the nanometre range. In the same year, Hou et al.[15] developed porous polystyrene-*block*-poly(2-vinylpyridine) PS-*b*-P2VP stamps that extended the application of capillary stamping method and resulted in the development of scanner-based[16] capillary stamping method with composite porous polystyrene–*block*-poly(2-vinylpyridine)/controlled porous glass (PS-*b*-P2VP/CPG) stamps.

(a)   (b)
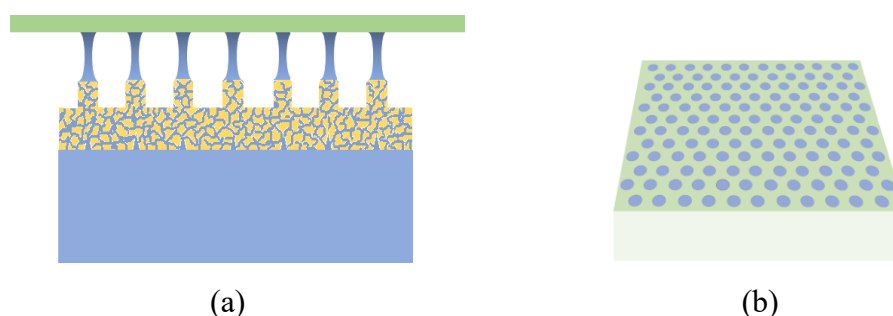
Figure 1. Illustration of the capillary stamping method. (a) Formation of the liquid bridges of polymer ink (blue) between the contact elements of the porous gold stamp (yellow) and the substrate (green). (b) Patterned surface of the substrate with the polymer ink.

The aim in this work is further improvement of capillary stamping process by development of porous metallic stamp that will enable the printing of the polymer melts and therefore further

expand the applications of capillary stamping process. Biggest advantage of melt printing in comparison to solution printing is that the evaporation of the volatile organic solvents during stamping process is circumvented, because during solvent evaporation, hardly controllable structure formation processes, such as liquid-liquid phase separation[17] and flow processes related to, for example, capillarity[18] may occur. Also, the printed structures offer higher homogeneity because of a lower tendency to deform then the structures obtained after the solvent evaporation.

Therefore, novel composite nanoporous gold stamps (np-Au) that are stable at elevated temperatures will be developed in the first part of this work. The stamp design is based on the use of polymer films as both ink reservoir and as stabilizing support for the thin, topographically patterned nanoporous gold layers. The continuous network of pores throughout the gold layer connected with the polymer film that serves as ink reservoir will enable the stamping in consecutive cycles which makes the stamping process efficient and easy.

As polystyrene is available with narrow molecular mass distributions over a broad molecular mass range, it has been selected as a polymer for the proof of concept for the composite np-Au stamp use in capillary stamping printing. Hence, printing of polystyrene at 200 °C on glass substrates will be carried out in this work. Printing of polystyrene with composite np-Au stamp will also be used for the optimization of the stamping procedure and setting a procedure that will be used as a standard stamping protocol in this work. Stamping of the polystyrene will be done for various durations of the dwelling times and the analysis of the influence of the dwell time on the size parameters (diameter and height) of the deposited structures will be investigated.

Further, the printing of the functional ferroelectric polymer poly(vinylidenefluoride)-trifluoroethylene (P(VDF-TrFE)) with composite np-Au stamps at 205 °C will be discussed. Stamping will be done on two different substrates, glass, and aluminium-coated Si wafers. As for the polystyrene, the stamping of P(VDF-TrFE) will be conducted with various stamping durations at both types of substrates and the influence of the size parameters (diameter and height) will be analyzed. Additionally, the ferroelectric properties of the printed P(VDF-TrFE) deposits on aluminium coated Si will be investigated.

2 State of the Art

2.1 Lithography techniques

The need for microstructured and nanostructured patterned surfaces has resulted in the development of a wide range of lithography techniques that manipulate surface structures at these scales. Surfaces patterned with polymers have wide applications in the fields of semiconductor microelectronics[19], medical research[20], biological research[21], development of masks and templates[22], production of optical components[23] and fundamental research in surface science[24]. Although polymer patterning techniques can be sorted in various ways, here the techniques are grouped as parallel vs serial methods, which then are based on additive or subtractive principle. In general, the advantage of parallel methods is the capability to pattern large areas in a short time at high throughput. On the other hand, serial methods offer the possibility to generate arbitrary patterns with higher resolution, but they are usually more expensive, slower than the parallel methods and the patterned areas are smaller. Each of the techniques can be characterized by the following parameters: resolution, cost, throughput and complexity[25]. As this work focuses on the stamp-based method of capillary printing of polymer melts, lithographic techniques directing to this method will be described in detail in the following chapter.

2.1.1 Serial patterning methods

Serial patterning techniques allow high flexibility in feature design as they pattern the surface in a pixel-to-pixel fashion. In this way, a variety of the designs can be generated on the surfaces. These methods are characterized by high resolution, high cost and low throughput. Because they enable printing of arbitrary designs these methods are intensively applied in scientific research[26].

2.1.1.1 Subtractive serial patterning methods

Since building a prototype instrument of electron beam lithography (EBL)[27] in the 1960s at International Business Machines (IBM), the technique has been intensively developed and improved for the patterning on the micro- and nano scale in the last 60 years[28]. In this method, electron beam is focused in a patterned fashion on the surface covered with a sensitive resist,

followed by pattern transfer (wet etching, reactive ion etching etc.) (Fig. 2.1a). It is a technique with high resolution, achieving patterning of sub-10 nm[29] features. A disadvantage of this method is that it is a slow patterning method with high cost and high complexity. As such, the method is used mostly for the production of templates in turn used in techniques with higher throughput such as nanoimprint lithography and photolithography[30,31]. Another technique achieving high resolution is focused ion beam lithography (FIB)[32]. Instead of electrons, cations (such as gallium cations) are used for direct writing on the substrates or for subtractive lithography (generation of 3D objects by removal of materials by means of FIB) (Fig. 2.1b). Therefore, the FIB method enables patterning not only on the photoresist, which is the case for the EBL method, but also enables direct writing on the substrate[31,32,33] with a resolution of sub-5 nm[34]. An important advantage of both the EBL and FIB methods is the possibility to pattern various materials (such as metals[35,36], polymers[37,38], ceramics[39]) with high precision and freedom of feature designs. On the other hand, low throughput, high cost and complexity of the processes (requires operation in vacuum) is the large disadvantage of these methods that restricts their applications[40].
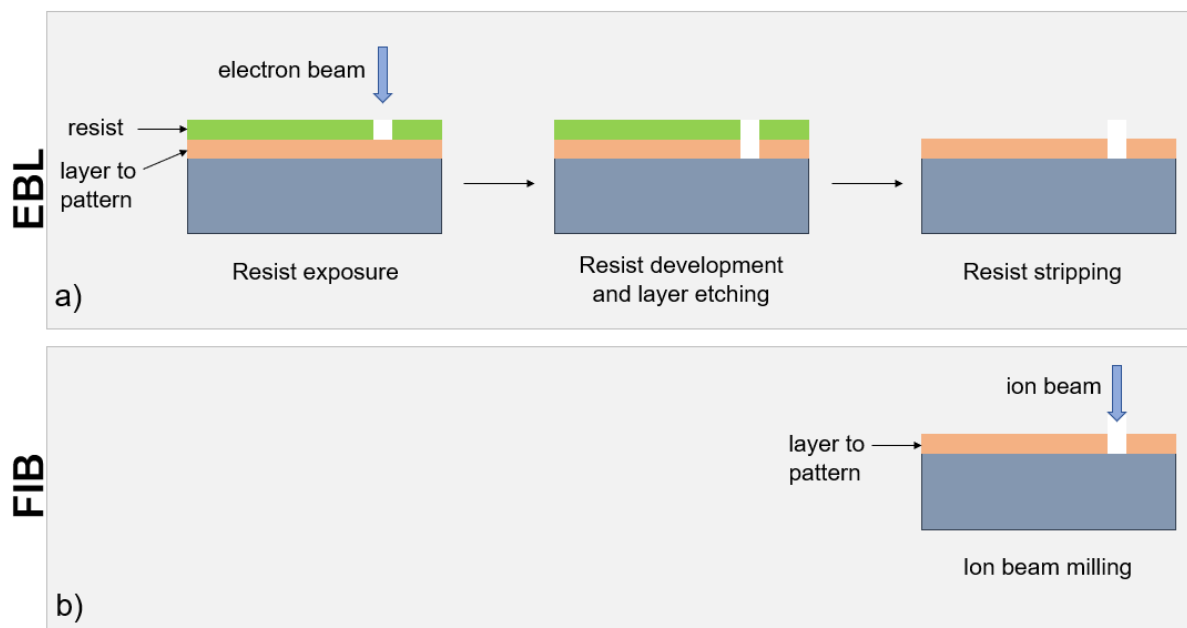

Figure 2.1 Schematic illustration of **a)** electron beam lithography (EBL) and **b)** focussed ion beam (FIB) lithography. The illustration was adapted from Nassiopoulou et.al.[41].

2.1.1.2 Additive serial patterning methods

Scanning probe lithography (SPL)[42] is another set of techniques that enables the generation of the complex patterns on surfaces using scanning probes. Modification of the surfaces is obtained by different interaction mechanisms. Therefore, depending on the interaction mechanism there are different types of SPL[40] such as thermal[43], mechanical[44], dip-pen[45], thermal dip-pen[46] and oxidative[47] SPL. Although SPL techniques can be carried out also in subtractive mode, additive variations are more relevant and will be presented here. Thermal SPL is method where surface modifications are induced by the thermal energy of a heated cantilever tip. As modifying of the material with a heated tip on the nanoscale happens in microseconds, mechanical scan movement of the cantilever remains the main limitation for the deposition speed. An example of the patterning results by thermal SPL is shown in Figure 2.3.
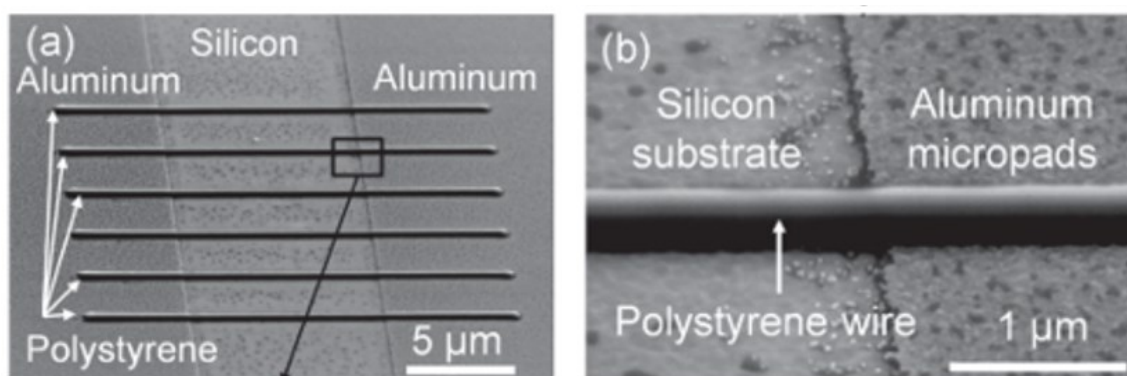

Figure 2.3 SEM images showing the polystyrene patterns deposited by thermal SPL. **a)** Arrays of polystyrene nanowires across two 25 nm thick aluminum micropads, **b)** zoomed image of a polystyrene nanowire across the boundary of an aluminum micropad[48].

Dip pen nanolithography (DPN) was developed by Mirkin[9] and coworkers in 1999 when they wrote alkanethiols with 30-nm resolution on a gold film. Since then, DPN has been used for pattering of various materials with different inks. In this method, cantilever tip is coated with the desired ink and as the tip moves above the surface of the substrate, a water meniscus is created between the surface and the tip. This way, ink is transferred onto the surface because of chemical or physical absorption (Fig. 2.4). Advantage of this method is that enables the deposition of a small amounts of ink on the surface. However, the method has low throughput which limits its use in the technological applications[9,49].

There are two approaches to pattern polymers with DPN. In the first, the polymer is directly deposited on the substrate from solution or from the melt (thermal DPN). Baba et al.[50] produced

carbon nanotube/polymer composite patterns, and O'Connell et al.[51] demonstrated direct writing of viscous polymer inks on silicon surfaces. In a second approach, a precursor of the target polymer is deposited on the surface followed by a site-specific polymerization reaction. Maynor et al.[52] fabricated polythiophene (poly-EDOT) nanowires with sub-100 nm line widths utilizing electrochemical polymerization. The resolution of DPN depends on multiple parameters such as scanning speed, choice of ink, and relative humidity[53]. O'Connell et al.[54] determined that the ink amount on the cantilever tip is the most determining factor in the size of the pattern.
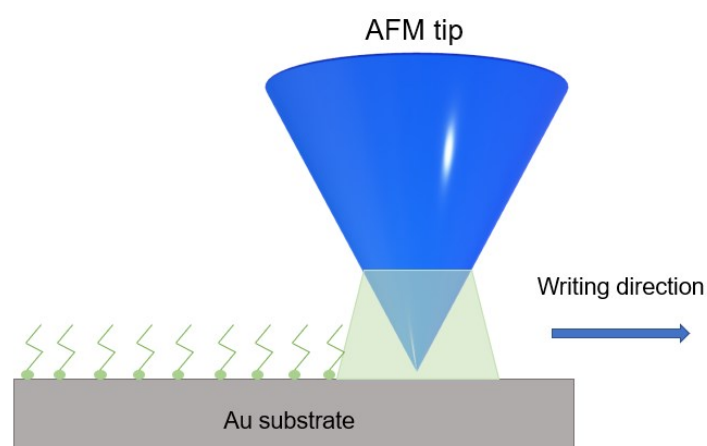

Figure 2.4 Scheme of dip-pen nanolithography that shows the deposition of 1-octadecanethiol from a cantilever tip on the Au surface by formation of a water meniscus in between. The illustration is adapted from Mirkin et al.[9].

A variation of the DPN technique that was developed by the Sheehan et al.[55] called thermal dip-pen nanolithography (tDPN) enables printing of polymers from the melts. It is an additive thermal SPL method where the desired ink that is loaded on the cantilever before the deposition. The ink is usually solid at the room temperature. The cantilever is integrated with the heater and when the tip is brought in the contact with the substrate it is heated above the melting point of the ink. The integrated heater allows the writing to be turned on and off as desired which offers more control of the deposition and deposition rate[56]. By changing the temperature of the cantilever, the viscosity of the melt is changed and thereby the deposition flow rate can be controlled[57]. An example of thermal DPN deposition of polyethene (PE) nanowires done by Felts et al. is shown in Figure 2.5.[58]
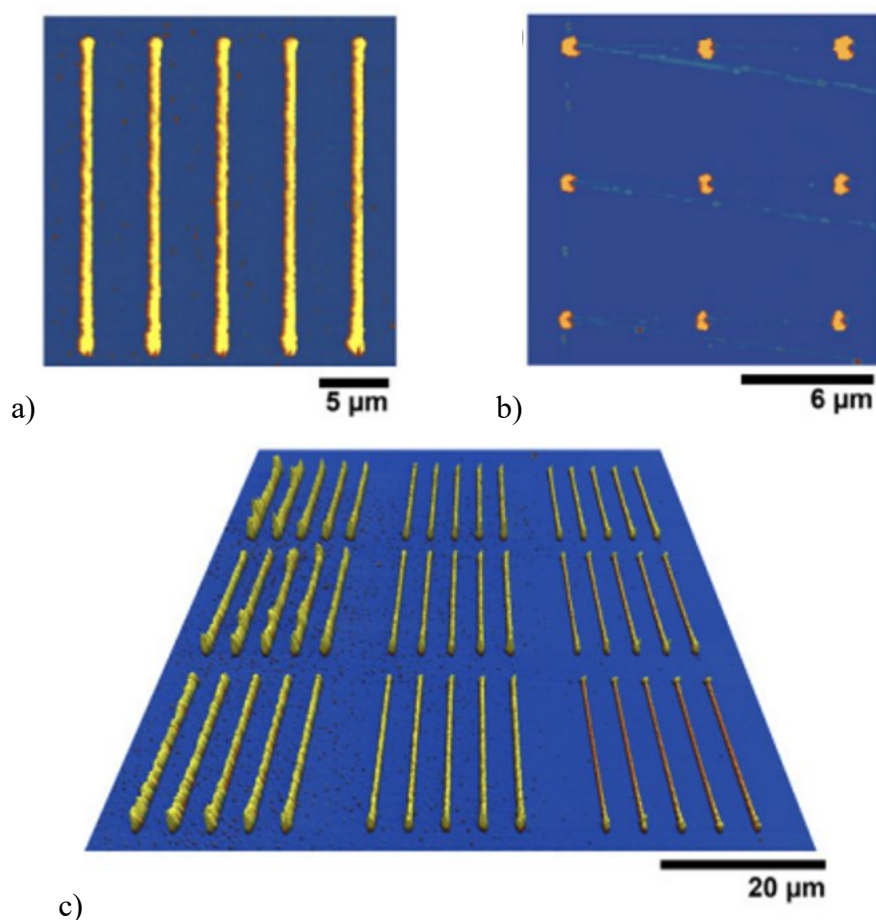
Figure 2.5 Example of thermal deposition of polyethylene (PE) nanowires by thermal DPN showing **a)** 20 µm long, 600 nm wide and 300 nm tall PE nanowires, **b)** PE nanodots, and **c)** array of PE nanowires written at different speeds[58].

A ballistic method that is considered as a key technology in the printing of polymer solutions is inkjet printing[59]. This method has been, for example, widely used in manufacturing processes for organic LEDs[60], polymer electronics[61], microlens arrays[62], sensors[63], and protein arrays[64]. In inkjet printing the ink is ejected through a nozzle in continuous or drop-by-drop manner. In the continuous mode the polymer ink is pumped through the nozzle in the form of a liquid jet, whereas the deposition of polymer ink in defined droplets with uniform distance between them is achieved by periodic perturbation which induces surface-tension driven breakup of the liquid jet. In both modes, after solvent evaporation the pattern on the substrate is formed. Periodic perturbation of the jet can be done by thermally or piezoelectrically induced pulses (Fig. 2.6). Thermal inkjet printers mostly use water as a solvent which limits the selection of the polymers that can be printed. On the other hand, piezo-based inkjet printers are suited for various solvents.
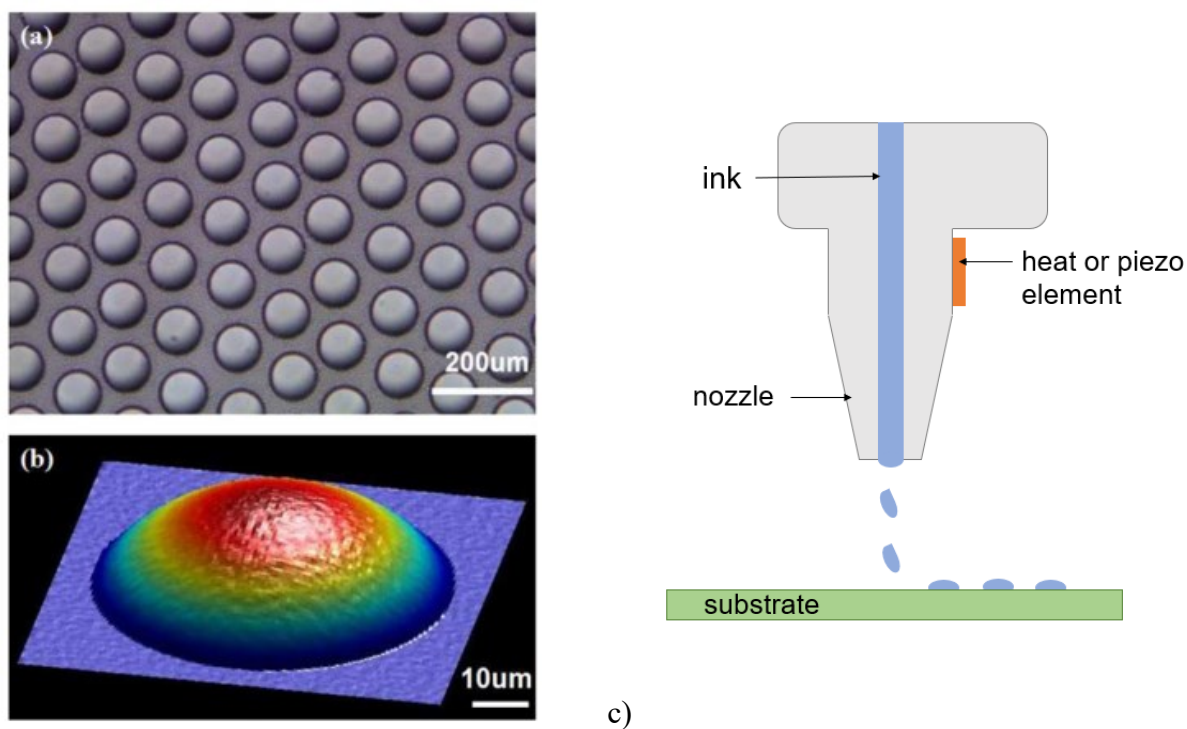
Figure 2.6 a) Microscopic image of inkjet printed microlenses and **b)** 3D profile of a single microlens (images taken from Tien et al.[62]). **c)** Schematic representation of inkjet drop-by-drop printing process (illustration adapted from Maleki et al.[65]).

Physical properties of the ink such as surface tension and viscosity are the crucial parameters that influence the volume and the shape of the deposited droplet[66]. Patterning of polymers with inkjet printing can also be done by deposition of reactive ink on a polymer film that selectively etches the polymer[67]. Also, polymers can be printed by the utilization of colloidal suspensions[68]. Reduction of the resolution under 10 μm while maintaining the properties of the polymer ink remains challenging.

2.1.2 Parallel lithographic patterning techniques

2.1.2.1 Subtractive parallel patterning methods

Photolithography, also known as optical lithography, is a high throughput method that has been used extensively for polymer patterning in the past four decades. It is a cost-effective method that is mostly used for fabrication of large area integrated devices. Resolution of the photolithography method is limited by the wavelength of the light that is used, and the attempts to reduce the size of the patterned features remains challenging. Dong et al.[69] showed the possibility to pattern with a resolution of 15 nm by surface plasmon interference. Patterns on surfaces are accomplished by exposing the photoresist layers on the substrates with UV light

through a patterned photomask. There are two types of photoresists: positive and negative, whereas positive one is more commonly used. During the irradiation exposure, photopolymerization, photo-crosslinking, functionalization, decomposition reactions or phase separation cause solubility changes of the photoresist in the exposed areas. After exposure, positive resist becomes more soluble whereas negative resist becomes less soluble[70]. Irradiation step is followed by removal of the exposed areas (positive resist) or unexposed areas (negative resist) with the solution called developer. After developing step, with dry or wet etching the predefined pattern from the photomask is transferred to the substrate. Final step is the photoresist removal with a solvent or by oxygen plasma. This method can be used for patterning polymer films as well as monolayers (e.g. polymer brushes)[71,72]. A schematic illustration of this method is shown at Figure 2.7. Examples of patterned polymer with photolithography are shown in Figure 2.8.
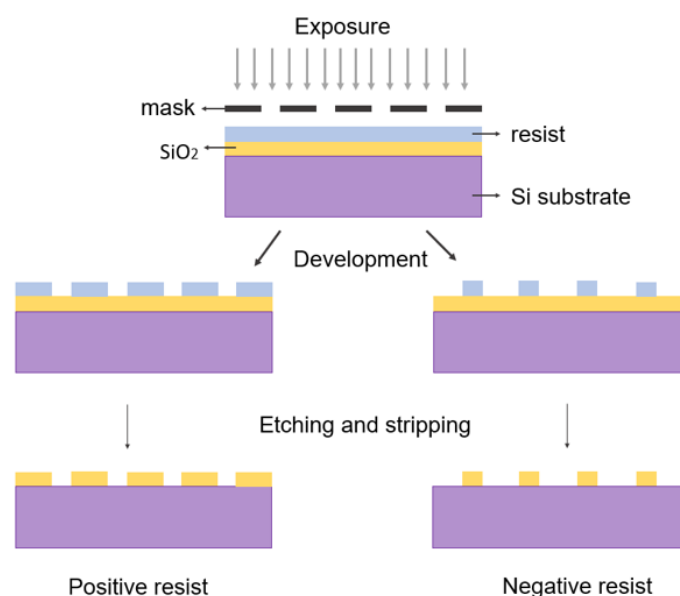

Figure 2.7 Schematic illustration of the photolitography method, showing the patterning process with positive and negative resists. Illustration is addapted from Schock et.al.[73].

Disadvantage of photolithography for patterning of polymers is the influence of direct photoirradiation which induces polymer degradation and results in their changed electronic and optical properties. Although functionalization of the polymer with cross-linkable reactive groups reduces the influence of the radiation, patterning of commercially feasible polymers has not yet been successful[74,75].
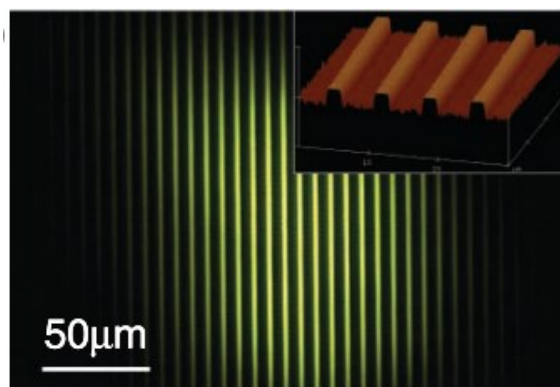
Figure 2.8 Example of polymer patterning by photolithography. Photoluminescence image of poly(9,9-di-n-octylfluorene-*alt*-benzothiadiazole) (F8BT) stripes with 2 µm width and 5 µm spacing between the stripes. AFM surface topography image is shown in the inset[76].

2.1.2.2 Additive parallel patterning methods

Microcontact printing method (µCP)[77] is easy contact method developed at Harvard University in the 90s by Whiteside and Kumar[12] that enables patterning of surfaces. In this method, usually elastomeric polydimethylsiloxane (PDMS) stamps with relief patterns are used for a transfer of ink on the counterpart surface. As the production of the PDMS is easy and cheap the method has found a broad spectrum of applications as in printing of metals[78], proteins[79], polymers[80], and DNA[81]. Due to the elastomeric properties of PDMS, the stamp is deformable which enables good contact between the contact elements of the stamp and the counterpart surface. Additionally, deformable PDMS stamp allows the removal of the stamp from the substrate without the smearing of the ink. Different kind of inks can be used because the stamp is quite inert, although the use of organic solvents is limited because it causes the swelling of the stamp[10].

To prepare the PDMS stamp, the mixture of PDMS prepolymer is mixed with curing agent, poured onto a template with patterned relief structures, and afterwards cured to crosslink the polymer. Preparation of the patterned master is commonly done by photolithography, but also by other methods such as e-beam writing and micro machining. Steps in preparation of the master by photolithography as well as development of the PDMS stamp are shown in the Figure 2.9[82].
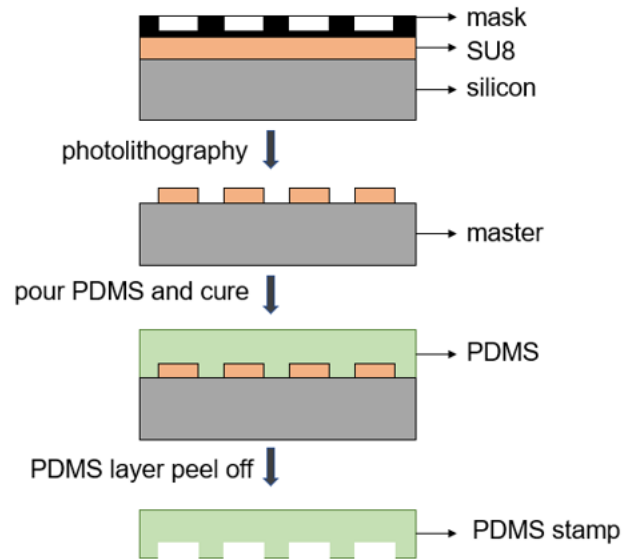
Figure 2.9 Photolithographic development of the master for the preparation of PDMS stamps and the development of the stamps against the master. Illustration adapted from Singh et al.[82].

Because the softness of PDMS there are limitations in the design of PDMS stamps regarding their dimensions. The height of the contact elements of the stamp should not be much larger than the width of the features because that leads to lateral collapse of the relief features with height-width aspect ratios $h/w > 5$ (Fig. 2.10b, c). Also, the height of the stamp cannot be smaller than the distance between the features, because that results in the sagging of the upper part of the stamp in between the features with aspect ratios $h/w < 0.5$. (Fig. 2.10d). Therefore, optimal aspect ratios for the development of the PDMS stamp are $0.5 < h/w < 5$, $h/d > 0.05$[83] (Fig. 2.10a).
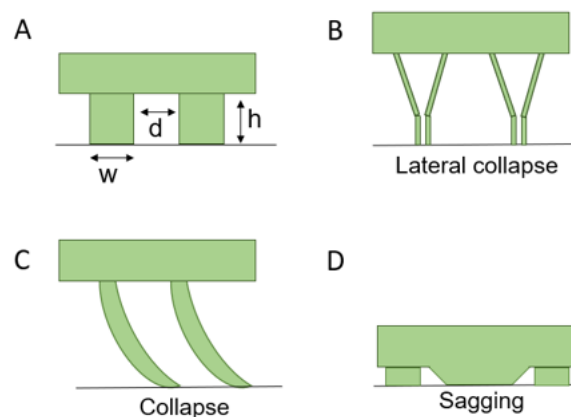

Figure 2.10 PDMS scheme illustrations showing **a)** ideal dimensions of PDMS stamp and possible problems that can occur from because of the softness of the stamp such as **b)** lateral collapse, **c)** collapse and **d)** sagging of the PDMS stamp[10].

A PDMS stamp is loaded with the ink and left to dry. After the solvent evaporation, the surface of the PDMS stamp with relief pattern is brought into contact with the substrate. After retraction of the stamp, the ink is transferred on the substrate replicating the pattern of the PDMS stamp (Fig. 2.11). Examples of structures fabricated by µCP are shown in Figure 2.12. Various polymer inks are suitable for µCP including conducting polymers and biological polymers[80,10].
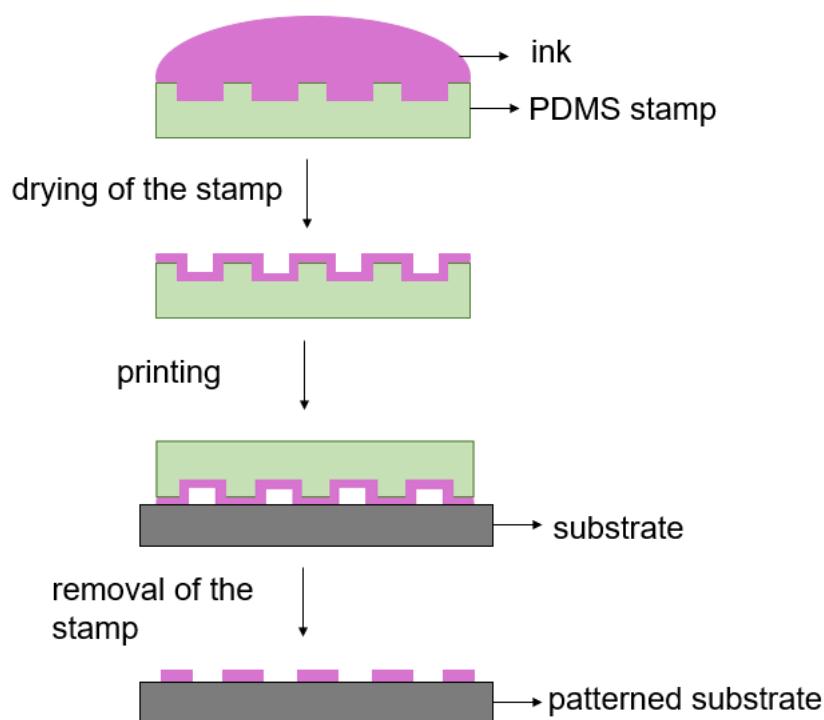

Figure 2.11 Illustration of the microcontact printing procedure. An inked PDMS stamp is dried and brought into contact with a substrate. After removal of the stamp, a patterned surface on the substrate is created[84].
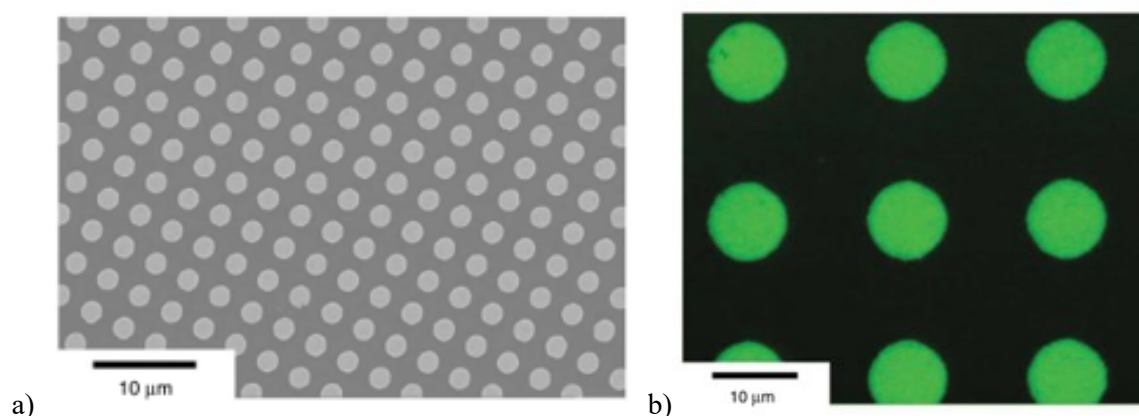

Figure 2.12 Examples of structures fabricated by µCP showing **a)** a SEM image of an array of silver discs, **b)** fluorescence optical micrography of an array of IgG dots[83].

To overcome the limitations and problems of using PDMS stamps in µCP, porous stamps were developed by Xu et al. in 2009. They developed PEI/PVP stamps consisting of blends of poly(etherimide) (PEI) and poly(vinylpyrrolidone) (PVP) polymers, and PES/PVP stamp

consisting of poly(ether sulfone) (PES) and poly(vinylpyrrolidone) (PVP) polymers by solvent-induced phase separation (Fig. 2.14). Pore sizes of the stamps lie in the range of several 100 nm and above and were successfully used for printing of various inks such as proteins and dendrimers. Porous structure of the stamps was used as ink reservoir, which enabled the multiple consecutive printing cycles without the reinking of the stamps[13].
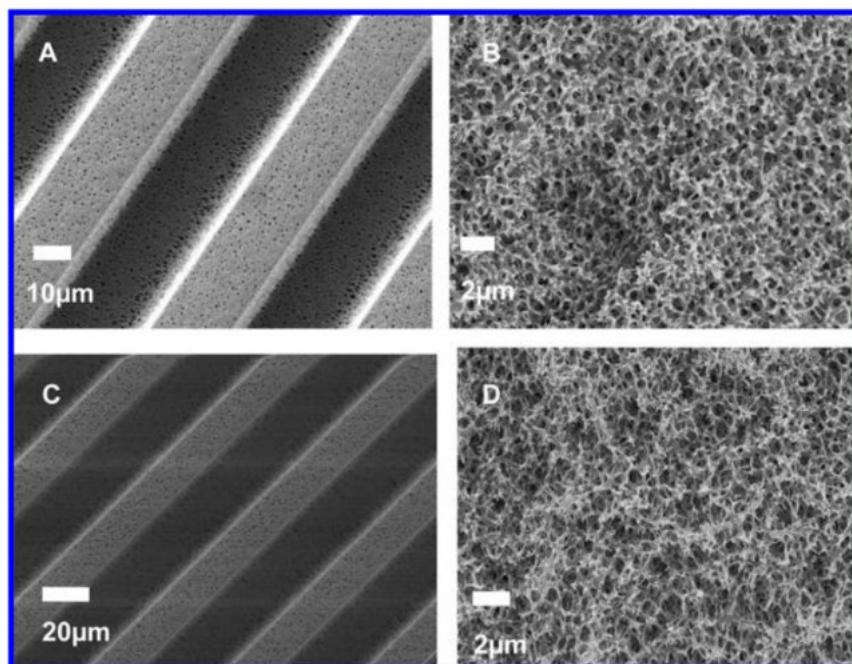

Figure 2.14 SEM images of porous stamps replicated against silicon mold with 20 μm wide lines showing **(a, b)** top and cross-section view of PEI/PVP and **(c, d)** top and cross-section view of PES/PVP porous stamps[13].

In 2018 Schmidt et al. developed mesoporous silica stamps by sol-gel synthesis, replicated against macroporous silicon (mSi) that enabled the printing from the organic solutions up to the nanometer range. Contact elements of the stamp were hexagonally ordered with the round tips with a diameter of ~ 450 nm and a pore size of 31 nm and 44 nm. After the filling the stamp with the ink by immersion of the stamp into the ink, contact elements of the stamp were brought into the contact with the substrate. Ink transfer from the stamp to the substrate was done through the formation of the liquid bridges between them. Due to the solvent evaporation the nonvolatile ink components were drawn into the liquid bridge. Retraction of the stamp by from the substrate resulted in the liquid bridges rupture leaving the deposited droplets of the ink on the substrate. Porous structure of the stamp allowed printing in multiple cycles without reinking, as the porous stamp also served an ink reservoir[14]. Capillary stamping with porous polystyrene-*block*-poly(2-vinylpyridine) PS-*b*-P2VP stamps of AgNO$_3$ droplets from solution on silicon wafers was reported by Han et al. in 2018. The stamping was done under ambient conditions obtaining the

droplets diameters of ~ 730 nm[15]. Scanner-based capillary stamping was developed in 2020 by Hou et al. by incorporating the composite porous polystyrene–*block*-poly(2-vinylpyridine)/controlled porous glass PS-*b*-P2VP/CPG stamps into the automated stamping system under defined atmospheric conditions. With this method more than 800 consecutive stamping cycles without reinking were possible with a smallest droplet diameters of ~ 4 µm, as well as simultaneous stamping of two different inks[16]. In 2021 Guo et al. printed rhodamine B dye with diameters of ~ 500 nm on glass slides using porous phenolic resin stamps by capillary stamping[85]. In 2022 using porous PS-b-P2VP stamps Alarslan et al. patterned indium tin oxide (ITO) substrates with micropatterned $LiNbO_3$ films[86]. And in the same year reported patterning of ITO substrates with ordered monolayers of nickel ferrite dots with diameters of ~ 700 nm by capillary stamping using DNHG-derived aerogel stamps under solvothermal conditions[87].

2.1.2.3 Imprint lithography

Nanoimprint lithography (NIL) is a parallel stamping method for topographical patterning of polymers. The process of NIL comprises the pressure induced transfer of topographical patterns of a mold into the softened thermoplastic polymer or liquid polymer precursor. During imprinting, polymer material fills the spaces between the microscale features of the mold and after lift-off of the mold, a negative copy of the master is obtained. There are two major types of NIL, thermal nanoimprint lithography (t-NIL) and ultraviolet assisted nanoimprint lithography (UV-NIL)[74].

In thermal NIL, also commonly known as hot embossing, polymer is softened by heating to lower the viscosity and Youngs modulus of the polymer and to make it easily deformable. Requirements that should be fulfilled are that Young's modulus of polymer should be lower than the one from the mold and that applied pressure should be higher than the sheer modulus of the polymer[88]. The polymer is heated above its glass transition temperature (T_g) and it has been shown that the optimal temperature is 70 - 80 °C above T_g of used material[26].

Imprint is done with hard or soft molds, each of which having advantages and disadvantages. Material from which the mold is made must be stable also at elevated temperatures. Molds that were initially used were rigid silicon molds. Major limitation when using hard molds are the defects in the patterned area because of wear of the master mold, side wall deposition and breaking of the molds after multiple imprint cycles. To overcome the limitations of using a rigid mold and increase quality of imprint, soft molds were developed. Flexibility of soft molds

allows better contact between mold and the substrate and imprint is less affected by particle contaminations. PDMS and ETFE are two most common materials for soft mold production[89]. Difficulties in patterning of highly viscous polymers with thermal NIL is the limitation of this method.

The second commonly used method of nanoimprint lithography is UV-NIL. In this method, photosensitive polymer precursors with high curing rate are patterned. After the imprint at room temperature, the polymer precursors are cured with UV radiation. UV-transparent molds are required for UV-NIL and are commonly made from quartz, hydrogen silsesquioxane[90] and indium tin oxide[91]. Advantages of UV-NIL in comparison to thermal NIL are shorter imprint times, lower applied pressure for the imprint, possibility to print on fragile substrates, no need for heating of the stamp, substrate or polymer precursor, and lower pressure during imprint and better filling of the cavities of the mold because of the lower viscosity of the polymer[92]. Limitation of this method is the sensitivity to oxygen and polymer shrinkage. To overcome this problems, new polymers such as oxygen insensitive thiolene polymers are used[93].

After the imprint, residual layer of polymer that is left between the features on the substrate is removed by etching (e.g. RIE). With this method patterns in a range from few hundred micrometers to 10 nm are obtained[94]. NIL methods have been used in wide range of applications such as in electronics[11], semiconductors[95], optics[96] and biotechnology[97]. Schematic illustration of the method is shown at Figure 2.15.
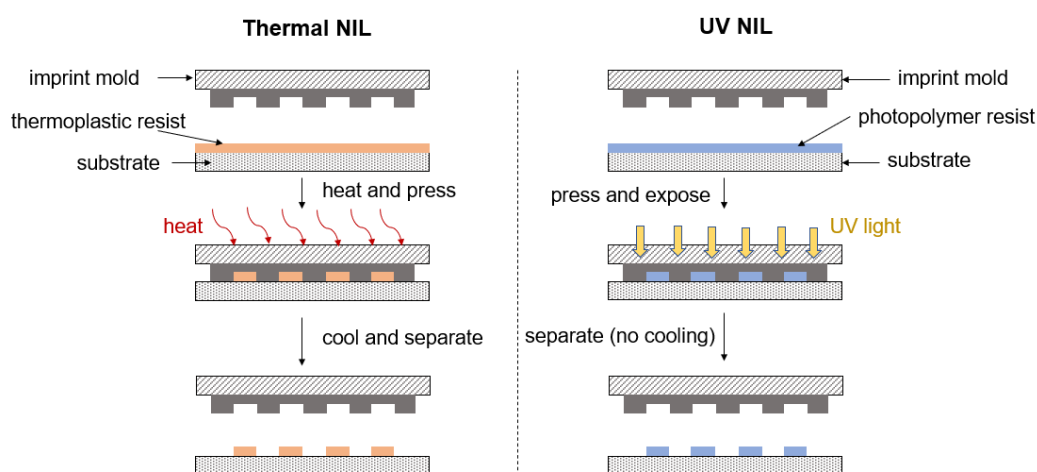

Figure 2.15 Scheme of thermal and UV nanoimprint lithography processes. Illustration is adapted from Kooy et al.[98].

2.2   Nanoporous gold by dealloying process

Although the process of dealloying in the context of corrosion has been known since more than a century, it started to raise scientific interest in the 1980s when nanoporous gold (np-Au) was used as a model for investigating the dealloying process and stress corrosion cracking[99,100]. Wide interest in dealloying was then triggered in the 2000s with the work of Erlebacher and coworkers[101], that led to better understanding of the process and nanoporous materials properties. Due to the high surface area (in the range of 3-10 m^2/g), mechanical and noble properties, and high electrical conductivity, np-Au has been widely researched for possible applications in various fields of nanotechnology such as in sensors[102], actuators[103], and electrodes[104] for electrochemical use[105].

Dealloying processes have mostly been researched on silver-gold (Ag-Au) alloys that are commonly used as a prototype for dealloyed materials. Nevertheless, many other alloys such as np-Ag[106], np-Ni[107], np-Cu[108], np-Pt[109] have been also of great interest for various applications and research.

Dealloying process, also known as selective dissolution or leaching, is corrosive process that occur because of the difference in the nobility of the elements in the alloy. Here, the less noble constituent of the alloy is removed from the alloy in a strongly corrosive environment. By the Hume-Rothery rules because of similar atomic radius, crystal structure, valence and electronegativity, the Ag-Au system forms totally miscible alloys in the solid phase[110]. In the Ag-Au alloy, as a result of the dissolution of the Ag (Ag is less noble element than Au) that create vacancies in the alloy, and because of the surface diffusion of the Au atoms, a porous network is created[111]. For dealloying to occur it is necessary that the Ag as less noble element is present above a certain percentage known as a parting limit. The Ag-Au alloy shows a parting limit of ~55 at. % Ag[112].

Evolution of porosity during the dealloying is shown in Figure 2.16 illustrating the results of an atomic scale Monte Carlo simulation[113]. In initial stages at electrochemical potentials above the composition dependent critical potential V_c (potential at which the less noble metal starts to dissolve), the Ag atoms from the binary Ag-Au alloy are dissolved and removed from the alloy in a so-called layer by layer manner (Fig. 2.16a). As a result, the Au atoms accumulate at step edges by uphill diffusion where the adatoms are moving from the low concentrations areas to the high concentration areas (Fig. 2.16b). This can be described by the Cahn-Hillard diffusion kinetics[114]. As the dealloying process continues, further Ag atoms are exposed to the electrolyte

around the base of the Au clusters that were formed during the previous dealloying steps and surface rearrangements. As the Au clusters grow and because there are not enough Au atoms to passivate them effectively, consequently the Au clusters are being undercut. As a result, the pores are created which leads to the increase in the surface area (Fig. 2.16c, d), and because some further Au atoms will nucleate into new mounds rather than diffuse to the existing ones. As a result, the porous network is formed (Fig. 2.16e) consisting of mostly Au rich surfaces and the Ag rich bulk. Due to their large surface areas, and environment where the surface atoms are enough mobile, the length scale of the pores inside the bulk tends to increase over time. This is because the Au atoms move from smaller to larger ligaments. This phenomena is known as coarsening (Fig. 2.16f)[113,115].
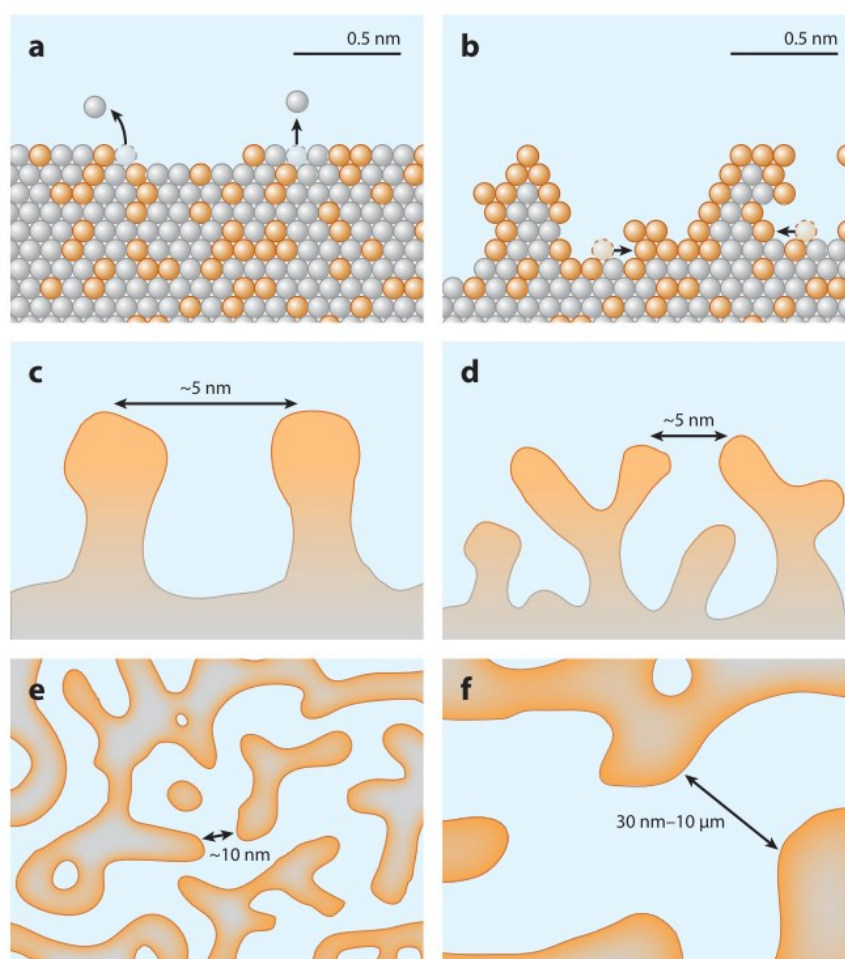
Figure 2.16 Schematic presentation of the porosity evolution model in the dealloying of Ag-Au alloy (Au atoms-orange colour, and Ag atoms-grey colour), showing **a)** dissolution of less noble Ag atoms from the alloy. **b)** As the removal of Ag atoms proceeds layer by layer, surface diffusion of Au atoms passivates the low-coordination sites which leads to the surface roughening. **c)** With further dealloying, there are not enough Au atoms to completely passivate the increasing surface area, which leads to **d)** undercutting and bifurcation of ligaments. **e)** Formed porous structure with Ag rich bulk and Au rich surfaces. **f)** Increase in the length scale as a result to coarsening, which leaves the structure with reduced Ag content. Illustration is taken from the McCue et al.[113].

There are two common routes how the dissolution of the Ag-Au alloy can be done. The first method is dealloying by nitric acid, also known as free corrosion, where the alloy is simply immersed into the nitric acid. The second is electrochemical dealloying that is carried out in electrochemical cell with perchloric acid as electrolyte. In comparison to the free-corrosion method, electrochemical dealloying offers better control of pore morphology[116] and parameters such as temperature of the electrolyte[117] and critical potential[118]. Major advantage of electrochemical dealloying is better control of the pore size in the alloy because the applied potential increases the Ag dissolution rate in comparison to the Au diffusion rate which results in finer porosity. Despite all the advantages of the electrochemical dealloying, in some cases the dealloying with nitric acid is preferable. For example, when there is no possibility to electrically connect the sample or in dealloying of thin films such as gold leaves that are generally dealloyed by free-corrosion in nitric acid[111].

2.3   Properties of polystyrene

Polystyrene (PS) is mostly used thermoplastic polymer due to its optical clarity, electrical isolation, chemical resistance, and low cost. Because of its properties PS is used in a wide range of applications such as electronics, food industry, automotive industry, and medicine[119,120,121]. Atactic polystyrene that was used in this work is amorphous due to the randomly distributed phenyl groups along the backbone[122, 123].

PS is obtained by additive polymerization of the monomer styrene and is vitrified at room temperature. Depending on the degree of polymerization the molecular weights of polymer molecules are not identical but have different chain lengths, which results in molecular weights distribution. Therefore, in case of polymers we speak about the average values of molecular weights such as number-average molecular weight (M_n) and weight-average molecular weight (M_w). Measure of polydispersity of the polymer mixture is called polydispersity index (PDI) and is given as a ratio between the weight-average and number-average molecular weights (M_w/M_n)[124]. Influence of the molecular weight on glass transition temperature is expressed with the Fox-Flory equation:

$$T_g = T_{g\infty} - \frac{K}{M_n}$$

where $T_{g\infty}$ is the glass transition temperature at infinitely high molecular weight and K is polymer specific constant[125]. For polystyrene T_g increases significantly with increase of M_n until reaching the entanglement molecular weight (M_e) which quantifies the average molecular weight of chain segments between two entanglements. Whereas beyond M_e, T_g does not change very much with increasing the M_n and approaches a constant value of ~ 100 °C for high molecular weight PS[126, 127].

Melt viscosity when the shear rate is zero is proportional to the molecular weight of the polymer until the critical entanglement molecular weight M_c[128], which is for PS from around 30 kDa to 40 kDa[129]. Beyond the M_c viscosity is proportional to the 3.4th power of M and therefore increases drastically with increasing the molecular weight of the polymer:

$$\eta = \begin{cases} k_1 M, & M < M_c \\ k_1 M^{3.4}, & M > M_c \end{cases}$$

where k_1 is coefficient[130]. Elongation, tensile strength, and tensile impact strength also increase with the increase of the molecular weight[131]. It has been established for many polymers that relation between M_c and M_e is $M_c \approx 2M_e$[132]. Reported entanglement molecular weights M_e and M_c for PS at 217 °C are ~18100 g/mol and ~ 31200 g/mol respectively, which is comparable to the temperature at which the stamping in this work was carried out[133].

Entanglement has a significant impact on the morphology, rheology, and mechanical properties of polymers. With high level of entanglement, the polymer toughness increases, and excessive entanglement causes the high melt viscosity which results in the processing difficulties. High value of M_e is the indication for a lower entanglement density. In this case the lower elastic modulus can be expected because the melt has not been yet restored to its equilibrium state[130]. In this work, polystyrene was used as model polymer ink with narrow molecular weight distribution for the proof of the principle of the capillary stamping method with composite np-Au stamps.

2.4   Properties of P(VDF-TrFE)

Poly(vinylidenefluoride)-trifluoroethylene (PVDF-TrFE) is a semi crystalline statistical copolymer with excellent ferroelectric, pyroelectric, and piezoelectric properties[134,135]. Due to its electromechanical properties and low dielectric constant P(VDF-TrFE) copolymers were intensively investigated for their possible applications in actuators, sensors, energy harvesting,

and flexible electronics[136, 137, 138].

P(VDF-TrFE) consists of the monomers vinylidene fluoride (VDF) and tri-fluoroethylene (TrFE) as. Repeating units of P(VDF-TrFE) copolymer is shown in the Figure 2.17.
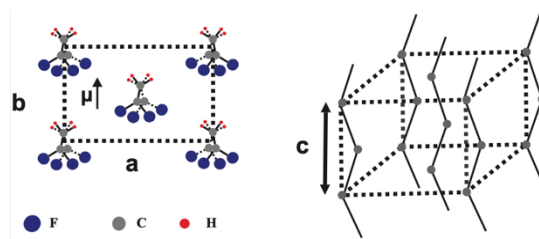

Figure 2.17 Repeating units of P(VDF-TrFE).

P(VDF-TrFE) is synthesized by radical polymerization of VDF and TrFE in dispersed suspension or emulsion media, with a 50-80 mol% content of VDF crystallizes from melt or solution directly into a ferroelectric β-phase without additional stretching as for PVDF[139]. Due to the larger interchain distance in P(VDF-TrFE) in comparison to the ferroelectric β-phase of PVDF the energy barriers for dipole (polarized C-F bond) rotations around the backbone axis (c-axis) are lower . Therefore, P(VDF-TrFE) shows a ferroelectric to paraelectric phase (rotator phase) transition[140], with a characteristic Curie temperature (T_c) below the melting point (T_m). The observed Curie temperatures of P(VDF-TrFE) vary from 60 °C to 135 °C as the molar fraction of VDF increases from 50 % to 80 %[141].

Crystallization of P(VDF-TrFE) takes place by chain-folding into a hexagonal paraelectric phase and transforms into an orthorhombic unit cell upon the paraelectric/ferroelectric phase transition with parallel chains in the extended *trans-trans* conformation. This results in lamellar crystallites separated by an amorphous matrix with chain-folds at the surface of the lamellae, inter-crystalline links, and entanglements[142]. Ferroelectric and hence piezo- and pyroelectric properties of P(VDF-TrFE) strongly depend on the degree of crystallinity. Therefore P(VDF-TrFE) is usually annealed in the paraelectric rotator phase with its higher chain mobilities to reach degrees of crystallinity of up to almost 90 %[143].

3   Experimental

3.1   Chemicals and materials

Table 3.1. Chemicals used in this work.

Chemical	Grade	M_w [g/mol]	M_n [g/mol]	PDI	Supplier
Dimethyldichlorosilane (DMDCS)					Merck
N-hexane	> 95 %				Fisher chemical
Nitric acid	64 – 66 %				Sigma Aldrich
Polystyrene		239 000	233 000	1.03	Polymer Standards Service (Mainz, Germany)
Poly (vinylidenefluoride)-trifluoroethylene (PVDF-TrFE)		209 740[144]	100 008[144]	2.09	Piezotech (SA, France)
Toluene					Sigma Aldrich
Butanone					Fluka

Macroporous silicon (mSi) templates were purchased from Smart membranes (Haale/Saale, Germany) and silicon wafers were purchased from Siegert Wafer GmbH (Aachen, Germany). Cover glass slides (18 mm x 18 mm; thickness 1 mm) used as substrates, were purchased from Th. Geyer GmbH & Co. KG.

3.2   Procedures and stamp development

Development of the composite nanoporous gold (composite np-Au) stamps with polymer ink film was done in consecutive steps: (1) silanization of the macroporous silicon templates (mSi), (2) deposition of a silver-gold alloy film on silanized mSi templates, (3) drop casting of polymer solution on the AgAu film deposited on the mSi template, (4) annealing of the polymer-AgAu-mSi samples and (5) dealloying of the metallic AgAu film from the polymer-AgAu-mSi sample. All the steps are described in detail below.

3.2.1   Silanization of macroporous silicon templates

Templates of macroporous silicon (mSi) were cut into pieces 1 x 1 cm^2 in size. The mSi had hexagonally ordered pores with an interpore pitch of 1.5 µm and a pore depth of 600 nm. At their openings, the macropores were ~ 900 nm wide and they narrowed to their bottoms to ~ 600 nm. The mSi were then put in a mixture of 500 µl (0.004 mol) of dimethyldichlorosilane (DMDCS) and 9.5 g n-hexane at 40 °C for 24 hours. Then, the samples were washed with ethanol and dried in air.

3.2.2   Deposition of Ag-Au films on macroporous silicon templates

Deposition of Ag-Au films on the mSi templates was done in a DC magnetron sputter coater using a 99.99 % purity Ag-Au target (68 mol % Ag and 32 mol % Au, corresponding to 54 mass % Au and 46 mass % Ag). The base pressure of the device was $5.7 \cdot 10^{-3}$ mbar under gas flow (7 sccm argon 5.0), working at 50 W in the power regulation mode with a target distance of 7 cm. After 90 min deposition time with a deposition rate of 30 nm/min, the obtained thickness of Ag-Au films was ~ 2.7 µm.

3.2.3   Electrochemical dealloying of AgAu-mSi

AgAu-mSi samples were set in a three-electrode Ag/AgCl cell with 200 ml 0.7 M HClO$_4$ electrolyte. In the potentiostatic regime dealloying was done at 0.8 V and in galvanostatic regime at 1.5 mA. Experiments were conducted in Autolab PGSTAT302N (Metrohm). instrument.

3.2.4 Development of composite nanoporous gold stamps with polystyrene films

3.2.4.1 Drop casting of polystyrene solution on the AgAu-mSi

For the preparation of polystyrene solution, 0.1 g of polystyrene was dissolved in 1 ml toluene and left overnight in a shaker at 300 rpm. Then, the solution was drop-casted in steps on the AgAu surface deposited on the mSi. First, 40 µl of the solution was dropped on the AgAu surface and left to dry at room temperature for ~ 30 min. During drying solvent evaporated, and thin solid films of polystyrene were formed on the AgAu surface. After ~ 30 min, an additional 40 µl of polystyrene solution was dropped on the previously formed PS film on the AgAu-mSi and left to dry for ~ 30 min. This step was repeated one more time and the total amount of used polystyrene solution was 120 µl. For the development of the stamps with thicker polystyrene films, 420 µl of polystyrene solution was dropped on the AgAu surface deposited on the mSi template in seven steps (each step was 60 µl) with ~ 30 min of drying time in between the steps.

3.2.4.2 Annealing of the PS-AgAu-mSi

PS-AgAu-mSi samples with thinner polystyrene films (with 120 µl of solution) were annealed for 8 hours at 200 °C in an argon atmosphere.

Thicker PS-AgAu-mSi samples (with 420 µl of solution) were first annealed for 18 hours at 200 °C and then for 5 hours at 210 °C in Ar atmosphere.

3.2.4.3 Dealloying of PS-AgAu-mSi sample by free corrosion

For dealloying, PS-AgAu-mSi samples were immersed in 15 ml of 21.7% HNO_3 solution in a beaker. After the samples were immersed in the nitric acid, the dissolution of the Ag from the AgAu film of the PS-AgAu-mSi sample started on the edges, because the AgAu film was covered on one side with the PS film and with the mSi on the other side. After some time in the HNO_3, the PS-AgAu separated from the mSi template. Because this separation process was spontaneous, the time required for the separation of the PS-AgAu from the mSi was different for each sample, which also influenced the overall dealloying time for each sample. After the separation from the mSi, the whole surface of the AgAu film was exposed to the HNO_3 on one side and the dealloying process was faster. Overall dealloying time was from 24 hours until 2 weeks, depending on the sample. The end of dealloying step was recognized by the color change of the metallic film from silver-gray to brown. The formation of the porosity throughout the film was observed visually with the color change of the metallic film from silver-gray to brown.

The obtained composite polystyrene nanoporous Au stamps were washed three times in distilled H_2O and then dried at 40 °C for 24 hours.

3.2.5 Development of composite nanoporous gold stamps with P(VDF-TrFE) films

3.2.5.1 Drop casting of P(VDF-TrFE) solution on the AgAu-mSi

A solution of 0.1 g/ml polyvinylidenefluoride-trifluoroethylene P(VDF- TrFE) in 2-butanone was prepared in an ultrasonic bath (Elmasonic P) at 60 °C, 100 W, 37 kHz for 45 min. Before the drop-casting of the polymer solution onto the AgAu-mSi samples, the latter were placed in a Petri dish and 200 µl of 21.7% HNO_3 was dropped on the AgAu surface for ~ 30 min. This step was repeated two times and in between the steps the AgAu-mSi samples were rinsed with distilled H_2O. After the second step, the samples were dried at 40 °C for ~ 1 h. Then, 40 µl of P(VDF-TrFE) solution was dropped on the AgAu surface of the coated mSi templates and left to dry for ~ 30 min at room temperature. This step was repeated two times. During the solvent evaporation, the AgAu-P(VDF-TrFE) films separated spontaneously from the mSi template and as a result, freestanding AgAu-PVDF-TrFE films were obtained.

3.2.5.2 Annealing of the P(VDF-TrFE)-AgAu-mSi

Because of the drop-casting process, during solvent evaporation bubbles remained trapped in the polymer films that were deposited on the Ag-Au-mSi samples. To remove the bubbles from the films and eliminate residual stress in the films, the samples were annealed in an argon atmosphere. AgAu-mSi samples with P(VDF-TrFE) films were annealed at 145 °C for 1 h in an argon atmosphere.

3.2.5.3 Dealloying of P(VDF-TrFE)-AgAu-mSi by free corrosion

P(VDF-TrFE)-AgAu samples were immersed in 15 ml of 21.7% HNO_3 solution for 48 h at room temperature. After the dealloying the samples were washed three times in distilled H_2O and dried at 40 °C for 24 hours.

24

3.3   Stamping procedures

3.3.1   Substrate preparation

In this work two different substrates were used for stamping experiments, glass slides and aluminium coated silicon wafers (Al/Si). Stamping of polystyrene ink was done only on glass substrates, while stamping of P(VDF-TrFE) ink was done on both glass, and Al/Si substrates.

(i) Cover glass slides (approx. 18 mm x 18 mm) with a thickness of 1 mm were cut into pieces with a size of approximately 9 x 9 mm^2 and cleaned in an ultrasonic bath in distilled water for 30 min and then three times in ethanol (15 min each). Before use, substrates were dried in an argon flow.

(ii) Silicon wafers (size 9 mm x 9 mm) were washed in ethanol in an ultrasonic bath and coated with aluminium in vacuum at 10^{-4} mbar in a thermal evaporator device Balzers BAE 120. Before use, Al/Si substrates were cleaned in argon stream for a few seconds.

3.3.2   Stamping procedures

Composite nanoporous gold stamps with PS and P(VDF-TrFE) were prepared with a size of 1 cm^2. For stamping, small pieces of the stamp were cut with a scalpel (~ 2 mm x 2 mm). In all experiments in this work, composite np-Au stamps were placed on the top of the stainless-steel holder (height 3.6 cm; diameter 3.5 cm; *m*=40g) inside the cylindrical oven (Fig. 3.1a) on the gold coated glass (at 20 mA in three consecutive cycles for 15 s in JEOL sputter coater) that served as a base for the placement of the stamp inside the oven (Fig. 3.1b) and was glued on the holder with double-sided polyimide tape.
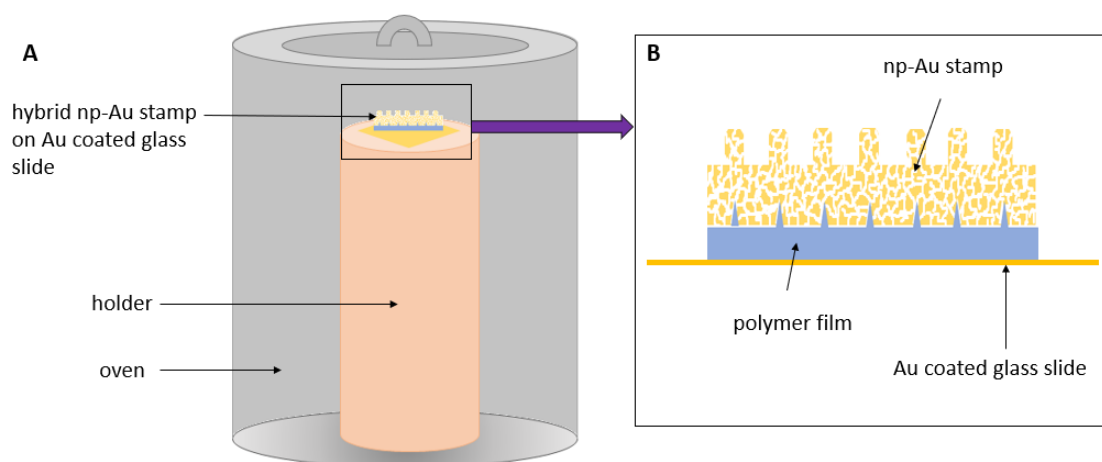
Figure 3.1 (a) Schematic illustration of the oven (gray) that was used in the stamping experiments with the composite np-Au stamp placed inside the oven on the stainless-steel holder (peach) and **(b)** enlarged illustration of the composite np-Au stamp (yellow) with polymer film (blue) that is placed on the Au coated glass slide (orange).

3.3.2.1 Stamping method I – by hand

Glass substrates were glued on the stainless-steel holder with double-sided polyimide tape as shown in the Figure 3.2. When the stamp was heated, the glass substrate was brought into the contact with the composite np-Au stamp in the oven by the hand.
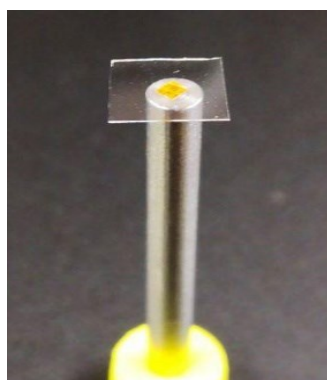
Figure 3.2 Image of the glass substrate (edge lengths ~ 9 mm) glued on the stainless-steel holder.

3.3.2.2 Stamping method II - without pressure

In the stamping method without pressure the substrate was placed on the heated composite np-Au stamp with tweezers. After the desired stamping time the substrate was retracted from the top of the stamp with the tweezers. In all the experiments the oven was closed during the stamping.

3.3.2.3 Stamping method III - with pressure

After placing the substrate on the stamp with the tweezers, as in the previous method, a cylindrical weight (d= 2 cm; h=1.64 cm; m=40 g) was placed on top of the substrate. The pressure applied on the stamp was ~ 0.4 MPa. During the stamping in all experiments that were done with this stamping method the oven was kept open.

3.3.3   Stamping of PS melts

Stamping of the polystyrene on the glass substrates was done with the composite np-Au stamps with a bulk polystyrene reservoir. Stamping of PS melts in all experiments was done at 200 °C. Temperature inside the oven was ~ 190 °C and was measured with the contactless thermometer on the piece of back side of anodic aluminum oxide (AAO) sample that was placed on the holder next to the composite np-Au stamp. For thermal equilibration the stamps were kept at the target temperature for ~ 20 min. Stamping of the PS melts on unmodified glass substrates (see section 3.3.1) was done with all three stamping methods. Stamping of PS on glass with the stamping method I was done with 5 min stamping time. Stamping times for the stamping method II was 10 min, 13 min, 20 min and 27 min. Stamping times for the method III were 5 min, 15 min, 16 min, 17 min, 18 min, 19 min, 20 min, 25 min and 30 min.

3.3.4   Stamping of P(VDF-TrFE) melts

Stamping of P(VDF-TrFE) ink was done on two different substrates, glass, and Al/Si substrates. In all experiments stamping was done with the stamping method III at 205 °C. Temperature inside the oven was ~ 195 °C and was measured with the contactless thermometer on the piece of back side of anodic aluminum oxide (AAO) sample that was placed on the holder next to the composite np-Au stamp. For thermal equilibration the stamps were kept at the target temperature for ~ 20 min.

(i) Stamping of P(VDF-TrFE) melts on glass substrates was done with stamping times of 10 min, 15 min, 16 min, 17 min, 18 min, 19 min, 20 min, 25 min and 30 min.

(ii) Stamping of P(VDF-TrFE) melts on Al/Si substrates was done with stamping times of 1 min, 2 min, 3 min, 4 min, 5 min, 6min, 7 min, 10 min, 15 min and 20 min.

3.4 Characterization methods

3.4.1 Atomic force microscopy

AFM measurements were performed in tapping mode on NT-MDT Ntegra device with aluminium coated silicon cantilevers with force constants of 30-70 N/m from MikroMasch.

3.4.2 Piezoelectric force microscopy

Piezoresponse force microscopy[145,146] (PFM) is a variation of the atomic force microscopy method that allows imaging and manipulation of domains in ferroelectric materials. In PFM a sharp conductive AFM tip is brought into an elastic contact with ferroelectric P(VDF-TrFE). Applying a sinusoidal current (AC) to the ferroelectric material is followed by a mechanical response, i.e. an expansion or compression of the material based on the inverse piezoelectric effect inherent to all ferroelectric materials. According to Landau-Ginzburg-Devonshire theory, the piezocoefficient of the orthorhombic P(VDF-TrFE) depends on the local polarization orientation ($d_{33} \sim P_{S3}$). Hence the piezoresponse follows the applied AC voltage in phase (0°) or with a phase shift of 180°, respectively as depict in Figure 3.3b below. PFM is therefore capable to measure and image local variations of the remnant polarization orientation. Furthermore, application of voltage pulse beyond the coercive field strength of the ferroelectric material allows to reorient the remnant polarization and to record local hysteresis loops similar to macroscopic hysteresis loops characteristic for ferroelectric behavior.

PFM measurements were carried out in a NT-MDT Ntegra AFM device. Imaging and local poling experiments (point poling and hysteresis loops) were performed by applying rectangular voltage pulse to the Al back electrode and AC voltage to a Pt/Ir coated cantilever beam (CSG01, Pt/Ir, typ. force constant 0.03 N/m from NanoAndMore (Wetzlar, Germany)). Voltage pulses were amplified to the appropriate voltage (± 15 V) by a homebuilt amplifier (University of Osnabrück). Local hysteresis loops were recorded with rectangular voltage pulses of 300 ms width and 300 ms waiting time with a triangular shaped envelope of the pulse train. Only the out-of-plan (vertical) piezoresponse was further analyzed during all experiments.

(a)	(b)
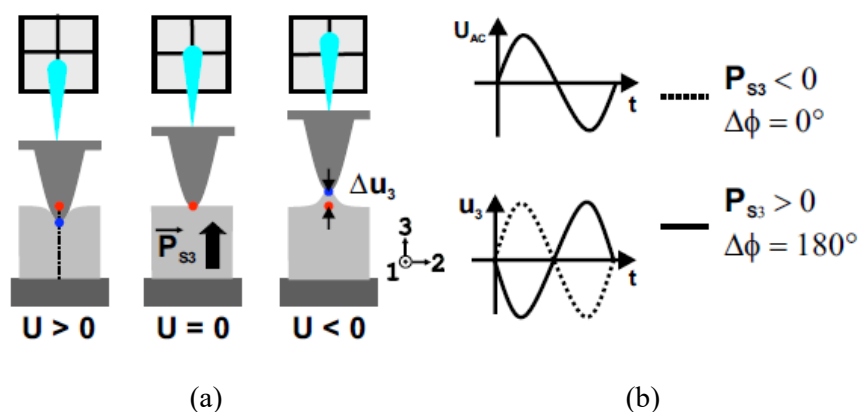
Figure 3.3 (a) Illustration of PFM for vertical domains ($P_{s3} \neq 0$). Inhomogeneous electrical field of the tip causes a dynamic local expansion or contraction of a surface of the sample with a maximum amplitude of Δu_3. **(b)** The orientation of the domain ("up"/"down") determines the sign of the piezo constant and thus the phase shift (0 or 180).

3.4.3 Scanning electron microscopy (SEM)

SEM measurements of the samples were done with a Zeiss Auriga scanning electron microscope using InLens and secondary electron chamber (SESI) detectors. Accelerating voltages used were varied depending on the investigated samples. For the imaging of the surfaces of nanoporous gold stamps, accelerating voltages of 7 kV or 15 kV were used. SEM of the stamped substrates was done at accelerating voltages of 3 kV and 15 kV. Before the measurements, substrates with stamped polymer inks were coated with gold in three consecutive cycles at 20 mA for 15 s in JEOL sputter coater or with platinum/iridium in three consecutive cycles at 20 mA for 15 s in Emitech K575X sputter coater.

3.4.4 Image analysis

The heights of the printed polymer dots were determined by analysis of the AFM images using the program Gwyddion. To determine diameter and the shape of polymer dots stamped on substrates, analysis of SEM images was done with the image analysis program Fiji-ImageJ. To get corresponding binary SEM images for analysis, a binarization threshold was chosen in such way that the size and the shape of the analyzed printed dots was invariant with respect to small brightness changes. From the particle analysis in the Fiji-ImageJ program, values for the area *A,* the perimeter *P* as well as the major and minor axis were obtained. From these results, the diameter of the dots *d,* the circularity *c* and the aspect ratio *AR* were calculated with the OriginLab program by the equations:

$$d = \sqrt{4 \cdot \frac{A}{\pi}} \qquad (1)$$

$$c = 4 \cdot \pi \cdot \frac{A}{P^2} \qquad (2)$$

$$AR = \frac{major\ axis}{minor\ axis} \qquad (3)$$

4 Results

4.1 Development of composite nanoporous gold stamps

The development of composite nanoporous gold (composite np-Au) stamps joined to bulk reservoirs of polymer ink is presented in this chapter. Composite np-Au stamps consist of a topographically patterned porous gold film (thickness of ~ 2.7 µm) with a polymer film attached to the metallic part. Stamps with two different polymer films were developed in this work: (1) composite np-Au stamps with polystyrene (PS) layer and (2) composite np-Au stamps with poly(vinylidenefluoride)-trifluoroethylene (PVDF-TrFE) layer. The PS layer thickness for thinner composite np-Au-PS stamps was ~ 120 µm and for thicker composite np-Au-PS stamps ~ 400 µm. The thickness of the P(VDF-TrFE) layer in the composite np-Au-P(VDF-TrFE) stamp was ~ 95 µm. In the stamp, the polymer film is not only ink reservoir but also support for the porous gold film, which enhances the stability of the stamp. Due to the high viscosity of the polymer melts, the polymer films support the composite np-Au films also above their glass transition temperatures or their melting points. Such design with a continuous supply of the ink during the stamping enabled the use of composite np-Au stamps for stamping of polymer melts in continuous cycles.

To obtain the patterned surface of the stamp, the silver-gold alloy was sputtered on the macroporous silicon templates (mSi) as illustrated in Figure 4.1a, b. The mSi had hexagonally ordered pores with an interpore pitch of 1.5 µm and a pore depth of 600 nm (Fig. 4.1c, d). At their openings, the macropores were ~ 900 nm wide and they narrowed to their bottoms to ~ 600 nm.

c)

d)
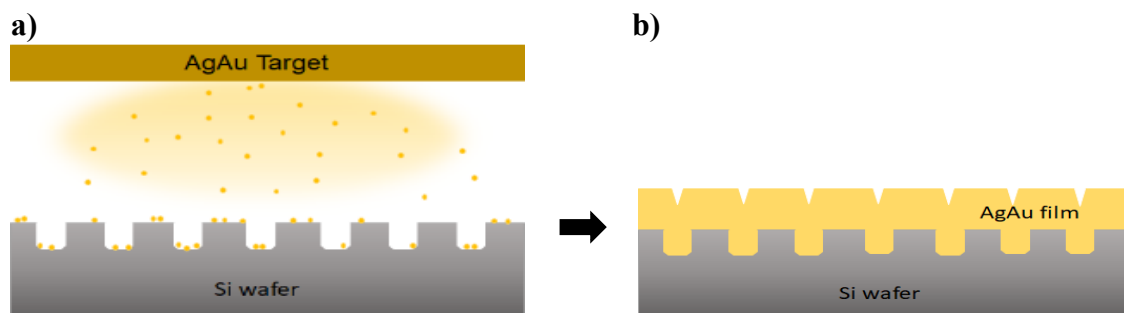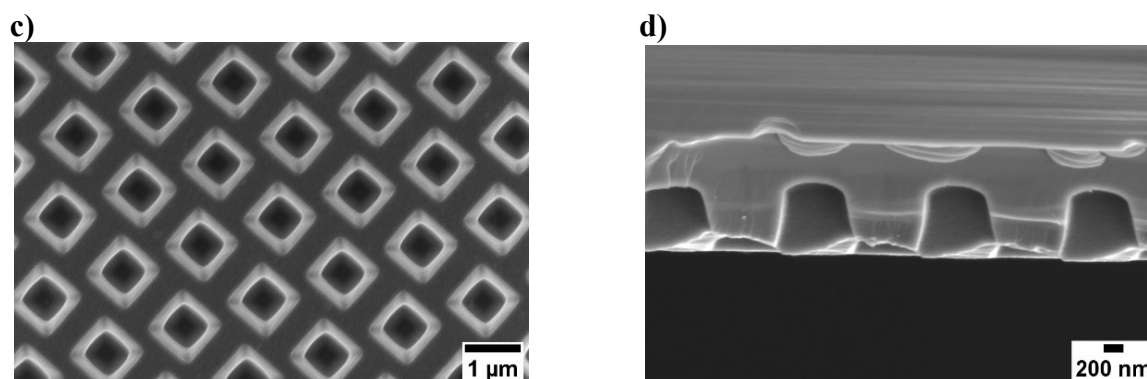
Figure 4.1 (a) Illustration of sputtering process of an Ag-Au film (yellow) on a mSi template (gray). **(b)** Topographically patterned Ag-Au film on mSi. **(c)** SEM image of mSi (top view), **(d)** SEM image of a cross-section view of the mSi pores.

After sputtering, a uniform film of Ag-Au alloy was formed on the mSi template with a thickness of ~ 2.7 μm. The porosity of the metallic film was achieved with the dealloying process. Dealloying refers to a process where the less noble element is selectively dissolved from the alloy, and consequently an interconnected and uniform porous network predominantly consisting of the more noble element is formed. In the Ag-Au alloy as a less noble element Ag is dissolved leaving the porous film that consists mostly of Au.

In first attempt, selective etching was done electrochemically because pore sizes can be better controlled in comparison to the free corrosion. Selective etching in Ag-Au film on mSi was done under both galvanostatic and potentiostatic conditions. During the process, there was severe cracking of the Ag-Au films on the mSi (Fig. 4.2). This led to the total separation or lift-off of the parts of the film from the mSi as seen in Figures 4.2c and 4.2d, which also caused the waviness of the metallic film. Nanoporous gold films developed in this way were difficult to handle and were consisting of many separated parts of the film, and as such could not be used as stamps for capillary stamping (see Figure 4.2a, c).
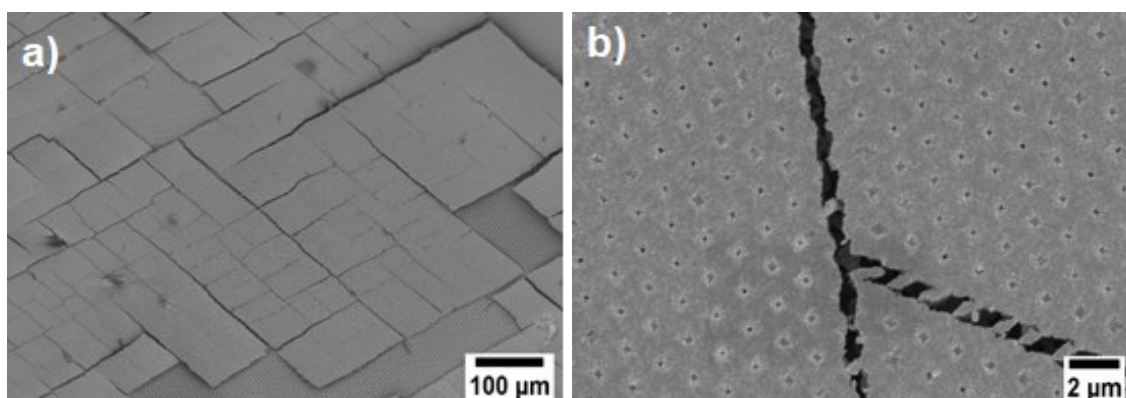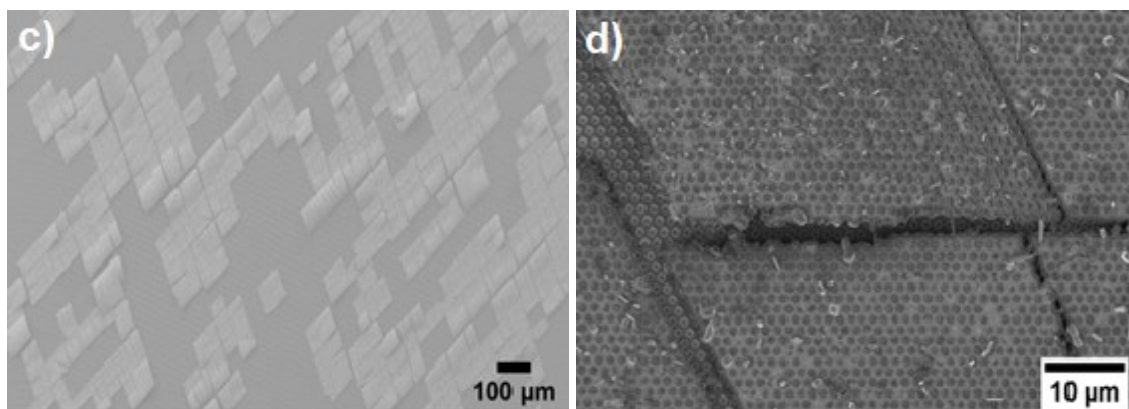
Figure 4.2 SEM images (top view) of Ag-Au layers on mSi after electrochemical dealloying, showing **(a, b)** cracks in an Ag-Au film after galvanostatic dealloying, **(c)** cracks in the Ag-Au film with parts of mSi without Ag-Au film after potentiostatic dealloying and **(d)** lift-off of parts of the Ag-Au film from the mSi template after potentiostatic dealloying.

Therefore, in the second approach, the metallic Ag-Au films were reinforced with the polymer film before the dealloying step (which was done then by free corrosion). The polymer films were formed on the top of the Ag-Au film on mSi by dropping a solution of the polymer that was used as ink in the stamping process (Fig. 4.3). After evaporation of the solvent, polymer films formed on the top of the Ag-Au films. After annealing, polymer-Ag-Au-mSi samples were immersed in nitric acid where Ag was etched from the Ag-Au films by free corrosion.
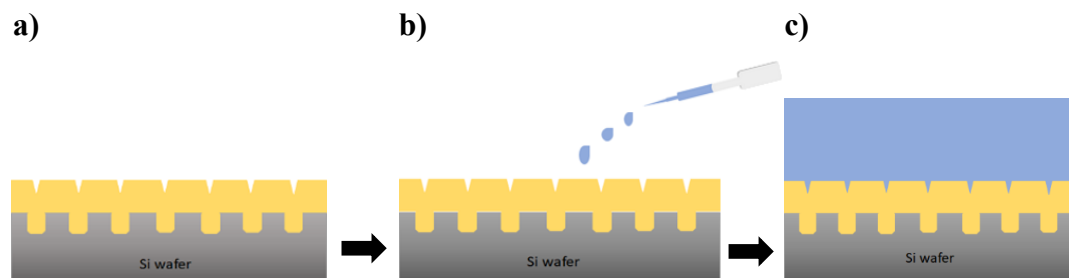
Figure 4.3 Polymer film fabrication by drop-casting: **(a)** dropping of polymer solution on Ag-Au film (yellow) on mSi (gray), **(b)** evaporation of the solvent from the solution in air and room temperature, and **(c)** formation of the solid polymer film (blue) on top of the Ag-Au film on mSi.

During the free corrosion process, formation of the porous morphology in the film started on the edges of the Ag-Au film because the film was covered with the mSi on one side and with the polymer film on the other. As dealloying evolved, the Ag-Au film spontaneously detached in a non-destructive manner from the mSi template (Fig. 4.4b). After that, the evolution of the continuous nanoporous network went much faster when the whole surface of the Ag-Au film was exposed to the dealloying agent. The formation of the continuous porous network throughout the whole Ag-Au film was indicated with the color change of the film from silver-

gray to brown (see Fig. 4.5a) color. In Figure 4.5b, a nanoporous gold stamp with a polystyrene film is shown. The size of the developed stamps was ~1 cm^2.
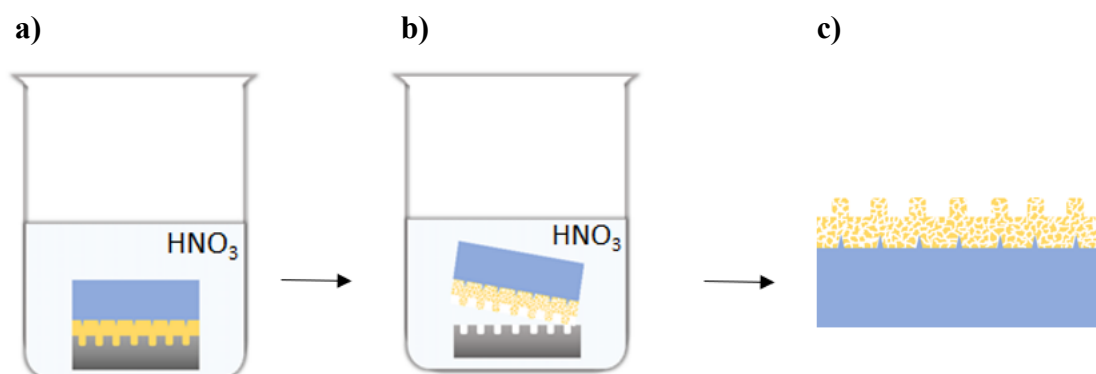
Figure 4.4 Illustration of the dealloying of the Ag-Au film in the mSi-AgAu-polymer sample. **(a)** Immersion of the mSi-AgAu-polymer sample into nitric acid, **(b)** detachment of the mSi template from the rest of the sample and dealloying of the Ag-Au film and **(c)** composite np-Au stamp.
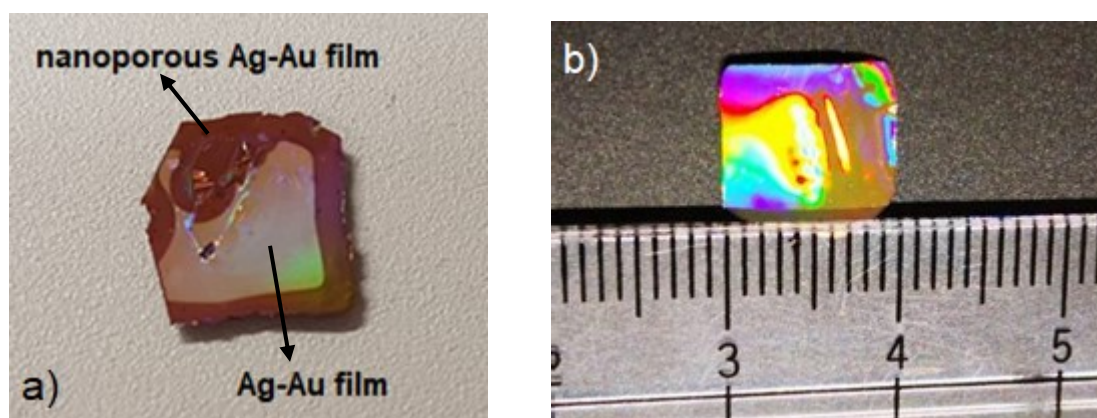
Figure 4.5 (a) Color change of the Ag-Au film during the dealloying process of AgAu-PS stamp. Brown color indicates the formation of the continuous porous network and silver-gray color the nonporous part of the film. **(b)** Composite np-Au stamp with polystyrene film (thickness of PS film of ~ 120 μm).

Obtained composite np-Au stamps (Fig. 4.5b) have a surface topographically patterned with arrays of contact elements. SEM images of top view and the cross-section view of the np-Au stamps with PS and P(VDF-TrFE) films are shown at Figure 4.6., Figure 4.7. and Figure 4.8.

The latter have a pitch distance of 1.5 μm (Fig. 4.7b) which corresponds to the pitch of the hexagonally ordered arrays of macropores in the mSi templates. The pore size in the gold stamp was in the range from ~ 40 nm to ~ 80 nm. Developed composite np-Au stamps with polymer ink reservoir showed mechanical stability and flexibility and were used in the stamping experiments presented in this work.
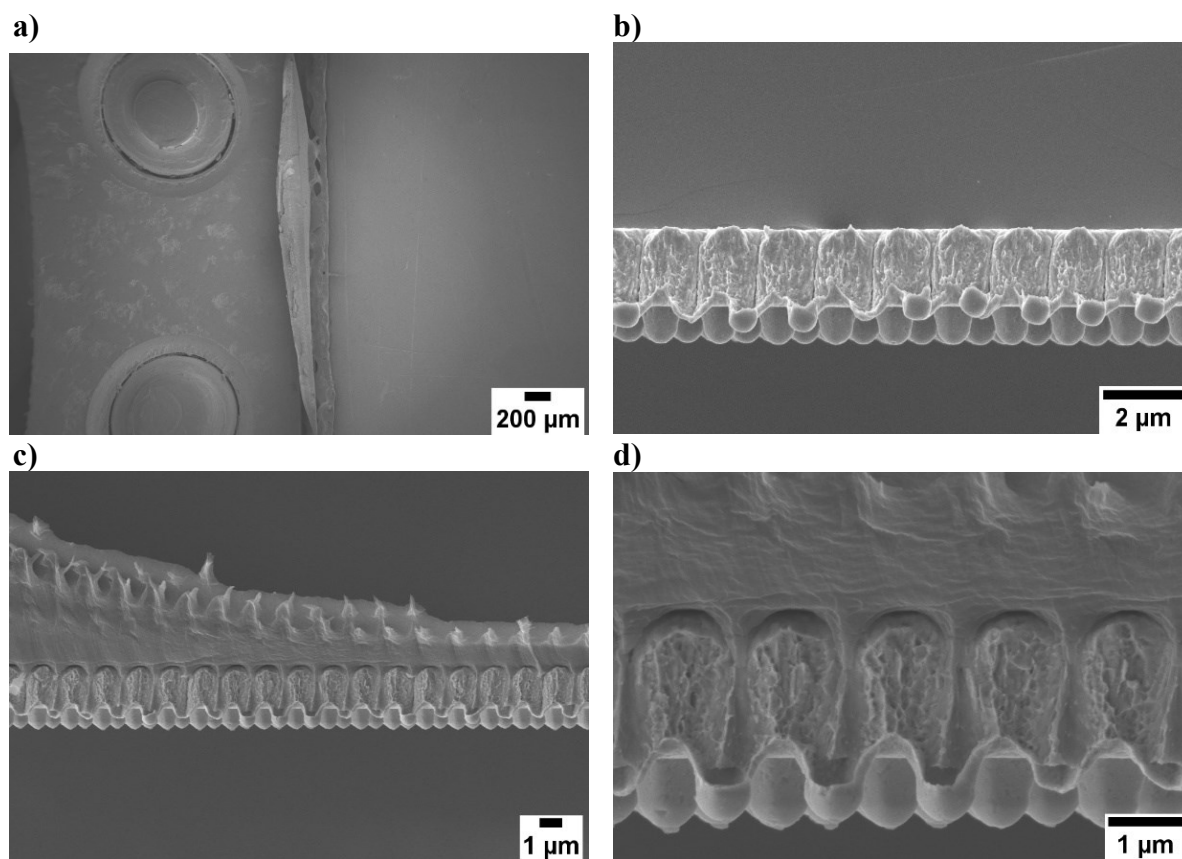
Figure 4.6. Cross-sectional SEM images showing **(a)** np-Au stamp with PS film, **(b)** Ag-Au layer of the compsite stamp before dealloying and **(c)** and **(d)** interface between Ag-Au film and polystyrene film.

c)

d)
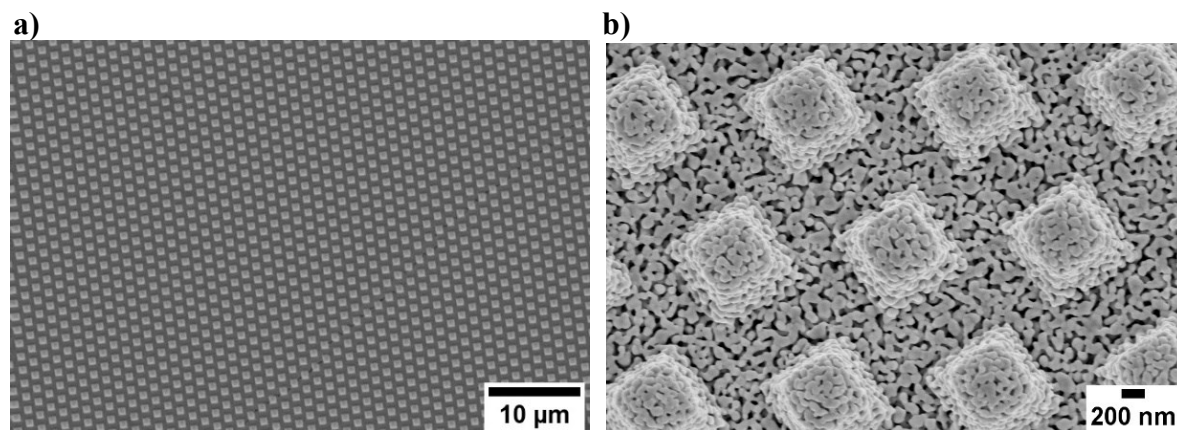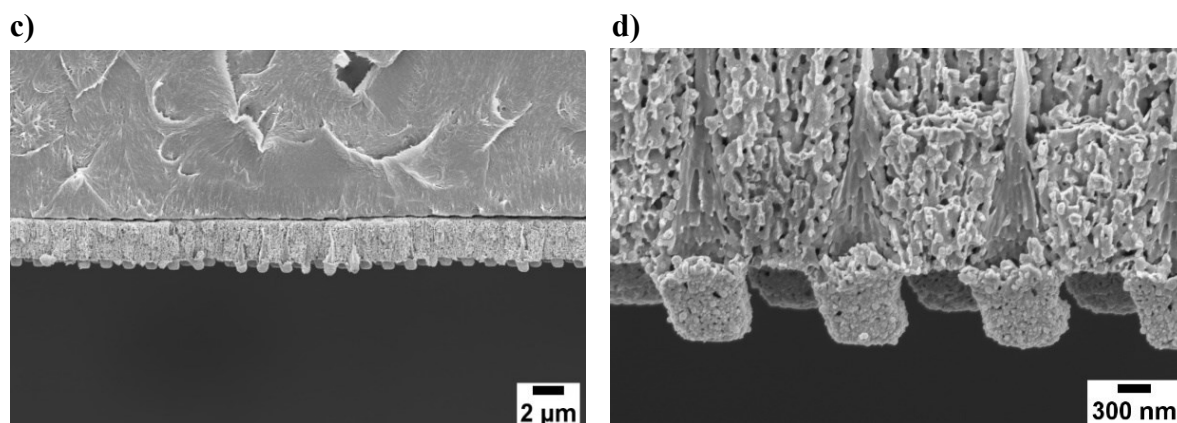
Figure 4.7 Composite np-Au stamp with PS film (thickness of PS film of ~120 μm). **(a)** Top view of topographically patterned composite np-Au film (SEM image), **(b)** enlarged SEM image of contact elements of the composite np-Au stamp, and **(c)** and **(d)** cross-section SEM image of the composite np-Au stamp.

a)

b)

c)

d)

e)
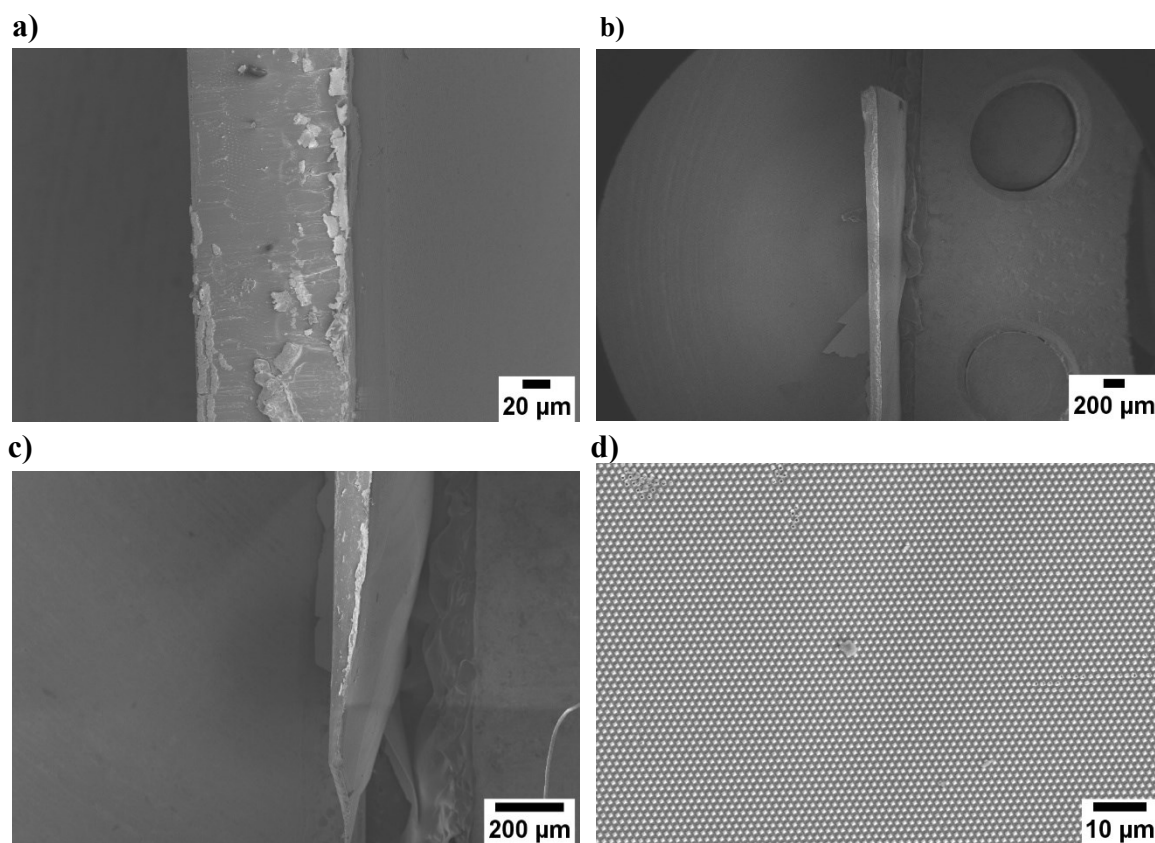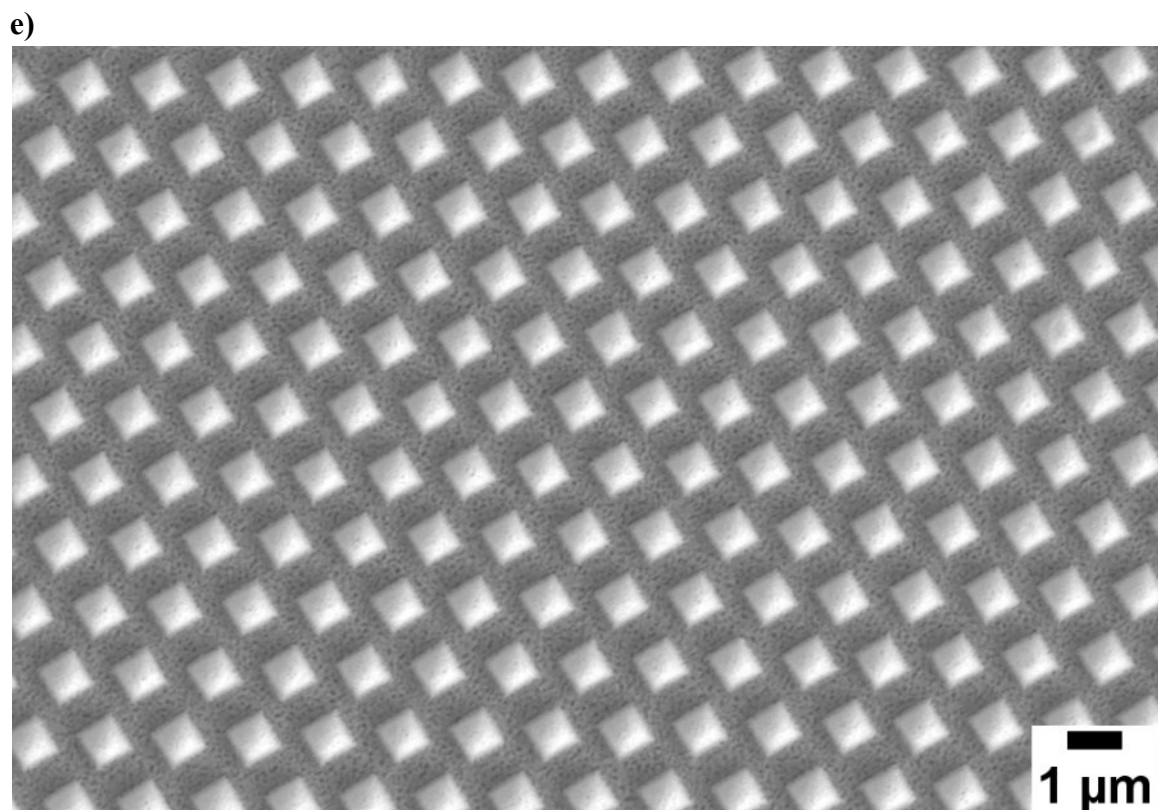
Figure 4.8. Composite np-Au stamp with P(VDF-TrFE) film (thickness of P(VDF-TrFE film of ~95 µm). **(a-c)** cross-section SEM image of the composite np-Au/P(VDF-TrFE) stamp, and **(d)** top view of topographically patterned composite np-Au film (SEM image), **(e)** enlarged SEM image of contact elements of the composite np-Au/P(VDF-TrFE) stamp.

4.2 Capillary stamping of polymer melts with composite np-Au stamps

For the stamping, a nanoporous gold stamp with a polymer film was placed in the oven and heated. During the heating process, the polymer film becomes viscous and imbibes the porous network of the metallic stamp. The stamping process was carried out after ~ 20 min after reaching the desired temperature in the oven. The stamping process is illustrated in Figure 4.9 and consists of four consecutive steps:

1. Approach (Fig. 4.9a). In this step, the substrate was brought into contact with the contact elements of the composite np-Au stamp.

2. Dwelling (Fig. 4.9b). Liquid bridges of the polymer melt (i.e., the ink) were formed between the dispensing elements of the composite np-Au stamp and the counterpart surface. Ink is continuously supplied from the polymer film which serves as an ink reservoir and supplies the contact elements of the composite np-Au stamp.

3. Retraction (Fig. 4.9c). After the dwelling, the substrate was retracted from the stamp. In this step, the liquid bridges formed between the contact elements of the stamp and the substrate were thinning.

4. Rupture (Fig. 4.9d). The final step in the thinning of the liquid bridges is their rupture, which resulted in large-area parallel lithographic deposition of polymer melt droplet arrays on the counterpart surface.
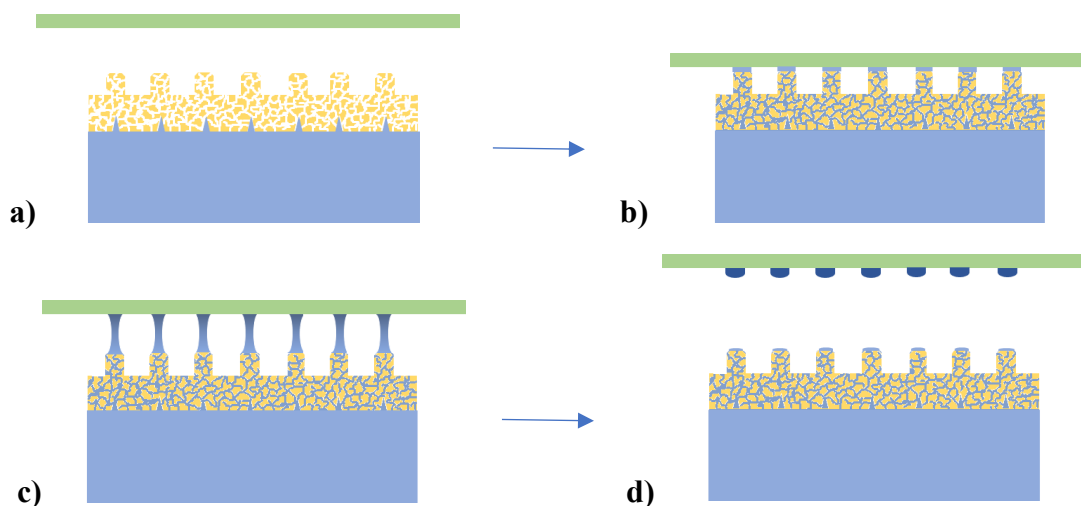
Figure 4.9 Illustration of the capillary stamping process. **(a)** Counterpart surface approaching the composite np-Au stamp. **(b)** Heating of the composite np-Au stamp and imbibition of the polymer melt in the pores of the composite np-Au stamp. The counterpart surface is in contact with the contact elements of the stamp and liquid bridges were created (dwell time). **(c)** Retraction of the counterpart substrate from the stamp. **(d)** Rupture of polymer melt liquid bridges and ink deposition on the counterpart surface.

Stamping of polymer melts with the composite np-Au stamp was done by three different methods:

I method – *Stamping by hand*. In this stamping process, the substrate was glued to the holder and brought in contact with the composite np-Au stamp. Substrates were heated after the contact formation. During the stamping process, the holder with the substrate was held by hand. Therefore, the stamping process is influenced by adding the pressure on the stamp-substrate contact surface that cannot be controlled or measured. Also, the proximity of the hand to the heating device was not practical in this method, and the stamping process needed to be optimized.

II method – *Stamping without pressure*. The substrate was placed gently on the stamp surface and left for stamping. After desired dwell time, the substrate was retracted with tweezers from the stamp.

III method – *Stamping with pressure.* In this method, the substrate was placed on the stamp with the tweezers and a weight of 40 g was placed on top of the substrate (pressure ~0,4 Mpa). After the stamping, the weight was removed from the substrate and the substrate retracted from the stamp.

4.2.1   Stamping of PS ink on glass substrates with stamping method I – by hand

Polystyrene (PS) is mostly used as a thermoplastic polymer due to its optical clarity, electrical isolation, chemical resistance, and low cost. It is used in a wide range of applications such as electronics, the food industry, the automotive industry, and medicine[119,120,121]. In this work, polystyrene was used as model polymer ink with narrow molecular weight distribution for the proof of the principle for the capillary stamping method with composite np-Au stamps.

In the first approach, polystyrene melts were stamped on glass substrates with stamping by method I – *by hand* described in detail in chapter 3.3.2.1. Stamping was done on unmodified glass substrates that had a surface terminated with hydroxyl groups. In Figure 4.10 SEM images of printed PS ink on a glass substrate at 200 °C after 5 min dwell time are shown. The printed PS dots are hexagonally ordered with a center-to-center distance of ~ 1.5 μm, which corresponds to the pattern and distance between contact elements of the composite np-Au stamp. Areas with hexagonally ordered printed polymer melts are visible in Figures 4.10a, b. As seen from these images, there are 'empty' areas where the printed dots are missing. The reason for this is so far unknown. Possible explanations for this could be the uneven distribution of the ink inside the composite np-Au film, uneven distribution of the pressure on the stamp during the stamping or lack of contact between the contact elements of the composite np-Au stamp with the substrate. In Figures 4.10c and 4.10d areas on the substrate with excess amount of the polymer ink are visible. This can be rationalized by defects on the surface of the composite np-Au stamp such as cleavages in the metallic film or the breaking of the contact elements of the composite np-Au stamp. These defects in the metallic films of the composite np-Au stamps could occur during the development process of the stamps or during the stamping process. Consequently, melted polymer ink leaked on the substrate in these areas during the stamping process, and islands of polymer ink on the substrate surface were formed. Two different shapes of the polymer deposits were deposited on the substrate (Fig. 4.10d, e). One was a dot-shaped deposit of the polymer ink and the second was a ring-shaped deposit. In Figure 4.10f an enlarged image of the ring-shaped deposits of PS on glass is shown. In the middle of the ring, small drops of PS ink are visible. From the image analysis of the SEM results average

values for diameter, circularity, and aspect ratio of the PS dots are obtained. The average diameter of the stamped PS dots on glass after 5 min dwell time is 659 nm $\pm$ 70 nm (Fig. 4.11b). The average circularity of the dots is 0.9 ± 0.02 and the average aspect ratio of 1.17 ± 0.07 (Fig. 4.11b, c). Stamping I – *by hand* has two main disadvantages: (1) stamping with longer dwell times than 5 min was not practical because the hand was near to the heating source and (2) hand adds the pressure on the stamp-substrate surface that cannot be measured or controlled.
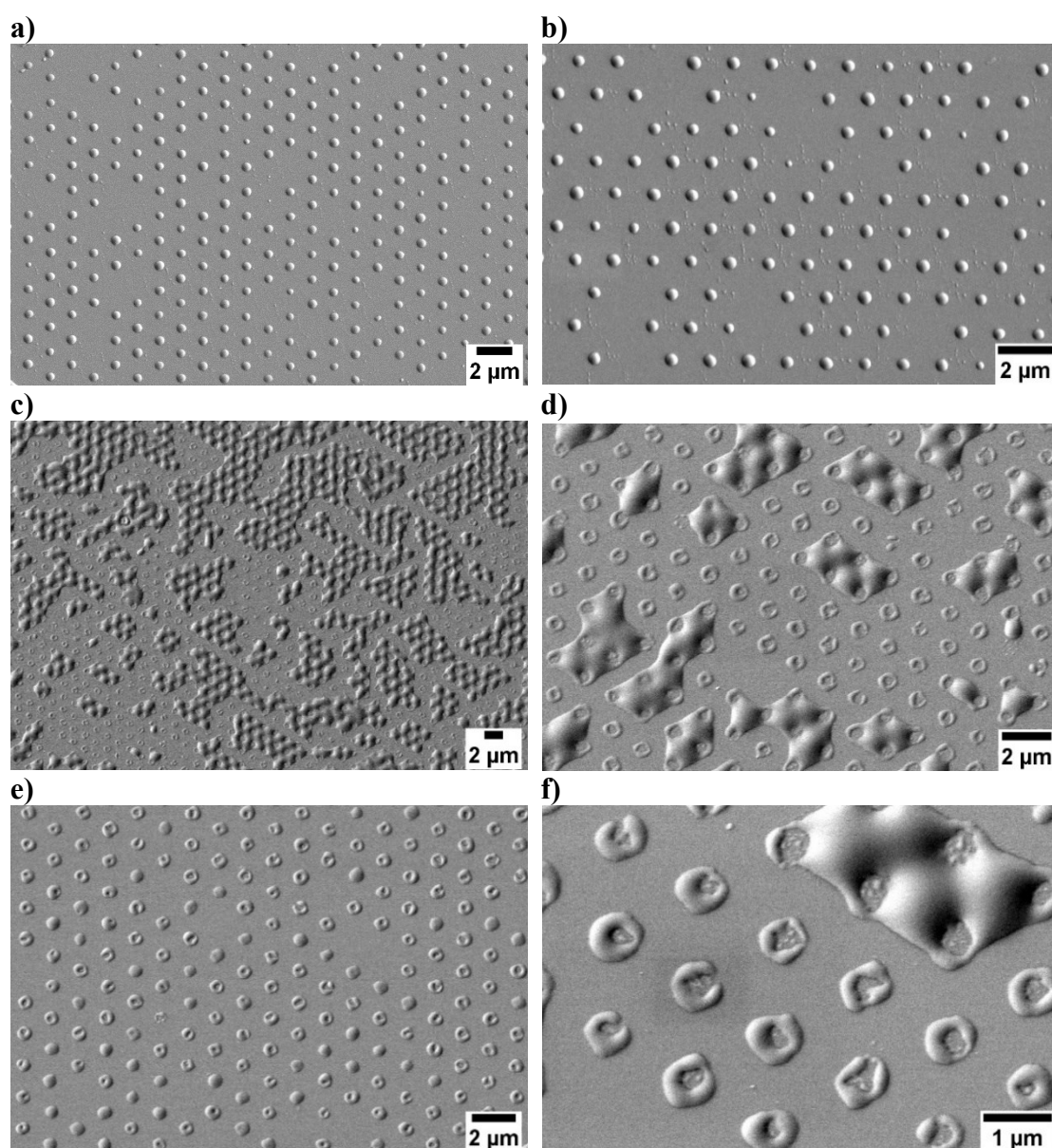
Figure 4.10 SEM images of PS stamped on the glass after 5 min dwell time at 200 °C with a stamping method I – *by hand.*
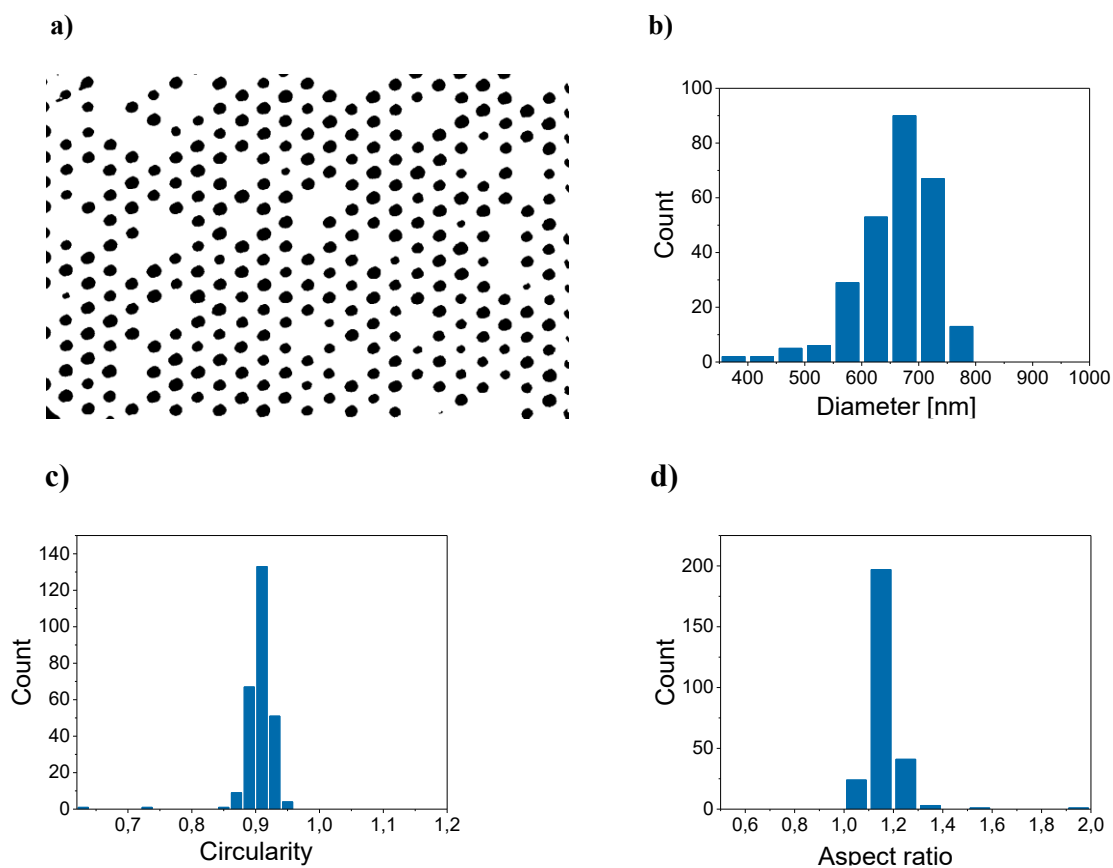
Figure 4.11 (a) Binarized SEM image (original image is shown in Fig. 4.8a) of stamped PS dots on glass and histograms of 267 analyzed stamped PS dots after 5 min dwell time at 200 °C, showing **(b)** diameters, **(c)** circularities, and **(d)** aspect ratios of stamped PS ink on glass (stamping method I – *by hand*).

The height distribution of the stamped PS dots on glass after 5 min dwell time was obtained from the analysis of the AFM image shown in Figure 4.12. From the analysis of 127 stamped PS dots, the average height of the PS dots is 64 nm ± 10 nm (Fig. 4.13).

c)
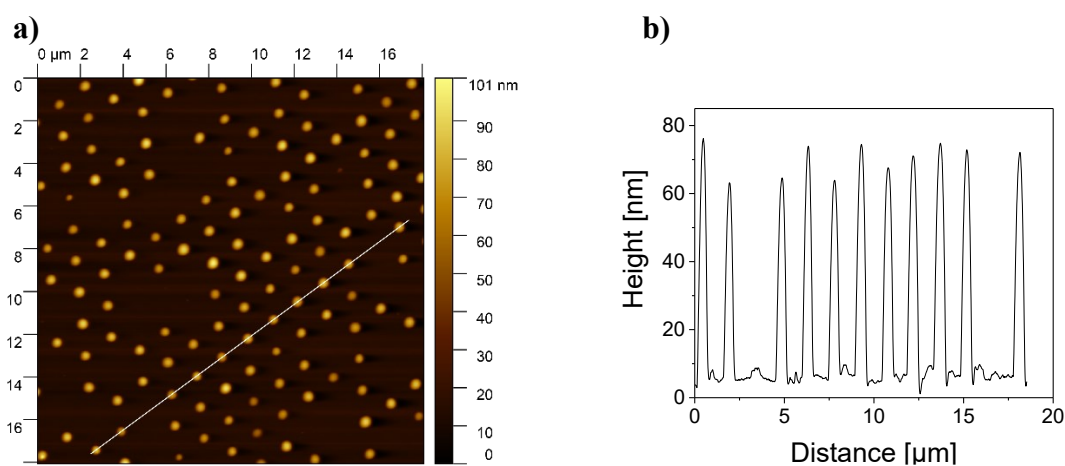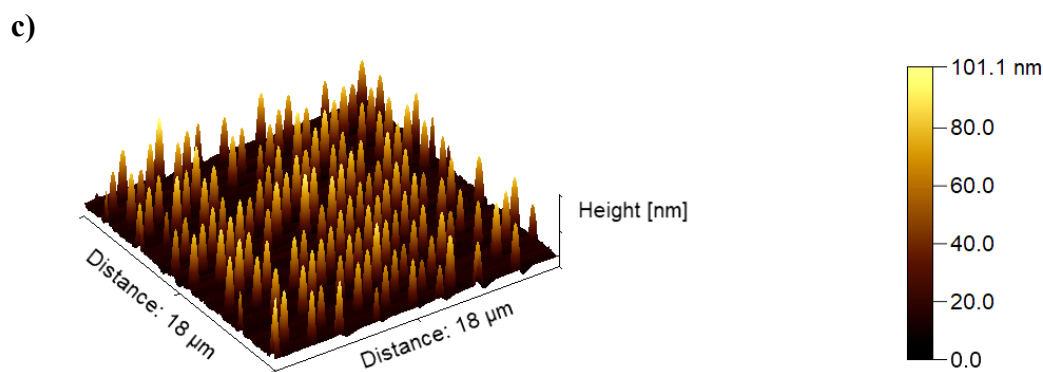
Figure 4.12 AFM image of PS dots stamped on glass after 5 min dwell time at 200 °C with stamping method I – *by hand*. **(a)** Topographical AFM image, **(b)** topographical profile along the line in the panel a) and **(c)** 3D AFM image.
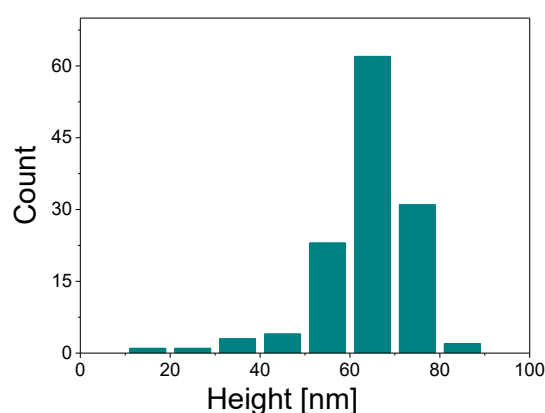
Figure 4.13 Histogram of 127 analyzed PS dot heights printed on glass substrate after 5 min dwell time (stamping method I -*by hand*). Heights were obtained from the analysis of the AFM image shown in the Figure 4.12a.

4.2.2 Stamping of PS ink on glass substrates with stamping method II – *without pressure*

The second stamping approach *without pressure* (see chapter 3.3.2.2) gives more control during the stamping process in comparison to the previously described method I – *by hand*. With this stamping method the main disadvantages of the previous stamping method I – *by hand* were resolved. This method enables longer stamping times and there is no pressure from the hand on the substrate/the composite np-Au stamp surface during the stamping. Therefore, stamping of PS ink on glass substrates was done with different stamping times. The influence of the stamping time on the PS dot diameter and height was investigated.

After 10 min dwell time, stamped PS dots have mostly regular round shapes as seen in Figure 4.14. In Figure 4.14a in the bottom-right part of the SEM image there is a visible distortion of the PS droplets in one direction. This can be rationalized by shear movement during the stamping process. As seen from the Figure 4.14b and c, there are some areas of the substrate

where the PS droplets were not deposited. The texture of the image shown in the Figure 4.14d comes from the Au layer that was sputtered before the SEM measurement.
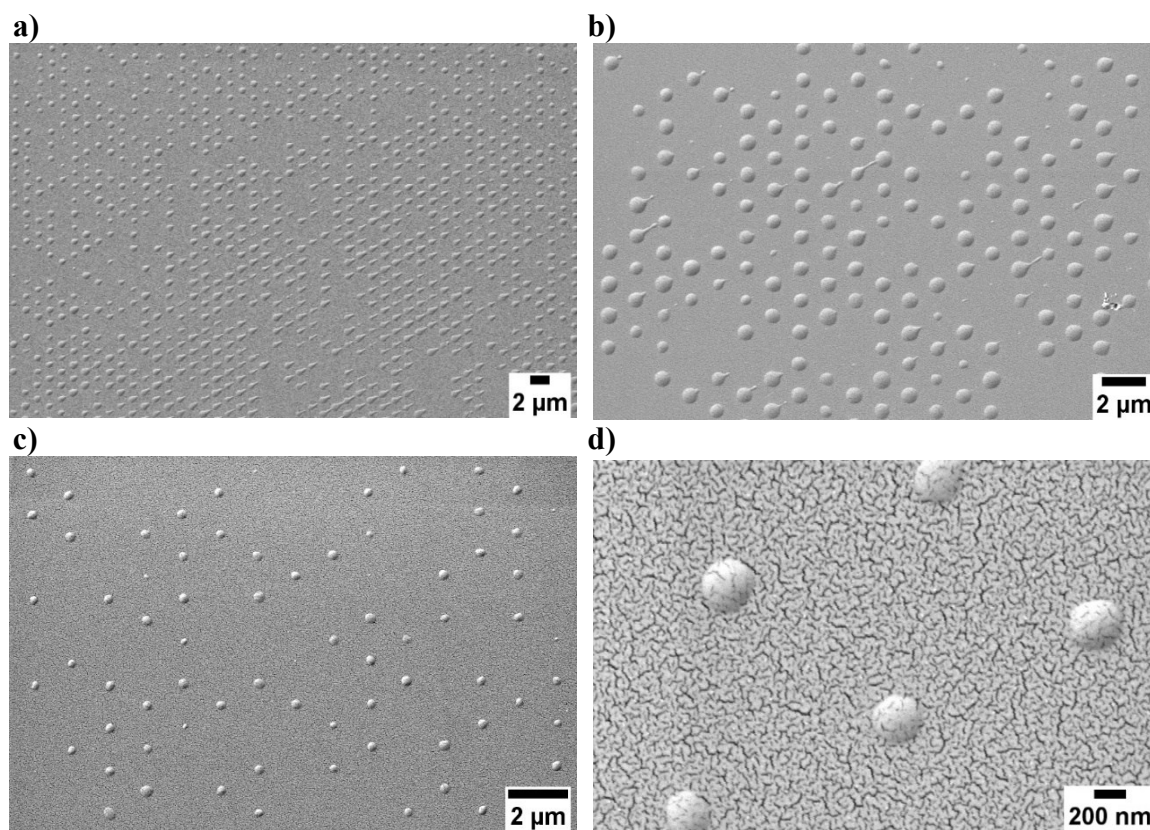
Figure 4.14 SEM images of stamped PS droplets on glass after 10 min dwell time at 200 °C generated by stamping method II – *without pressure*.

From the image analysis of the SEM image shown in Figure 4.14b histograms of the diameters, circularities, and aspect ratios of the printed PS dots were acquired and summarized in Figure 4.15. From the analysis of 147 printed dots, an average diameter of 895 nm ± 122 nm, an average circularity of 0.9 ± 0.02, and an average aspect ratio of 1.11 ± 0.06 were obtained.

c)

d)
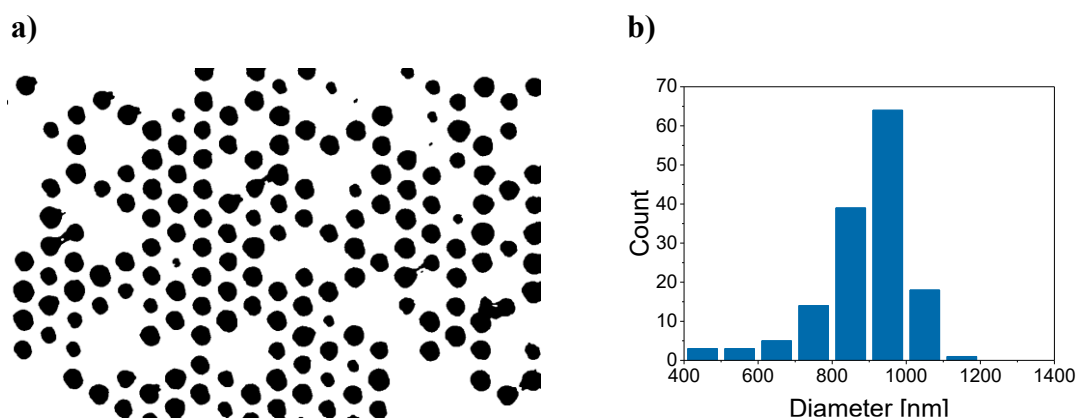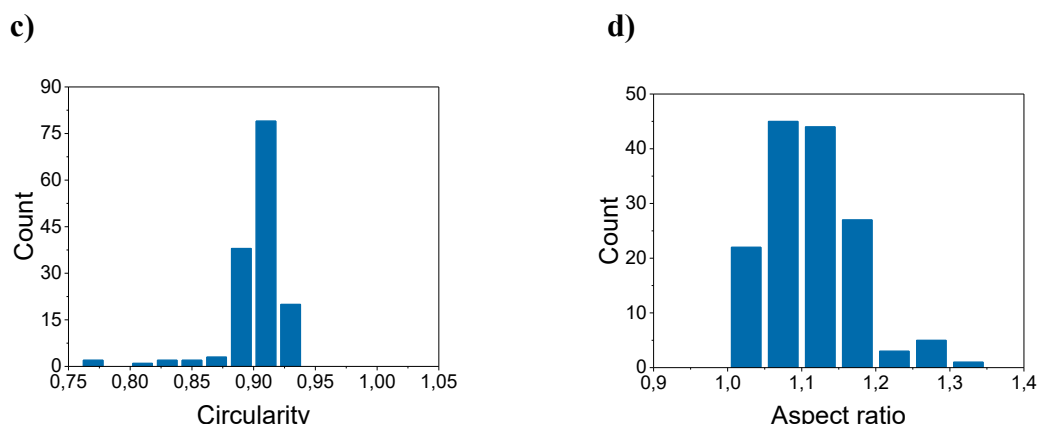
Figure 4.15 (a) Binarized SEM image (original image shown in the Fig. 4.14b) of stamped PS dots on glass after 10 min dwell time (stamping method II – *without pressure*). **(b)** Diameters, **(c)** circularities, and **(d)** aspect ratios histograms of 147 analyzed PS dots on glass acquired from the binarized SEM image.

SEM results from the stamping applying a dwell time of 13 min is presented in Figure 4.16. In Figure 4.16c merging of the neighboring dots is visible. This stamping defect is even more present in the areas shown in Figure 4.16f, g.

a)

b)

c)

d)

e)

f)

g)

h)
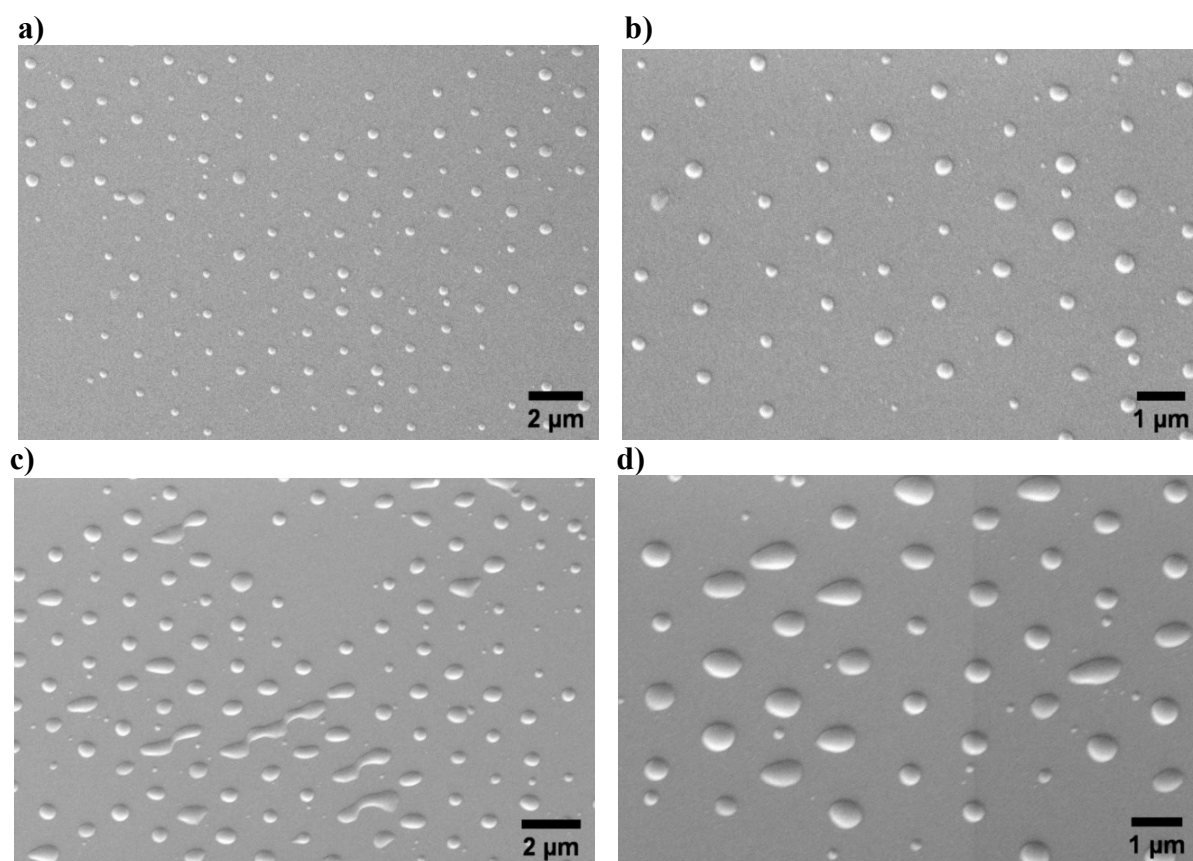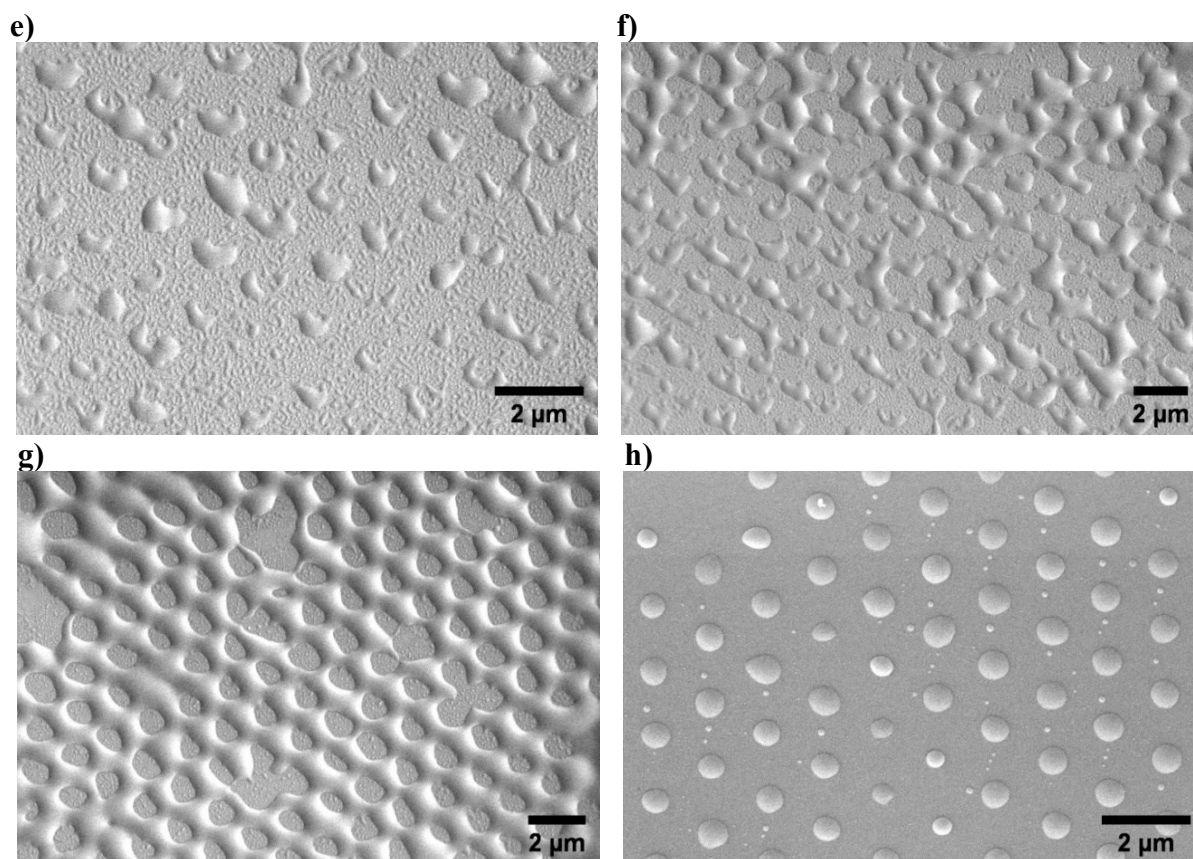
Figure 4.16 SEM images of stamped PS dots on glass after 13 min dwell time at 200 °C (stamping method II – *without pressure*).

Frequency densities of diameters, circularities, and aspect ratios of the PS dots stamped on glass applying a dwell time of 13 minare obtained from the image analysis of Figure 4.16a. The average diameter of the stamped dots amounts to 622 nm ± 130 nm, the average circularity to 0.91 ± 0.03 and the average aspect ratio to 1.08 ± 0.04.

a)

b)

c)

d)
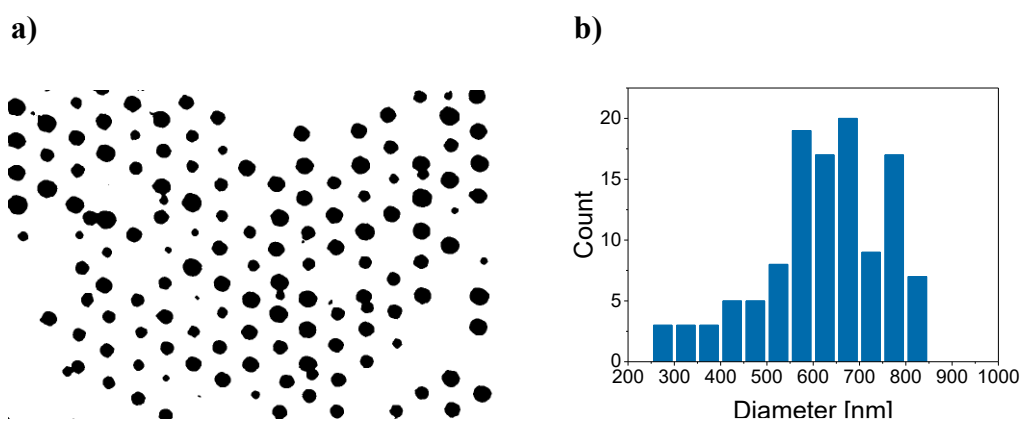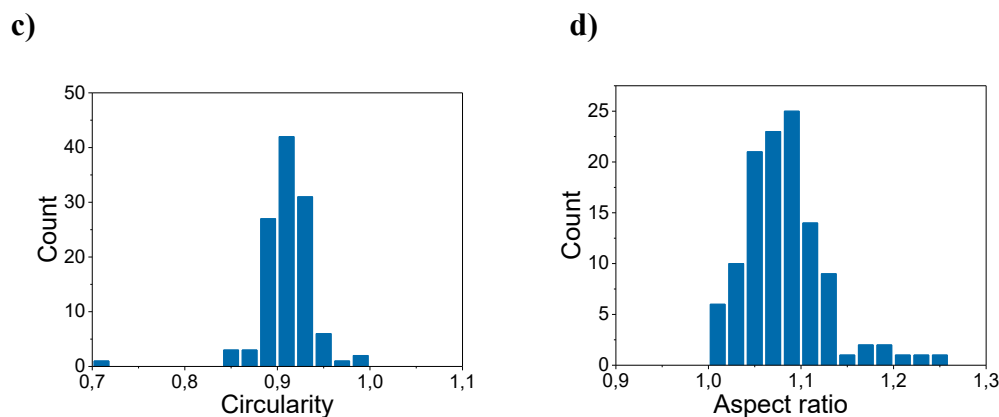
Figure 4.17 (a) Binarized SEM image (see original SEM image in Fig. 4.16a) of stamped PS dots on glass applying a dwell time of 13 min at 200 °C (stamping method II – *without pressure*) and **(b)** diameter, **(c)** circularity, and **(d)** aspect ratio histograms of 116 analyzed PS dots on glass obtained by image analysis.

Stamping results after 20 min dwell time (Fig. 4.18) show less 'free spaces' between printed dots in comparison to the previous stamping results obtained with dwell times of 10 min and 13 min. In the SEM images shown in Figure 4.18 distortions of the printed PS dots is visible. A possible reason for this outcome may be the tilting of the substrate during the retraction of the glass from the composite np-Au stamp, while the deposited ink is still in the viscous form. The base of the dots deposited on the glass substrate has retained the shape of a circle, but the volume of the dots is tilted to one side (Fig. 4.18f). From the image analysis of Figure 4.18g frequency densities of the diameters, circularities, and aspect ratios were determined (Fig. 4.19). From these histograms, an average diameter of 891 nm ± 112 nm, an average circularity of 0.84 ± 0.09, and an aspect ratio of 1.23 ±0.17 of the stamped PS dots were obtained.

a)

10 µm
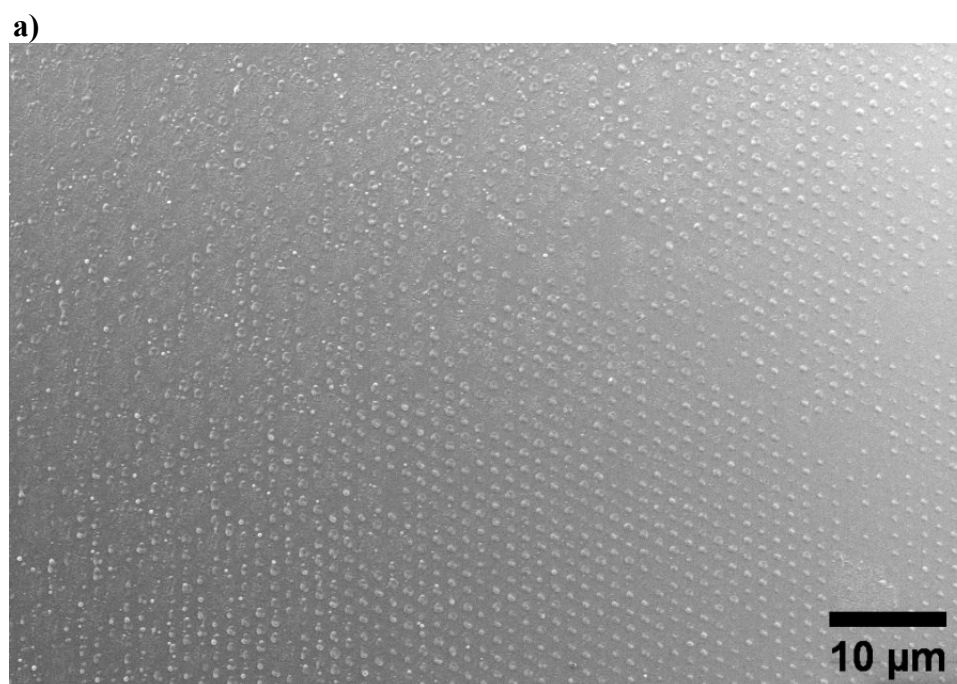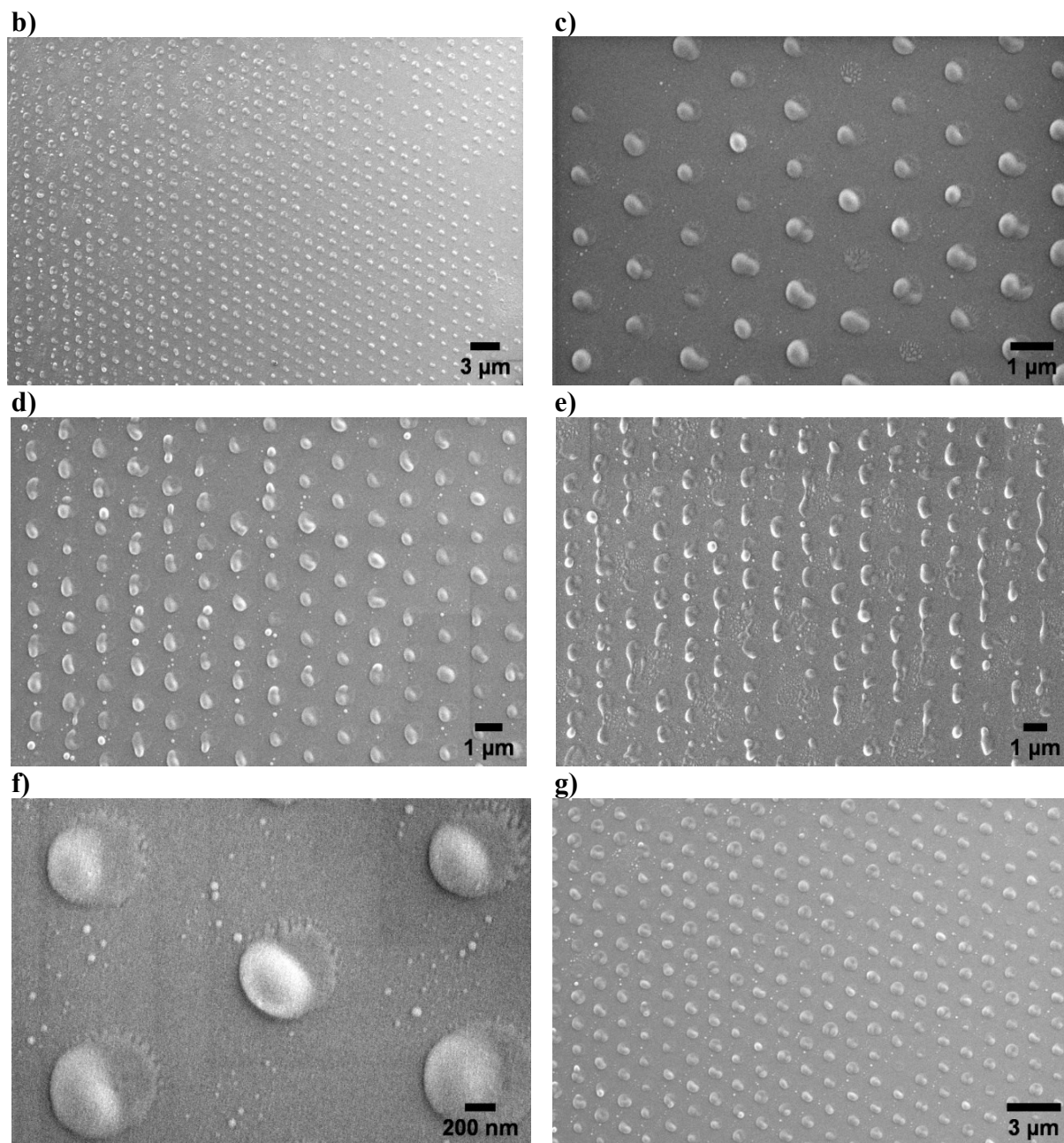
Figure 4.18 SEM images of stamped PS dots on glass substrates after 20 min dwell time at 200° C (stamping method II – *without pressure*).

c)

d)
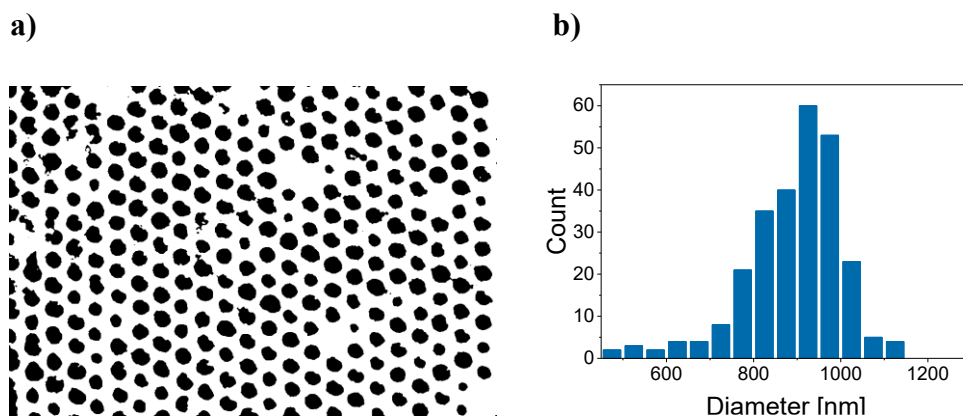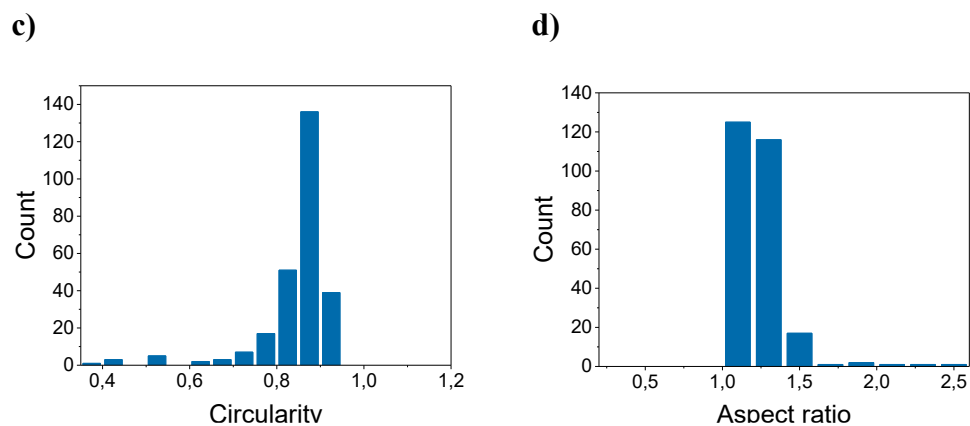
Figure 4.19 (a) Binarized SEM image (see original SEM image in Figure 4.16G) of stamped PS dots on glass after 20 min dwell time at 200 °C (stamping method II – *without pressure*). **(b)** Diameter, **(c)** circularity, and **(d)** aspect ratio histograms of 264 analyzed PS dots on glass acquired by image analysis.

Stamping results after 27 min dwell time are shown in Figure 4.20. An average diameter of 909 nm $\pm$ 68 nm, an average circularity 0.89 ± 0.01, and an average aspect ratio of 1.13 ± 0.05 were obtained for the PS dots from the corresponding histograms shown in Figure 4.21. The histograms were obtained by image analysis of the SEM image shown in Figure 4.20.
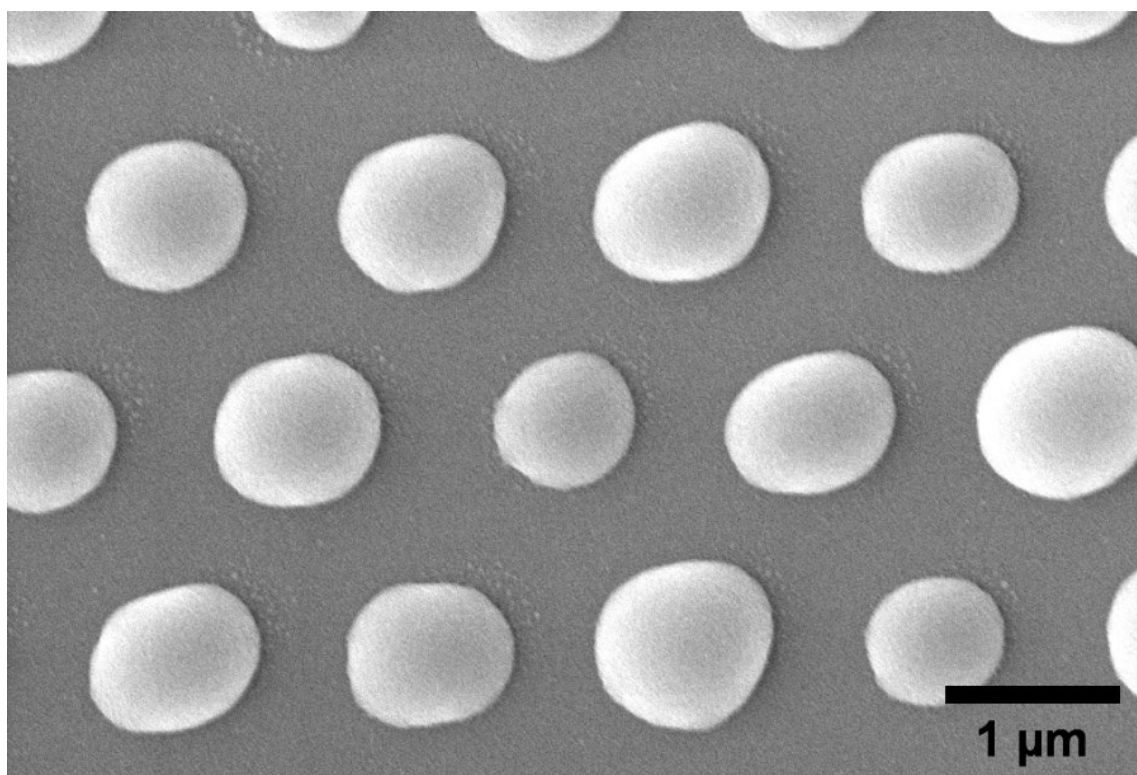
Figure 4.20 SEM image of stamped PS dots on glass after 27 min dwell time (stamping method II – *without pressure*).
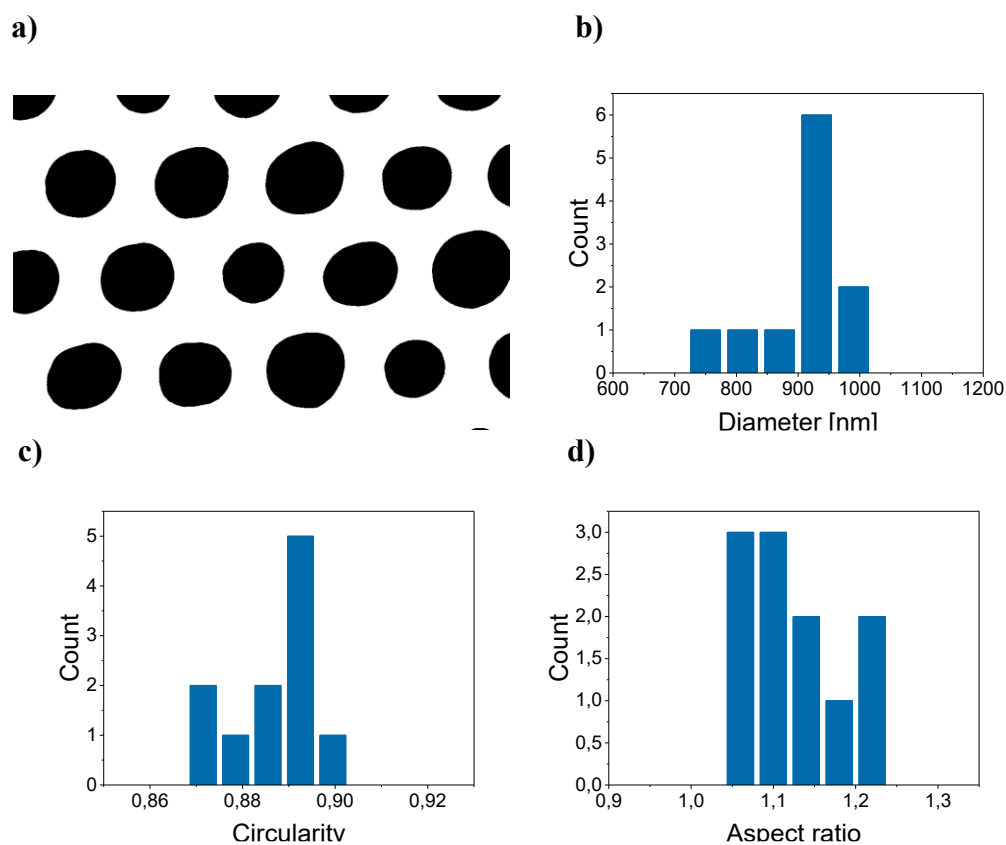
Figure 4.21 (a) Binarized SEM image (see original SEM image in Fig. 4.20) of stamped PS dots on glass after 27 min dwell time (stamping method II – *without pressure*). **(b)** Diameter, **(c)** circularity, and **(d)** aspect ratio histograms of 11 analyzed PS dots on glass acquired from the image analysis.
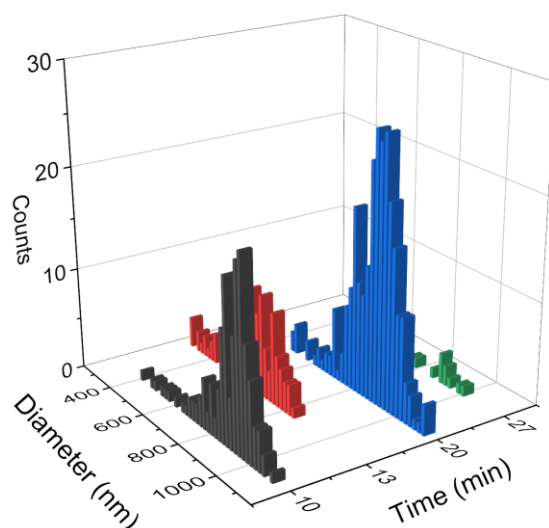
Figure 4.22 Histograms of the diameters of PS dots on glass obtained with stamping method II – *without pressure* after 10 min (black), 13 min (red), 20 min (green), and 27 min (blue) stamping time.

Table 4.1.

Stamping time [min]	Average diameter [nm]	Average circularity	Average aspect ratio
10	895 ± 122	0.90 ± 0.02	1.11 ± 0.06
13	622 ± 130	0.91 ± 0.03	1.08 ± 0.04
20	891 ± 112	0.84 ± 0.09	1.23 ± 0.17
27	909 ± 68	0.89 ± 0.01	1.13 ± 0.05

The histograms of the diameter values of PS droplets obtained by image analysis of the SEM images for stamping times of 10 min, 13 min, 20 min and 27 min are shown in the Figure 4.22. The diameters sizes of the PS dots are in the range from 200 nm to 1200 nm, where majority of the PS dots has diameters in the range from 500 nm to 1000 nm. For stamping times of 10 min, 13 min and 27 min the peaks of the frequency densities (i.e., the diameter intervalls with the highest population) are shifted to larger diameters, with the exeption for the stamping time of 13 min. Nevertheless, there is no direct correlation between the mean diameter of the deposited PS dots and the stamping time.

4.2.3   Stamping of PS ink on glass substrates with stamping method III – *with pressure*

In the third stamping approach, stamping of PS ink on glass substrates was done with stamping method III – *with pressure*. The method is explained in detail in Chapter 3.3.2.3. Stamping was done with the following stamping times: 5 min, 15 min, 16 min, 17 min, 18 min, 19 min, 20 min, 25 min and 30 min.

Large areas of glass substrates were printed with PS ink with this method after 5 min dwelling time as seen in Fig. 4.23a. The printed PS dots form hexagonal arrays that correspond to the pattern of the dispensing elements of the composite np-Au stamp with a distance between the stamped PS dots of ~ 1.5 µm. The deposited PS dots have uniform shape and no residual PS ink is located in between of them. As in the case of the stamping methods I (*by hand*) and II (*without pressure*), in some aeras of the substrate there sites where the PS dots are missing. From image analysis of the SEM image shown in Figure 4.23a, the histograms of diameters, circularities, and aspect ratios of the stamped PS dots after 5 min dwell time were obtained. The average diameter of the PS dots was 813 nm ± 60 nm, the average circularity 0.93 ± 0.03, and the average aspect ratio 1.22 ± 0.09 (Figure 4.24).

216 stamped PS dots on glass after 5 min dwell time imaged by AFM (Fig. 4.25) were analyzed and a frequency density of the dot hights was obtained (Fig. 4.26). The average height of the stamped PS dots was 81 nm ± 10 nm.

a)

b)

c)
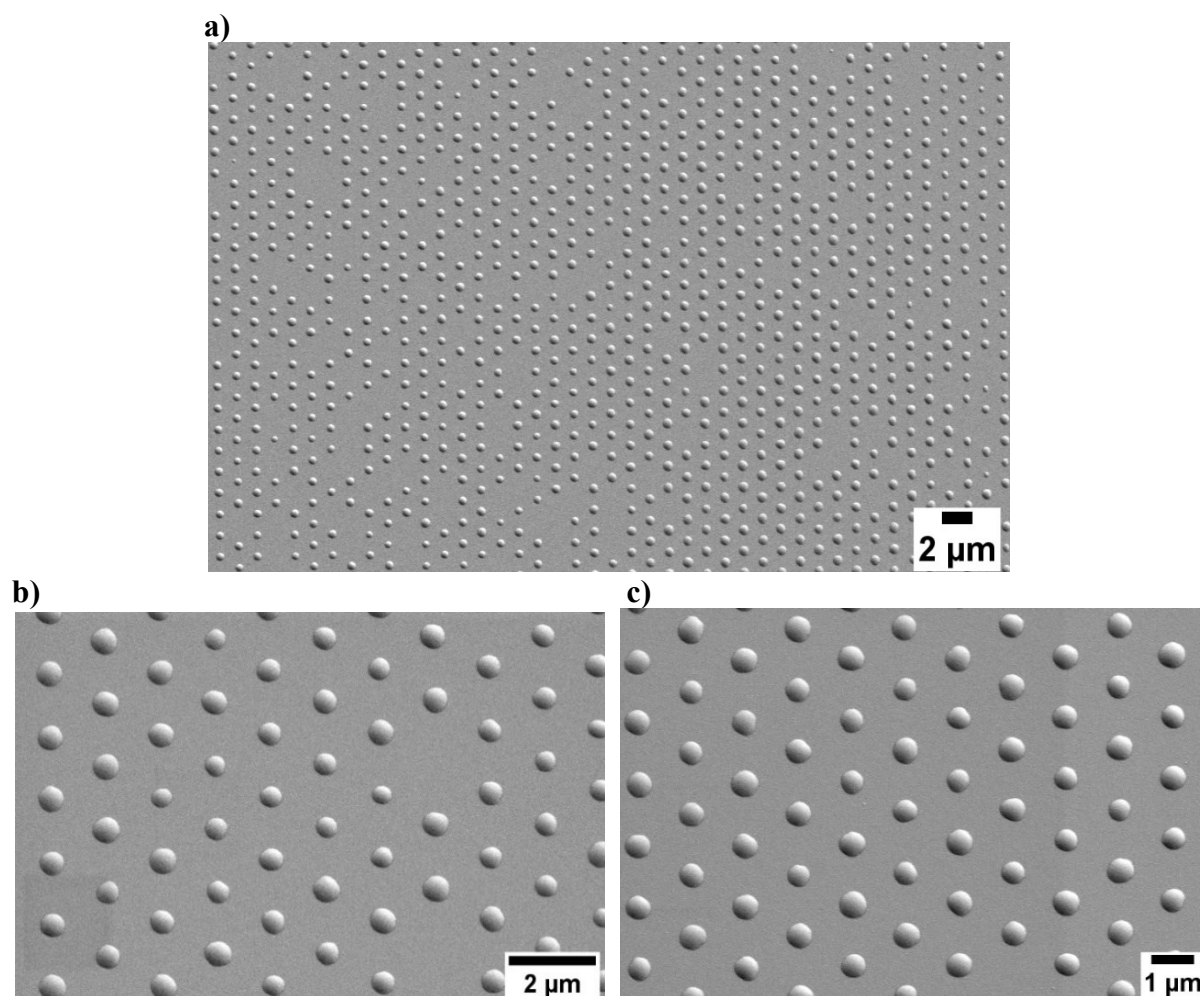
Figure 4.23 SEM images of PS dots stamped on glass with 5 min dwell time at 200 °C (stamping method III – *with pressure*).

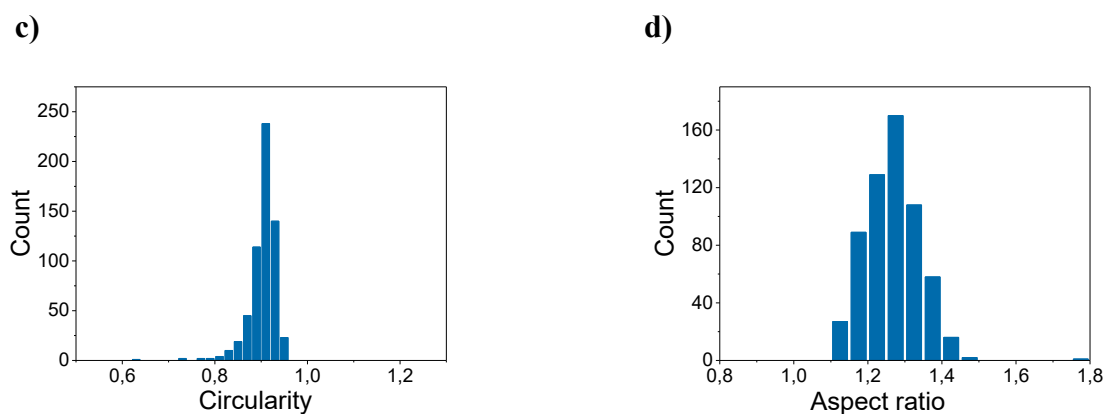a)

b)

c)

d)
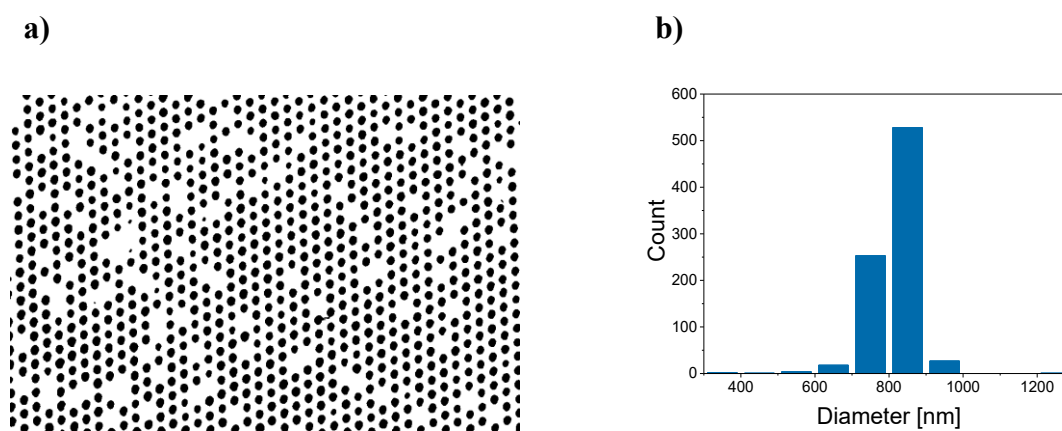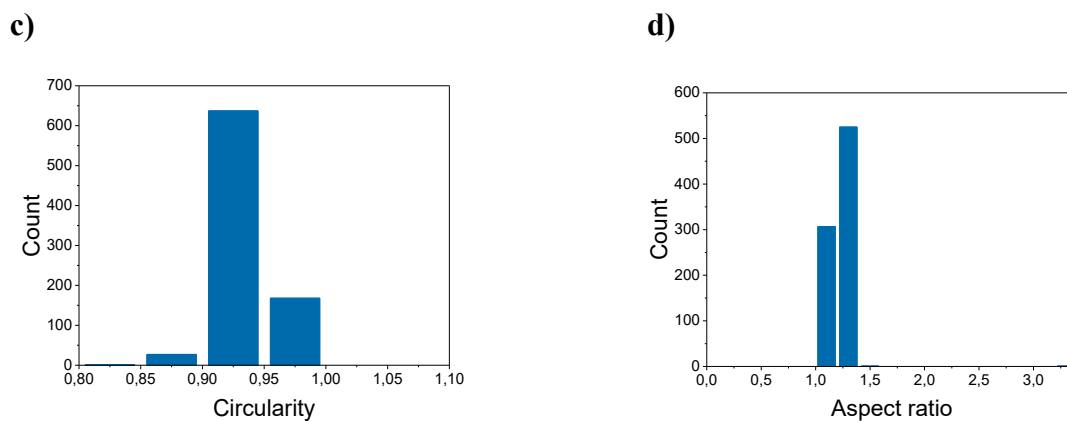
Figure 4.24 (a) Binarized SEM image (original image in Fig. 4.23a) of PS dots on glass stamped with 5 min dwell time at 200 °C (stamping method III – *with pressure*). **(b)** Diameter, **(c)** circularity, and **(d)** aspect ratio histograms of 834 analyzed PS dots on glass acquired by image analysis.
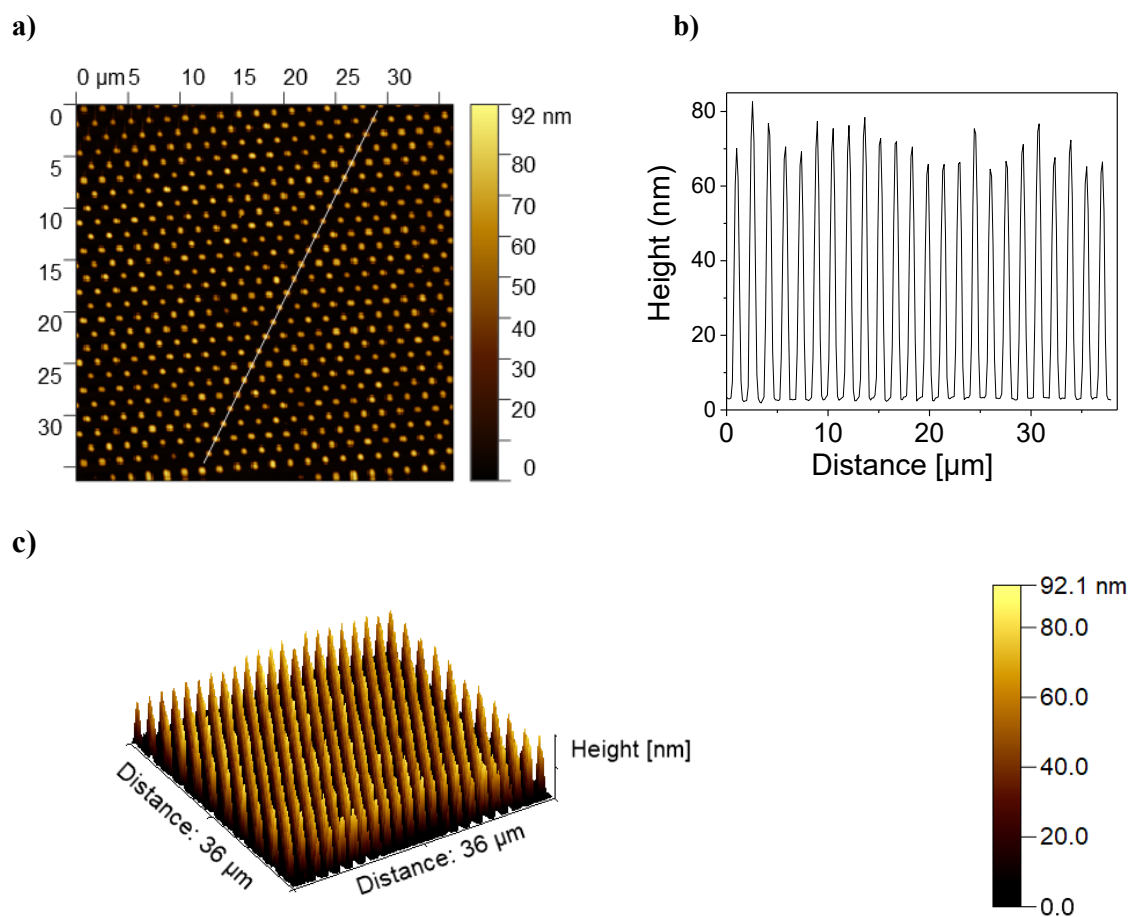
a)

b)

c)
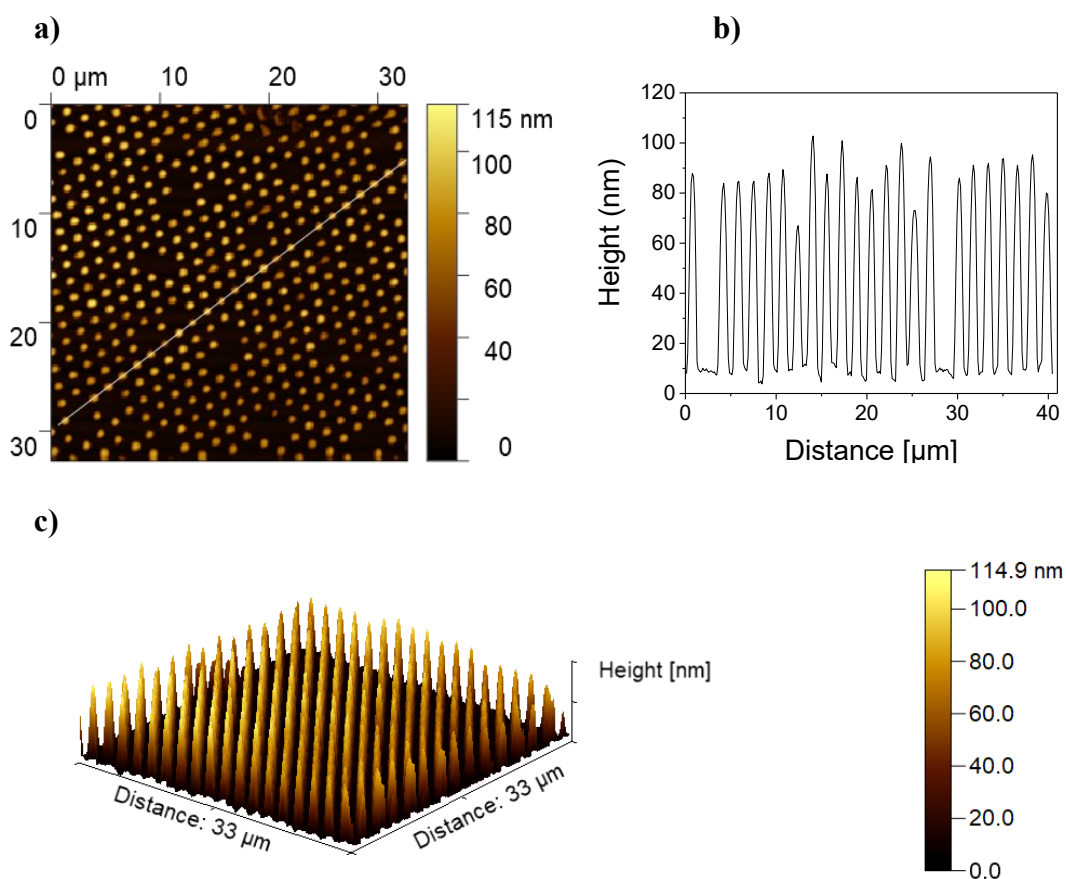
Figure 4.25 AFM measurement of PS dots stamped on glass at 200 °C with 5 min dwell time by stamping method III – *with pressure*. **(a)** Topographical AFM image, **(b)** topographical profile along the line in the panel (a) and **(c)** 3D AFM image.
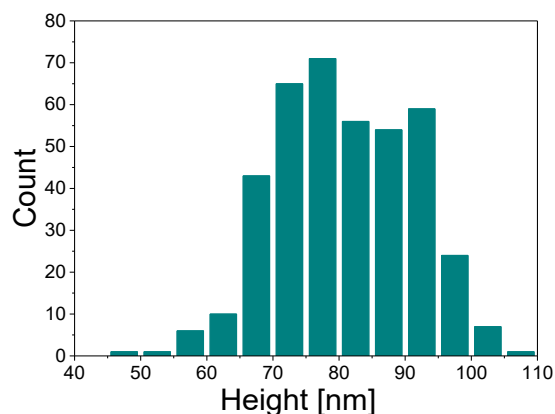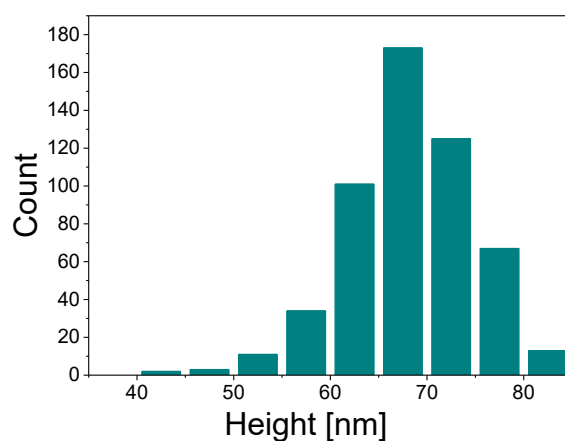
Figure 4.26 Histogram of the heights of 398 analyzed PS dots printed on glass substrate with 5 min dwell time (stamping method III – *with pressure*). Heights were obtained by the analysis of the AFM image shown in the Figure 4.25a.

Figure 4.27 shows SEM images of stamped PS dots on glass after 15 min dwell time. As seen from the images, large areas of the glass surface were printed with the PS dots. The distance between the printed PS dots is ~ 1.5 µm and the space between the printed dots is ink-free. Printed PS dots appear in two different shapes, as dots and ring-shaped (Fig. 4.27b). These different shapes of the PS deposits were seen in Chapter 4.2.1 with the stamping of PS ink I - *by hand*. Histograms obtained by image analysis (Fig. 4.27c) are presented in Figure 4.28. From this analysis, an average diameter of 901 nm ± 67 nm, an average circularity of 0.93 ± 0.03, and an average aspect ratio of 1.13 ± 0.09 of the stamped PS dots were obtained. A height histogram (Fig. 4.30) of stamped PS dots was obtained from an AFM measurement (Fig. 4.29) and the analysis of 559 stamped dots, with an average height of 60 nm ± 7nm.
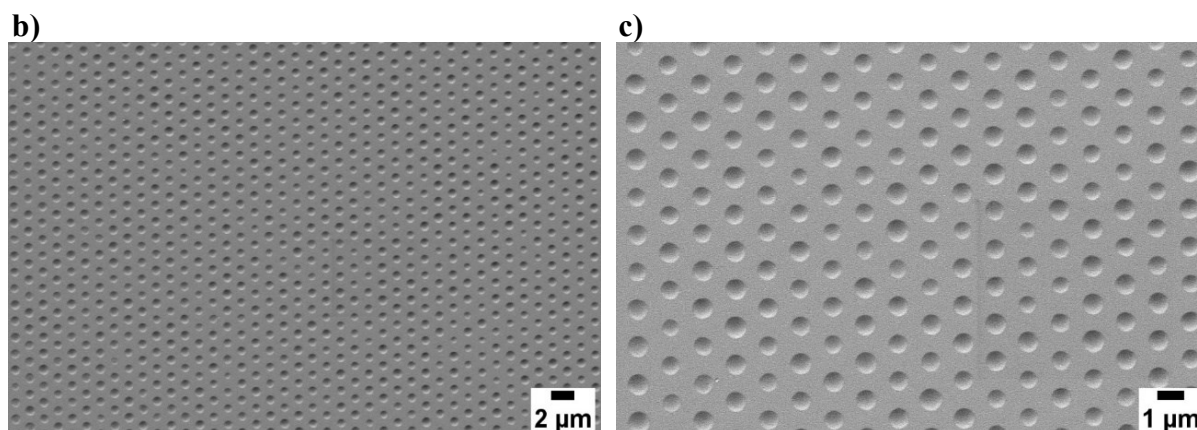
a)

b)

c)

d)
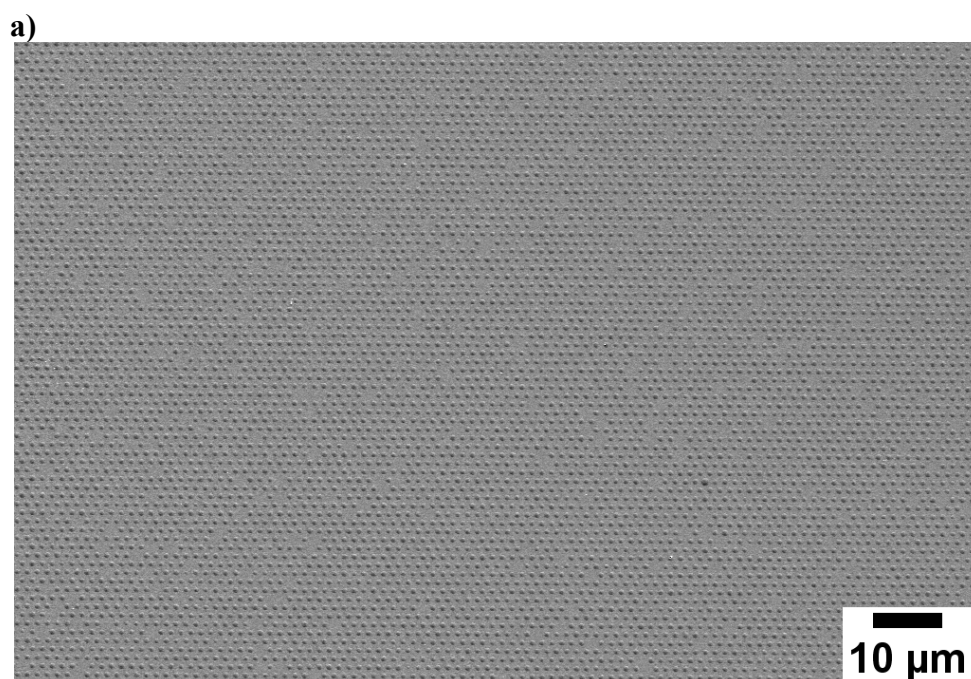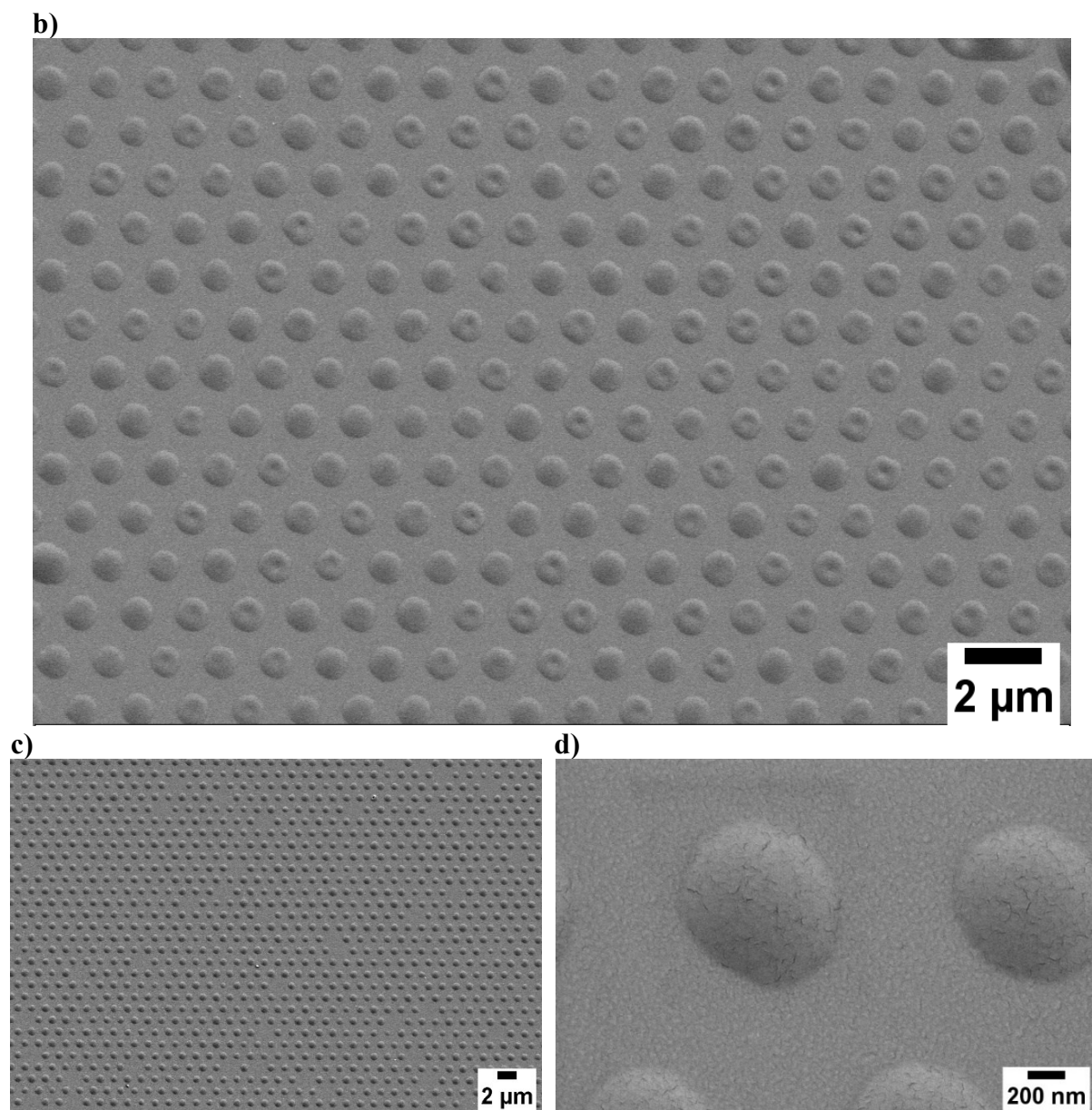
Figure 4.27 SEM images of PS dots stamped on glass at 200 °C with 15 min dwell time (stamping method III – *with pressure*).
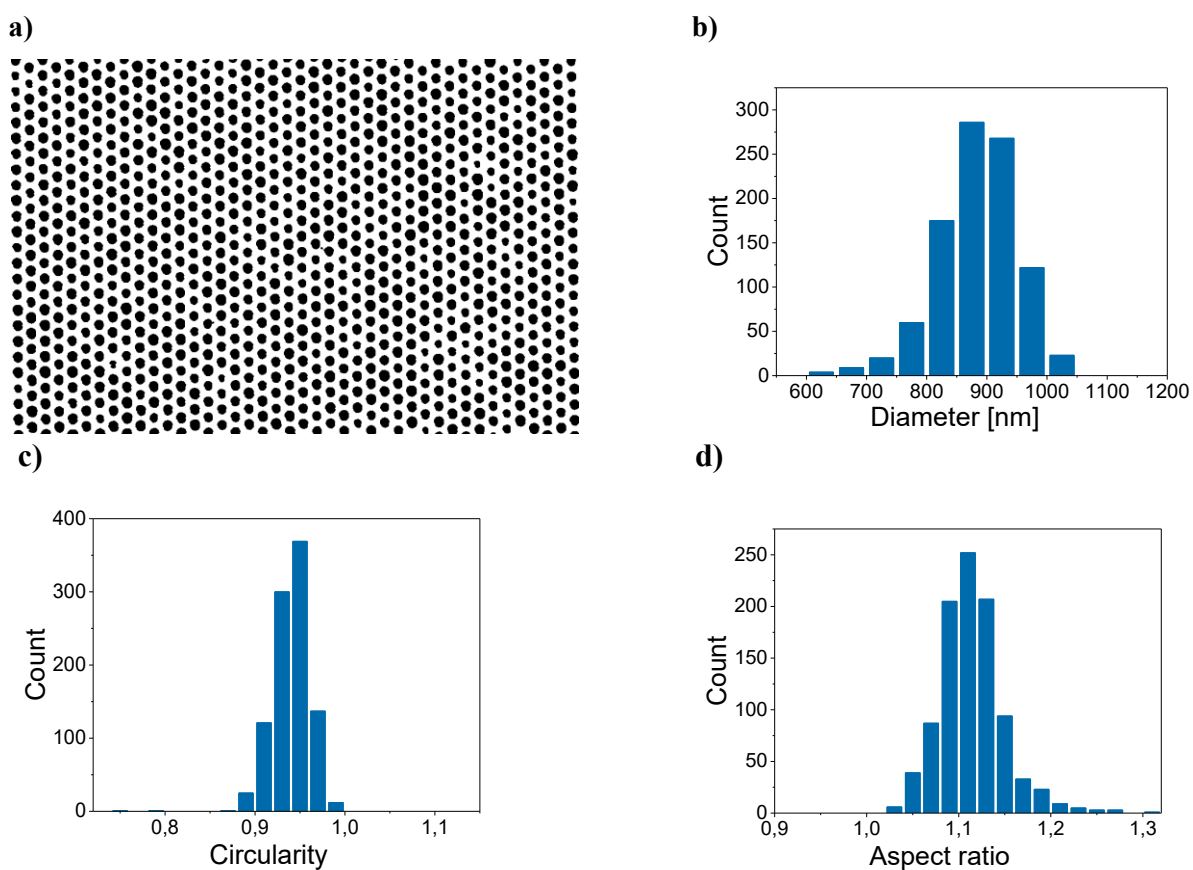
a)

b)

c)

d)
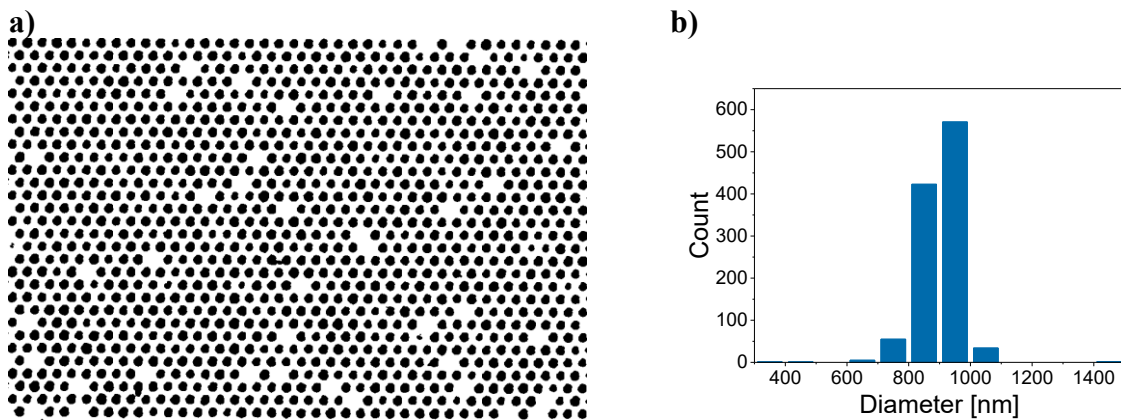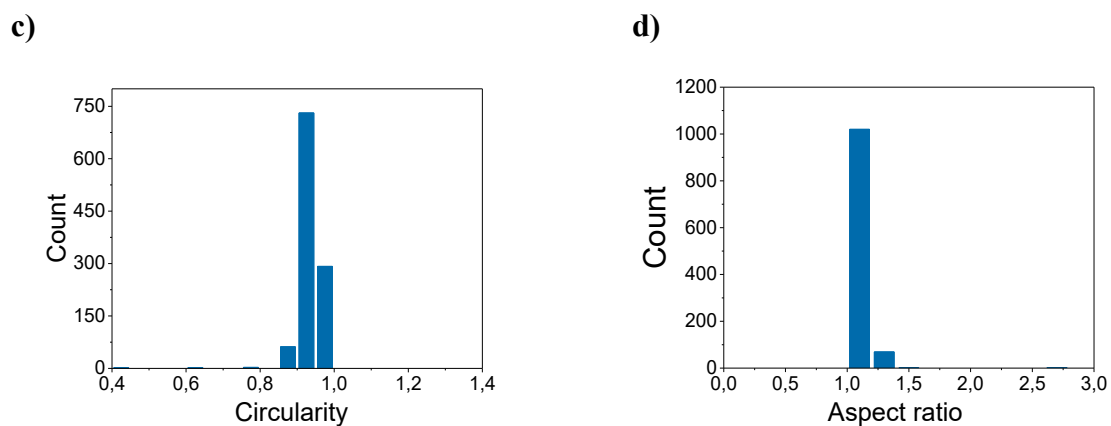
Figure 4.28 (a) Binarized SEM image (original image: Figure 4.27c) of PS dots on glass stamped at 200 °C with 15 min dwell time (stamping method III – *with pressure*). **(b)** Diameter, **(c)** circularity and **(d)** aspect ratio histograms of 1092 analyzed PS dots on glass determined by image analysis.
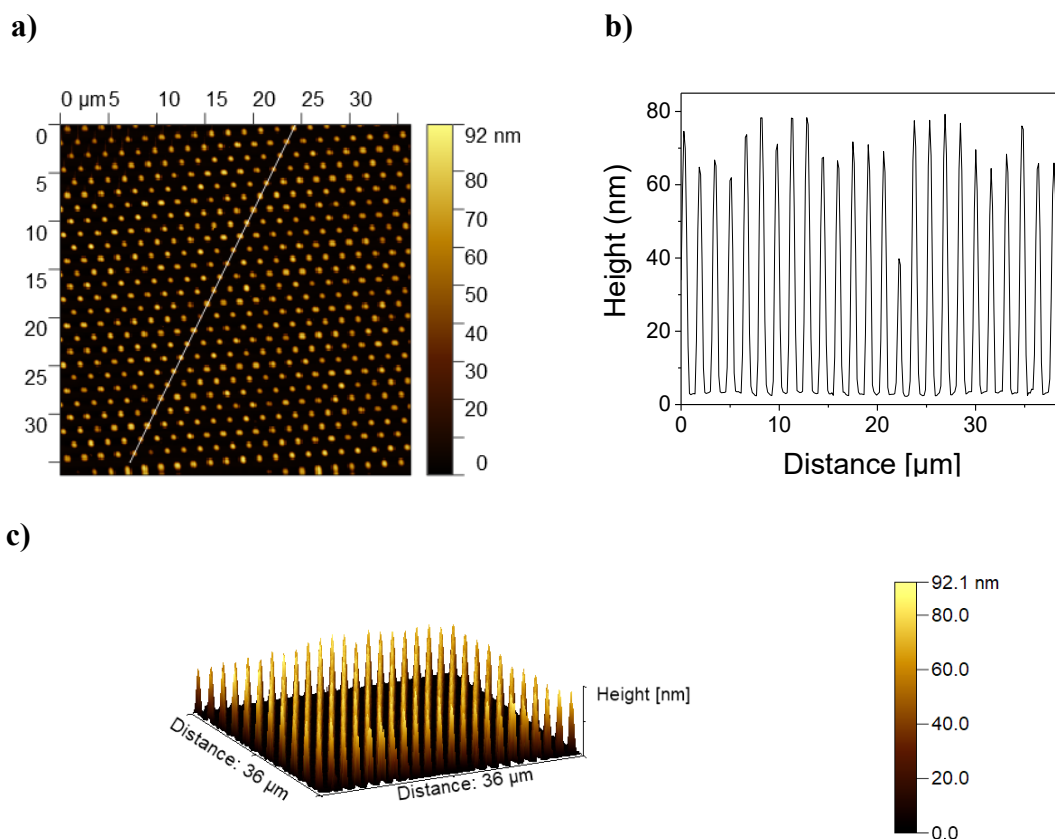
a)

b)

c)
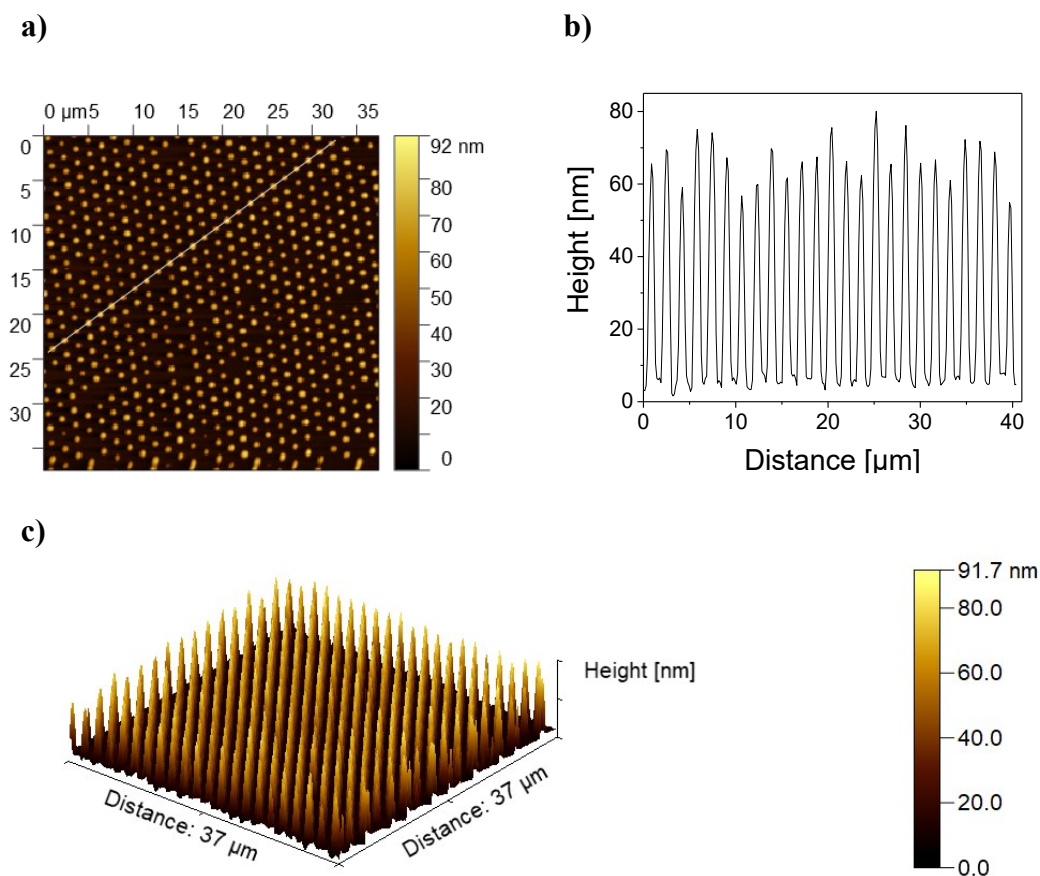
Figure 4.29 AFM imaging of PS dots stamped on glass at 200 °C with 15 min dwell time using stamping method III – *with pressure.* **(a)** Topographical AFM image, **(b)** topographical profile along the line in the panel (a) and **(c)** 3D AFM image.
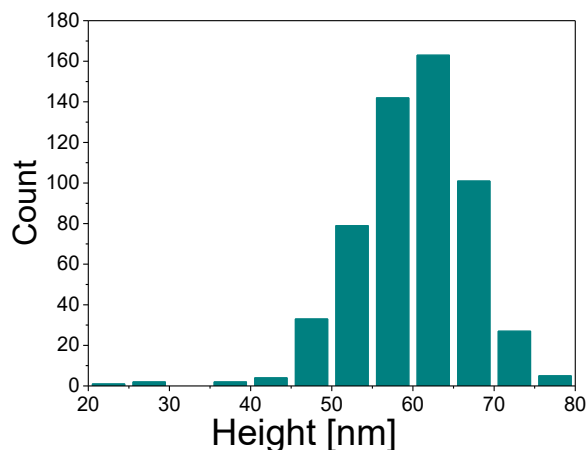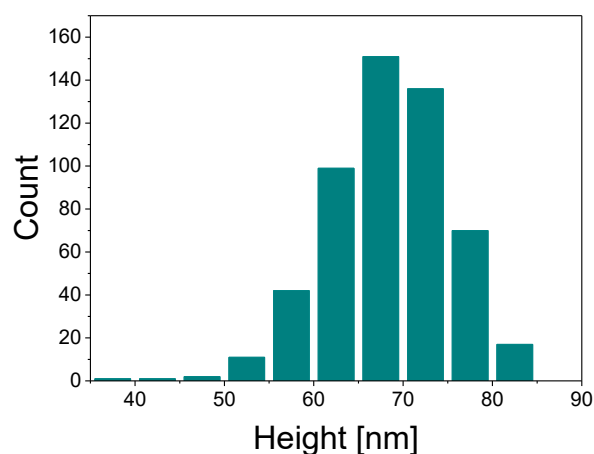
Figure 4.30 Histogram of the heights of 559 analyzed PS dots printed on a glass substrate with 15 min dwell time (stamping method III – *with pressure*). Heights were obtained from the analysis of the AFM image shown in the Figure 4.29a.

SEM images of PS dots stamped with a dwell time of 16 min show large stamped areas with ink-free spaces between the stamped PS dots. Both droplet-shaped and ring-shaped deposits are present on the substrate. Histograms obtained by image analysis (Fig. 4.31c) are shown in Figure 4.32, revealing an average diameter of the PS dots of 800 nm ± 71 nm, an average circularity of 0.9 ± 0.03, and an average aspect ratio of 1.27 ± 0.07. From the AFM measurements (Fig. 4.33) a frequency density of the heights of the PS dots stamped with 16 min stamping time was obtained (Fig. 4.34). The average dot height amounted to 68 nm ± 6 nm.

a)
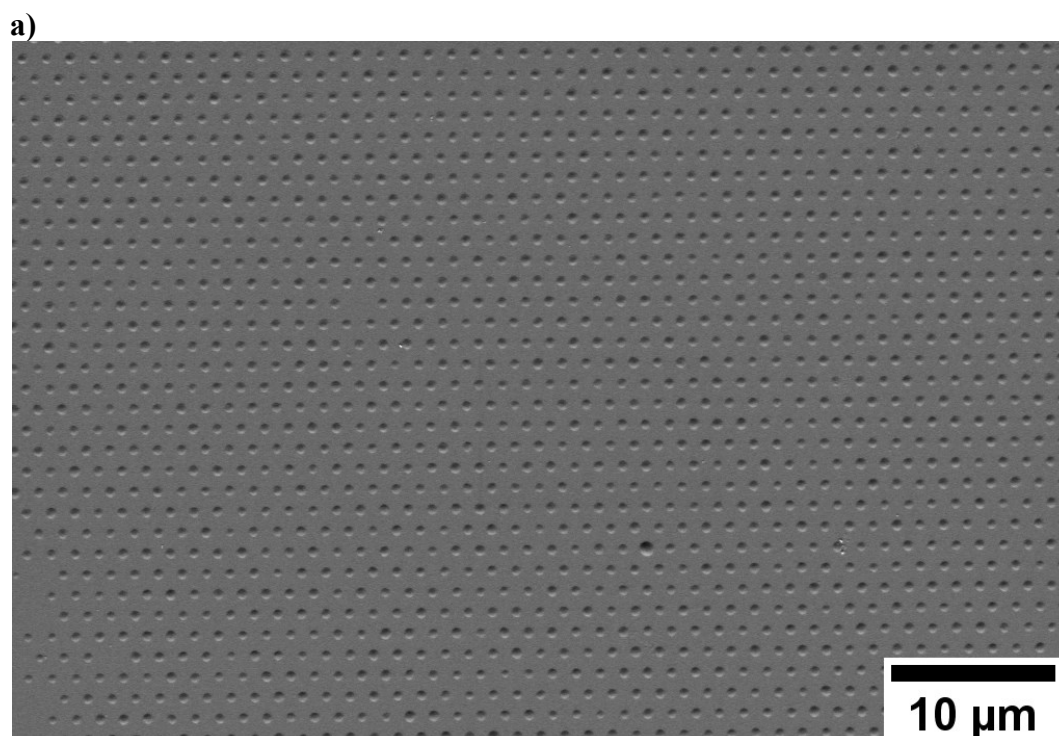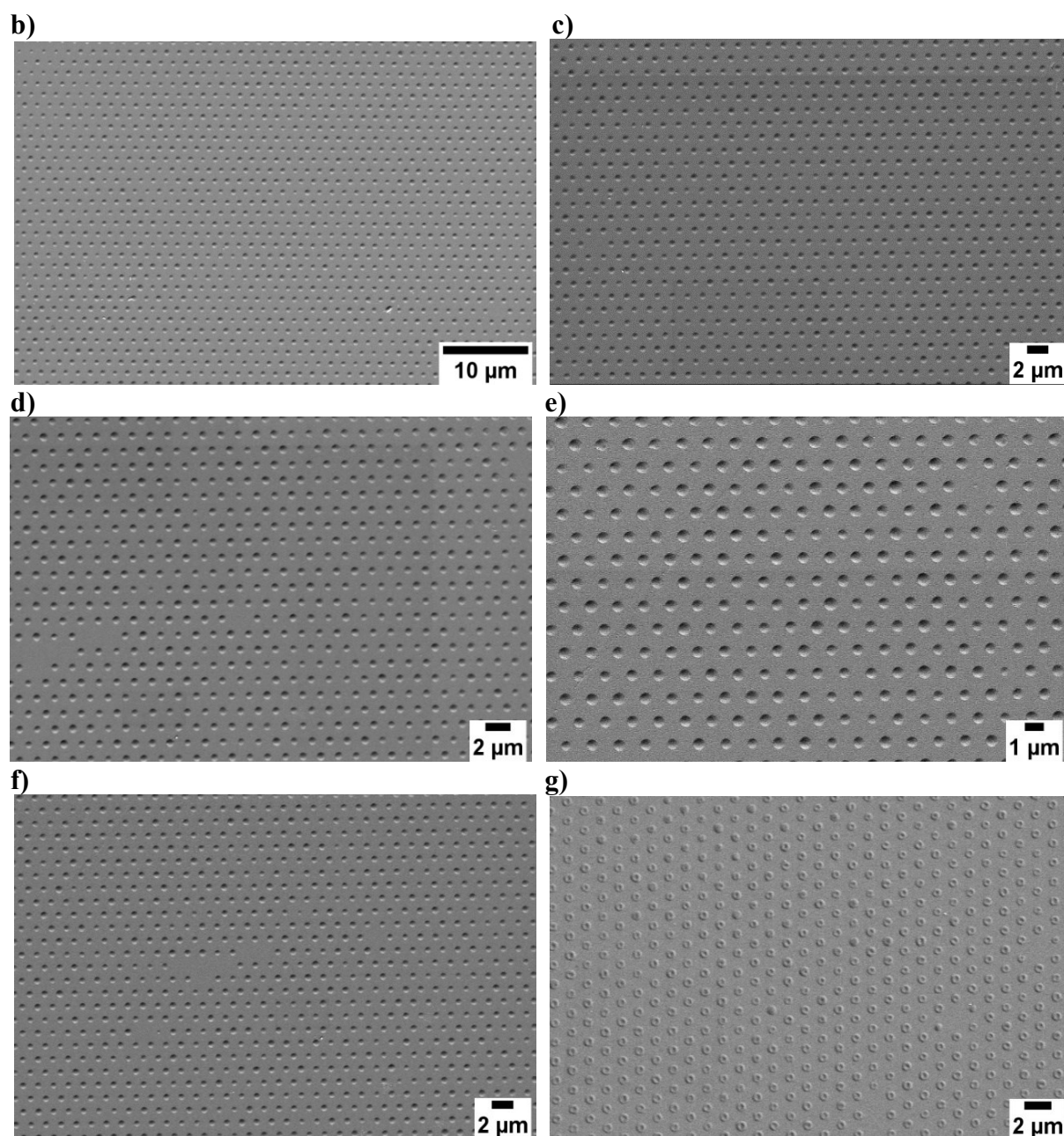
Figure 4.31 SEM images of PS dots stamped on glass at 200 °C with a dwell time of 16 min (stamping method III – *with pressure*).

c)

d)
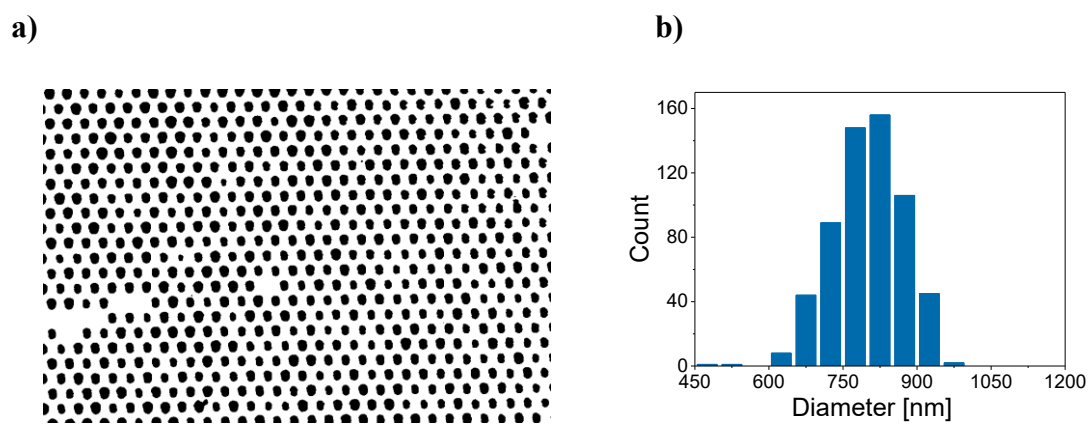
Figure 4.32 (a) Binarized SEM image (original image: Fig. 4.31d) of PS dots on glass stamped at 200 °C with 16 min dwell time (stamping method III – *with pressure*). **(b)** Diameter, **(c)** circularity and **(d)** aspect ratio histograms of 600 analyzed PS dots on glass acquired by image analysis.

a)

b)

c)

Figure 4.33 AFM imaging of PS dots on glass stamped at 200 °C with a dwell time of 16 min applying stamping method III – *with pressure.* **(a)** Topographical AFM image, **(b)** topographical profile along the line in panel (a) and (c) 3D AFM image.

Figure 4.34 Histogram of the heights of 529 analyzed PS dots printed on a glass substrate with 16 min dwell time (stamping method *with pressure*). Heights were obtained from the analysis of the AFM image shown in the Figure 4.33a.

Stamping of PS ink on glass substrate with 17 min dwelling time resulted in large printed areas with very little defects (Fig. 4.35). Histograms obtained by image analysis of Figure 4.35b shown in Figure 4.36 revealed an average PS dot diameter of 883 nm ± 66 nm, an average circularity of 0.94 ± 0.02, and an average aspect ratio of 1.11 ± 0.03. From the AFM measurements (Fig. 4.37) the height frequency density of the PS dots stamped with 17 min dwellling time is obtained (Fig. 4.38) with an average dot height of 68 nm ± 7 nm.

a)
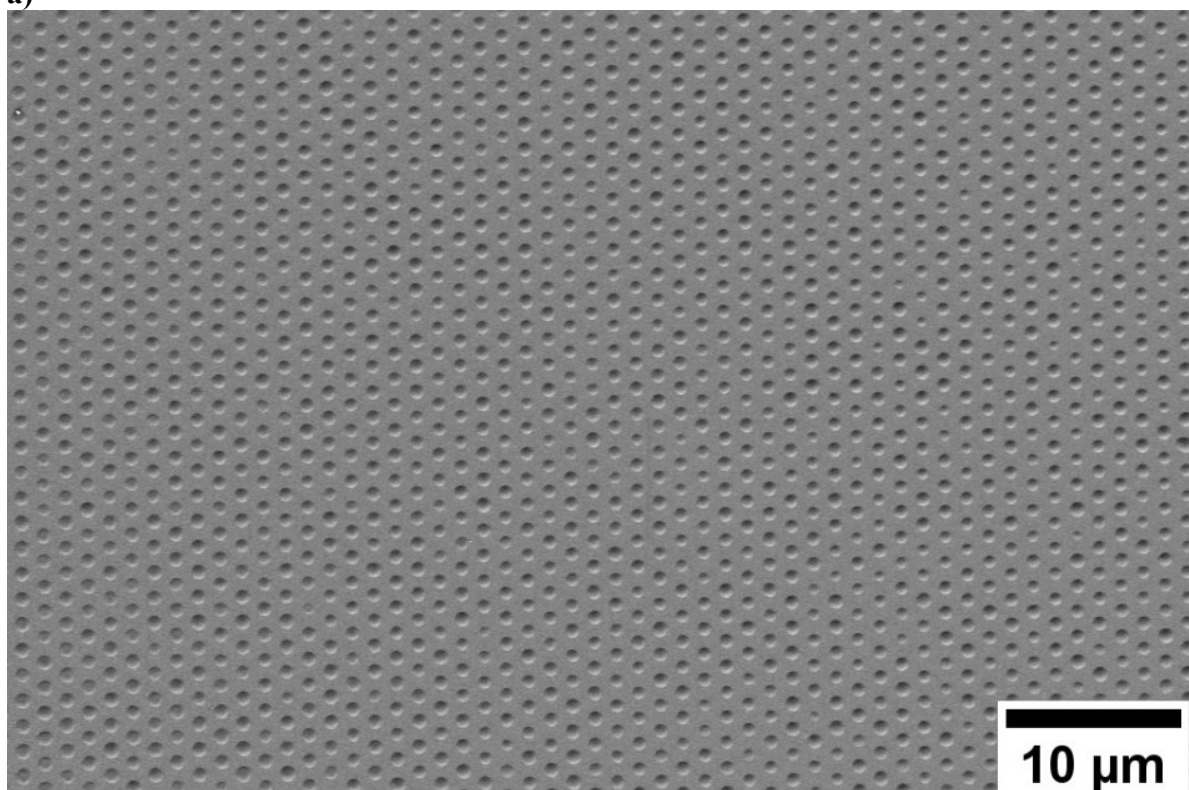
Figure 4.35 SEM images of PS dots stamped on glass at 200 °C with 17 min dwell time (stamping method *III – III – with pressure*).

Figure 4.36 (a) Binarized SEM image (see original SEM image in Fig. 4.35B) of PS dots on glass stamped at 200 °C with 17 min dwell time (stamping method III – *with pressure*). **(b)** Diameter, **(c)** circularity, and **(d)** aspect ratio histograms of 967 analyzed PS dots on glass acquired from the image analysis.
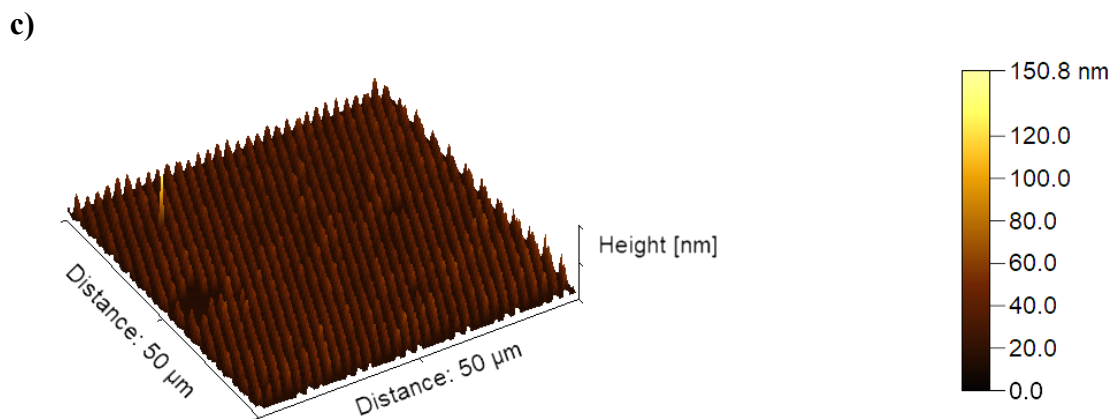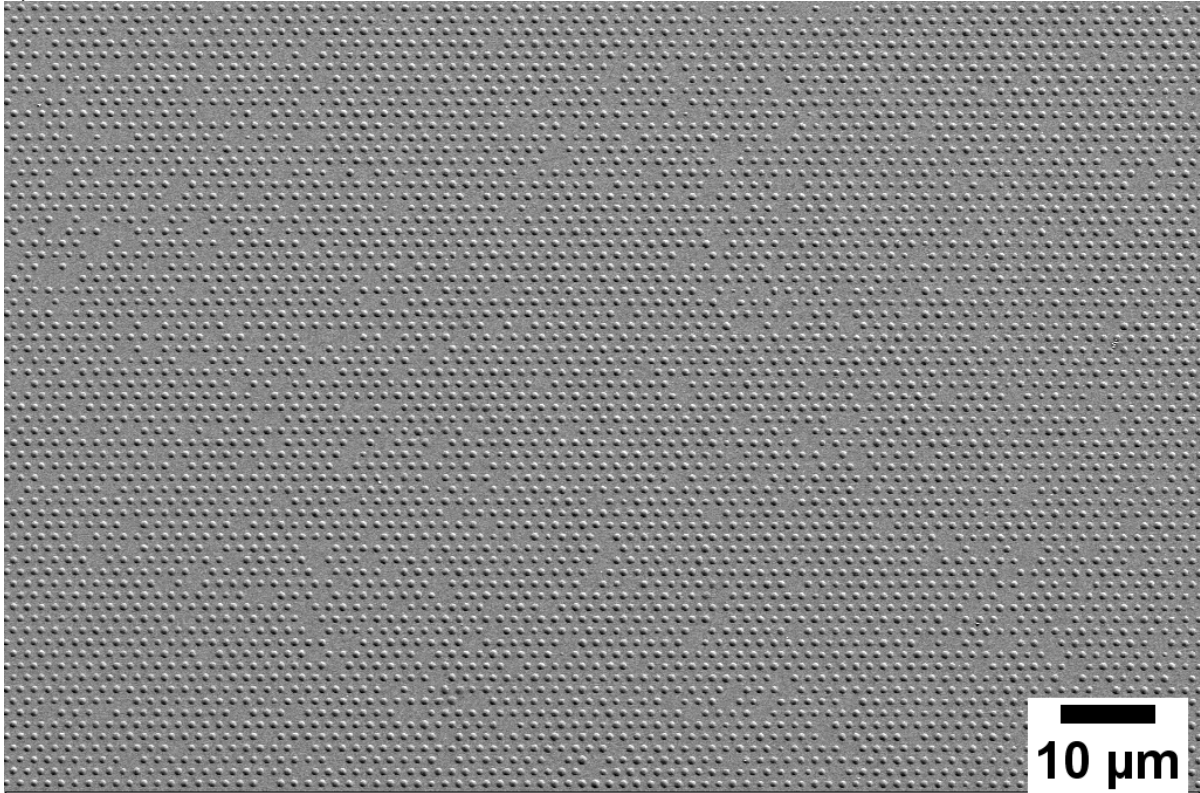
a)

b)

c)

Figure 4.37 AFM image of PS dots stamped on glass at 200 °C with 17 min dwell time by stamping method *with pressure.* **(a)** Topographical AFM image, **(b)** topographical profile along the line in the panel (a) and **(c)** 3D AFM image.


Figure 4.38 Histogram of 530 analyzed PS dots heights printed on glass substrate with 17 min dwell time (stamping method III – *with pressure*). Heights were obtained from the analysis of the AFM image shown in Figure 4.37a.

After 18 min dwell time, stamping results show simillar results, i.e., large printed areas of PS dots on glass substrates with little defects (Fig. 4.39). Image analysis yielded the histograms shown in Figure 4.40 revealing an average dot diameter of 819 nm ± 58 nm, an average circularity of 0.94 ± 0.02, and an average aspect ratio of 1.18 ± 0.06. From the AFM

measurement shown in Figure 4.41 the height frequency density of the PS dots stamped with 18 min dwell time is obtained (Fig. 4.42) with an average dot height of 33 nm $\pm$ 6 nm.
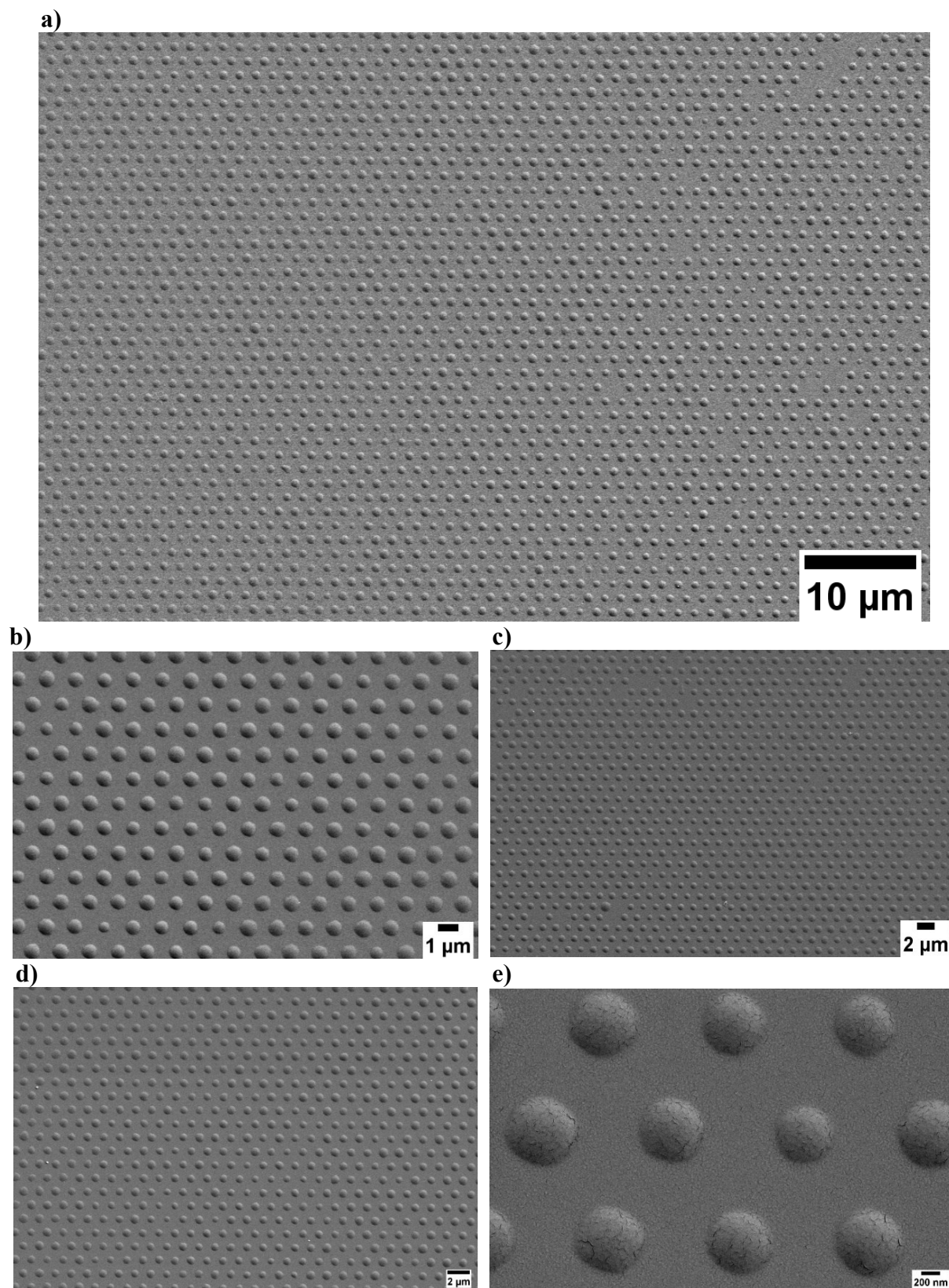
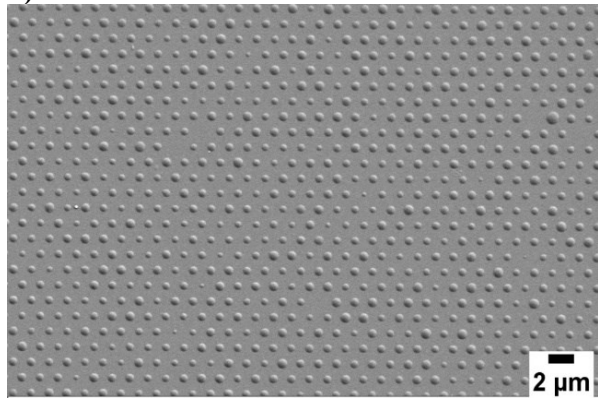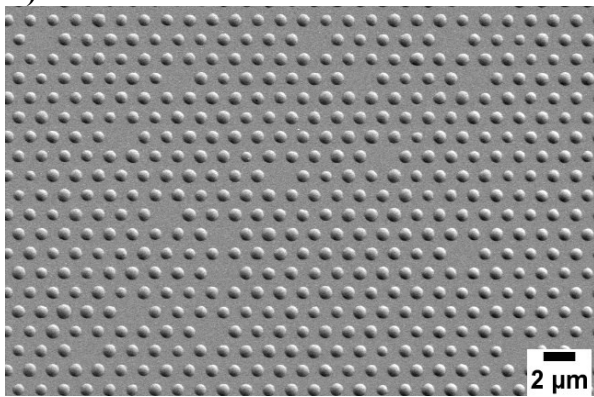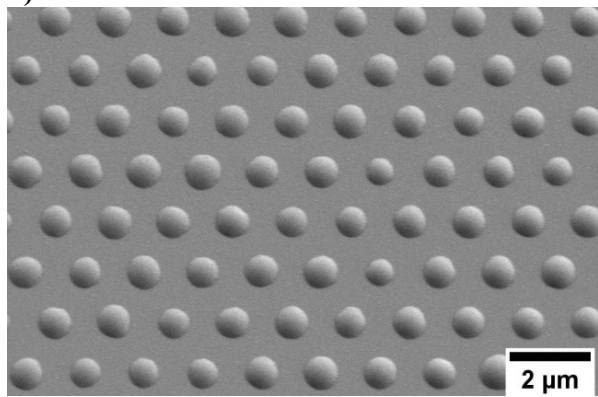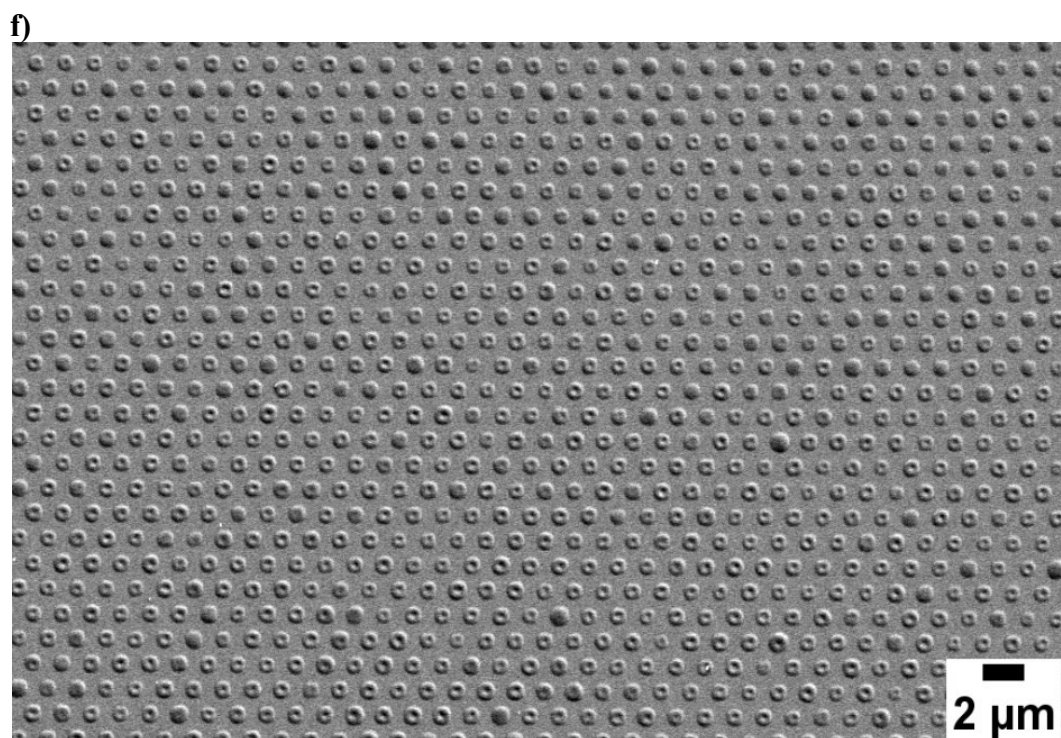**Figure 4.39** SEM images of PS dots stamped on glass at 200 °C with 18 min dwell time (stamping method III – *with pressure*).
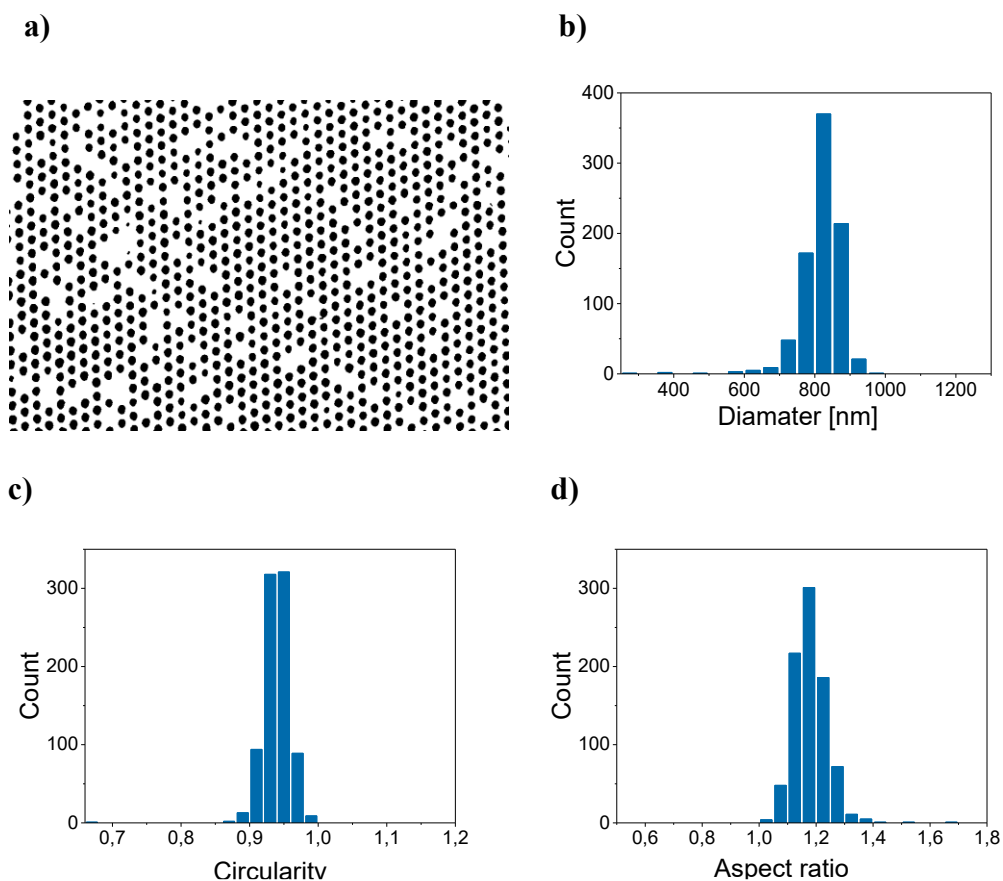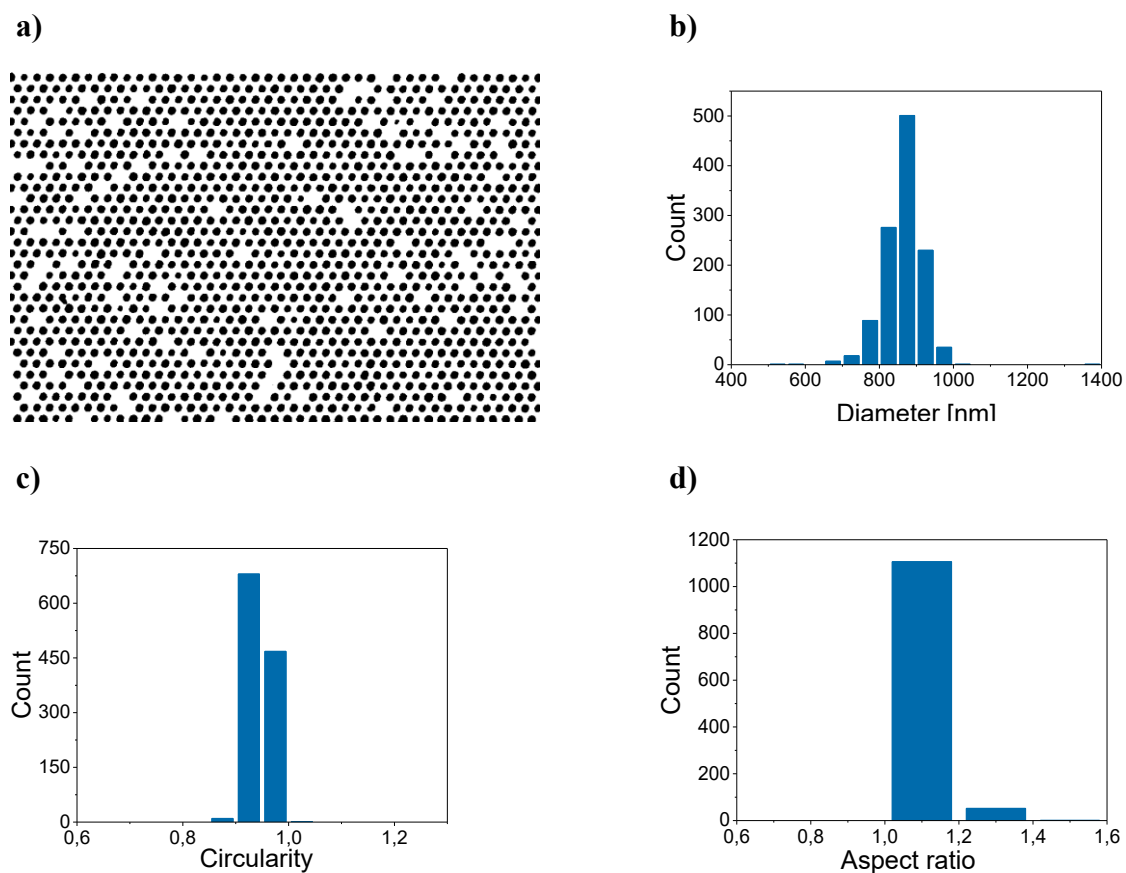
Figure 4.40 (a) Binarized SEM image (see original SEM image in Fig. 4.39C) of stamped PS dots on glass after 18 min dwell time at 200 °C (stamping method III – *with pressure*). **(b)** Diameters, **(c)** circularities, and **(d)** aspect ratios histograms of 847 analyzed PS dots on glass acquired from the image analysis.
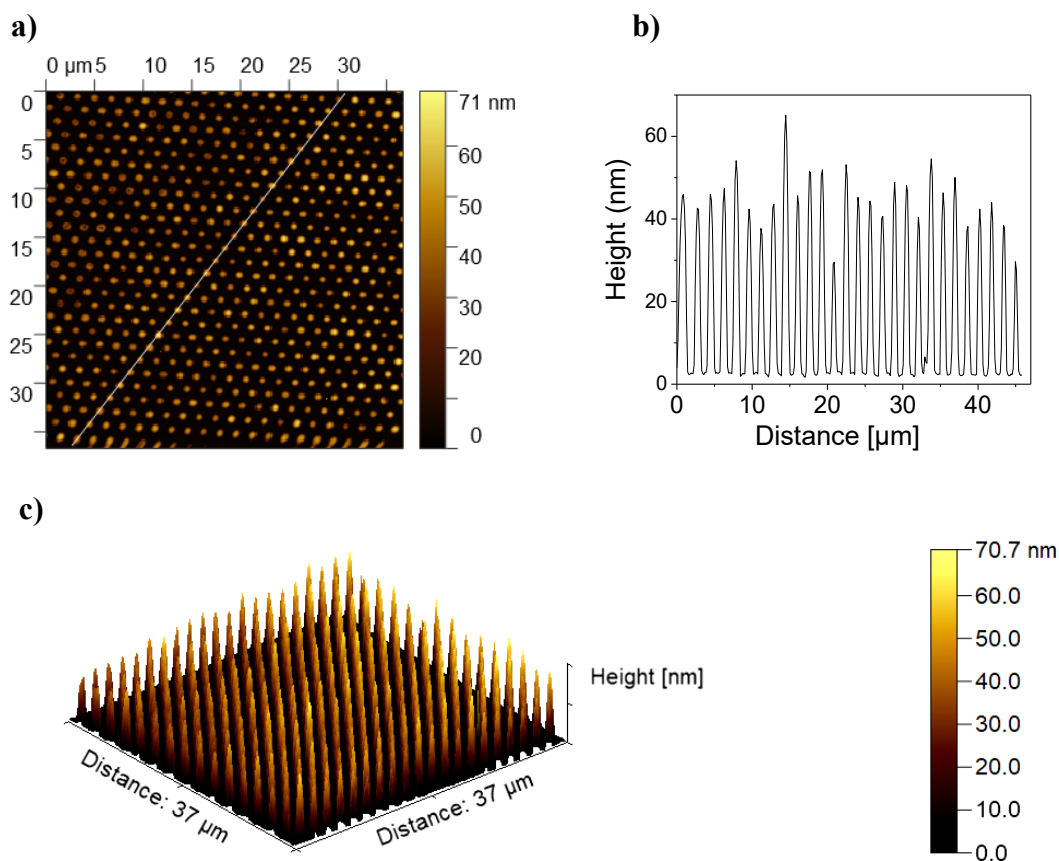

63

c)
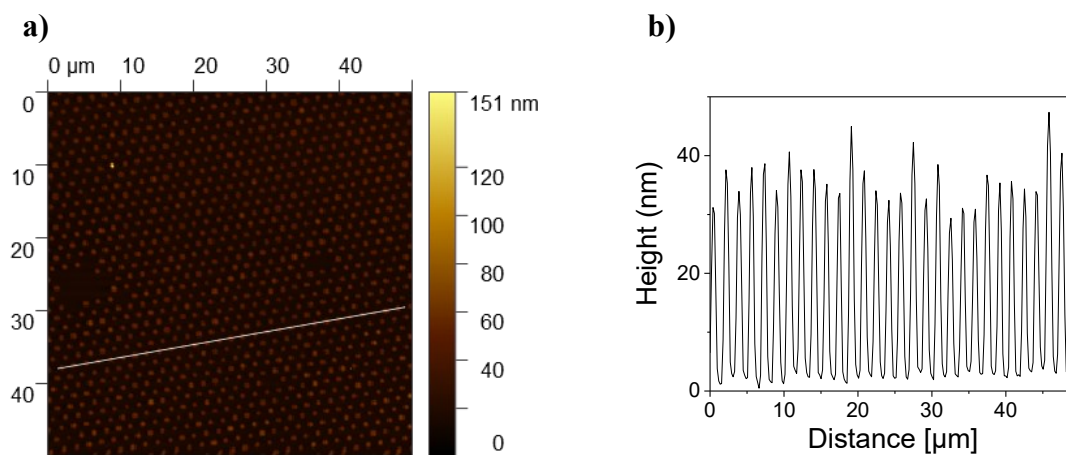
Figure 4.41 AFM image of PS dots stamped on glass at 200 °C with 18 min dwell time by stamping method *with pressure.* **(a)** Topographical AFM image**, (b)** topographical profile along the line in panel (a) and **(c)** 3D AFM image.
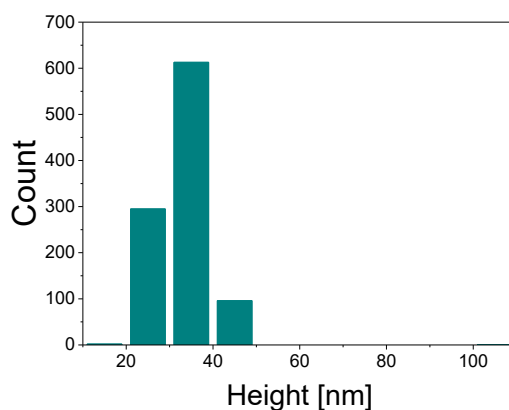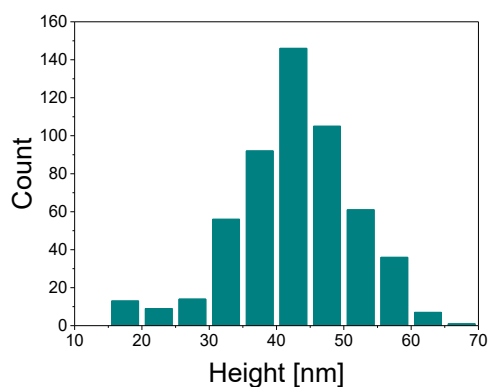

Figure 4.42 Height histogram of 1007 analyzed PS dots printed on a glass substrate with 18 min dwell time (stamping method III – *with pressure*). Heights were obtained from the analysis of the AFM image shown in Figure 4.41a.

Stamping with 19 min dwell time resulted in the formation of large area arrays of PS dots on glass substrates (Fig. 4.43). Deposits of PS ink are visible in two shapes, droplet-shaped and ring-shaped (Fig. 4.43f). Histograms obtained by image analysis are shown in Figure 4.44, revealing an average dot diameter of 865 nm ± 52 nm, an average circularity of 0.94 ± 0.02, and an average aspect ratio of 1.11 ± 0.07. From the AFM measurement seen in Fig. 4.45 a height frequency density of the PS dots stamped with 19 min dwell time is obtained (Fig. 4.46) revealing an average dot height of 43 nm ± 9 nm.

65

f)
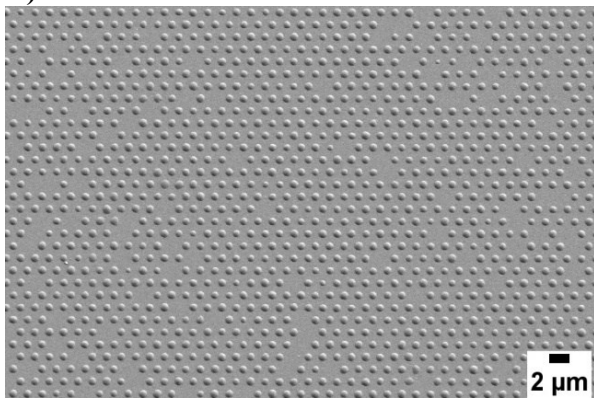
Figure 4.43 SEM images of PS dots stamped on glass at 200 °C after 19 min dwell time (stamping method III – *with pressure*).

a)

b)

c)

d)

Figure 4.44 (a) Binarized SEM image (see original SEM image in Figure 4.41b) of PS dots stamped on glass with 19 min dwell time at 200 °C (stamping method III – *with pressure*). **(b)** Diameter, **(c)** circularity, and **(d)** aspect ratio histograms of 1160 analyzed PS dots on glass acquired by image analysis.
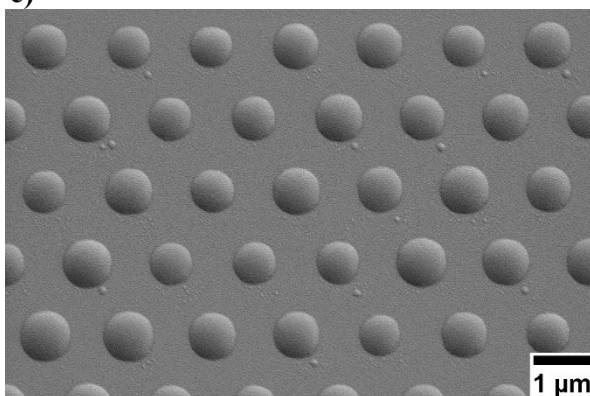
a)

b)

c)

Figure 4.45 AFM image of PS dots stamped on glass at 200 °C with 19 min dwell time by stamping method *with pressure*. **(a)** Topographical AFM image, **(b)** topographical profile along the line in the panel (a) and **(c)** 3D AFM image.

Figure 4.46 Height histogram of 540 analyzed PS dots s printed on a glass substrate with 19 min dwell time (stamping method III – *with pressure*). Heights were obtained from the analysis of the AFM image shown in Fig. 4.45a.

SEM images of the PS dots stamped with 20 min dwell time show large stamped areas with PS deposits in both shapes, droplet- and ring-shaped (Fig. 4.47). Histograms obtained by image analysis are shown in Figure 4.48. The average dot diameter amounts to 827 nm ± 48 nm, the average circularity to 0.94 ± 0.02, and the average aspect ratio to 1.09 ± 0.03. From the AFM

measurement shown in Figure 4.49 a height histigram of the PS dots stamped with 20 min dwell time is obtained (Fig. 4.50). The average dot height is 46 nm ± 8 nm.

a)

b)

c)

d)

f)

g)
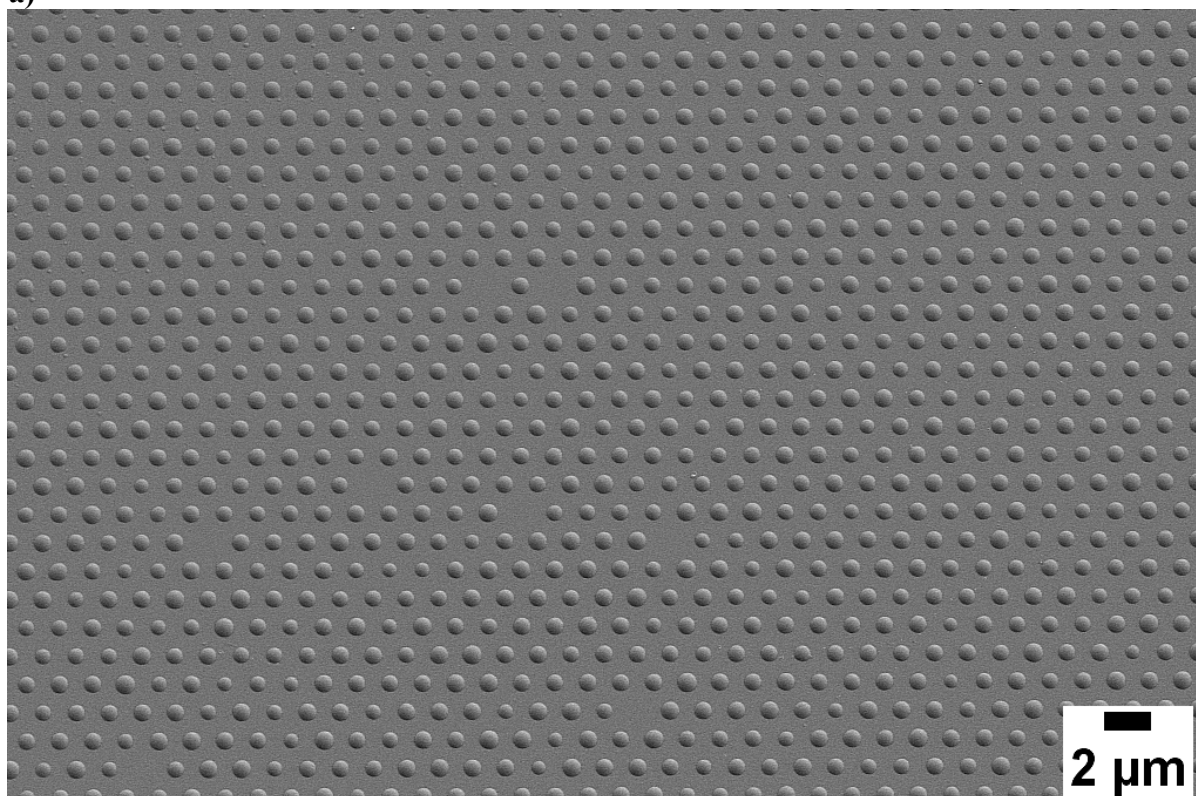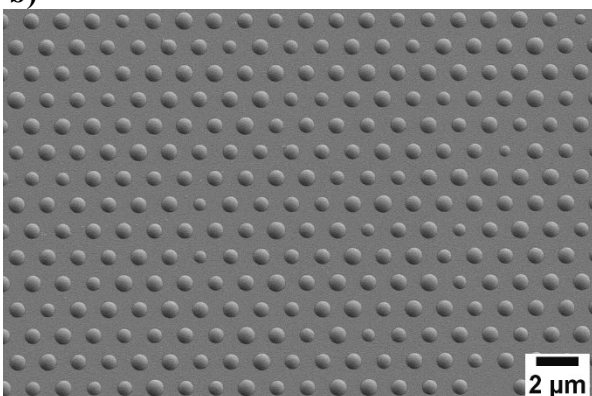
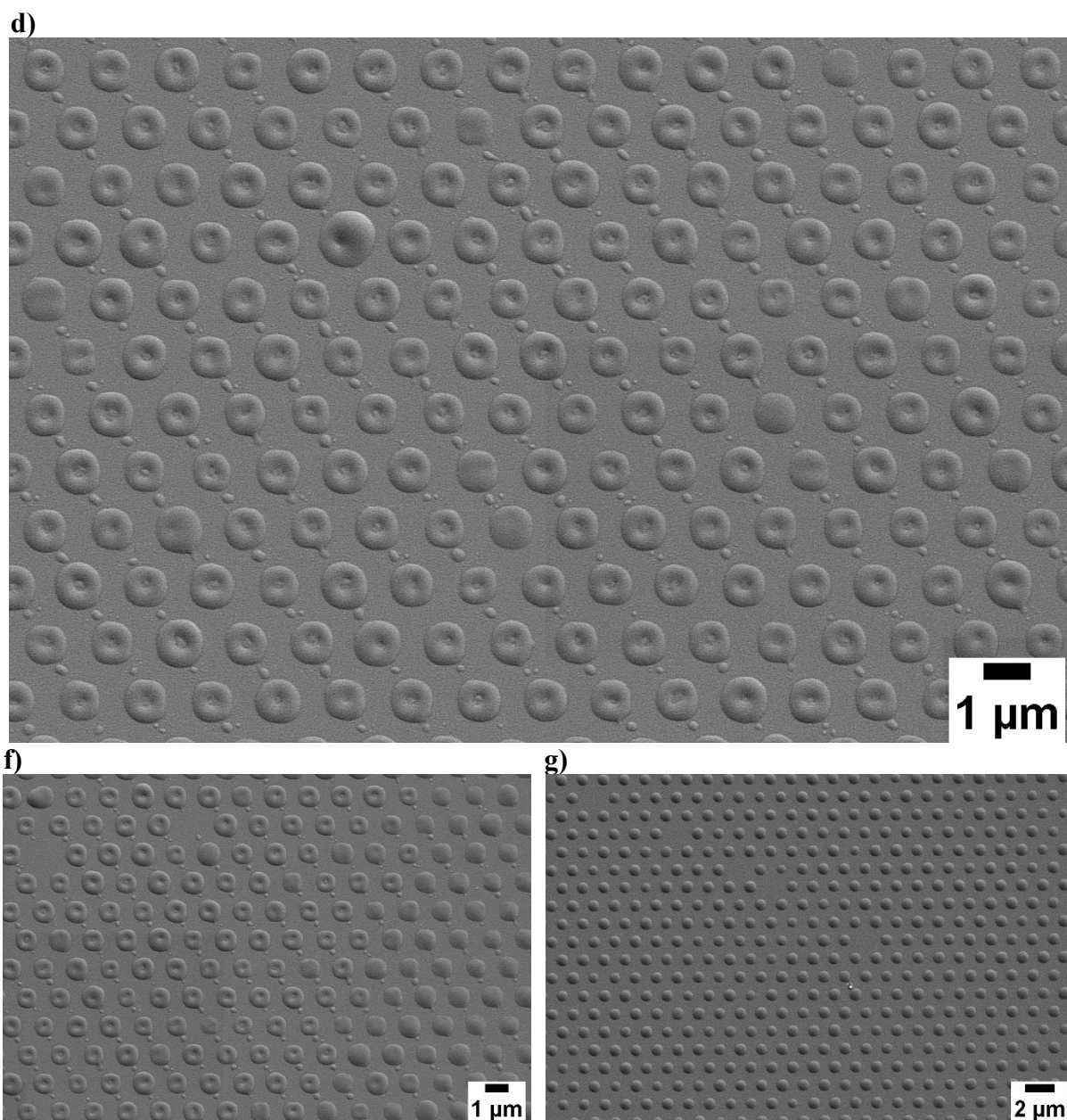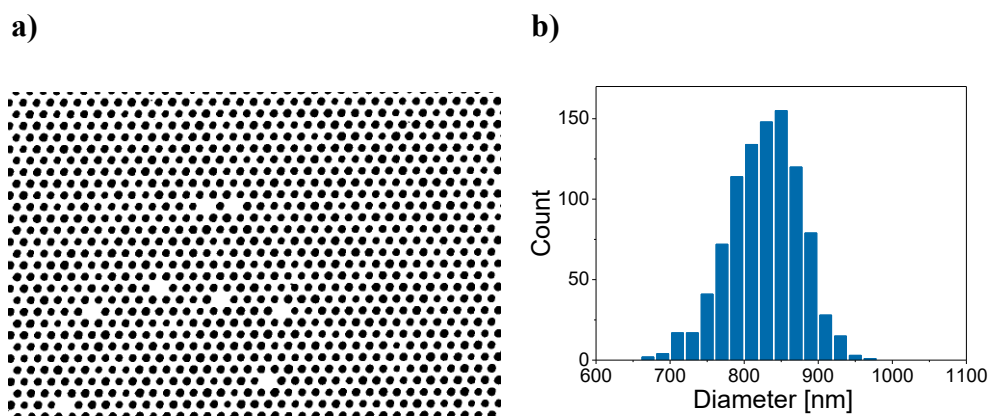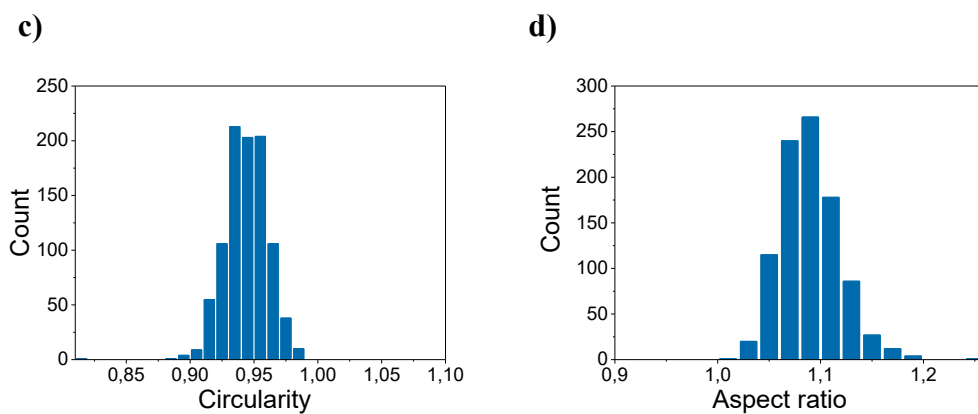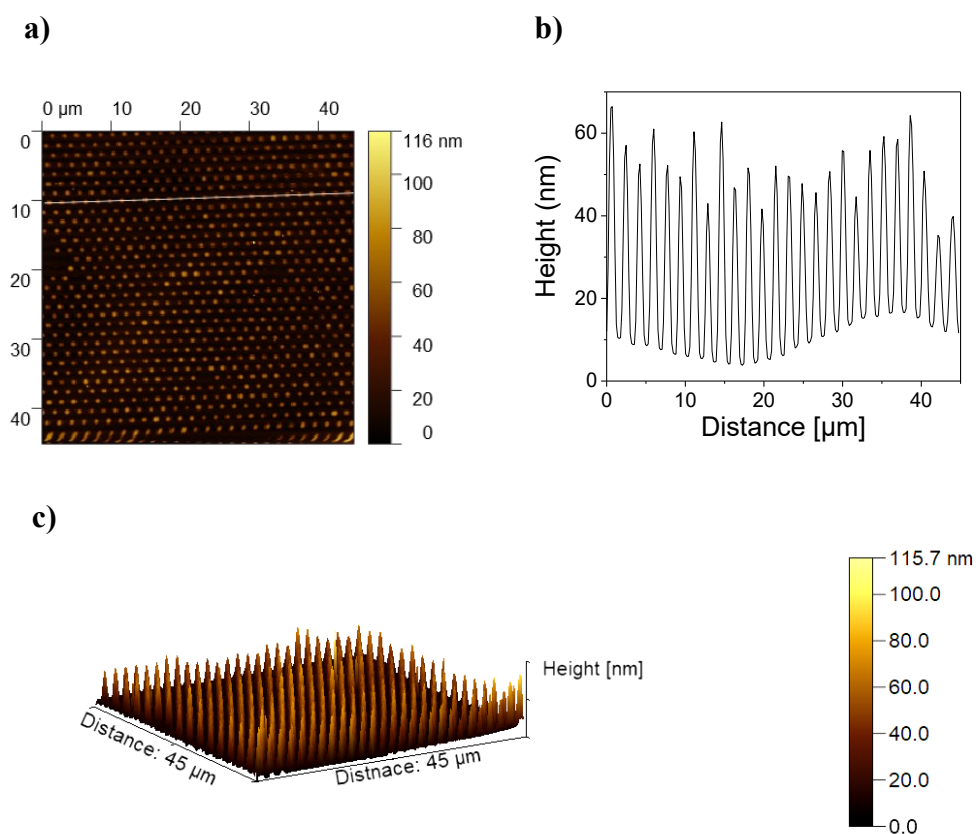**Figure 4.47** SEM images of PS dots stamped on glass at 200 °C with 20 min dwell time (stamping method III – *with pressure*).

a)

b)

c)

d)

Figure 4.48 (a) Binarized SEM image (see original SEM image in Fig. 4.47a) of PS dots stamped on glass with 20 min dwell time at 200 °C (stamping method III – *with pressure*). **(b)** Diameter, **(c)** circularity, and **(d)** aspect ratio histograms of 950 analyzed PS dots on glass acquired by image analysis.

a)

b)

c)

Figure 4.49 AFM image of PS dots stamped on glass at 200 °C with 20 min dwell time by stamping method *with pressure*. (a) Topographical AFM image, (b) topographical profile along the line in panel (a) and (c) 3D AFM image.
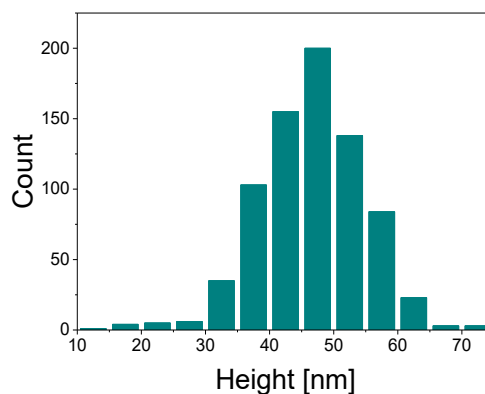
Figure 4.50 Height histogram of 760 analysed PS dots after 20 min dwell time, acquired from AFM measurement that is shown in Fig. 4.49.

SEM results of the PS dots stamped with 25 min stamping time show large stamped areas on glass substrates (Fig. 4.51). The printing results in dot arrays with only a few defects. Image analysis of Figure 4.51c yielded histograms shown in Figure 4.52 revealing the average diameter of 879 nm ± 75 nm, the average circularity of 0.92 ± 0.01, and the average aspect ratio of 1.10 ± 0.03. From the AFM measurement shown in Fig. 4.53 the height frequency density of the PS dots stamped with 25 min dwell ti©e is obtained (Fig. 4.54), which reveals an average dot height of 49 nm ± 8 nm.
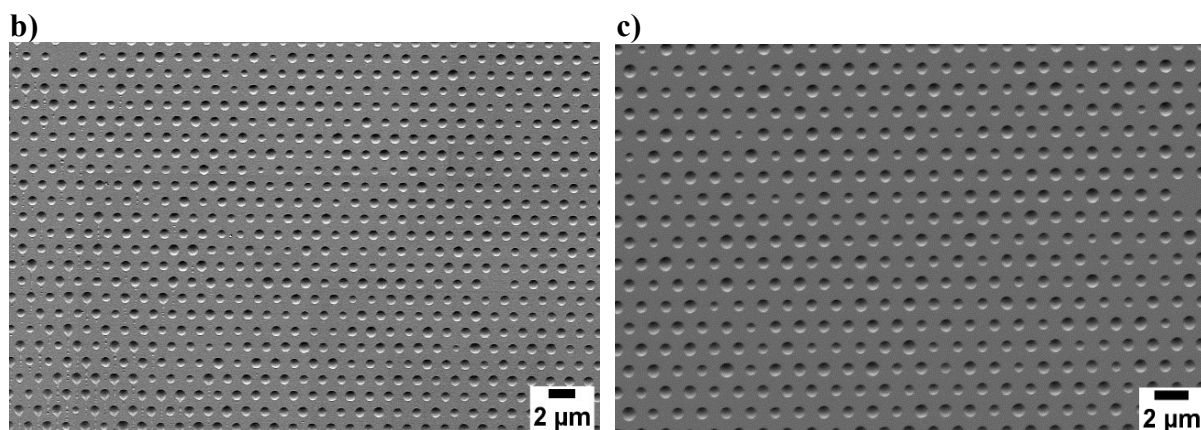
a)
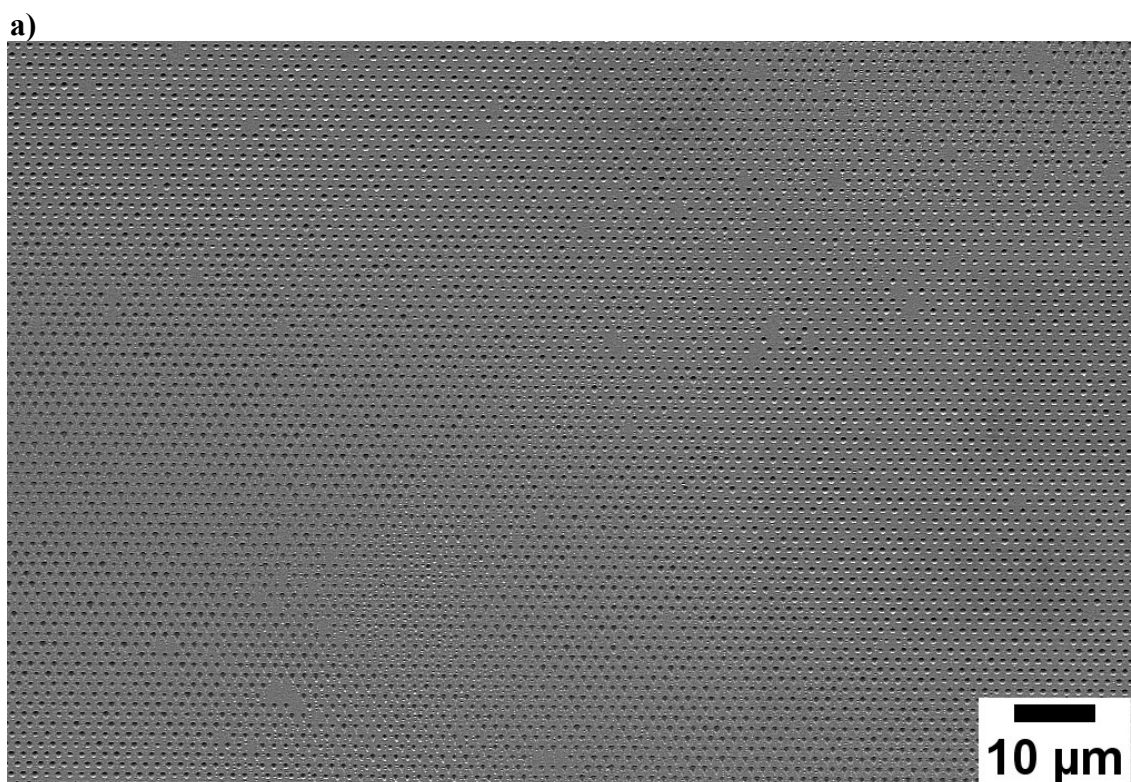
Figure 4.51 SEM images of PS dots stamped on glass at 200 °C with 25 min dwell time (stamping method III – *with pressure*).
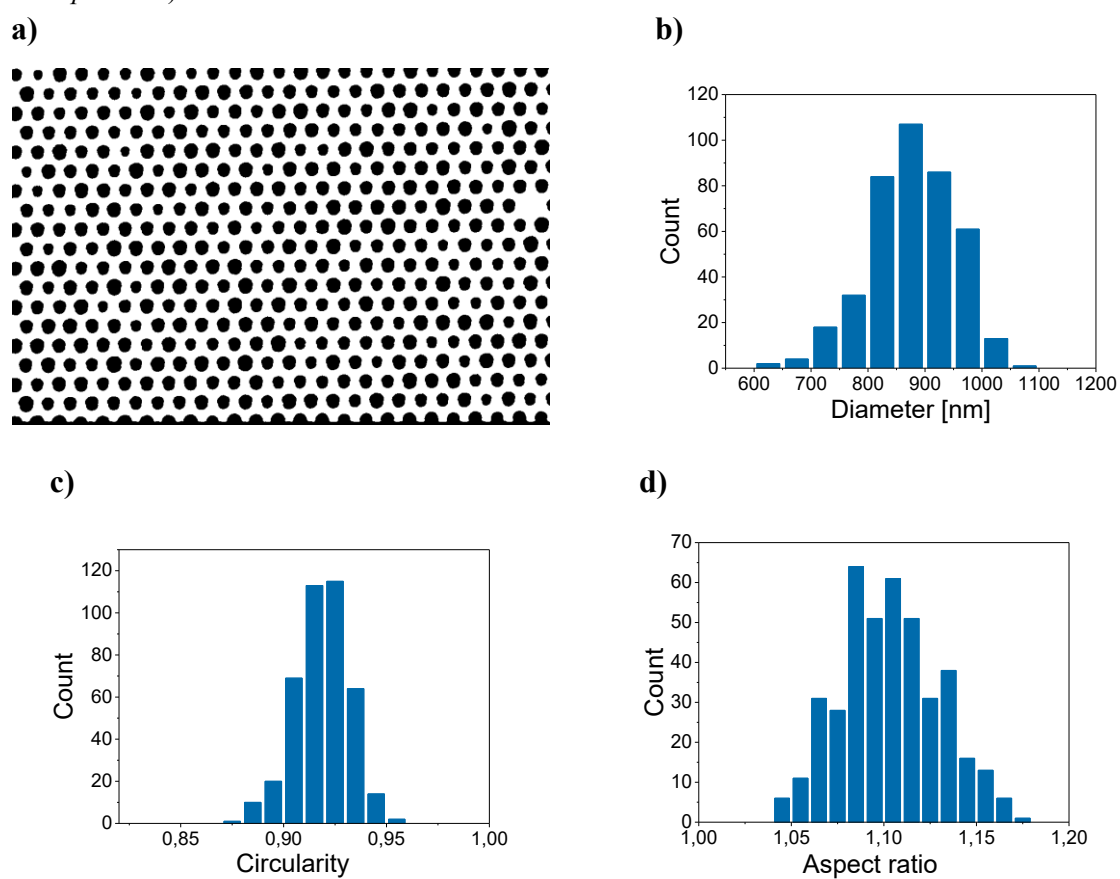

Figure 4.52 (a) Binarized SEM image (see original SEM image in Fig. 4.51c) of PS dots stamped on glass with 25 min dwell time at 200 °C (stamping method III – *with pressure*). **(b)** Diameter, **(c)** circularity, and **(d)** aspect ratio histograms of 408 analyzed PS dots on glass acquired by image analysis.
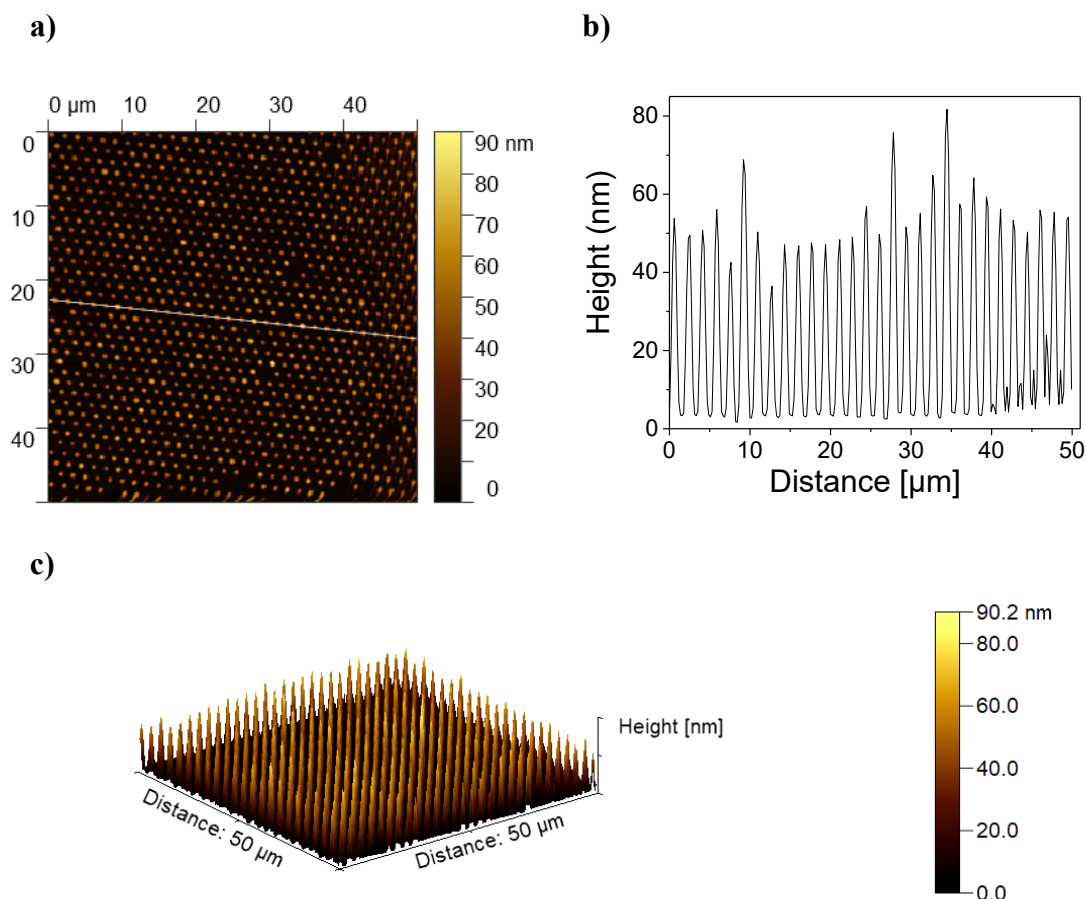
a)

b)

c)

Figure 4.53 AFM image of PS dots stamped on glass at 200 °C with 25 min dwell time by stamping method *with pressure*. **(a)** Topographical AFM image, **(b)** topographical profile along the line in panel (a) and **(c)** 3D AFM image.
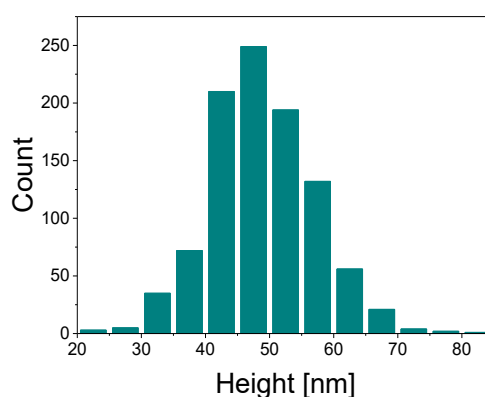

Figure 4.54 Height histogram of 984 analyzed PS dots printed on a glass substrate with 25 min dwell time (stamping method III – *with pressure*). Heights were obtained from the analysis of the AFM image shown in the Figure 4.53a.

In Figure 4.55 PS dots on a glass substrate printed with 30 min dwell time are shown. Histograms obtained by image analysis of Figure 4.55b shown in Figure 4.56 revealed an average dot diameter of 967 nm ± 57 nm, an average circularity of 0.91 ± 0.01, and an average

aspect ratio of 1.17 ± 0.03. From the AFM measurements shown in Figure 4.57 a height frequency densityn of the PS dots stamped with 30 min stamping time is obtained (Fig. 4.58) revealing an average dot height of 69 nm ± 8 nm.
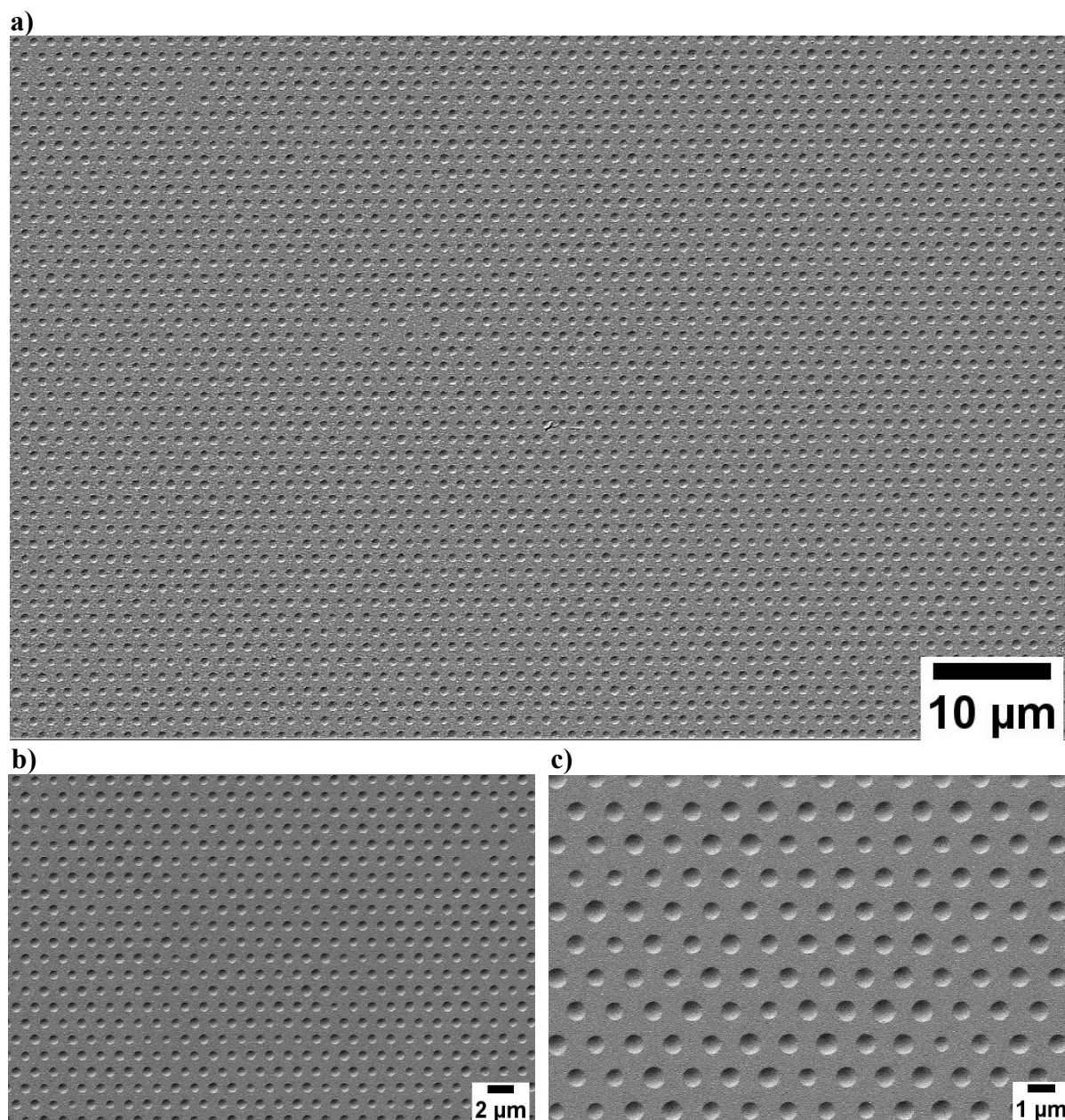
a)

b)

c)

Figure 4.55 SEM images of PS dots stamped on glass at 200 °C with 30 min dwell time (stamping method III – *with pressure*).
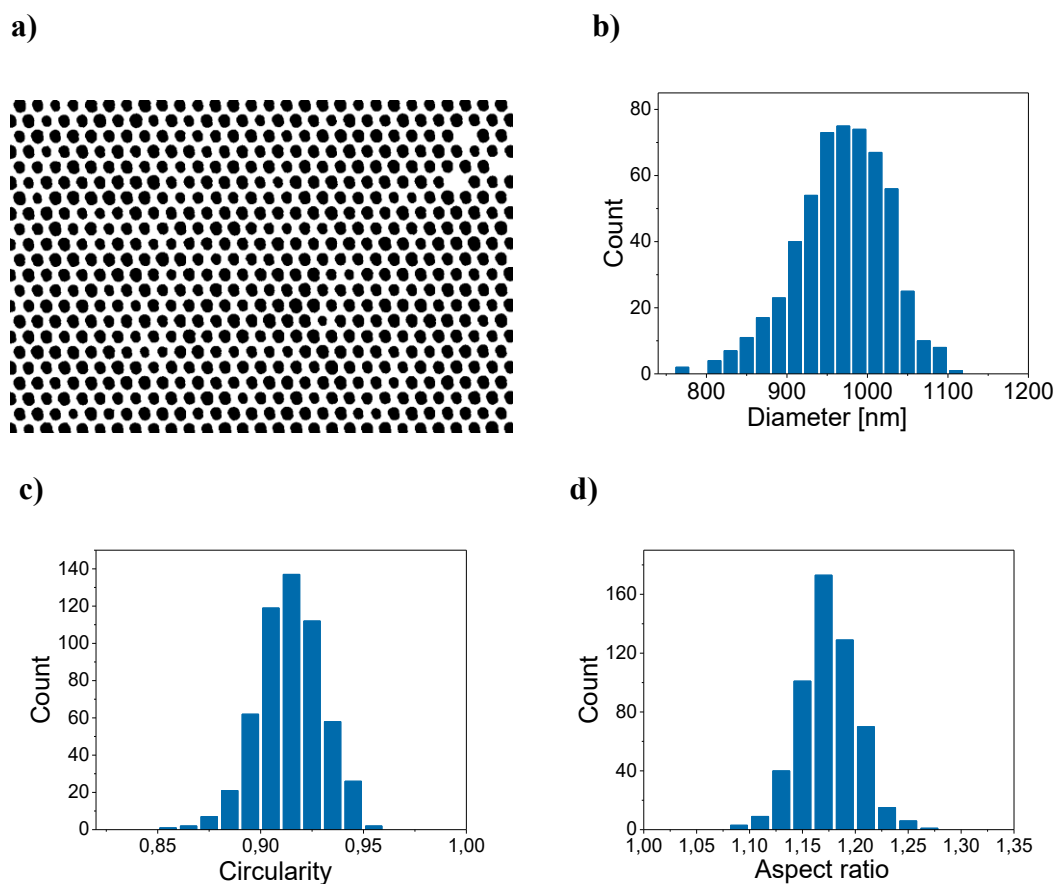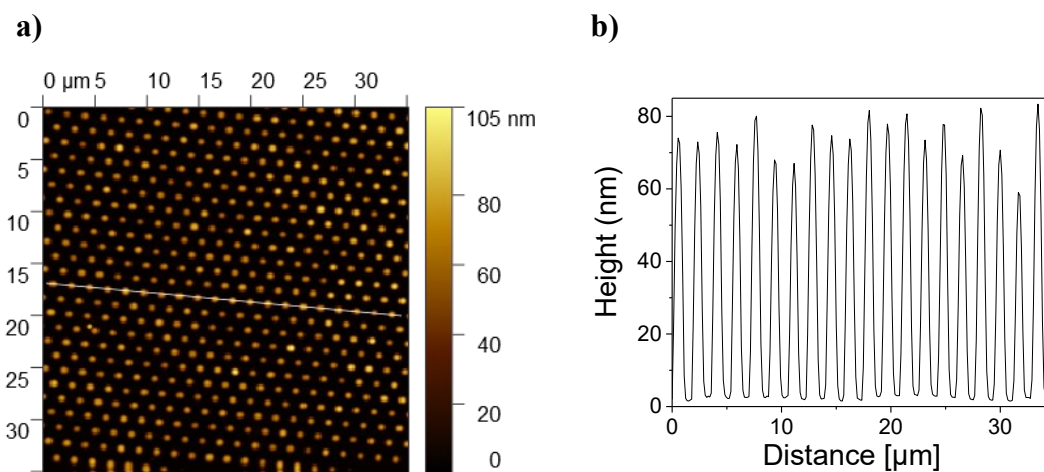
Figure 4.56 (a) Binarized SEM image (see original SEM image in Fig. 4.55b) of PS dots stamped on glass with 30 min dwell time at 200 °C (stamping method III – *with pressure*). **(b)** Diameter, **(c)** circularity, and **(d)** aspect ratio histograms of 547 analyzed PS dots on glass acquired by image analysis.
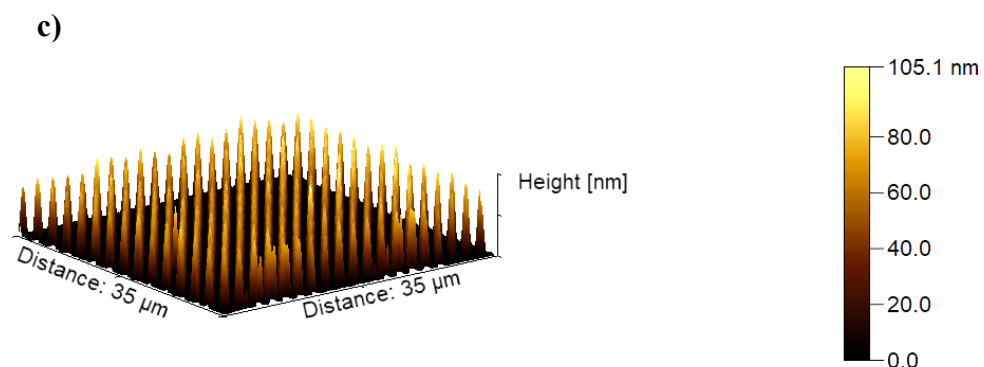
c)

Figure 4.57 AFM image of PS dots stamped on glass at 200 °C with 30 min dwell time by stamping method *with pressure*. **(a)** Topographical AFM image, **(b)** topographical profile along the line in the panel (a) and **(c)** 3D AFM image.
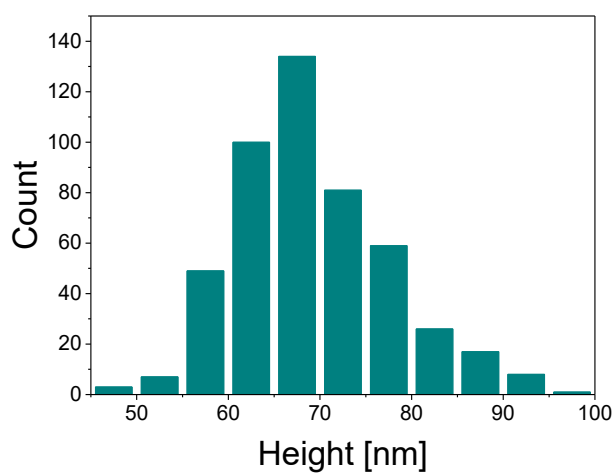

Figure 4.58 Height histogram of 485 analyzed PS dots printed on a glass substrate with 30 min dwell time (stamping method III – *with pressure*). Heights were obtained from the analysis of the AFM image shown in Figure 4.57a.
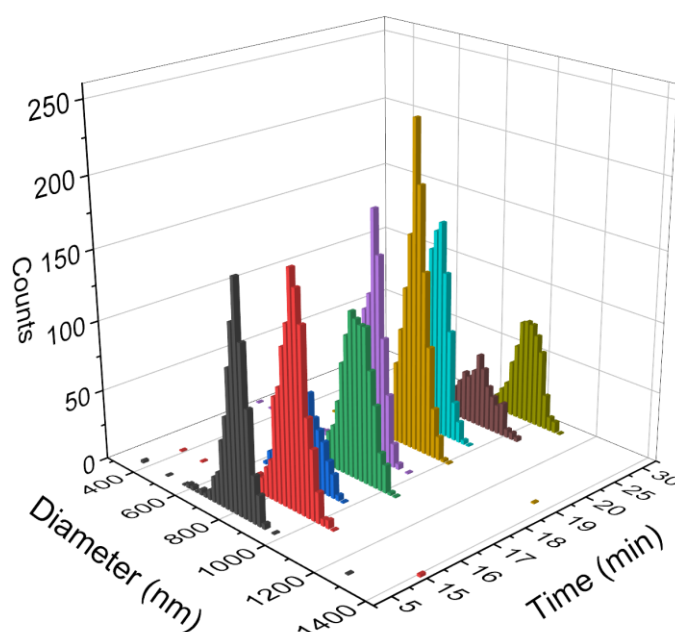
Figure 4.59 Summary histogram with diameter values of PS dots on glass obtained by stamping method III – *with pressure* after 5 min (black), 15 min (red), 16 min (blue), 17 min (green), 18 min (purple), 19 min (mustard yellow), 20 min (light blue), 25 min (brown) and 30 min (navy green) dwell time.

Table 4.2.

Stamping time [min]	Average diameter [nm]	Average circularity	Average aspect ratio
5	813 ± 60	0.93 ± 0.03	1.22 ± 0.09
15	901 ± 67	0.93 ± 0.03	1.13 ± 0.09
16	800 ± 71	0.90 ± 0.03	1.27 ± 0.07
17	883 ± 66	0.94 ± 0.02	1.11 ± 0.03
18	819 ± 58	0.94 ± 0.02	1.18 ± 0.06
19	865 ± 52	0.94 ± 0.02	1.11 ± 0.07
20	827 ± 48	0.94 ± 0.02	1.09 ± 0.03
25	879 ± 75	0.92 ± 0.01	1.10 ± 0.03
30	967 ± 57	0.91 ± 0.01	1.17 ± 0.03

As seen in Figure 4.59 the diameters of the PS deposits lie in the range from 200 nm to 1500 nm, with most of the deposits having diameters from 600 nm to 1100 nm. Average diameters for the PS deposits are in the range from 800 nm to 967 nm (Table 4.2). Therefore, from these results there is no correlation between dwell time and diameter of the PS deposits. Average circularities of the droplets are in the range from 0.90 to 0.94. Slight deviation from the ideal circle can be rationalized by slight shear during the stamping process.
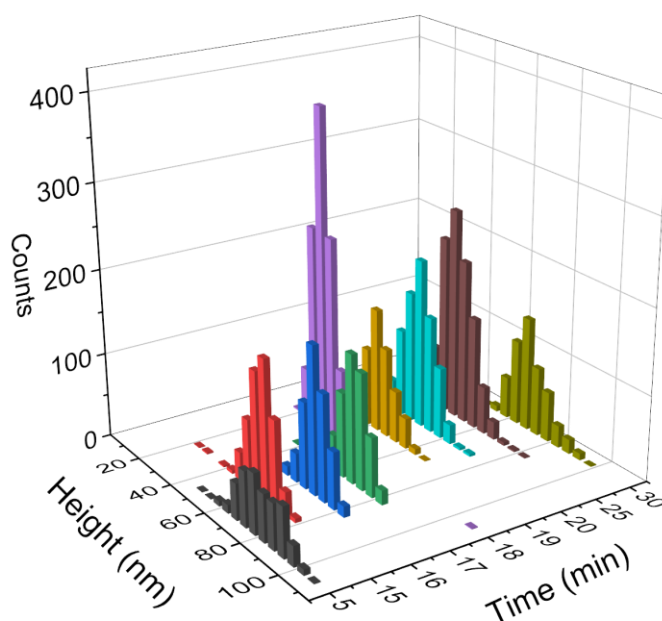
Figure 4.60 Summary histogram of all heights of stamped PS dots on glass with the method III – *with pressure* after 5 min (black), 15 min (red), 16 min (blue), 17 min (green), 18 min (purple), 19 min (yellow), 20 min (turquoise), 25 min (brown) and 30 min (navy green).

Heights of the PS droplets stamped on the glass substrates after various stamping times are in the range from 10 nm to 110 nm (Fig. 4.60). Arithmetic average values of heights of the PS dots for each stamping time are shown in Table 4.3 and are in the range from 33 nm to 81 nm. From the obtain results there is no direct correlation between the stamping times and the hights of the deposited PS droplets.

Table 4.3.

Stamping time [min]	Average height [nm]
5	81 ± 10
15	60 ± 7
16	68 ± 6
17	68 ± 7
18	33 ± 6
19	43 ± 9
20	46 ± 8
25	49 ± 8
30	69 ± 8

4.3 Stamping of P(VDF-TrFE) ink with composite np-Au stamps

Stamping of P(VDF-TrFE) was done on glass substrates without further surface modification and aluminium-coated silicon substrates at 205 °C. All stamping experiments were done by the method III – *with pressure* described in Chapter 3.3.2.3.

4.3.1 Stamping of P(VDF-TrFE) ink on glass substrates

With this method, large areas of the glass substrates were printed with composite np-Au stamps and stamping times of 15 min in a single step, as seen in Figure 4.61a. Patterns of deposited P(VDF-TrFE) dots correspond to the hexagonal pattern of the contact elements of the composite np-Au stamp, with an approximate distance between the printed dots of ~ 1.5 µm. In Figure 4.61 two common stamping defects are visible. The first defect is a 'free space' area on the glass where deposited droplets are missing (Figure 4.61d). Overflow of the ink is the second defect that is visible in Figure 4.61e, f. A possible explanation for the overflow of the ink is the presence of defects in the nanoporous metallic contact layer of the composite np-Au stamps, such as breakage of the contact elements or cleavages in the metallic film that occur during some of the preparation steps. Consequently, during the dwelling time, the polymer ink leaks on the substrate to larger extent. The lines visible at printed dots are presumably lamellar structures of P(VDF-TrFE) copolymer (Fig. 4.61c and d).

From the binarization of the SEM image (from Fig 4.61b) of P(VDF-TrFE) dots stamped with 15 min dwell time, an average diameter of 1023 nm ± 72 nm, an average circularity of 0.88 ± 0.04 and an average aspect ratio of 1.18 ± 0.05 were obtained (Fig. 4.62) considering 536 stamped dots. From the AFM measurement (Fig. 4.63), 266 P(VDF-TrFE) dots stamped on glass with 15 min dwell time were analysed and a frequency distribution of the dot heights was obtained (Fig. 4.64). The average height of the stamped P(VDF-TrFE) dots was 116 nm ± 14 nm.
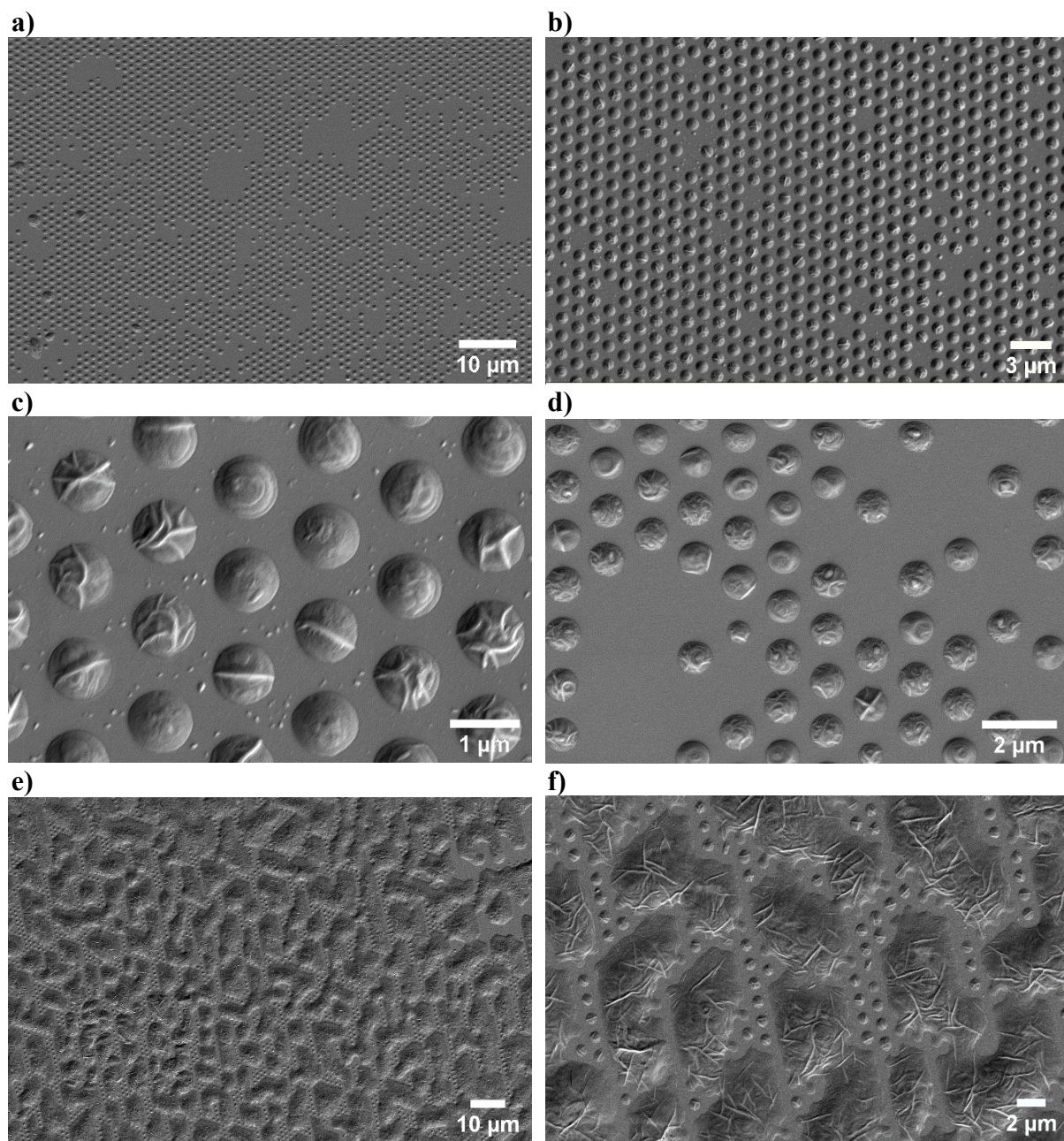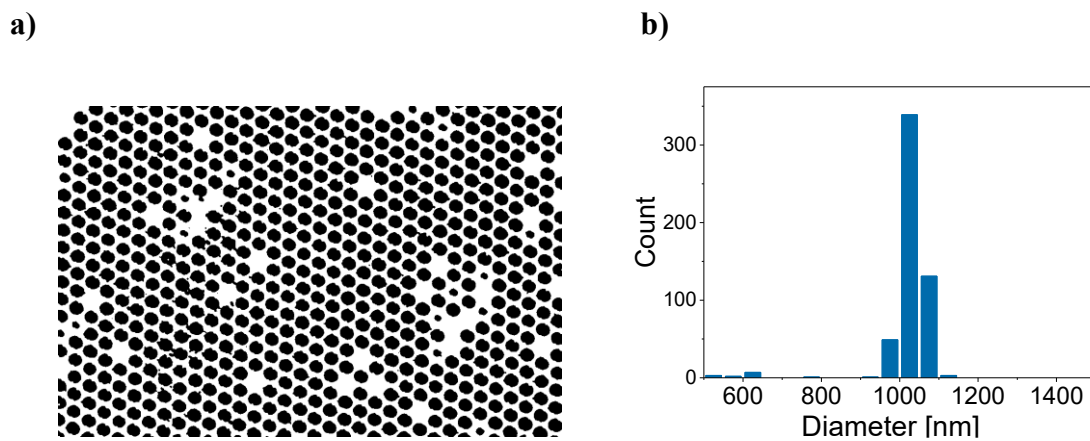
Figure 4.61 SEM images of stamped P(VDF-TrFE) dots on glass after 15 min dwell time at 205 °C.
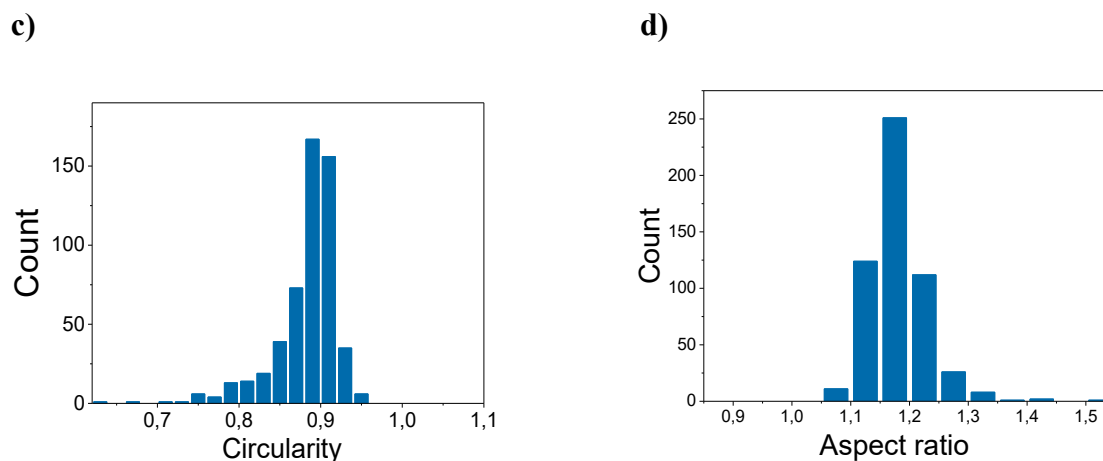

80

c)

d)

Figure 4.62 (a) Binarized SEM image (see original SEM image in Figure 4.61B) of stamped P(VDF-TrFE) dots on glass after 15 min dwell time at 205 °C   (stamping method III – *with pressure*). Histograms of **(b)** diameters, **(c)** circularities, and **(d)** aspect ratios of 536 analyzed P(VDF-TrFE) dots on glass acquired by image analysis.
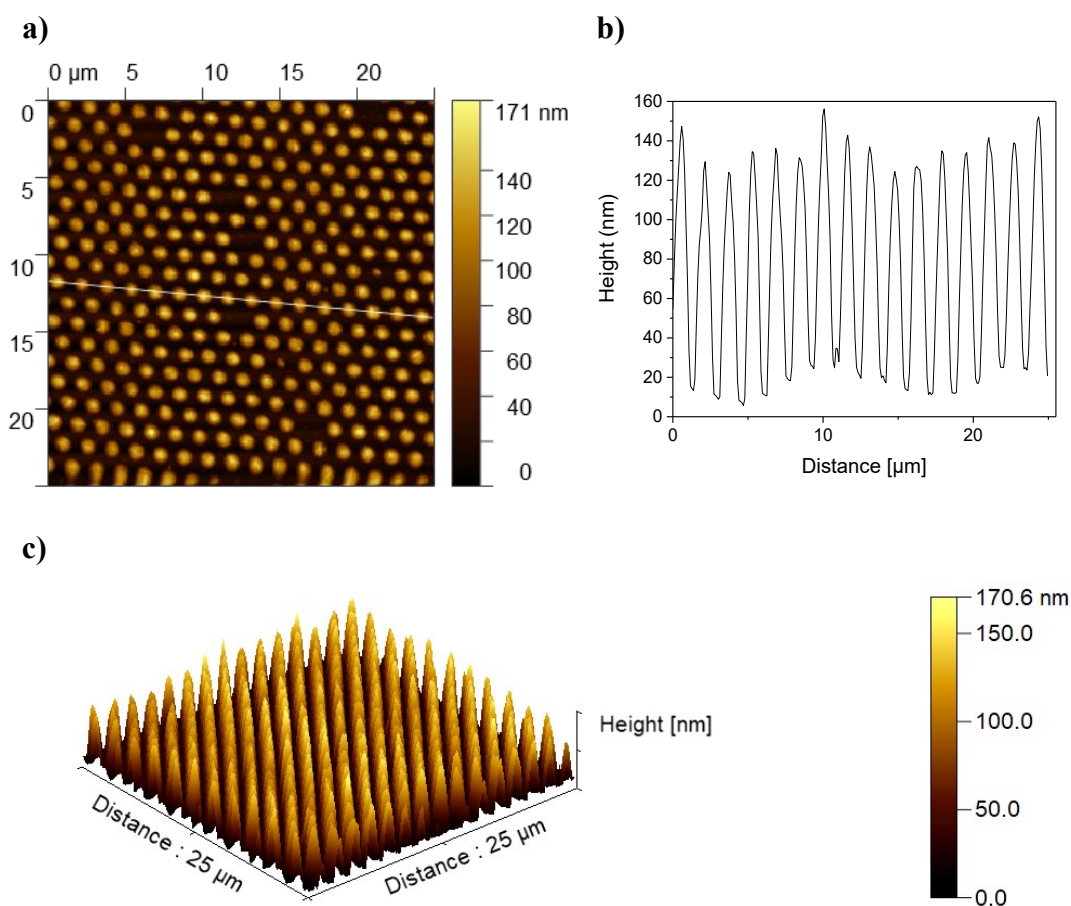
a)

b)

c)

Figure 4.63 AFM image of P(VDF-TrFE) dots stamped on glass at 205 °C   after 15 min dwell time showing **(a)** a topographical AFM image, **(b)** a topographical profile along the line in the panel (a) and **(c)** a 3D AFM image.
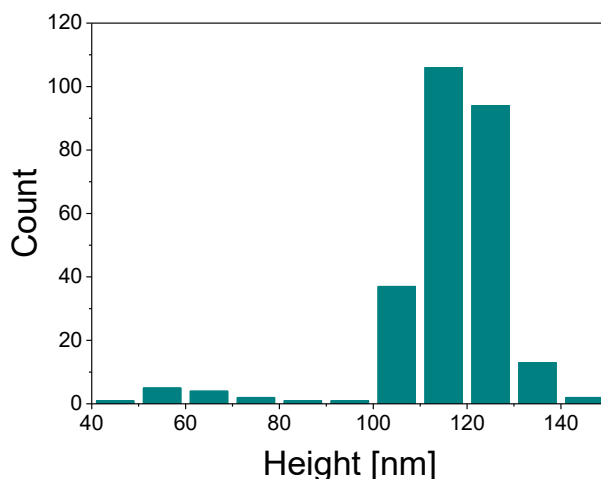
Figure 4.64 Height histogram of 266 analyzed P(VDF-TrFE) dots printed on a glass substrate with 15 min dwell time. Heights were obtained from the analysis of the AFM image shown in Figure 4.63a.

From the binarization of the SEM image (Fig 4.65) of P(VDF-TrFE) dots stamped with 16 min dwell time an average dot diameter of 1001 nm ± 150 nm, a average circularity of 0.92 ± 0.01 and an average aspect ratio of 1.10 ± 0.09 were obtained (Fig. 4.66) considering 243 stamped dots. From the AFM measurement (Fig. 4.67) 366 P(VDF-TrFE) dots stamped on glass with 16 min dwell time were analysed and a frequency distribution of the dot heights was obtained (Fig. 4.68). The average height of the stamped P(VDF-TrFE) dots was 93 nm ± 18 nm.

Large substrate areas were printed, as shown in the SEM images (Fig 4.65), with overflow and 'free dot' space defects that were previously described. Large I in the sizes of the deposited dots can be seen in the Figure 4.65c, e. In Figure 4.65e on the left side of the SEM image there is an area of a droplets in between two lines of islands of deposited ink. These droplets are visibly smaller in comparison to the other part of the image on the right. The reason for this could be the changed distance between the glass substrate and deposition elements of the composite np-Au stamp, due to the large lines of the overflowed ink on the sides.
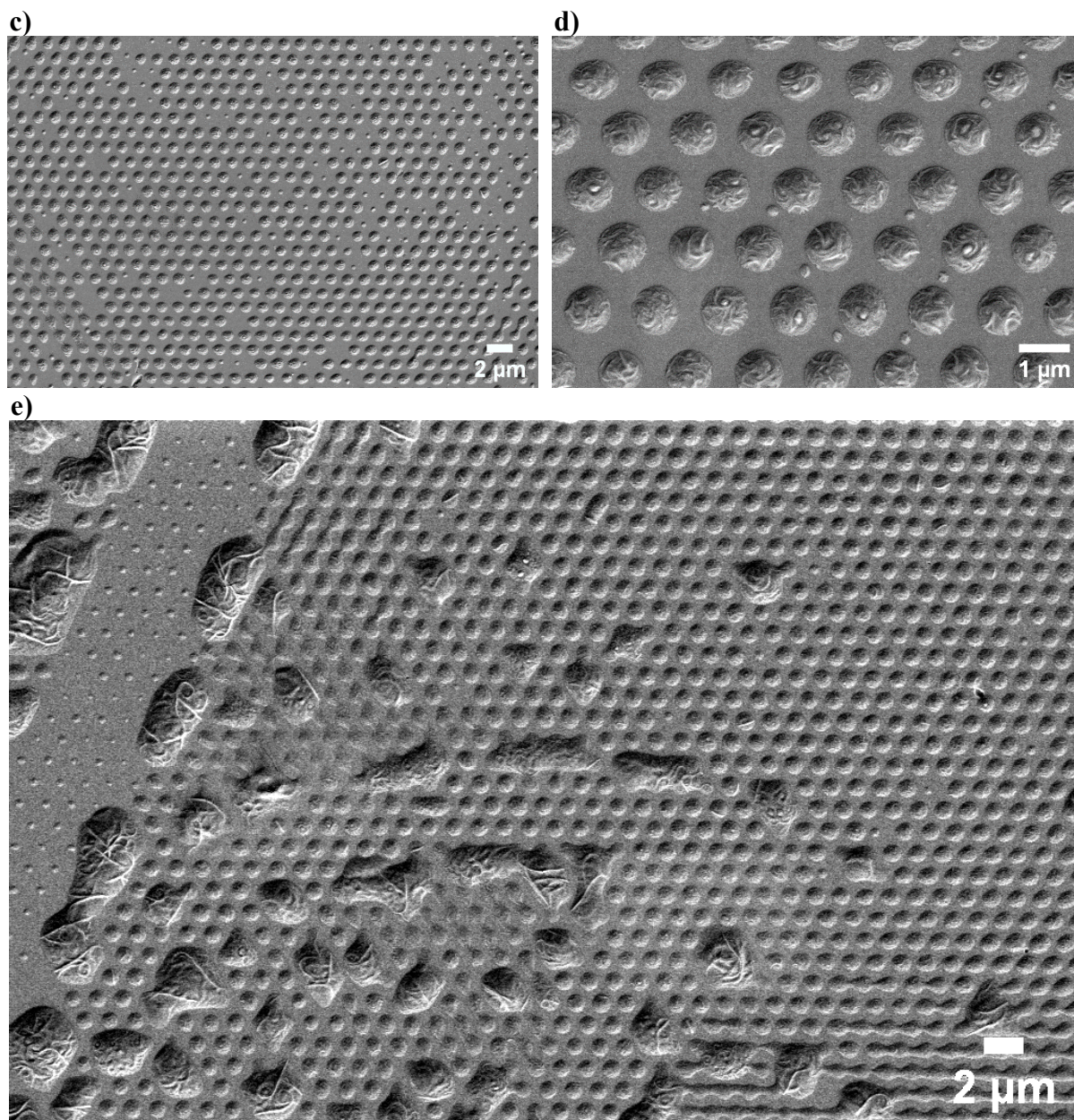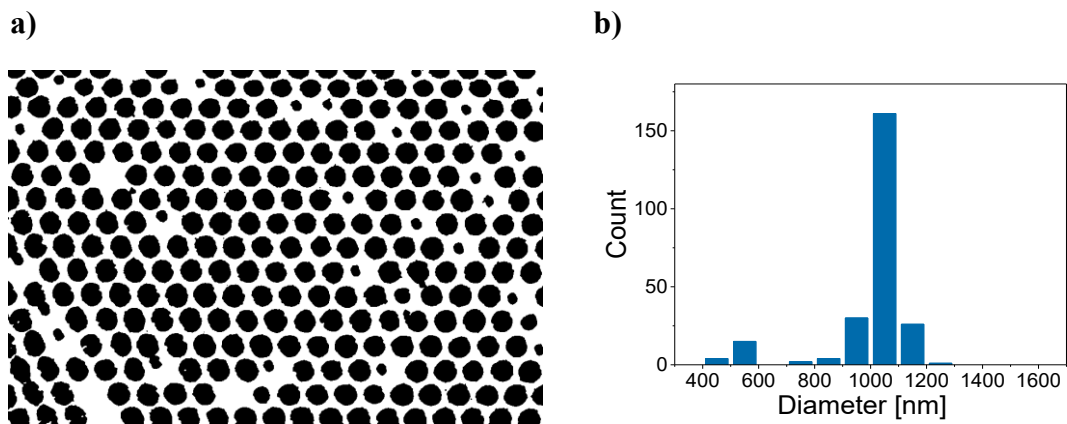
a)

b)
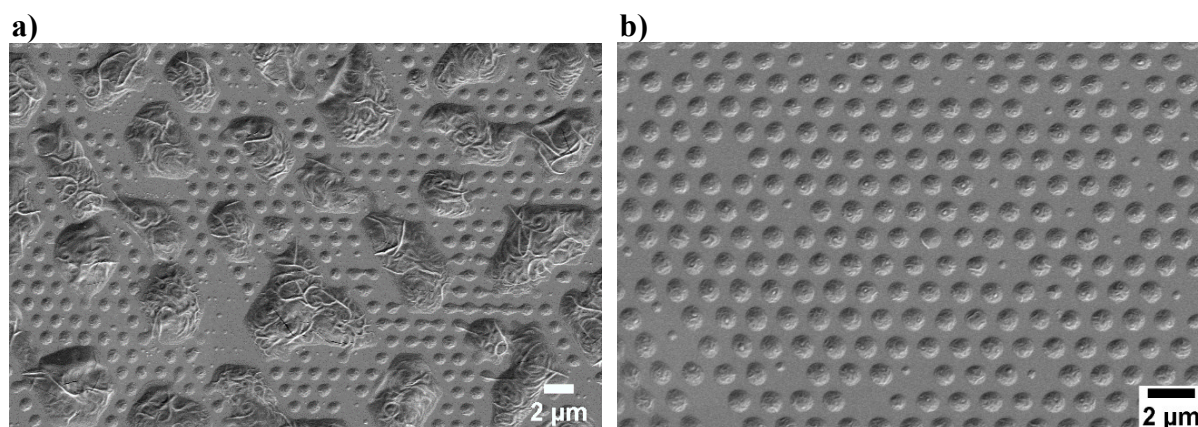
Figure 4.65 SEM images of stamped P(VDF-TrFE) dots on glass at 205 °C after 16 min dwell time.
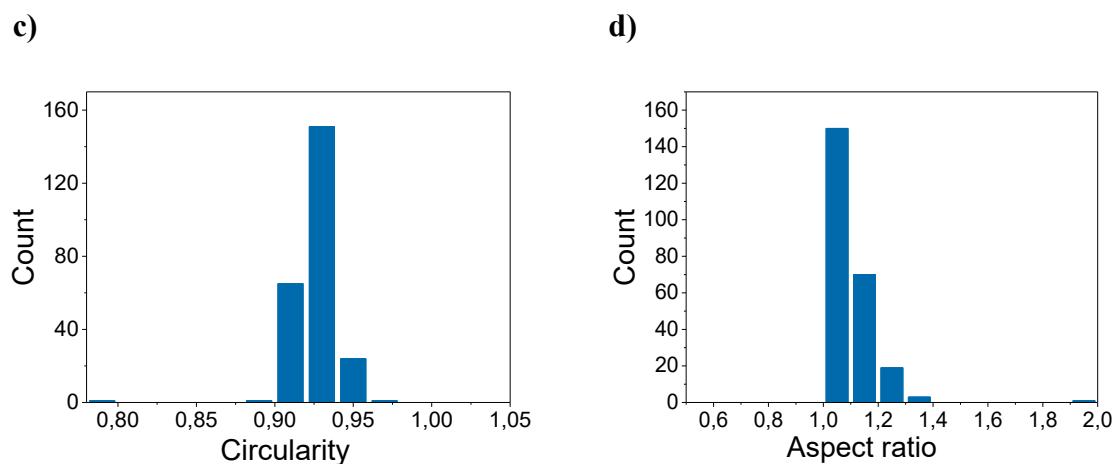
c)

d)

Figure 4.66 (a) Binarized SEM image (see original SEM image in Figure 4.65B) of stamped P(VDF-TrFE) dots on glass after 16 min dwell time at 205 °C (stamping method III - *with pressure*). Histograms of **(b)** diameters, **(c)** circularities, and **(d)** aspect ratios of 243 analyzed P(VDF-TrFE) dots on glass acquired by image analysis.
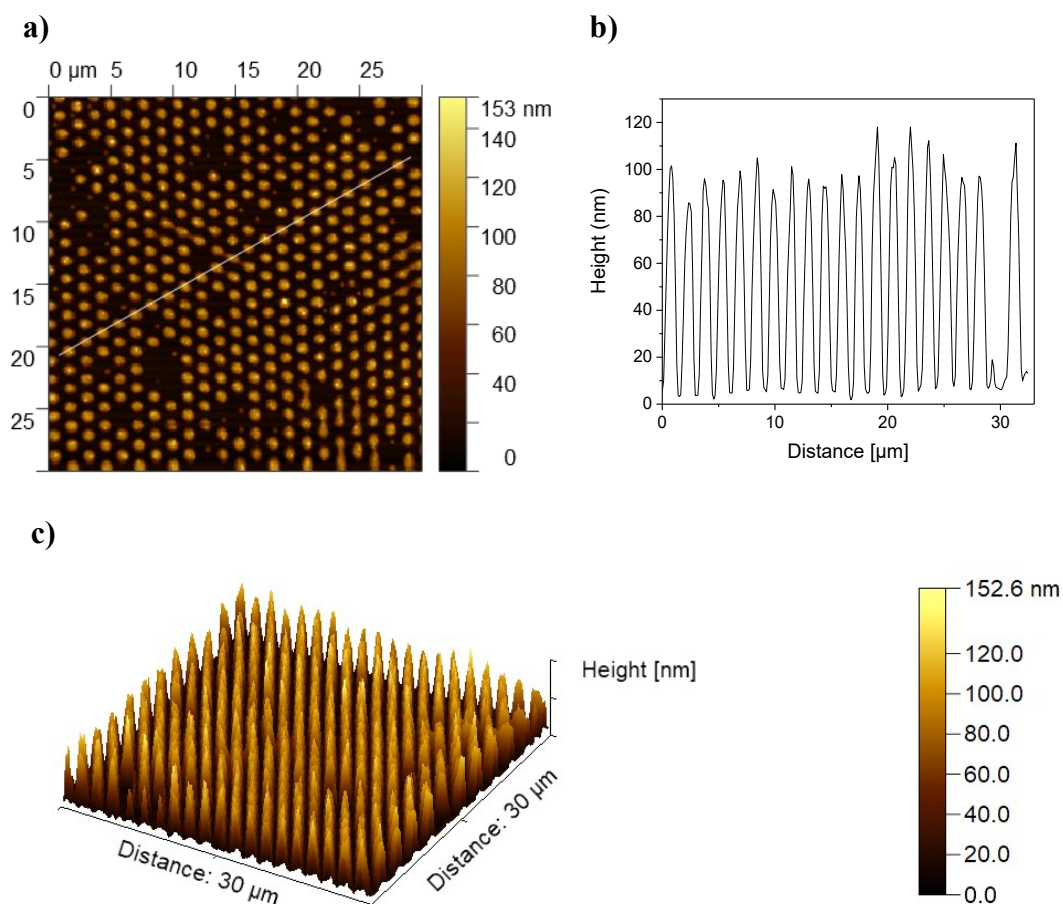
a)

b)

c)

Figure 4.67 AFM image of P(VDF-TrFE) dots stamped on glass at 205 °C after 16 min dwell time **(a)** topographical AFM image, **(b)** topographical profile along the line in the panel (a) and **(c)** 3D AFM image.
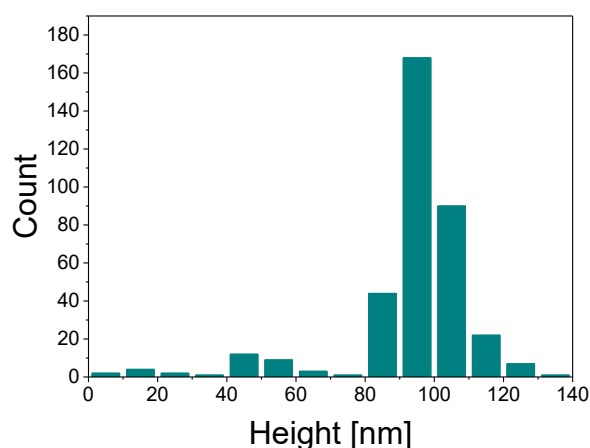
Figure 4.68 Height histogram of 366 analyzed P(VDF-TrFE) dots printed on a glass substrate after 16 min dwell time. Heights were obtained by analysis of the AFM image shown in the Figure 4.67a.

After 17 min stamping time, large areas of the glass substrate were printed in a single step. In Fig. 4.69 the already mentioned defects 'empty areas', where the deposited droplets of ink are missing, and ink overflow are visible. Besides these common defects that were already mentioned, distortions of the printed droplets are visible in Figure 4.69f. This defect is most probably a consequence of sliding of the glass substrate at the surface of the composite np-Au stamp before the retraction of the glass from the composite np-Au stamp.

From the image analysis (from Fig 4.69a) of the P(VDF-TrFE) dots stamped with 17 min dwell time an average diameter of 1057 nm $\pm$ 31 nm, an average circularity of 0.92 $\pm$ 0.01 and an average aspect ratio of 1.07 $\pm$ 0.02 were obtained (Fig. 4.70) considering 515 stamped dots. From the AFM measurement (Fig. 4.71) 168 stamped P(VDF-TrFE) dots on glass after 17 min dwell time were analysed and a frequency distribution of the dot heights was obtained (Fig. 4.72). The average height of the stamped P(VDF-TrFE) dots was 84 nm $\pm$ 19 nm.

a)

g)

h)

10 µm

2 µm
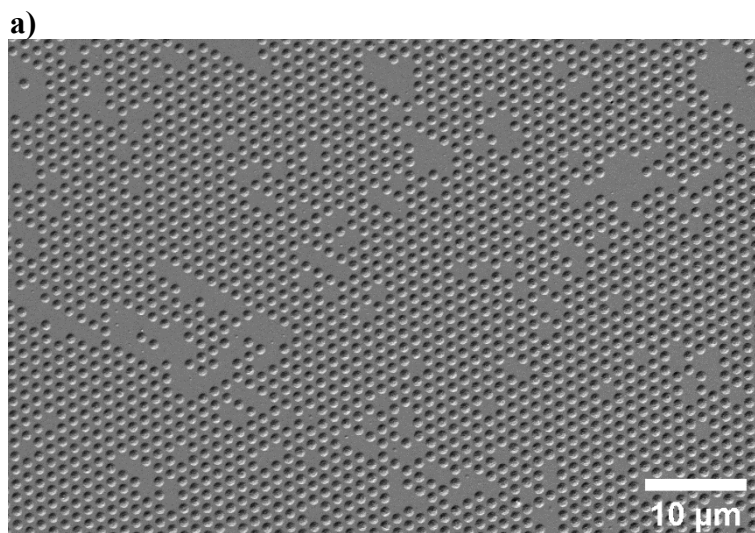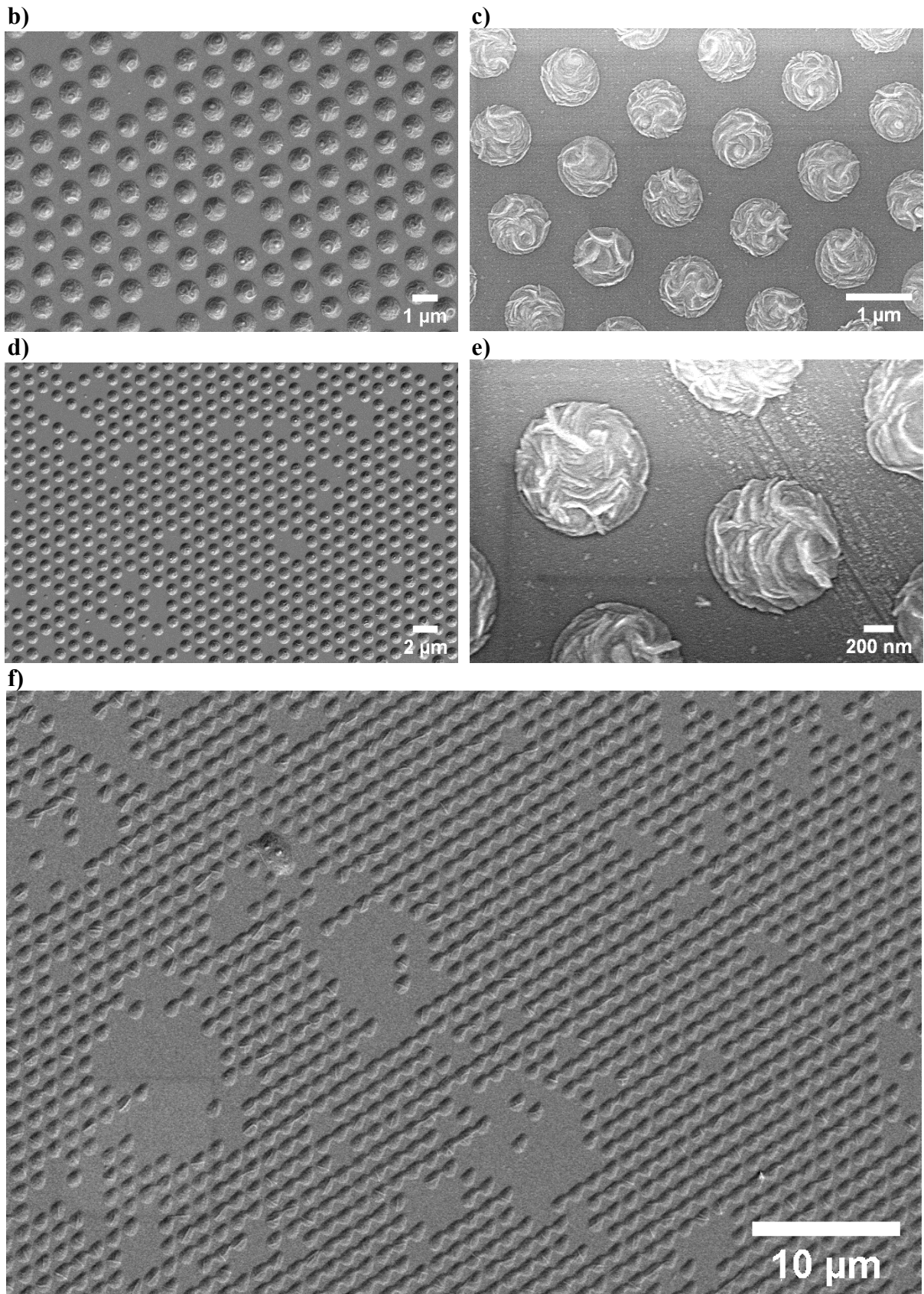
Figure 4.69 SEM images of stamped P(VDF-TrFE) dots on glass 205 °C after 17 min dwell time.

a)

b)

c)

d)

Figure 4.70 (a) Binarized SEM image (see original SEM image in Figure 4.69D) of stamped P(VDF-TrFE) dots on glass after 17 min dwell time at 205 °C (stamping method III - *with pressure*). Histograms of **(b)** diameters, **(c)** circularities, and **(d)** aspect ratios obtained by considering 515 analyzed P(VDF-TrFE) dots on glass acquired by image analysis.

a)

b)

c)

Figure 4.71 AFM image of P(VDF-TrFE) dots stamped on glass at 205 °C after 17 min dwell time. **(a)** topographical AFM image, **(b)** topographical profile along the line in the panel (a) and **(c)** 3D AFM image.
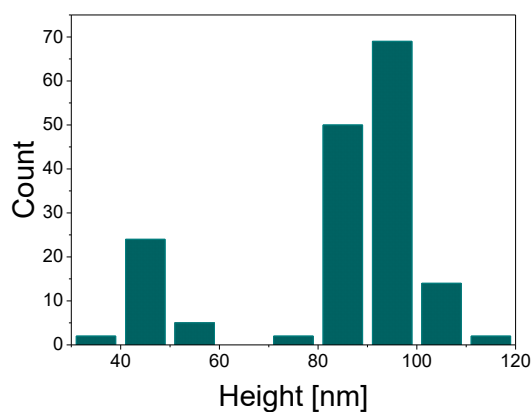
Figure 4.72 Height histogram of 168 analyzed P(VDF-TrFE) dots printed on a glass substrate after 17 min dwell time. Heights were obtained by analysis of the AFM image shown in the Figure 4.71a.

After 18 min stamping time, large areas of the glass substrate were printed (Figure 4.73). Stamping defects, 'empty' areas and ink overflow, that were already discussed in this chapter are visible at the SEM images shown in Fig. 4.73. From the binarization of the SEM image (from Fig 4.73d) of the P(VDF-TrFE) dots stamped with 18 min dwell time, an average dot

diameter of 1052 nm ± 54 nm, an average circularity of 0.89 ± 0.02 and an average aspect ratio of 1.19 ± 0.04 were obtained (Fig. 4.74) considering 358 stamped dots. From the AFM measurement (Fig. 4.75) 277 P(VDF-TrFE) dots on glass stamped with 18 min dwell time were analysed and a frequency distribution of the dot heights was obtained (Fig. 4.76). The average height of the stamped P(VDF-TrFE) dots was 99 nm ± 21 nm.
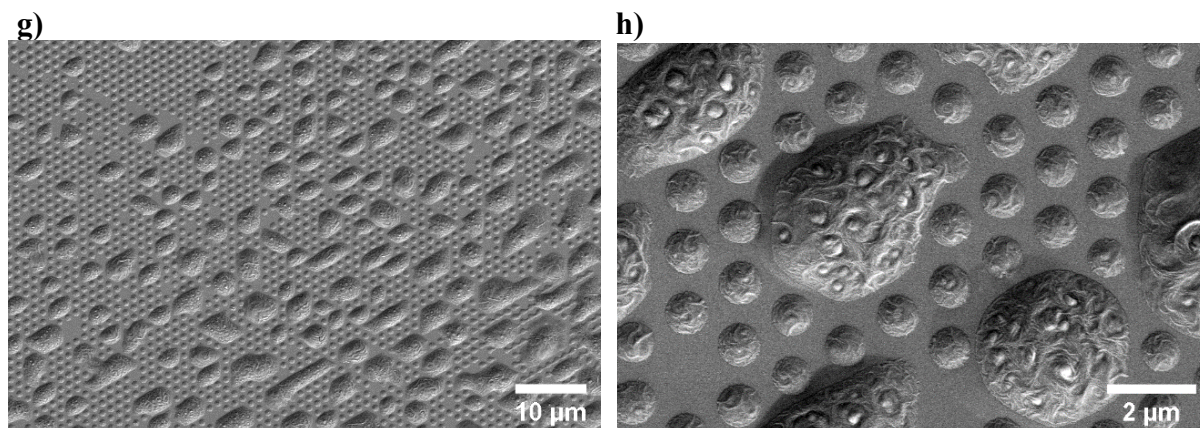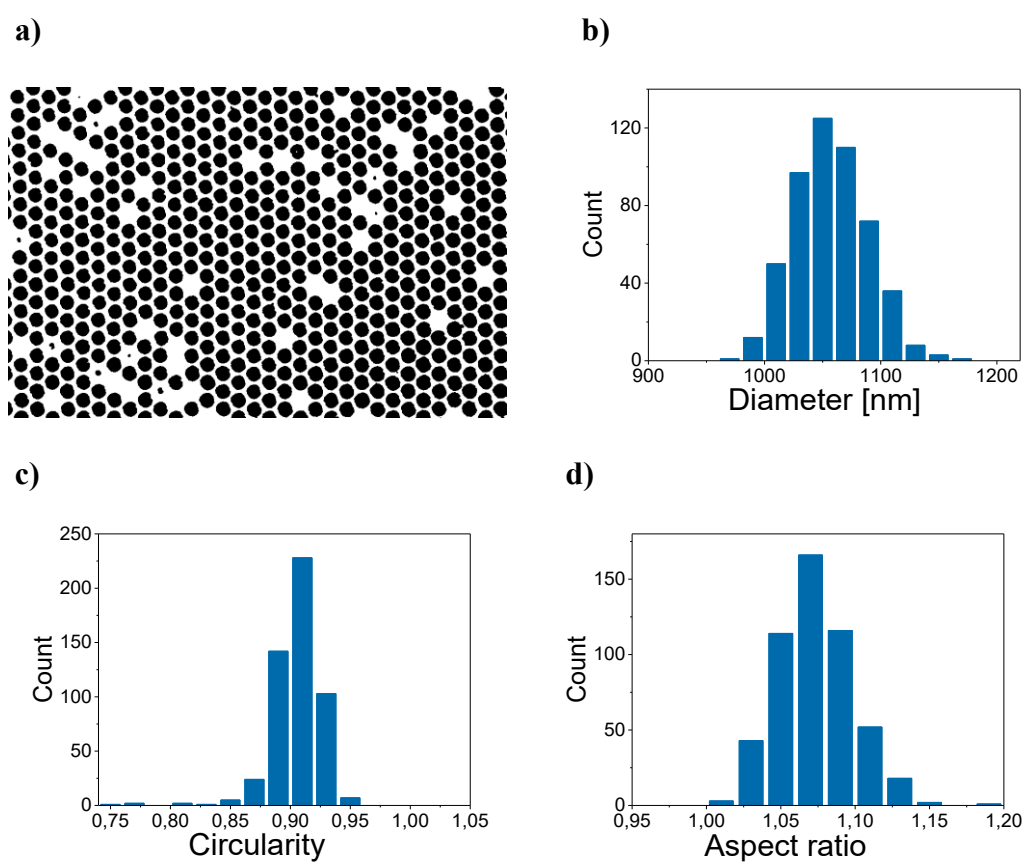

Figure 4.73 SEM images of stamped P(VDF-TrFE) dots on glass 205 °C after 18 min dwell time.

a)

b)

c)

d)

Figure 4.74 (a) Binarized SEM image (see original SEM image in Fig. 4.61d) of stamped P(VDF-TrFE) dots on glass after 18 min dwell time at 205 °C (stamping method III - *with pressure*). Histograms of **(b)** diameters, **(c)** circularities, and **(d)** aspect ratios of 358 analyzed P(VDF-TrFE) dots on glass acquired by image analysis.

a)

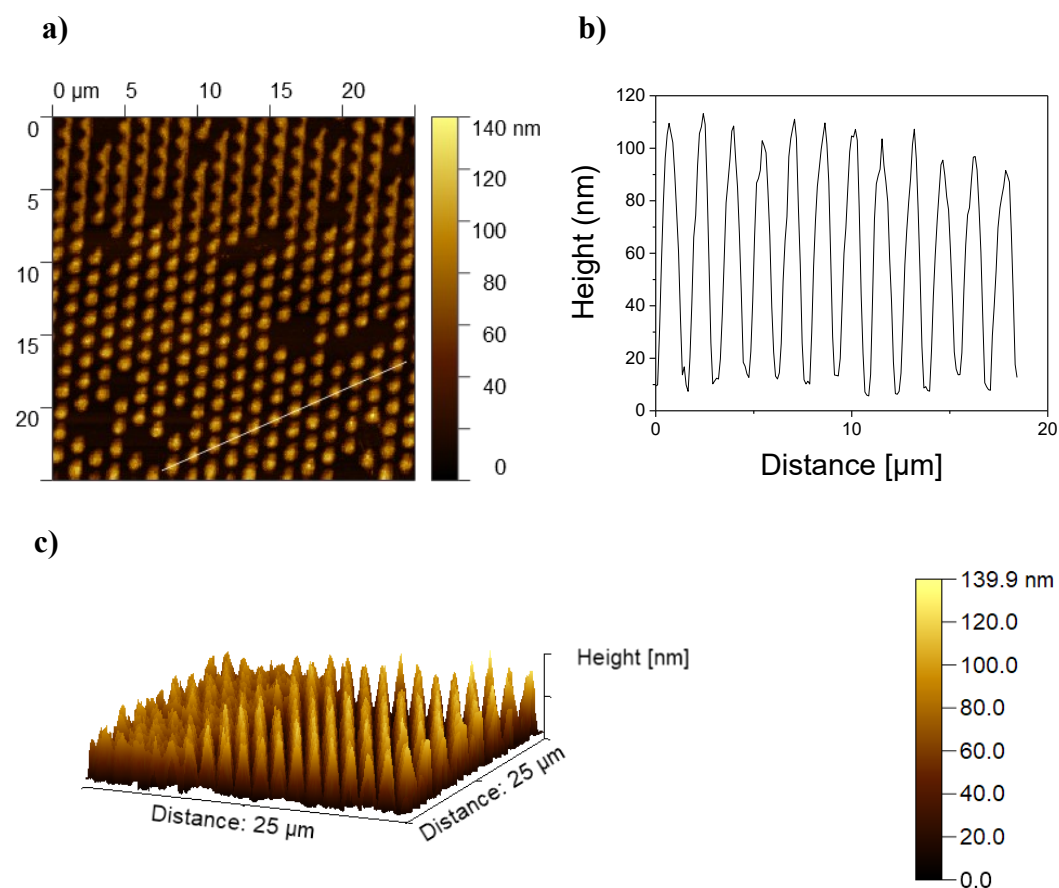

b)

c)
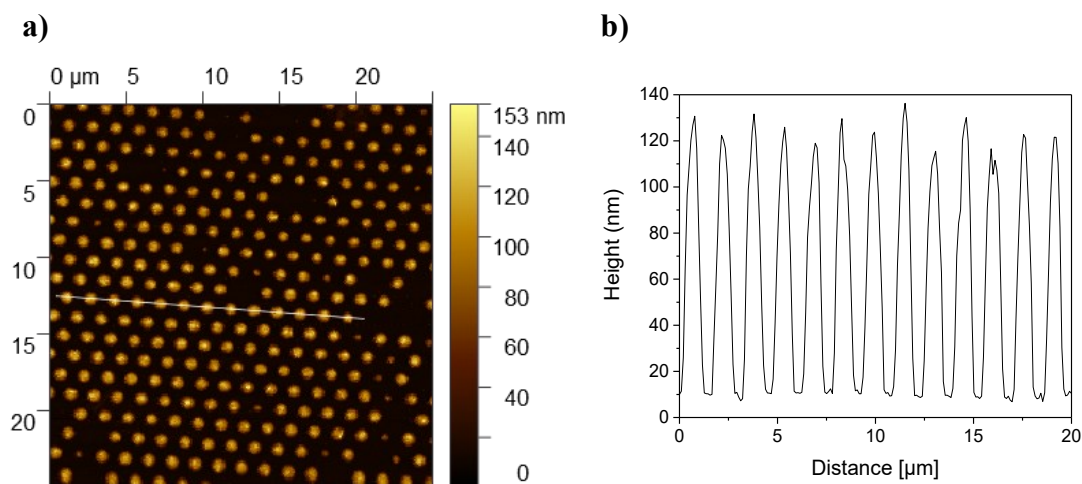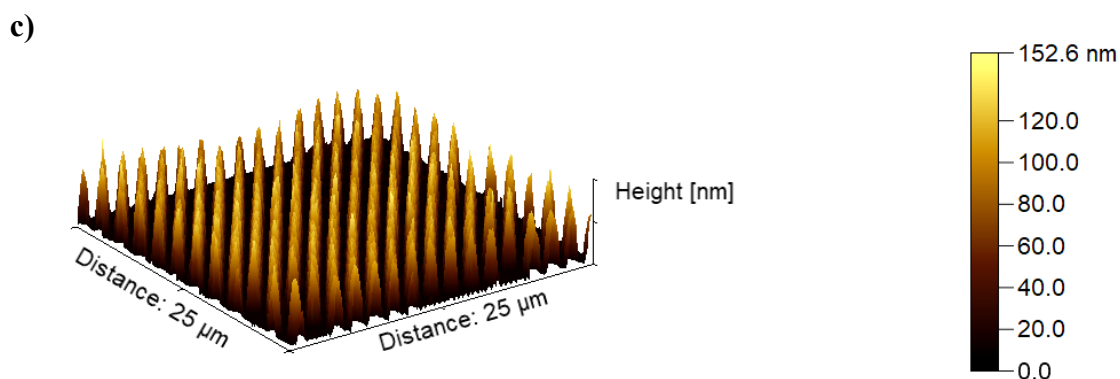
Figure 4.75 AFM image of P(VDF-TrFE) dots stamped on glass at 205 °C after 18 min dwell time **(a)** topographical AFM image, **(b)** topographical profile along the line in the panel (a) and **(c)** 3D AFM image.

Figure 4.76 Height histogram of 277 analyzed P(VDF-TrFE) dots printed on a glass substrate with 18 min dwell time. Heights were obtained from the analysis of the AFM image shown in the Figure 4.75a.

Large areas of glass substrate were printed with P(VDF-TrFE) ink after 19 min stamping time (Fig. 4.77). On the top of the SEM image (Fig 4.77d) dots with smaller diameters are present at the bootom of the image dots with a larger diameter. The reason for this defect can be the difference in the contact distance between the glass substrate and the composite np-Au stamp that results in a difference in the applied pressure on the composite np-Au stamp during the stamping.

From the binarization of the SEM image (from Fig 4.77c) of the P(VDF-TrFE) dots stamped with 19 min dwell time an average dot diameter of 1131 nm ± 36 nm, an average circularity of 0.85 ± 0.04 and an average aspect ratio of 1.09 ± 0.04 were obtained (Fig. 4.78) considering 102 stamped dots. From the AFM measurement (Fig. 4.79) 277 P(VDF-TrFE) dots stamped on glass with 19 min dwell time were analysed and frequency distribution of dot heights was obtained (Fig. 4.80). The average height of the stamped P(VDF-TrFE) dots was 106 nm ± 19 nm.
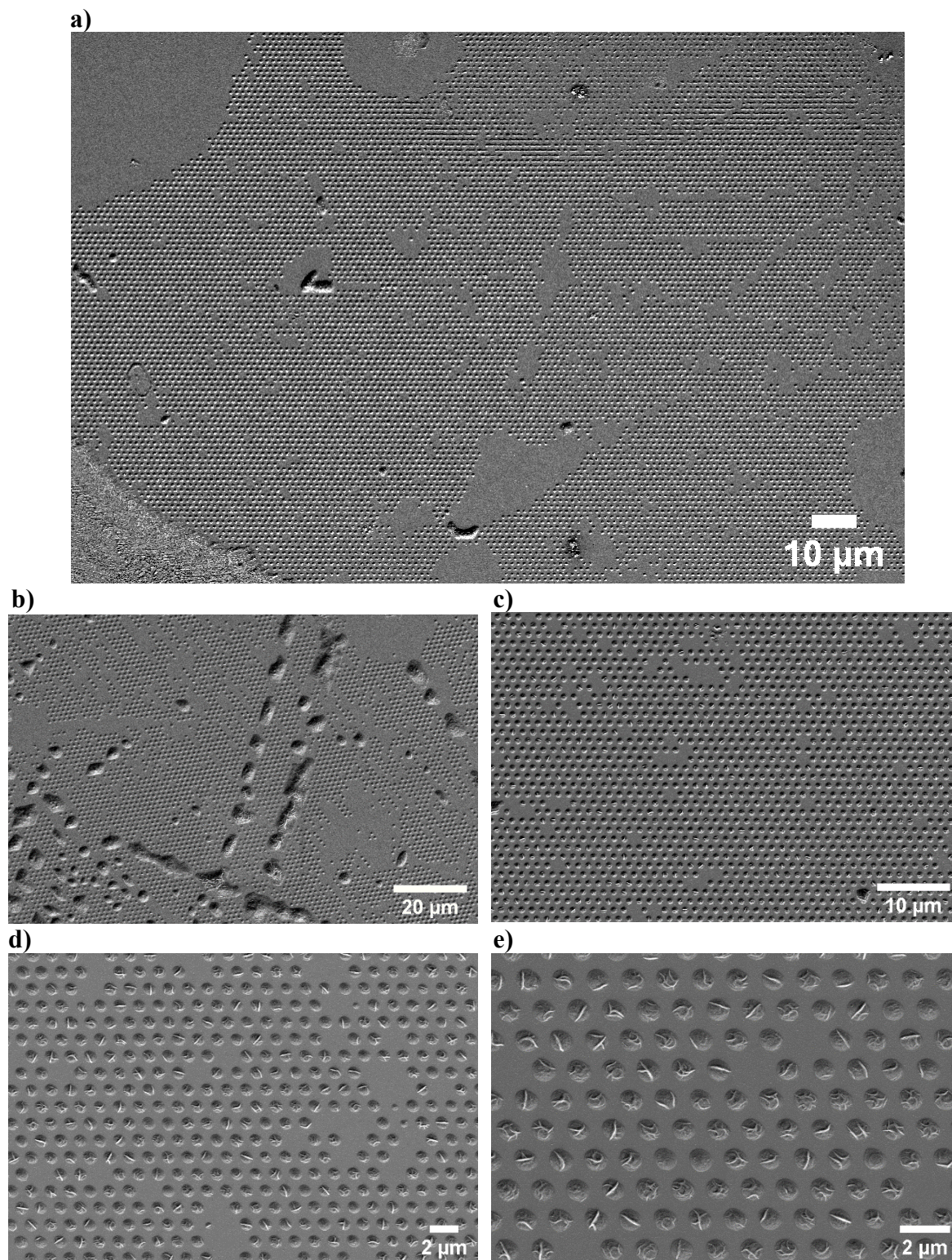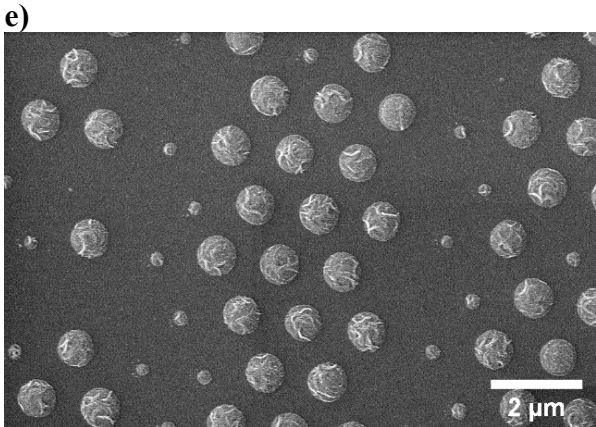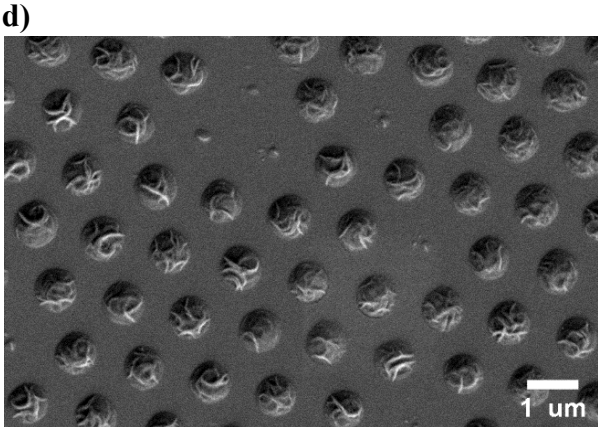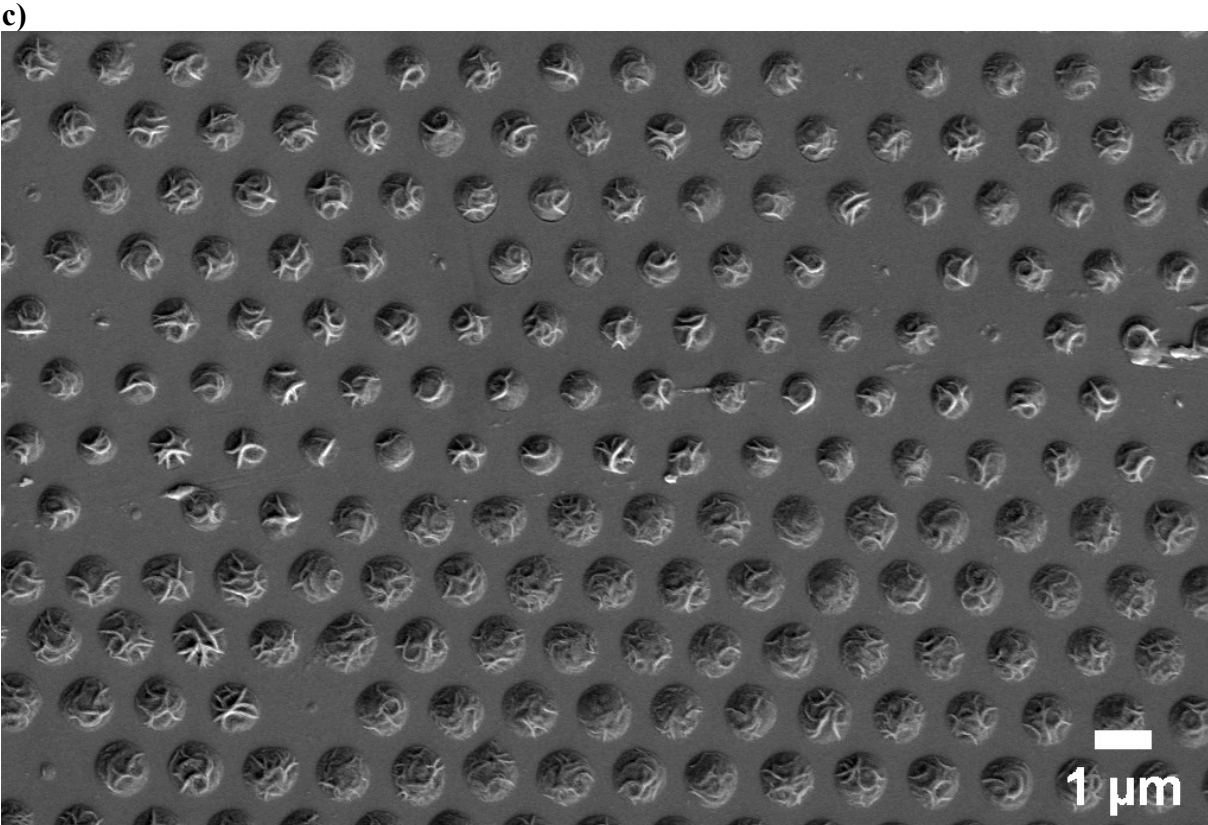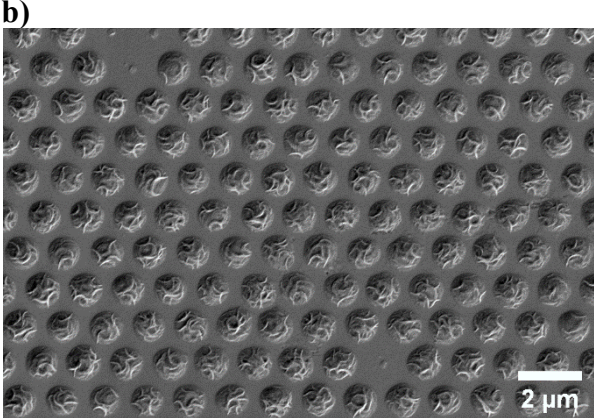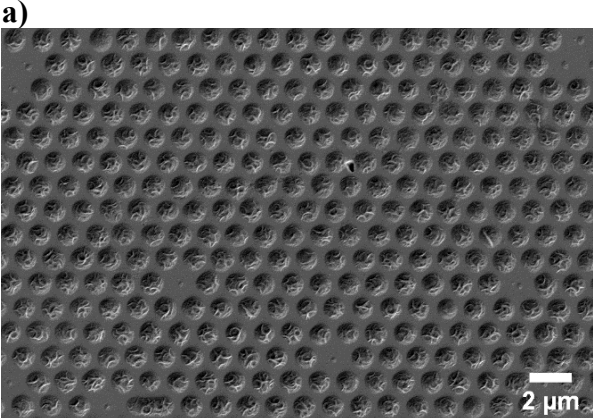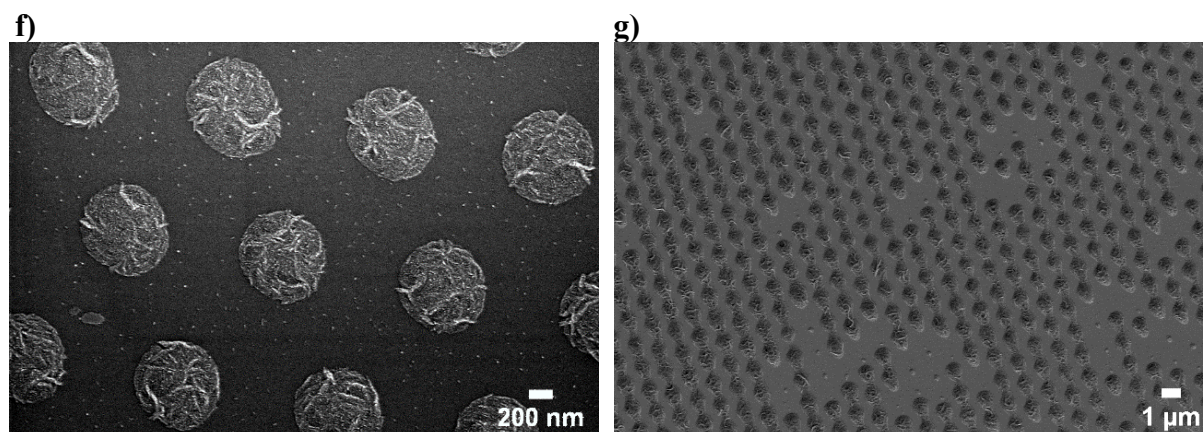
Figure 4.77 SEM images of stamped P(VDF-TrFE) dots on glass 205 °C after 19 min dwell time.
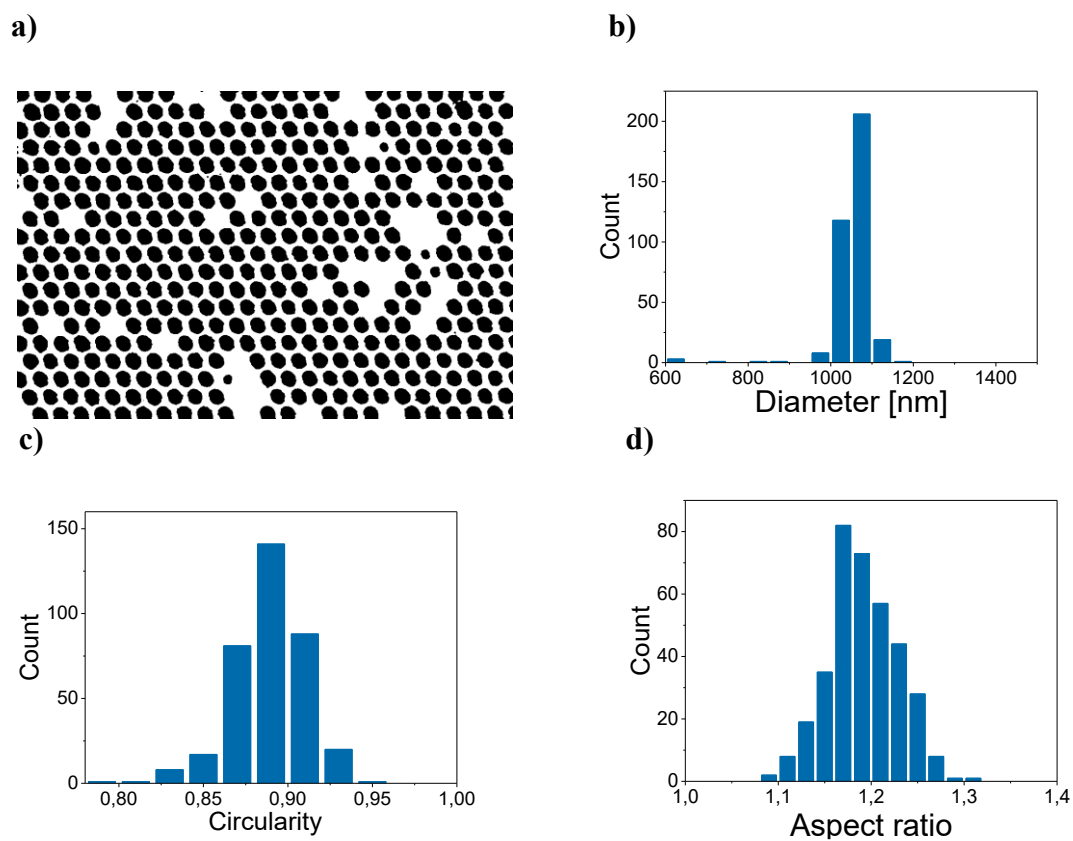

Figure 4.78 (a) Binarized SEM image (see original SEM image in Figure 4.61B) of stamped P(VDF-TrFE) dots on glass after 19 min dwell time at 205 °C (stamping method III - *with pressure*). Histograms of **(b)** diameters, **(c)** circularities, and **(d)** aspect ratios of 102 analyzed P(VDF-TrFE) dots on glass acquired by image analysis.

a)

b)

c)

Figure 4.79 AFM image of P(VDF-TrFE) dots stamped on glass at 205 °C after 19 min dwell time. **(a)** topographical AFM image, **(b)** topographical profile along the line in the panel (a) and **(c)** 3D AFM image.
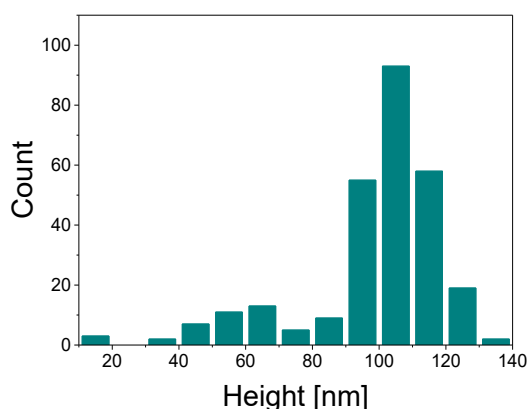

Figure 4.80 Height histogram of 231 analyzed P(VDF-TrFE) dots printed on a glass substrate with 19 min dwell time. Heights were obtained from the analysis of the AFM image shown in the Figure 4.79a.

In Figure 4.81d two different shapes of printed P(VDF-TrFE) dots are visible (after 20 min dwell time), ring-shaped dots and full shape dots. A possible explanation for the occurrence of ring-shaped dots is discussed in Chapter 4.2.1.

From the binarization of the SEM image (from Fig 4.81e) of P(VDF-TrFE) dots stamped with 20 min dwell time an average diameter of 960 nm ± 40 nm, an average circularity of 0.87 ± 0.02 and an average aspect ratio of 1.14 ± 0.04 were obtained (Fig. 4.82) considering 199 stamped dots. From the AFM measurement (Fig. 4.83) 220 P(VDF-TrFE) dots stamped on glass with 20 min dwell time were analysed and a frequency distribution of the dot heights was obtained (Fig. 4.84). The average height of the stamped P(VDF-TrFE) dots was 81 nm ± 14 nm.

a)

b)

c)

d)

e)

f)

96

g)

h)

i)
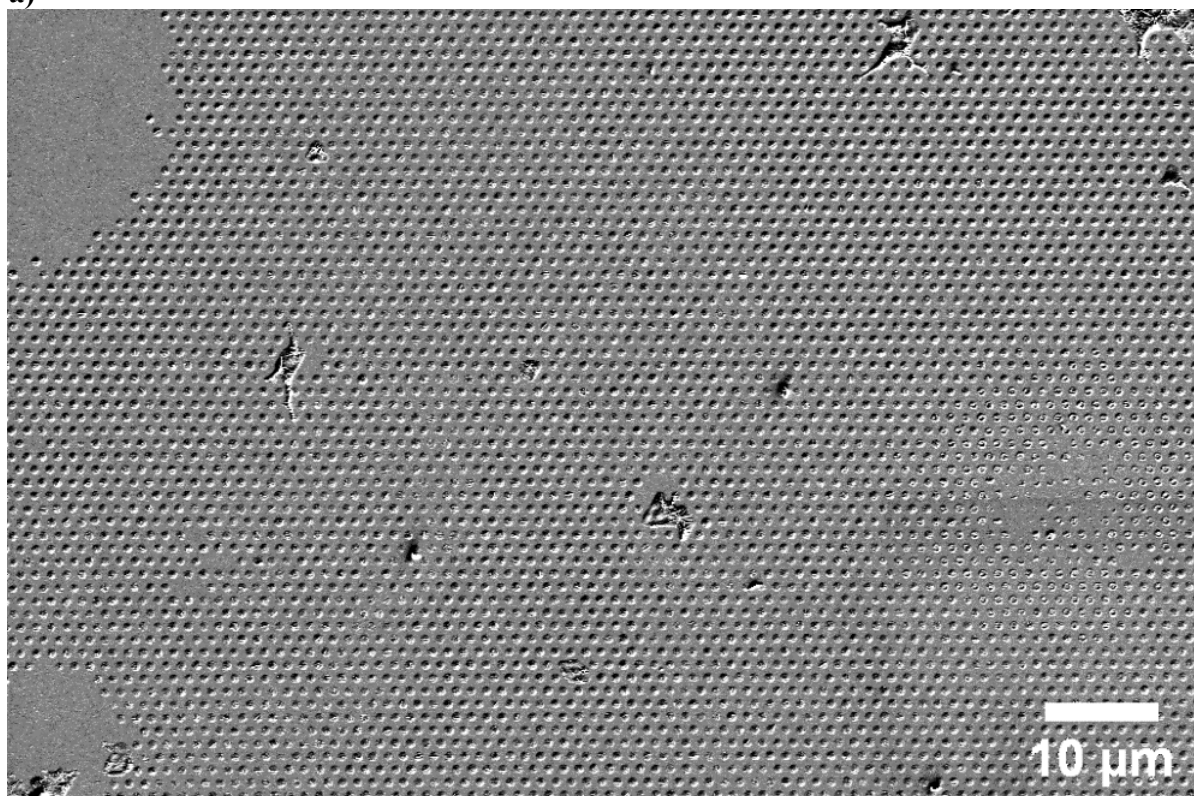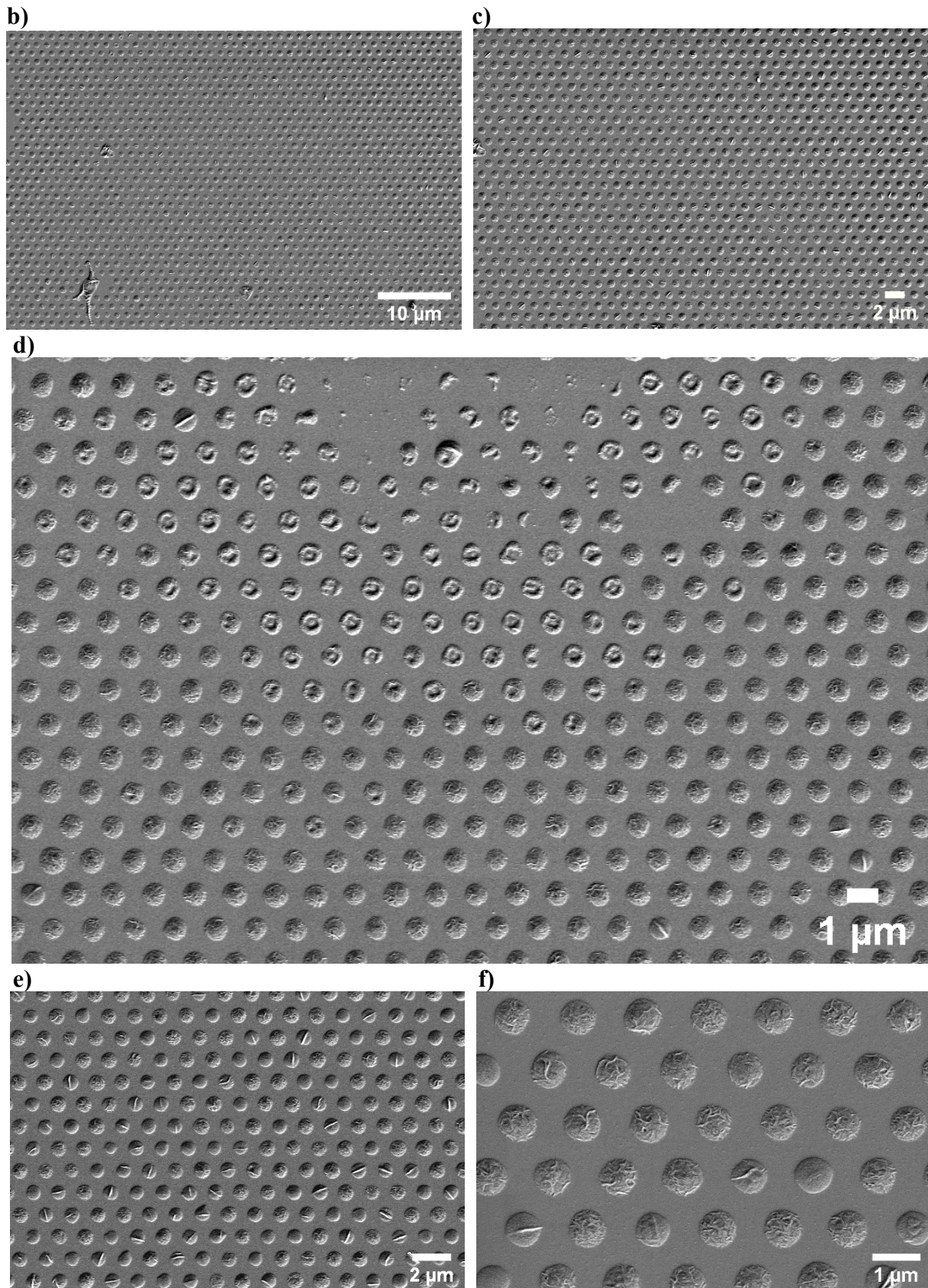
Figure 4.81 SEM images of P(VDF-TrFE) dots on glass stamped at 205 °C with 20 min dwell time.

a)

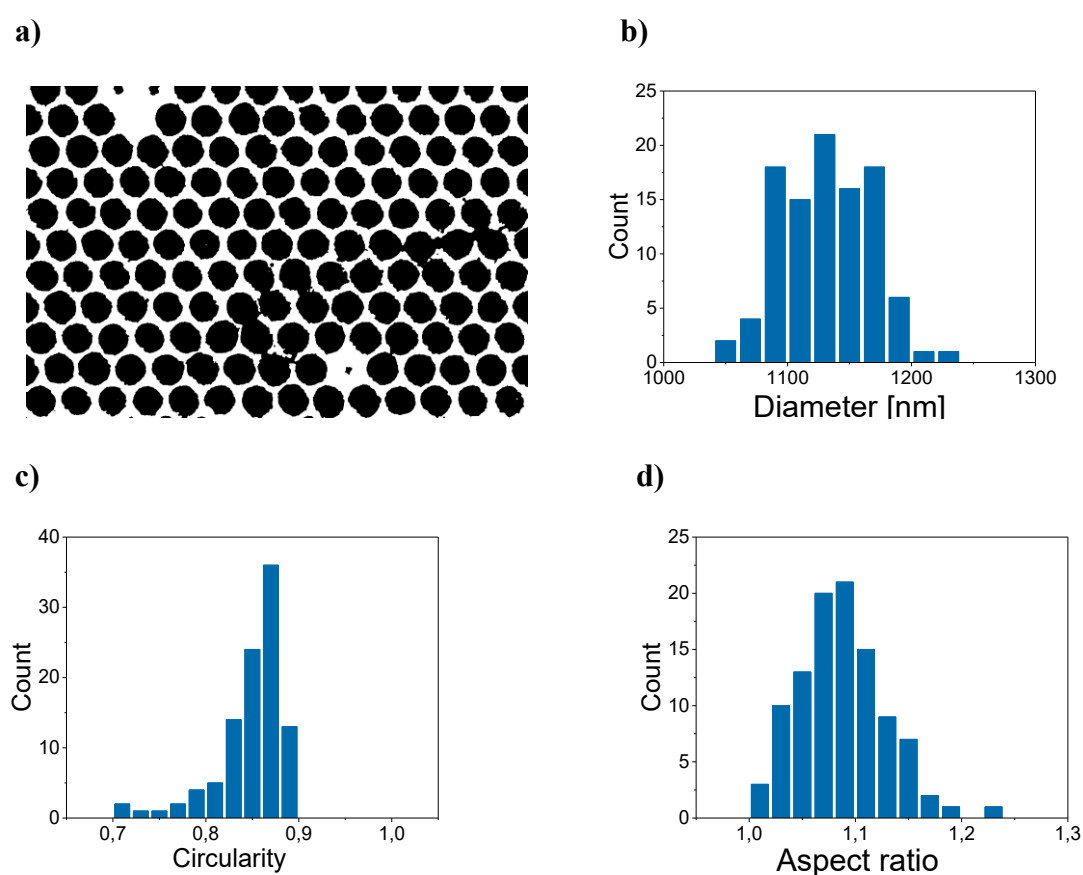
b)

c)

d)

Figure 4.82 (a) Binarized SEM image (see original SEM image in Fig. 4.61e) of stamped P(VDF-TrFE) dots on glass after 20 min dwell time at 205 °C (stamping method III- *with pressure*). Histograms of **(b)** diameters, **(c)** circularities, and **(d)** aspect ratios histograms of 199 analyzed P(VDF-TrFE) dots on glass acquired by image analysis.

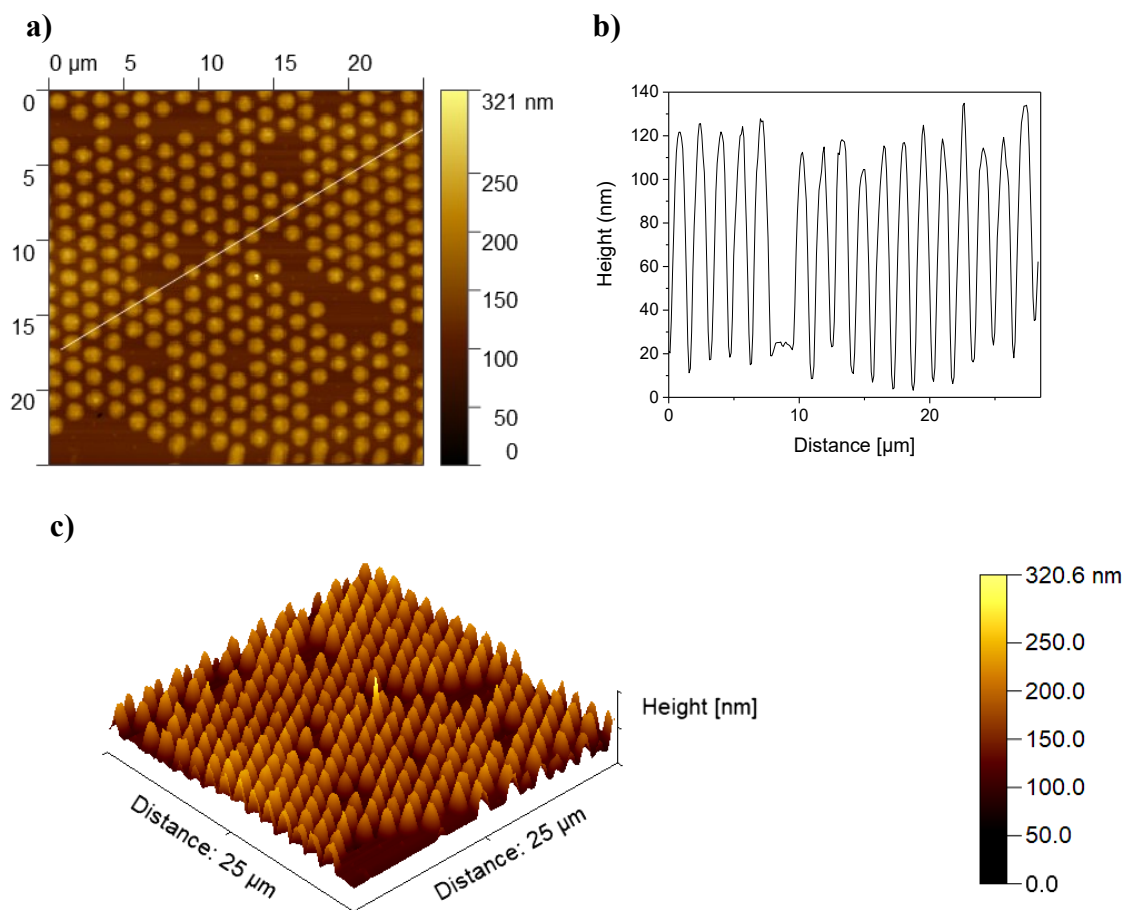**a)**

b)

c)

Figure 4.83 AFM image of P(VDF-TrFE) dots stamped on glass at 205 °C after 20 min dwell time. **(a)** topographical AFM image, **(b)** topographical profile along the line in the panel (a) and **(c)** 3D AFM image.
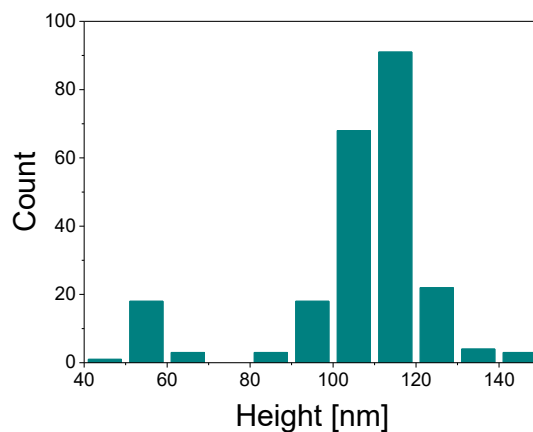
Figure 4.84 Height histogram of 220 analyzed P(VDF-TrFE) dots printed on glass substrate after 20 min dwell time. Heights were obtained from the analysis of the AFM image shown in the Figure 4.83a.

After 25 min stamping time, large surface areas of the glass substrate (Fig. 4.85) were printed. The printed area shows all three defects that were mentioned earlier: 'empty' areas, ink overflow and distortion of the droplets. From the binarization of the SEM image (from Fig 4.85e) of P(VDF-TrFE) dots stamped with 25 min dwell time an average diameter of 1169 nm ± 102 nm, an average circularity of 0.82 ± 0.02 and an average aspect ratio of 1.23 ± 0.03 were obtained (Fig. 4.86) considering 45 stamped dots. From the AFM measurement (Fig. 4.87) 80 stamped P(VDF-TrFE) dots on glass after 25 min dwell time were analysed and a frequency distribution of the dot heights was obtained (Fig. 4.88). The average height of the stamped P(VDF-TrFE) dots was 102 nm ± 23 nm.

a)
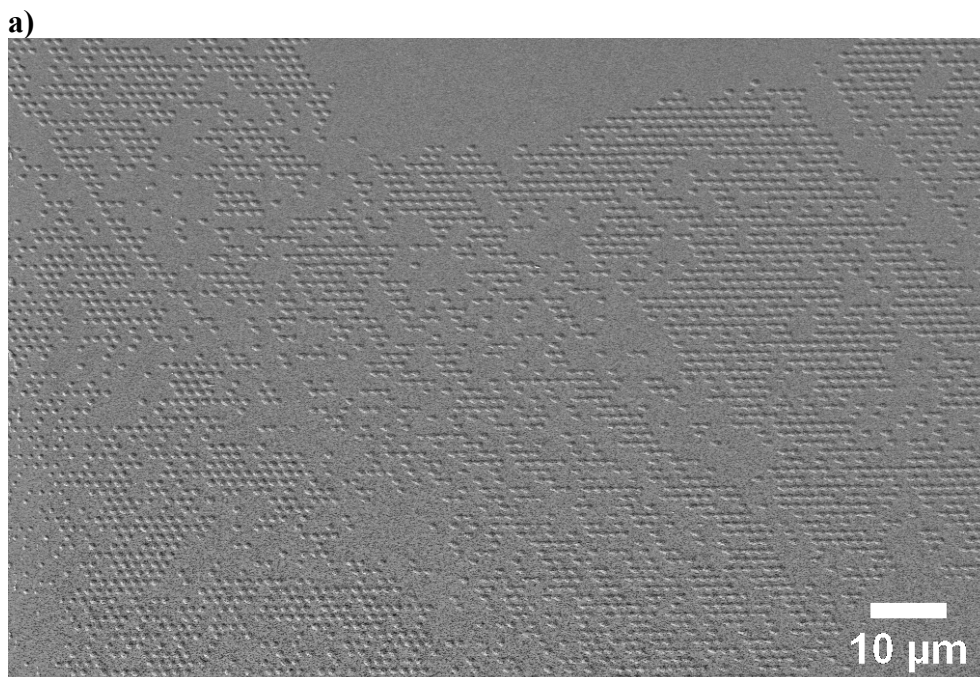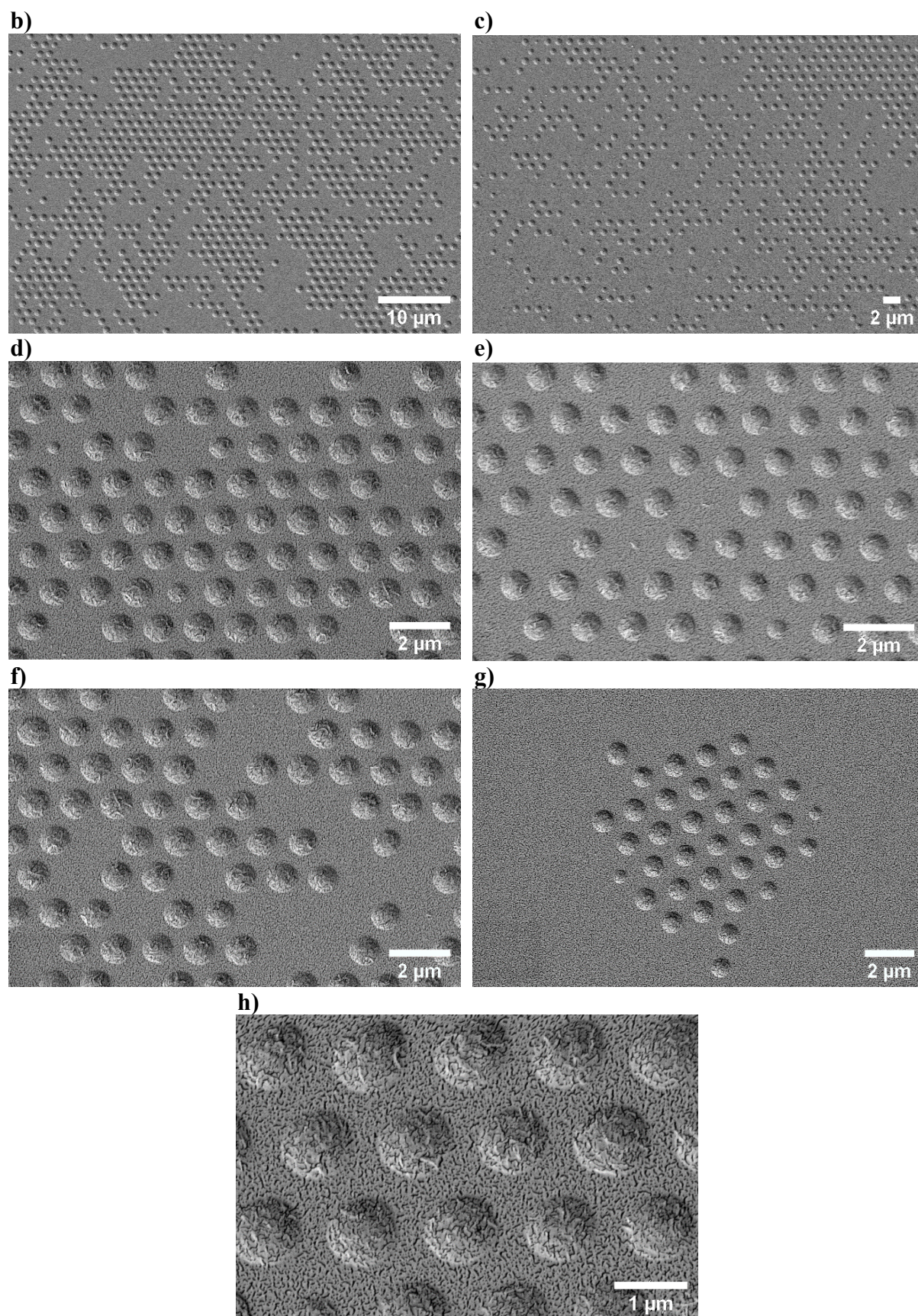
Figure 4.85 SEM images of P(VDF-TrFE) dots on glass stamped at 205 °C with 25 min dwell time.
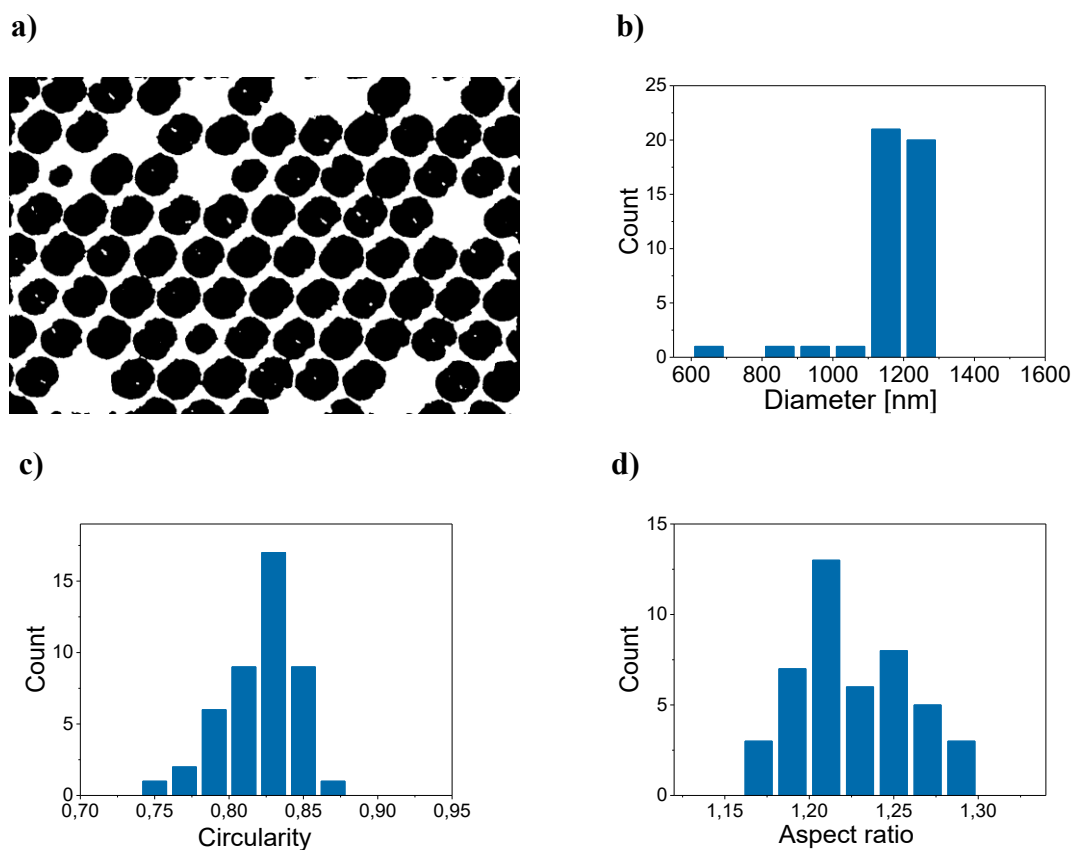
Figure 4.86 (a) Binarized SEM image (see original SEM image in Fig. 4.61d) of stamped P(VDF-TrFE) dots on glass after 25 min dwell time at 205 °C (stamping method III - *with pressure*). Histograms of **(b)** diameters, **(c)** circularities, and **(d)** aspect ratios of 45 analyzed P(VDF-TrFE) dots on glass acquired by image analysis.

c)
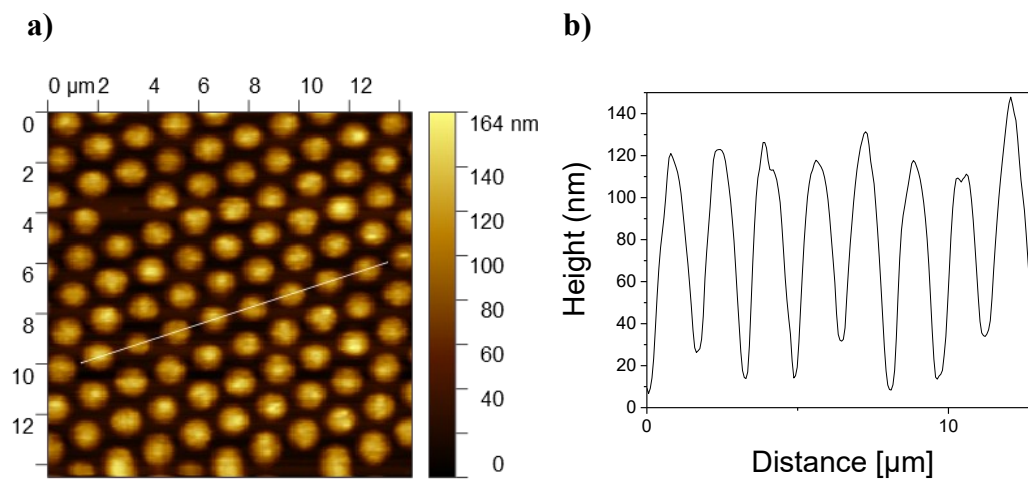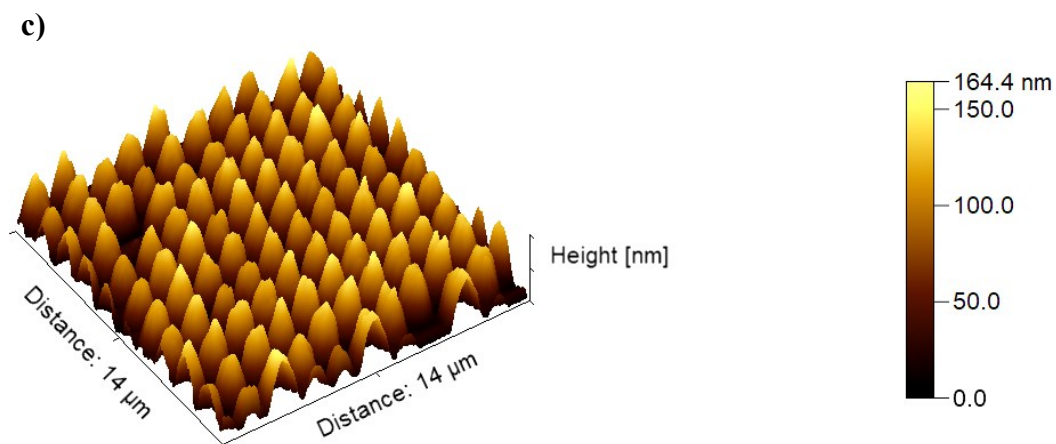
Figure 4.87 AFM image of P(VDF-TrFE) dots stamped on glass at 205 °C after 25 min dwell time. **(a)** topographical AFM image, **(b)** topographical profile along the line in the panel (a) and **(c)** 3D AFM image.
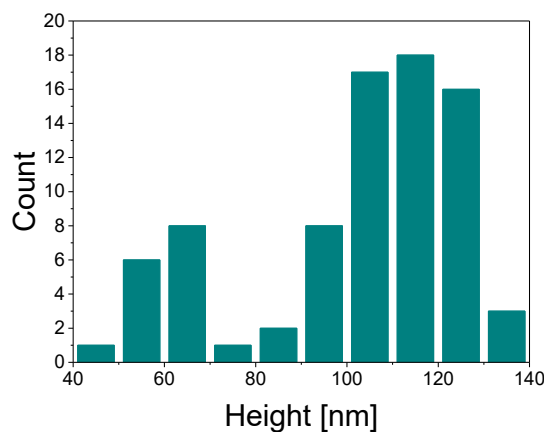
Figure 4.88 Height histogram of 80 analyzed P(VDF-TrFE) dots printed on glass substrate with 25 min dwell time. Heights were obtained from the analysis of the AFM image shown in the Figure 4.87a.

Stamping with composite np-Au stamp after 30 min dwell time resulted in the large, printed area on the glass substrate with the P(VDF-TrFE) ink droplets (Fig. 4.89). Overflow of the ink on the glass substrate and the 'empty' area defects are visible in the SEM images shown in the Fig. 4.89. From the binarization of the SEM image (from Fig 4.89d) of P(VDF-TrFE) dots stamped with 30 min dwell time an average diameter of 1103 nm ± 117 nm, an average circularity of 0.78 ± 0.04 and an average aspect ratio of 1.26 ± 0.07 were obtained (Fig. 4.90) considering 76 stamped dots. From the AFM measurement (Fig. 4.91) 99 P(VDF-TrFE) stamped dots on glass with 30 min dwell time were analysed and a frequency distribution of the dot heights was obtained (Fig. 4.92). The average height of the stamped P(VDF-TrFE) dots was 94 nm ± 29 nm.
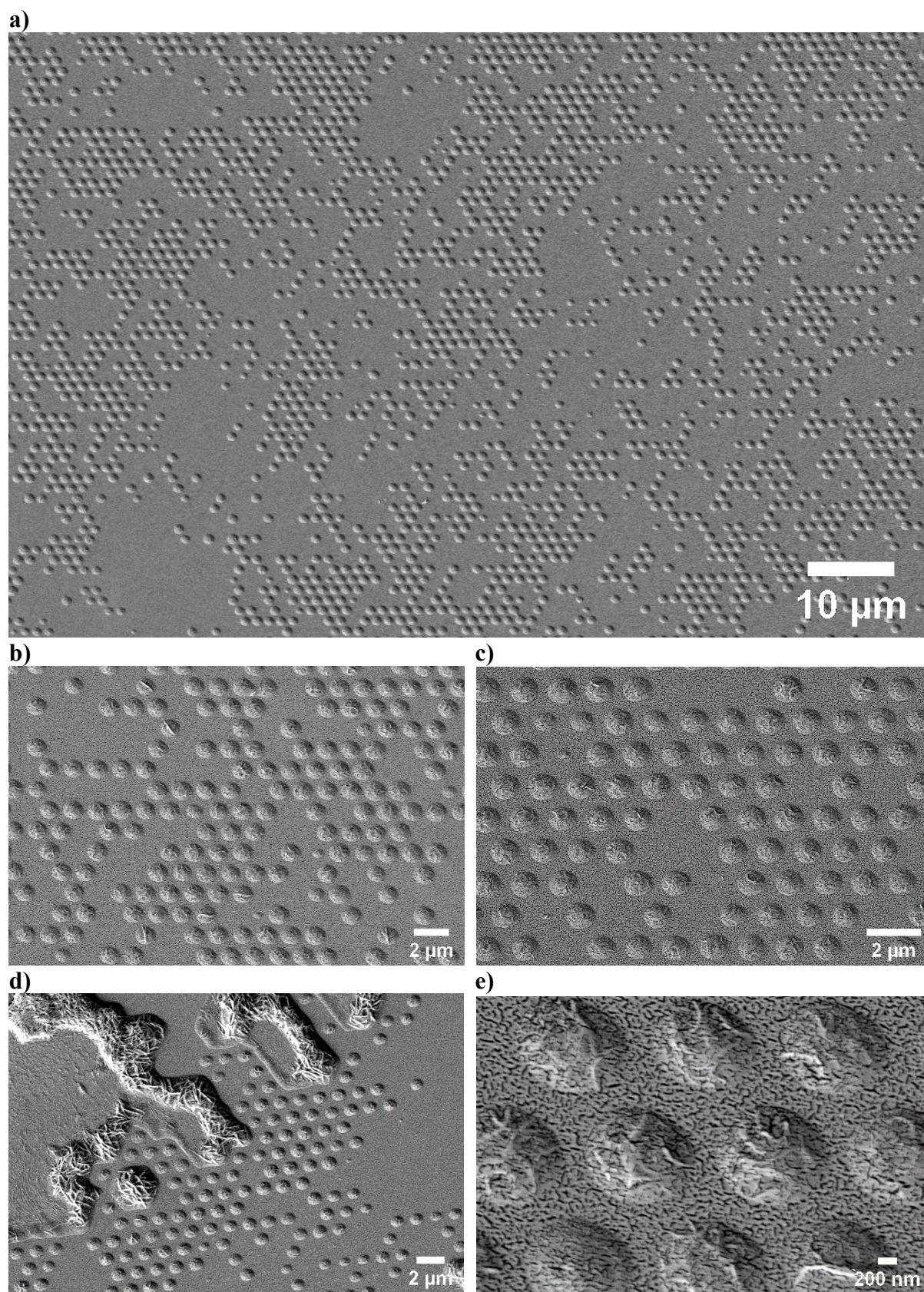
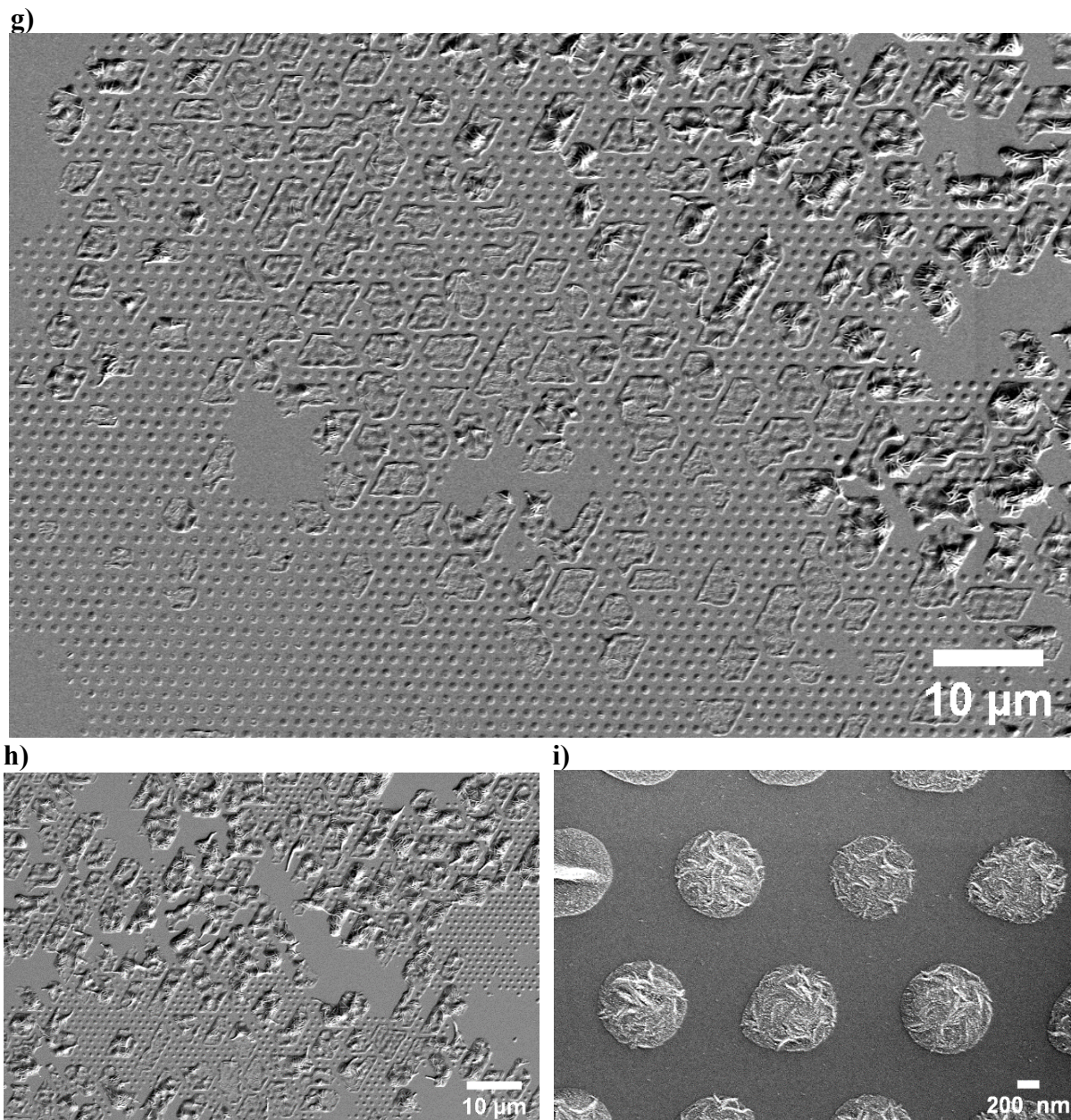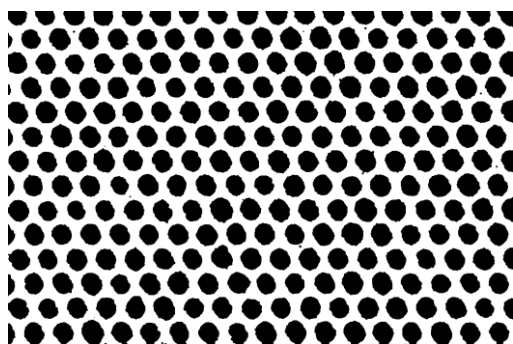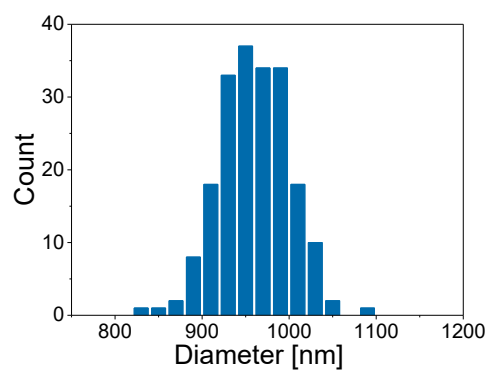**Figure 4.89** SEM images of stamped P(VDF-TrFE) dots on glass 205 °C after 30 min dwell time.

a)
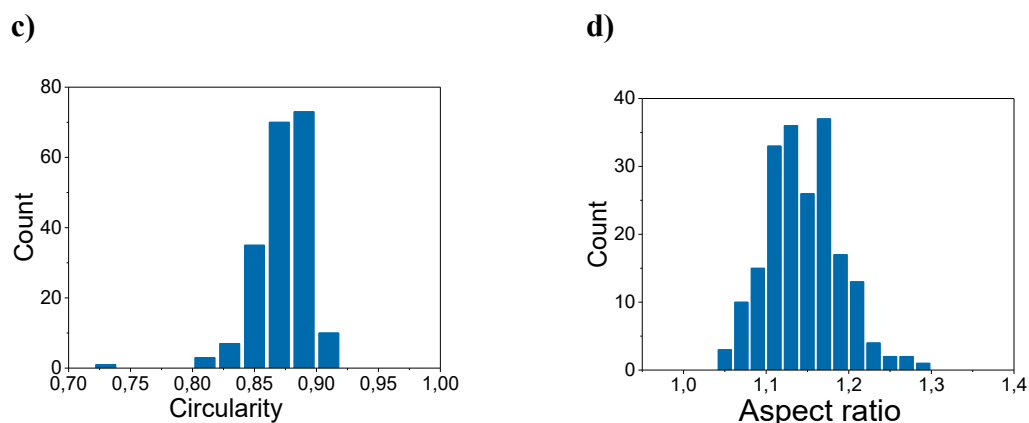

b)

c)

d)
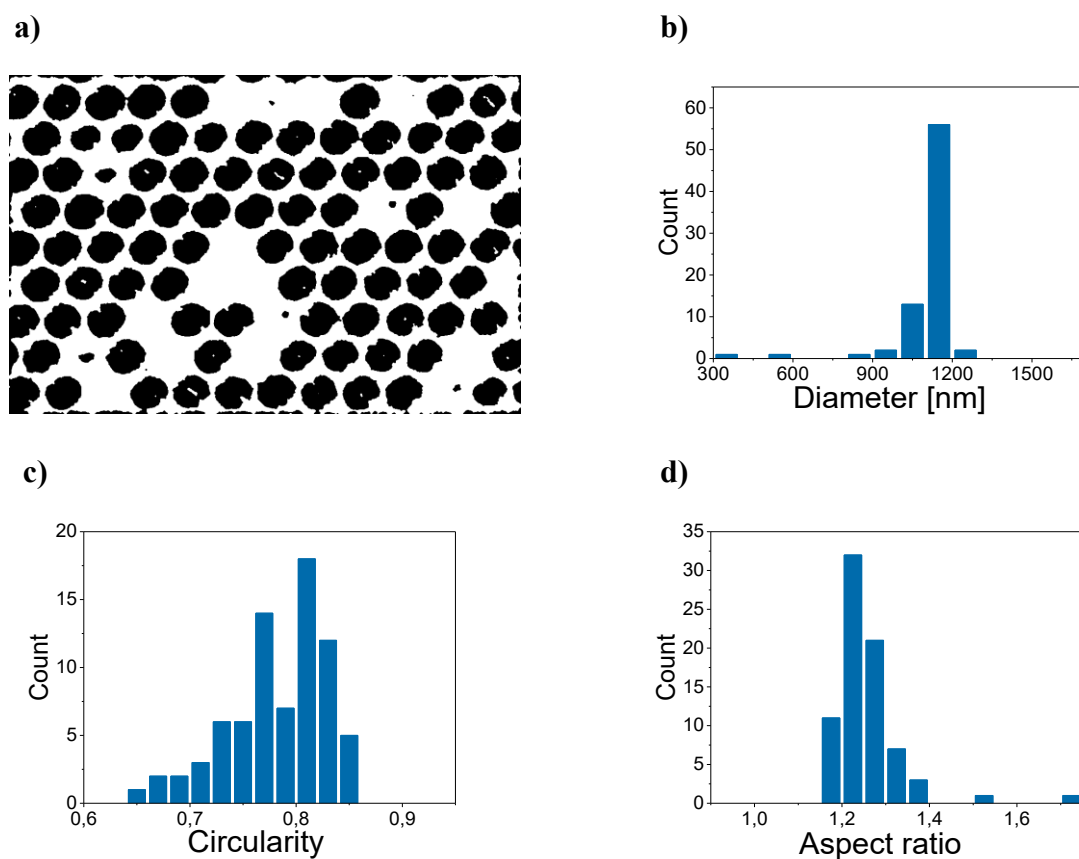
Figure 4.90 (a) Binarized SEM image (see original SEM image in Fig. 4.61c) of stamped P(VDF-TrFE) dots on glass after 30 min dwell time at 205 °C   (stamping method III - *with pressure*). Histograms of **(b)** diameters, **(c)** circularities, and **(d)** aspect ratios of 76 analyzed P(VDF-TrFE) dots on glass acquired by image analysis.
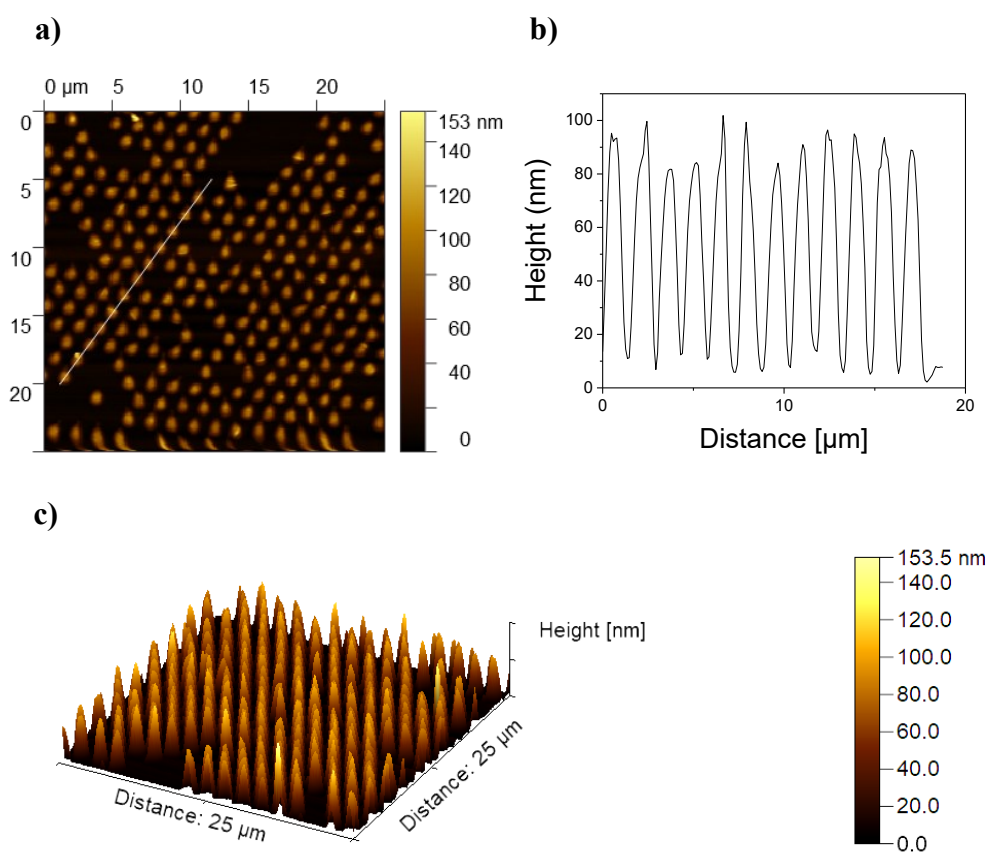
a)

b)

c)
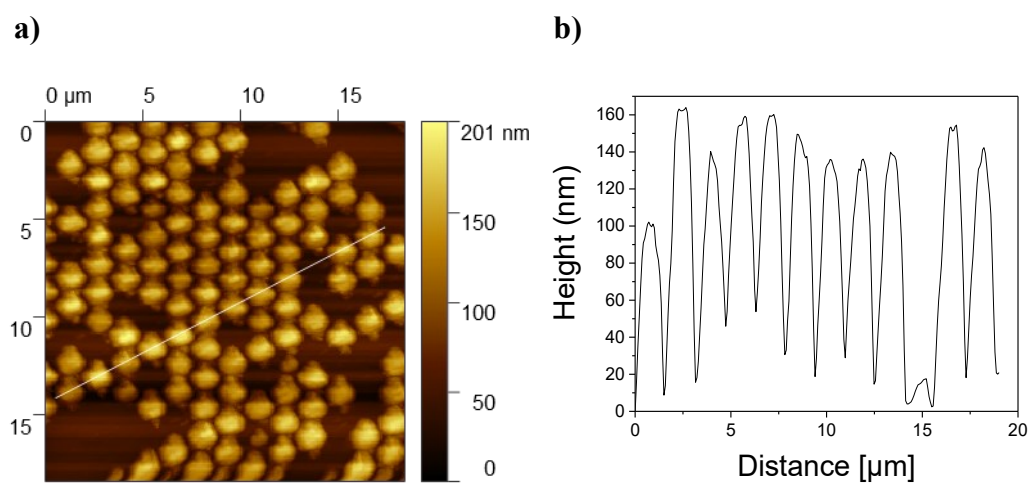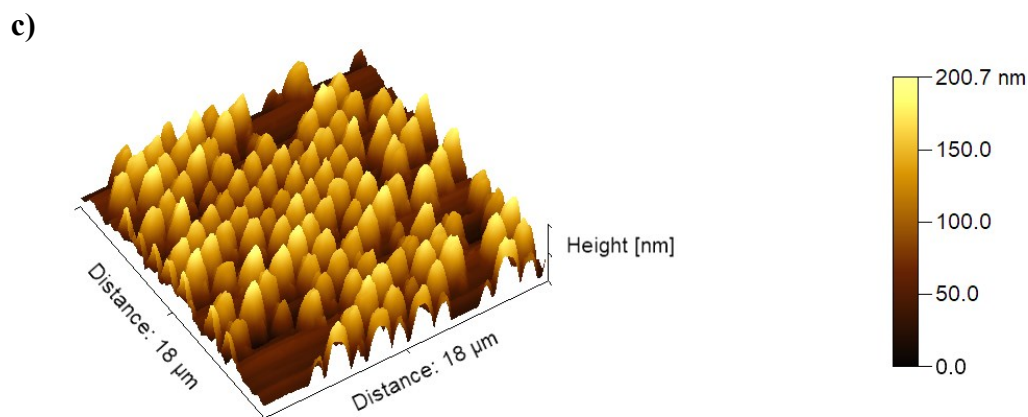
Figure 4.91 AFM image of P(VDF-TrFE) dots stamped on glass at 205 °C after 30 min dwell time. **(a)** topographical AFM image, **(b)** topographical profile along the line in the panel (a) and **(c)** 3D AFM image.
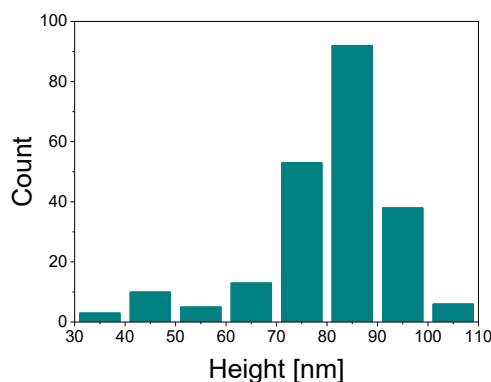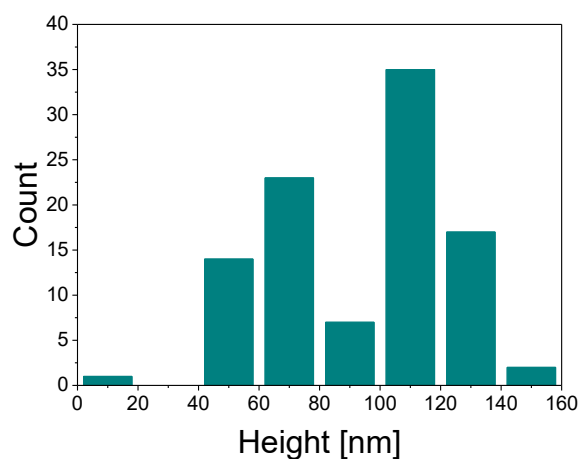

Figure 4.92 Histogram of 99 analyzed P(VDF-TrFE) dots heights printed on a glass substrate with 30 min dwell time. Heights were obtained from the analysis of the AFM image shown in the Figure 4.91a.

In Figure 4.93 histograms of the diameters of P(VDF-TrFE dots stamped on glass substrates for all dwell times are shown (Table 4.4). There is no evident correlation between the diameter of the printed dots with the dwell time. Average diameters of the stamped P(VDF-TrFE) dots for the different stamping times are in the range from 960 nm to 1169 nm. The circularity of the stamped P(VDF-TrFE) dots is in the range from 0.8 to 0.9 and the aspect ratio in the range from 1.1 to 1.2. From this data is apparent that the printed P(VDF-TrFE) dots were uniform in their shape after multiple stamping cycles and after different stamping times. Average heights of the printed P(VDF-TrFE) dots for different stamping times are summerized in the Table 4.5 and are in the range from 81 nm to 116 nm. From this data, there is no direct correlation between the height of the printed dots and the stamping time.
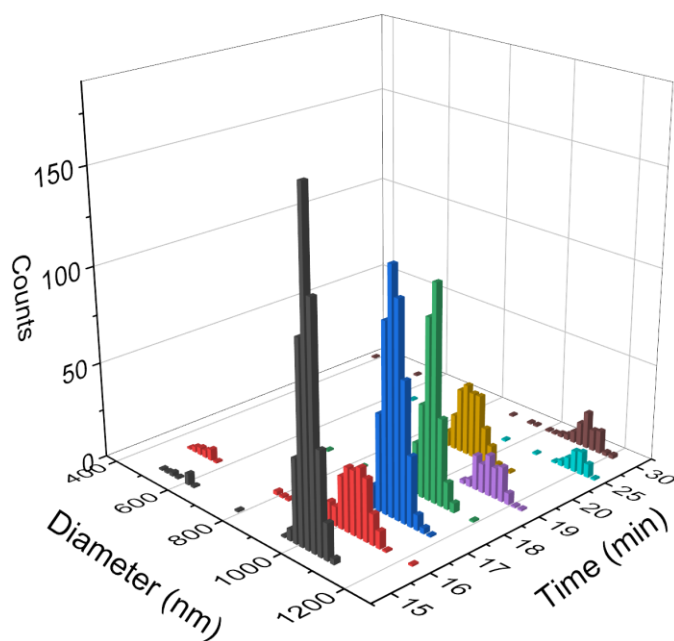
Figure 4.93 Summary histogram with diameter values of P(VDF-TrFE) dots stamped on glass with 15 min (black), 16 min (red), 17 min (blue), 18 min (green), 19 min (purple), 20 min (yellow), 25 min (turquoise) and 30 min (brown) stamping time.
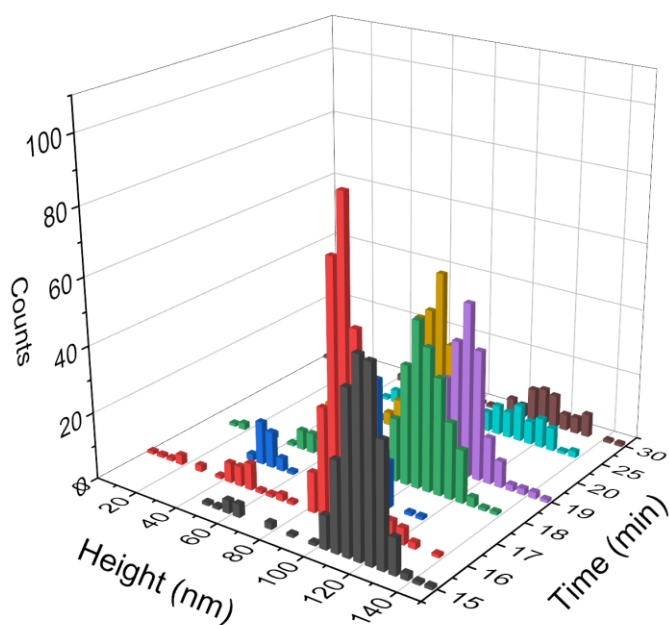
Figure 4.94 Summary histogram of all heights of P(VDF-TrFE) dots stamped on glass with 15 min (black), 16 min (red), 17 min (blue), 18 min (green), 19 min (purple), 20 min (yellow), 25 min (turquoise) and 30 min (brown).

Table 4.4.

Stamping time [min]	Average diameter [nm]	Average circularity	Average aspect ratio
15	1023 ± 72	0.88 ± 0.04	1.18 ± 0.05
16	1002 ± 150	0.92 ± 0.01	1.10 ± 0.09
17	1057 ± 31	0.90 ± 0.02	1.07 ± 0.02
18	1052 ± 54	0.89 ± 0.02	1.19 ± 0.04
19	1131 ± 36	0.85 ± 0.04	1.09 ± 0.04
20	960 ± 40	0.87 ± 0.02	1.14 ± 0.04
25	1169 ± 102	0.82 ± 0.02	1.23 ±0.03
30	1103 ± 117	0.78 ± 0.04	1.26 ± 0.07

Table 4.5.

Stamping time [min]	Average height [nm]
15	116 ± 14
16	93 ± 18
17	84 ± 19
18	99 ± 21
19	106 ± 19
20	81 ± 14
25	102 ± 23
30	94 ± 29

4.3.2 Stamping of P(VDF-TrFE) on aluminium-coated silicon substrates

Here, aluminium coated silicon was used as a substrate for printing of P(VDF-TrFE) polymer ink. Stamping was done with composite np-Au stamp with the stamping method III – *with pressure* at 205 °C. The stamping results for different stamping times are presented below.

Analysis of 654 P(VDF-TrFE) dots stamped on an Al/Si substrate with 1 min dwell time in the binarized version (Fig. 4.94a) of the SEM image seen in Figure 4.95c revealed an average dot diameter of 894 nm ± 83 nm, an average circularity of 0.85 ± 0.07 and an average aspect ratio of 1.19 ± 0.13 (Fig. 4.96). From the AFM measurement (Fig. 4.97) 99 P(VDF-TrFE) dots on Al/Si stamped with 1 min dwell time were analysed and a frequency distribution of the dot heights was obtained (Fig. 4.98). The average height of the stamped P(VDF-TrFE) dots was 52 nm ± 14 nm.

Figure 4.95 SEM images of P(VDF-TrFE) droplets stamped on an aluminium (Al) coated silicon (Si) substrate with a composite np-Au stamp at 205 °C with 1 min dwell time.

c)

d)

Figure 4.96 (a) Binarized SEM image (see original SEM image in Fig. 4.95c) of P(VDF-TrFE) dots stamped on an aluminium (Al) coated silicon (Si) substrate with 1 min dwell time at 205 °C (stamping method III - *with pressure*). Histograms of **(b)** diameters, **(c)** circularities, and **(d)** aspect ratios of 654 analyzed P(VDF-TrFE) dots.

a)

b)

c)
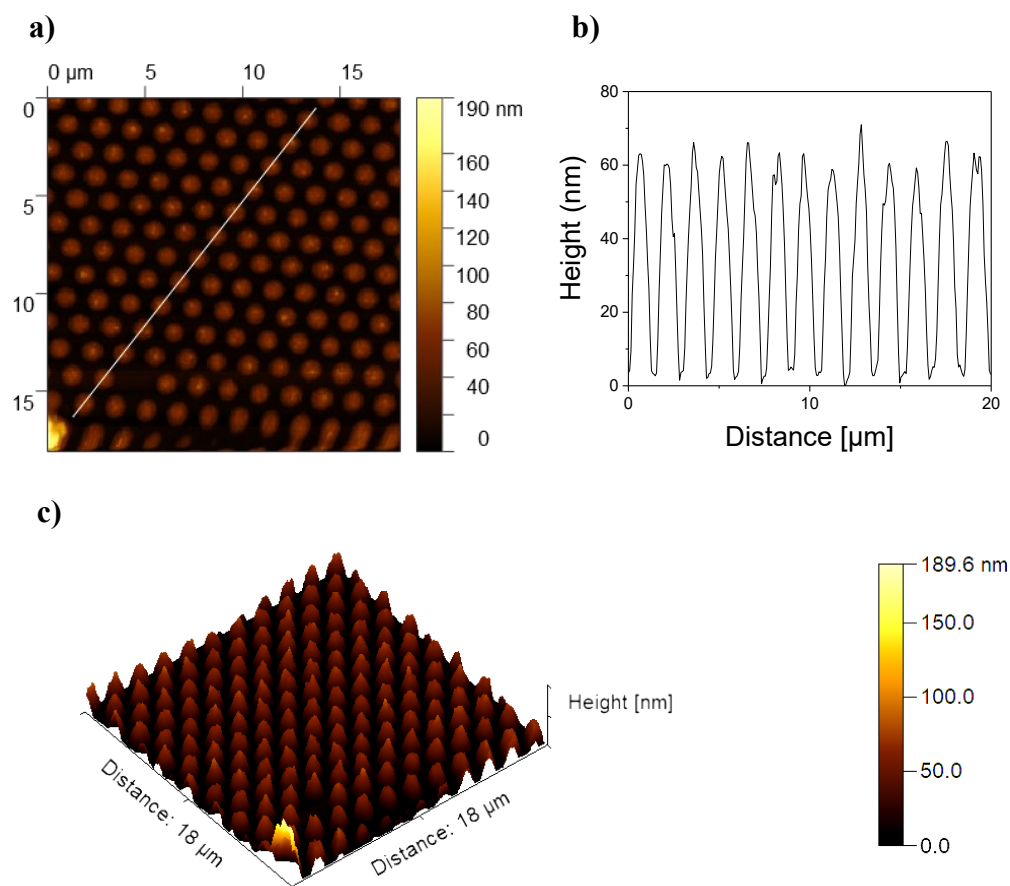
Figure 4.97 AFM image of P(VDF-TrFE) dots stamped on an aluminium (Al) coated silicon (Si) substrate at 205 °C with 1 min dwell time showing: **(a)** topographical AFM image, **(b)** topographical profile along the line in the panel (a) and **(c)** 3D AFM image.

Figure 4.98 Height histogram of 126 analyzed P(VDF-TrFE) dots printed on an aluminium (Al) coated silicon (Si) substrate after 1 min dwell time. Heights were obtained by the analysis of the AFM image shown in the Figure 4.97a.

From the binarization of the SEM image (from Fig 4.99c) of the P(VDF-TrFE) dots stamped on Al/Si substrate with 2 min dwell time an average diameter of 957 nm ± 49 nm, an average circularity of 0.83 ± 0.07 and an average aspect ratio of 1.26 ± 0.08 were obtained (Fig. 4.100) considering 607 stamped dots. From the AFM measurement (Fig. 4.101) 145 P(VDF-TrFE) dots stamped on Al/Si with 2 min dwell time were analysed and a frequency distribution of the dot heights was obtained (Fig. 4.102). The average height of the stamped P(VDF-TrFE) dots was 64 nm ± 17 nm.

a)

b)

c)

d)

e)

f)

g)

h)
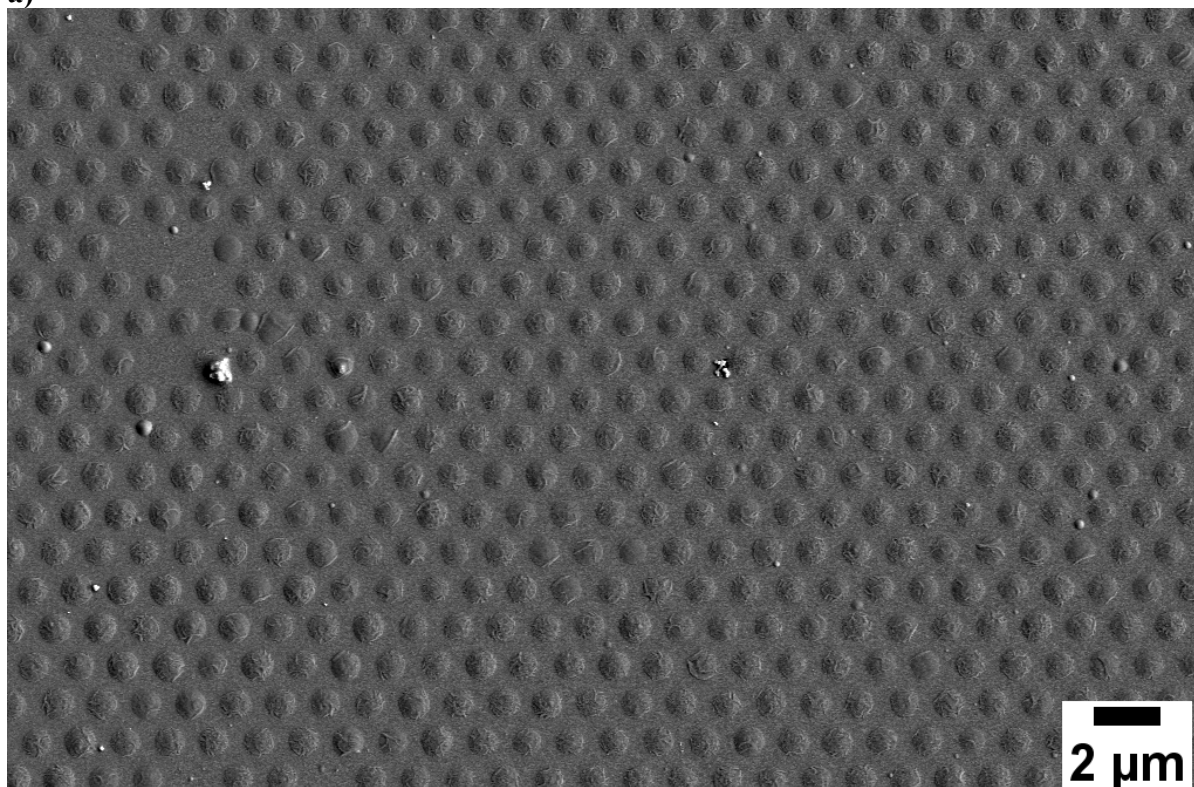
Figure 4.99 SEM images of P(VDF-TrFE) dots stamped on an aluminium (Al) coated silicon (Si) substrate with a composite np-Au stamp at 205 °C and with 2 min dwell time.

Figure 4.100 (a) Binarized SEM image (see original SEM image in Fig. 4.99c) of P(VDF-TrFE) dots stamped on an aluminium (Al) coated silicon (Si) substrate with 2 min dwell time at 205 °C (stamping method III - *with pressure*). Histograms of **(b)** diameters, **(c)** circularities, and **(d)** aspect ratios of 607 analyzed P(VDF-TrFE) dots.

c)
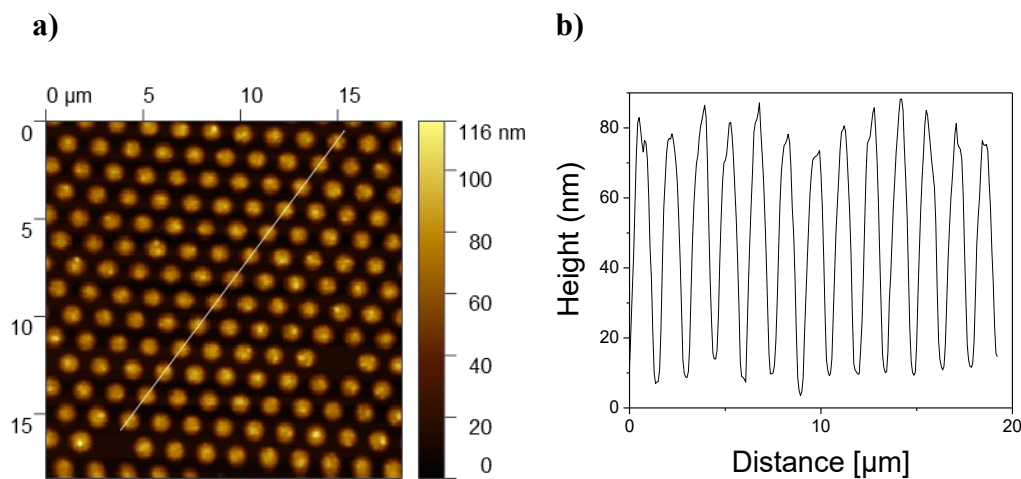
Figure 4.101 AFM image of P(VDF-TrFE) dots stamped on an aluminium (Al) coated silicon (Si) substrate at 205 °C with 2 min dwell time showing: **(a)** topographical AFM image, **(b)** topographical profile along the line in the panel (a) and **(c)** 3D AFM image.

Figure 4.102 Height histogram of 145 analyzed P(VDF-TrFE) dots on an aluminium (Al) coated silicon (Si) substrate printed with 2 min dwell time. Heights were obtained from the analysis of the AFM image shown in the Figure 4.101a.

From the binarization of the SEM image (from Fig 4.103e) of P(VDF-TrFE) dots stamped on Al/Si substrate with 3 min dwell time an average diameter of 940 nm $\pm$ 93 nm, an average circularity of 0.86 $\pm$ 0.05 and an average aspect ratio of 1.25 $\pm$ 0.07 were obtained (Fig. 4.104) considering 337 stamped dots. From the AFM measurement (Fig. 4.105) 36 P(VDF-TrFE) dots stamped on Al/Si with 3 min dwell time were analysed and a frequency distribution of the dot heights was obtained (Fig. 4.106). The average height of the stamped P(VDF-TrFE) dots was 39 nm $\pm$ 19 nm.
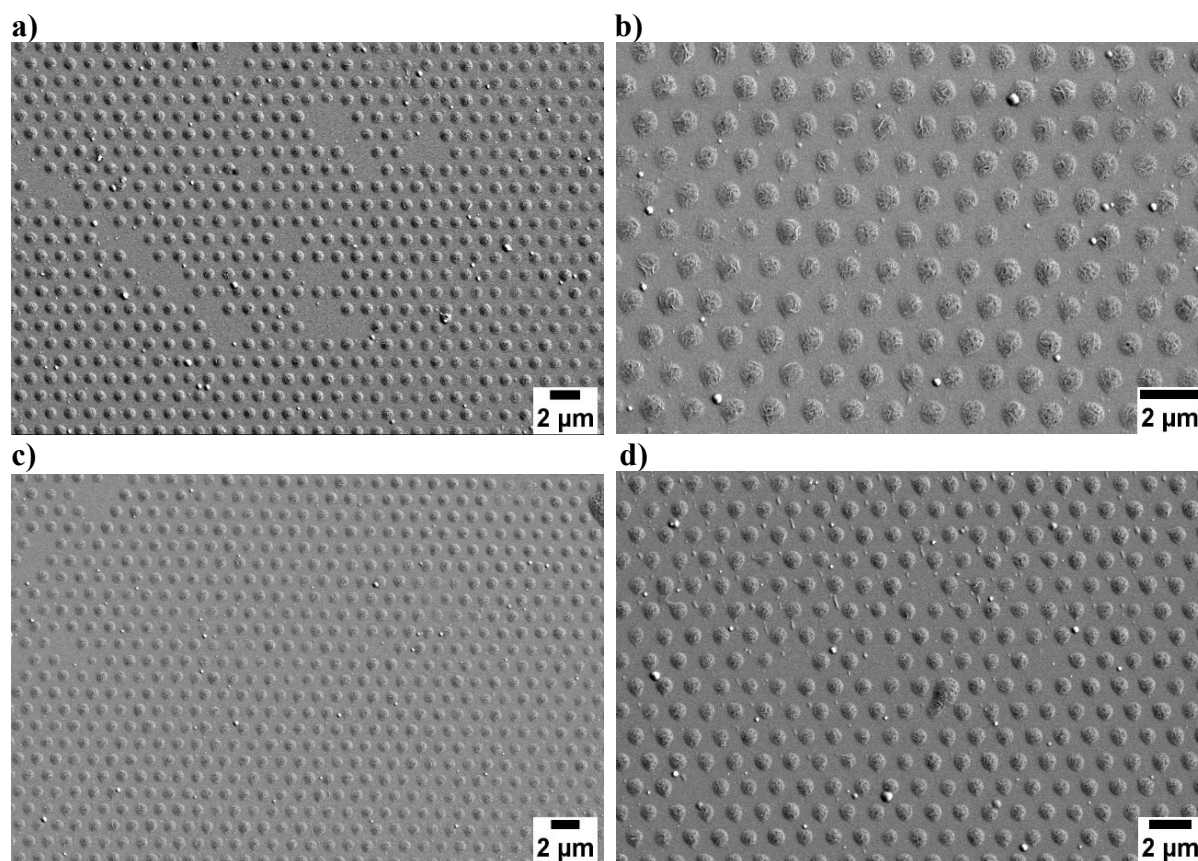
a)

b)

c)

d)

e)

f)

Figure 4.103 SEM images of P(VDF-TrFE) dots stamped on an aluminium (Al) coated silicon (Si) substrate with a composite np-Au stamp at 205 °C and with 3 min dwell time.

a)

b)

c)

d)

Figure 4.104 (a) Binarized SEM image (see original SEM image in Fig. 4.103b) of P(VDF-TrFE) dots stamped on an aluminium (Al) coated silicon (Si) substrate with 3 min dwell time at 205 °C (stamping method III - *with pressure*). Histograms of **(b)** diameters, **(c)** circularities and **(d)** aspect ratios of 337 analyzed P(VDF-TrFE) dots.

a)

b)

c)
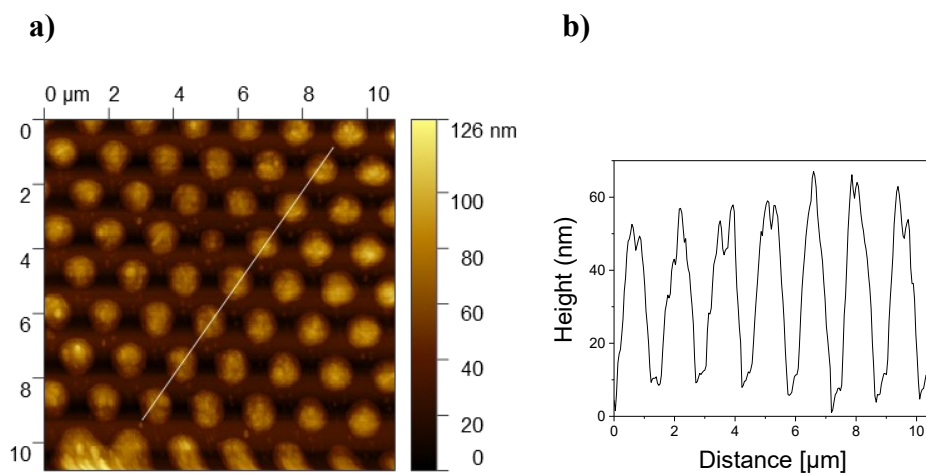
Figure 4.105 AFM image of P(VDF-TrFE) dots stamped on an aluminium (Al) coated silicon (Si) substrate at 205 °C after 3 min dwell time showing: **(a)** topographical AFM image, **(b)** topographical profile along the line in the panel (a) and **(c)** 3D AFM image.

Figure 4.106 Height histogram of 36 analyzed P(VDF-TrFE) dots printed on an aluminium (Al) coated silicon (Si) substrate with 3 min dwell time. Heights were obtained from the analysis of the AFM image shown in the Figure 4.105a.

From the binarization of the SEM image (from Fig 4.107a) of P(VDF-TrFE) dots stamped on an Al/Si substrate with 4 min dwell time an average diameter of 925 nm ± 60 nm, an average circularity of 0.86 ± 0.05 and an average aspect ratio of 1.28 ± 0.11 were obtained (Fig. 4.108) considering 626 stamped dots. From the AFM measurement (Fig. 4.109) 403 P(VDF-TrFE) dots stamped on Al/Si with 4 min dwell time were analysed and a frequency distribution of the dot heights was obtained (Fig. 4.110). The average height of the stamped P(VDF-TrFE) dots was 75 nm ± 15 nm.
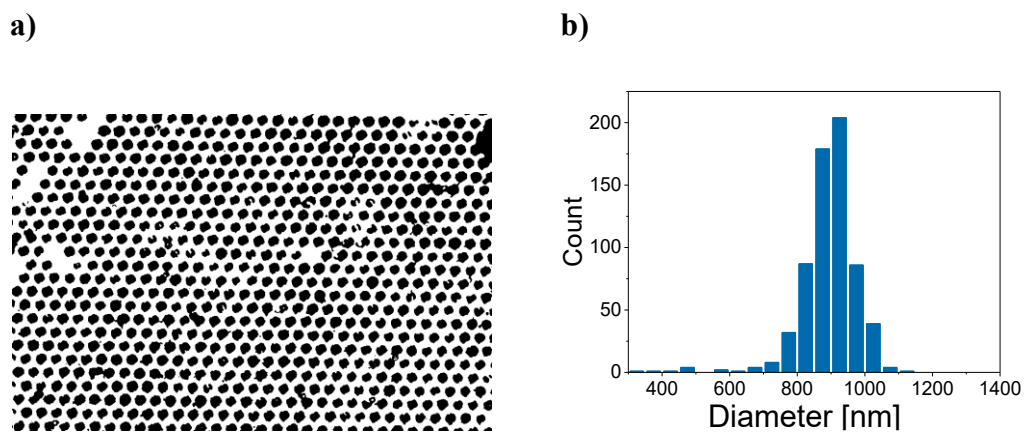
Figure 4.107 SEM images of P(VDF-TrFE) dots stamped on an aluminium (Al) coated silicon (Si) substrate with a composite np-Au stamp at 205 °C and with 4 min dwell time.
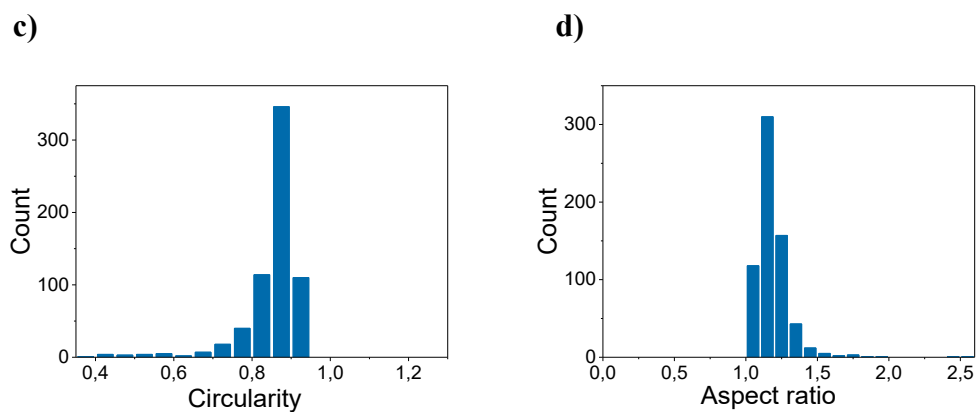

Figure 4.108 (a) Binarized SEM image (see original SEM image in Fig. 4.107a) of P(VDF-TrFE) dots stamped on an aluminium (Al) coated silicon (Si) substrate with 4 min dwell time at 205 °C (stamping method III - *with pressure*). Histograms of **(b)** diameters, **(c)** circularities, and **(d)** aspect ratios of 626 analyzed P(VDF-TrFE) dots.

117

a)

b)

c)

Figure 4.109 AFM image of P(VDF-TrFE) dots stamped on an aluminium (Al) coated silicon (Si) substrate at 205 °C with 4 min dwell time showing: **(a)** topographical AFM image, **(b)** topographical profile along the line in the panel (a) and **(c)** 3D AFM image.
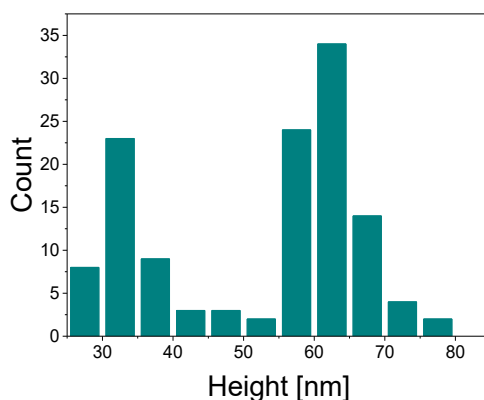

Figure 4.110 Height histogram of 403 analyzed P(VDF-TrFE) dots printed on an aluminium (Al) coated silicon (Si) substrate with 4 min dwell time. Heights were obtained from the analysis of the AFM image shown in the Figure 4.109a.

From the binarization of the SEM image (from Fig 4.111b) of P(VDF-TrFE) dots stamped on an Al/Si substrate with 5 min dwell time an average diameter of 1085 nm ± 71 nm, an average circularity of 0.79 ± 0.10 and an average aspect ratio of 1.29 ± 0.68 were obtained (Fig. 4.112) considering 160 stamped dots. From the AFM measurement (Fig. 4.113) 470 stamped P(VDF-

TrFE) dots on Al/Si after 5 min dwell time were analysed and a frequency distribution of the dot heights was obtained (Fig. 4.114). The average height of the stamped P(VDF-TrFE) dots was 77 nm ± 13 nm.

a)

b)

c)

d)

e)
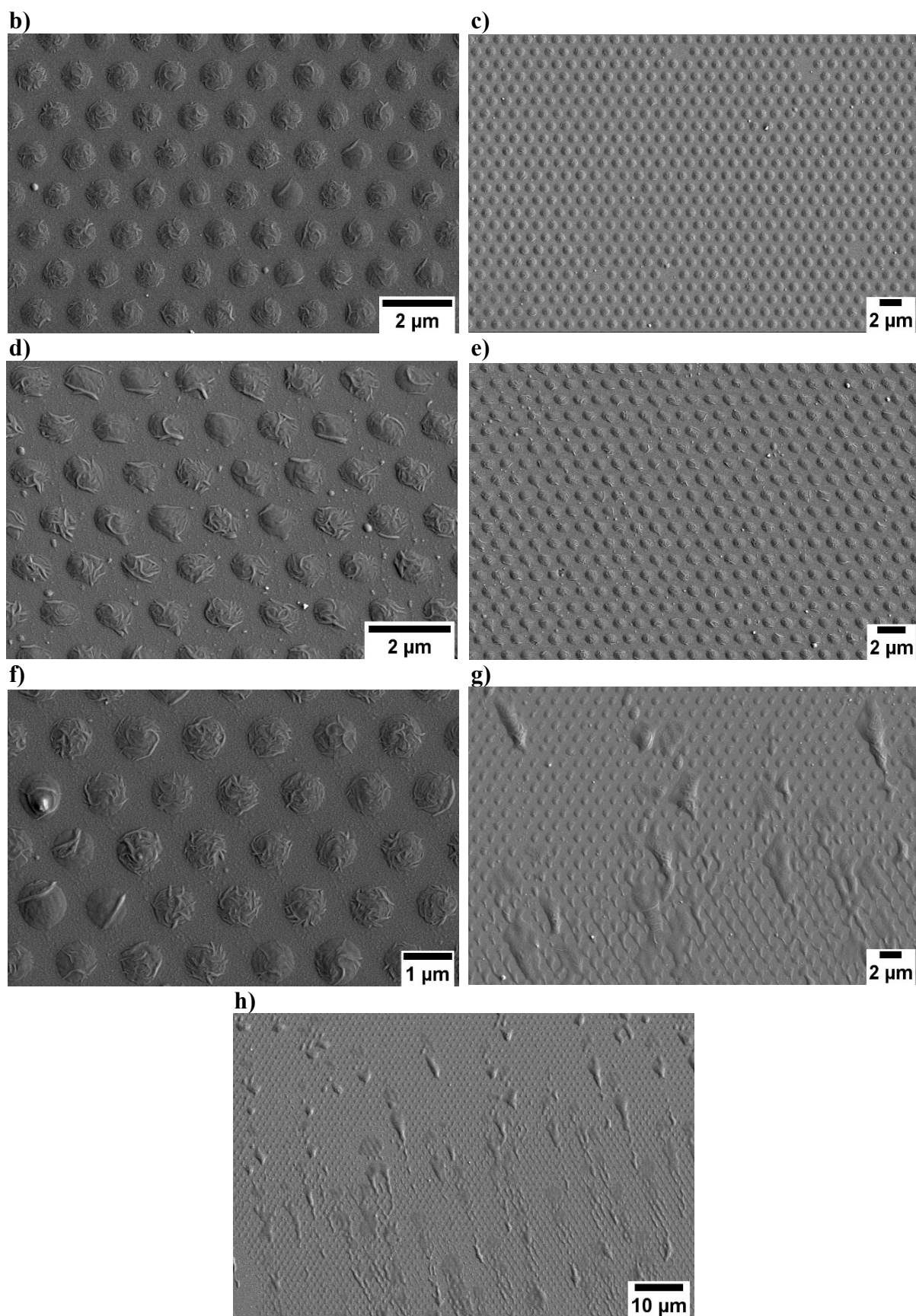
f)

g)

h)
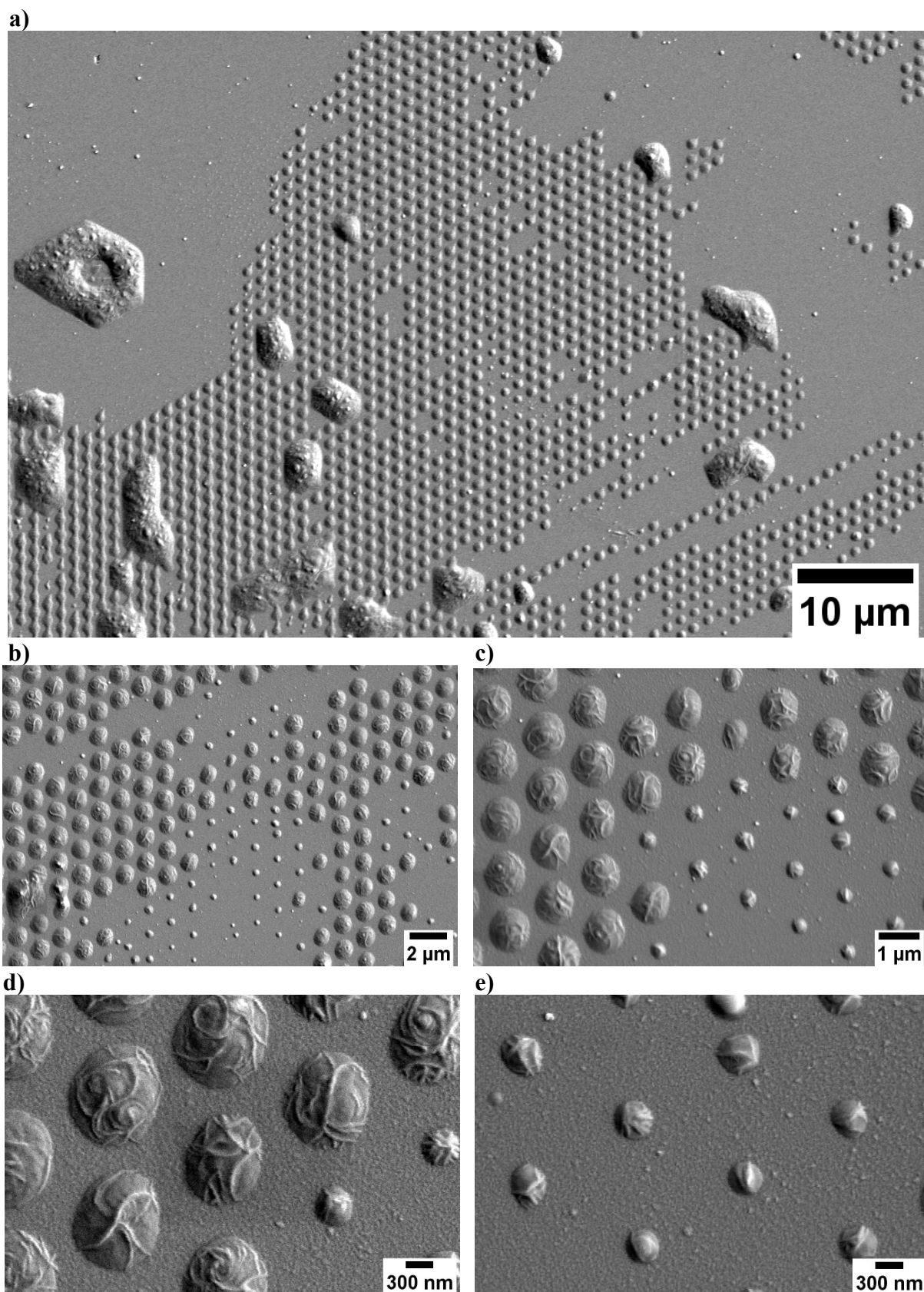
Figure 4.111 SEM images of P(VDF-TrFE) dots stamped on an aluminium (Al) coated silicon (Si) substrate with a composite np-Au stamp at 205 °C and with 5 min dwell time.
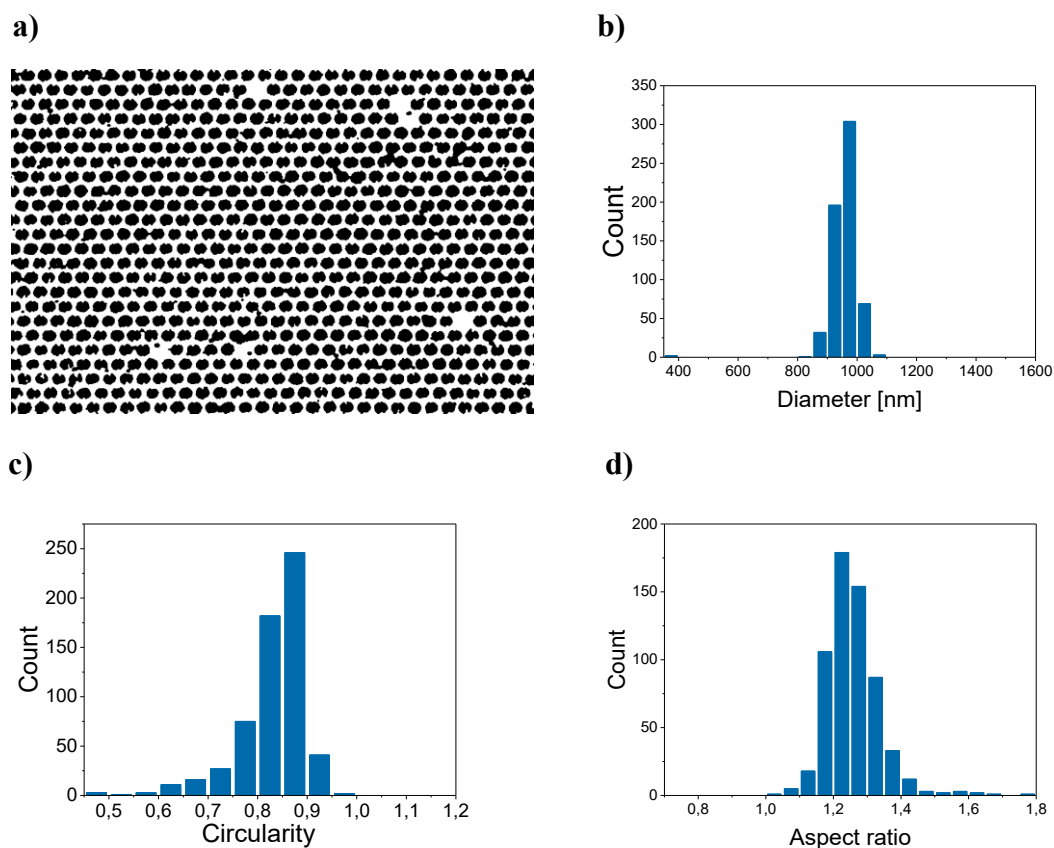
a)

b)

c)

d)

Figure 4.112 (a) Binarized SEM image (see original SEM image in Fig. 4.111b) of P(VDF-TrFE) dots stamped on an aluminium (Al) coated silicon (Si) substrate with 5 min dwell time at 205 °C (stamping method III - *with pressure*). Histograms of **(b)** dameters, **(c)** circularities, and **(d)** aspect ratios of 160 analyzed P(VDF-TrFE) dots.
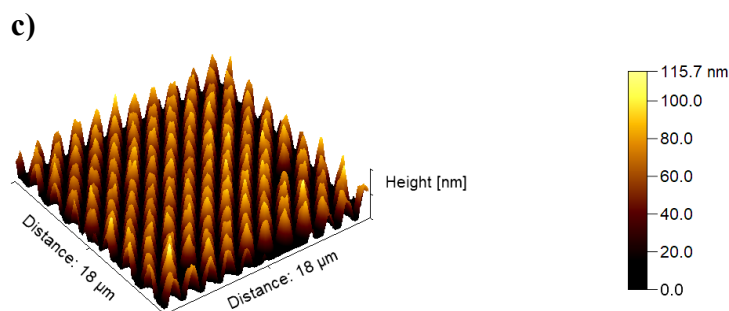
a)

b)

c)
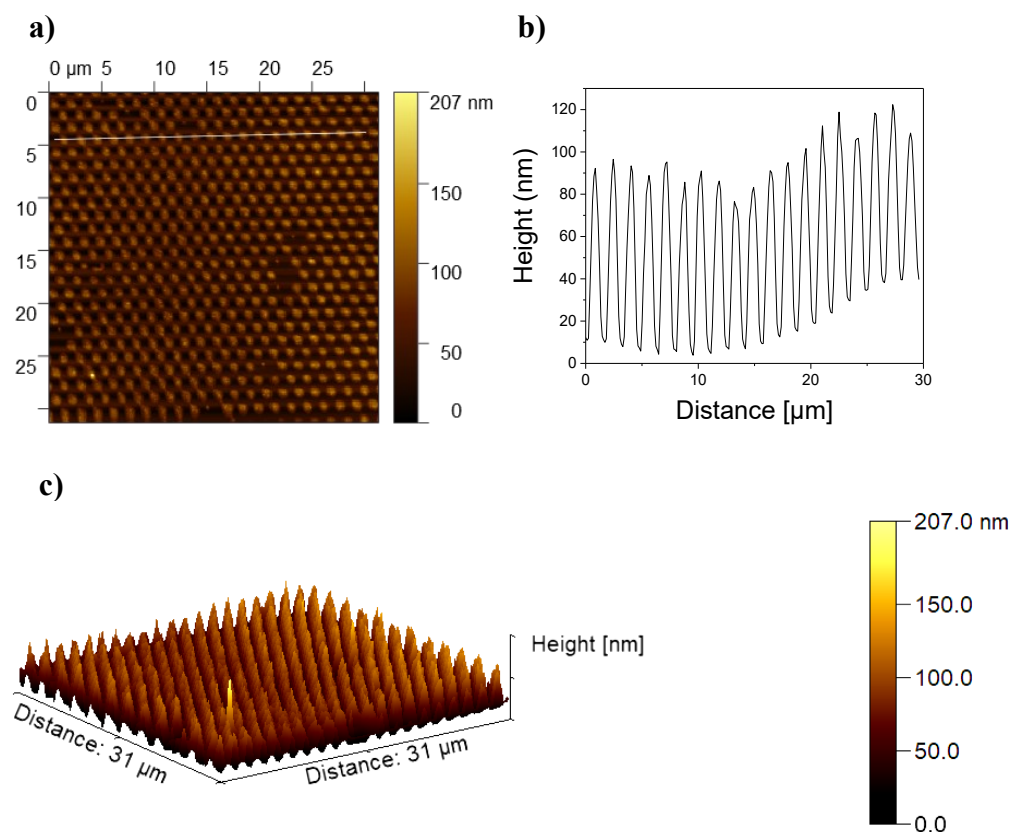
Figure 4.113 AFM image of P(VDF-TrFE) dots stamped on an aluminium (Al) coated silicon (Si) substrate at 205 °C with 5 min dwell time showing: **(a)** topographical AFM image, **(b)** topographical profile along the line in the panel (a) and **(c)** 3D AFM image.
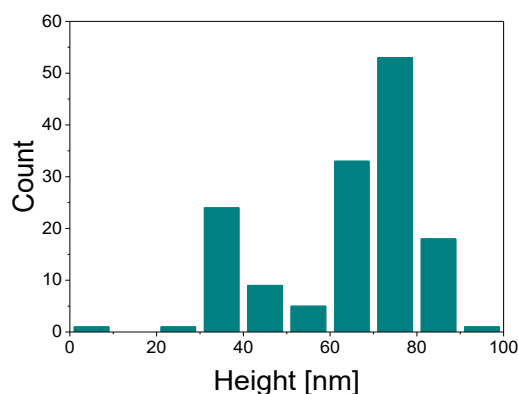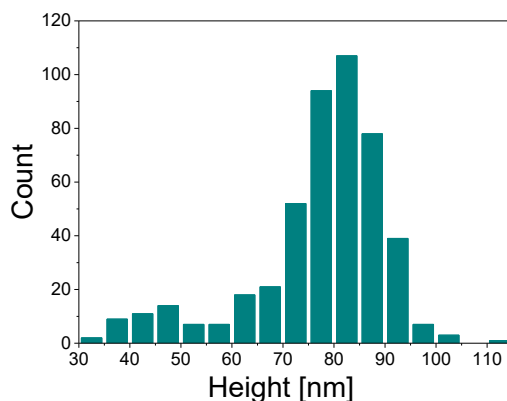
Figure 4.114 Height histogram of 470 analyzed P(VDF-TrFE) dots printed on an aluminium (Al) coated silicon (Si) substrate with 5 min dwell time. Heights were obtained from the analysis of the AFM image shown in the Figure 4.113a.

From the binarization of the SEM image (from Fig 4.115a) of P(VDF-TrFE) dots stamped on an Al/Si substrate with 6 min dwell time an average diameter of 954 nm ± 78 nm, an average circularity of 0.77 ± 0.08 and an average aspect ratio of 1.32 ± 0.16 were obtained (Fig. 4.116) considering 314 stamped dots. From the AFM measurement (Fig. 4.117) 391 stamped P(VDF-TrFE) dots on Al/Si after 6 min dwell time were analysed and a frequency distribution of the dot heights was obtained (Fig. 4.118). The average height of the stamped P(VDF-TrFE) dots was 62 nm ± 13 nm.
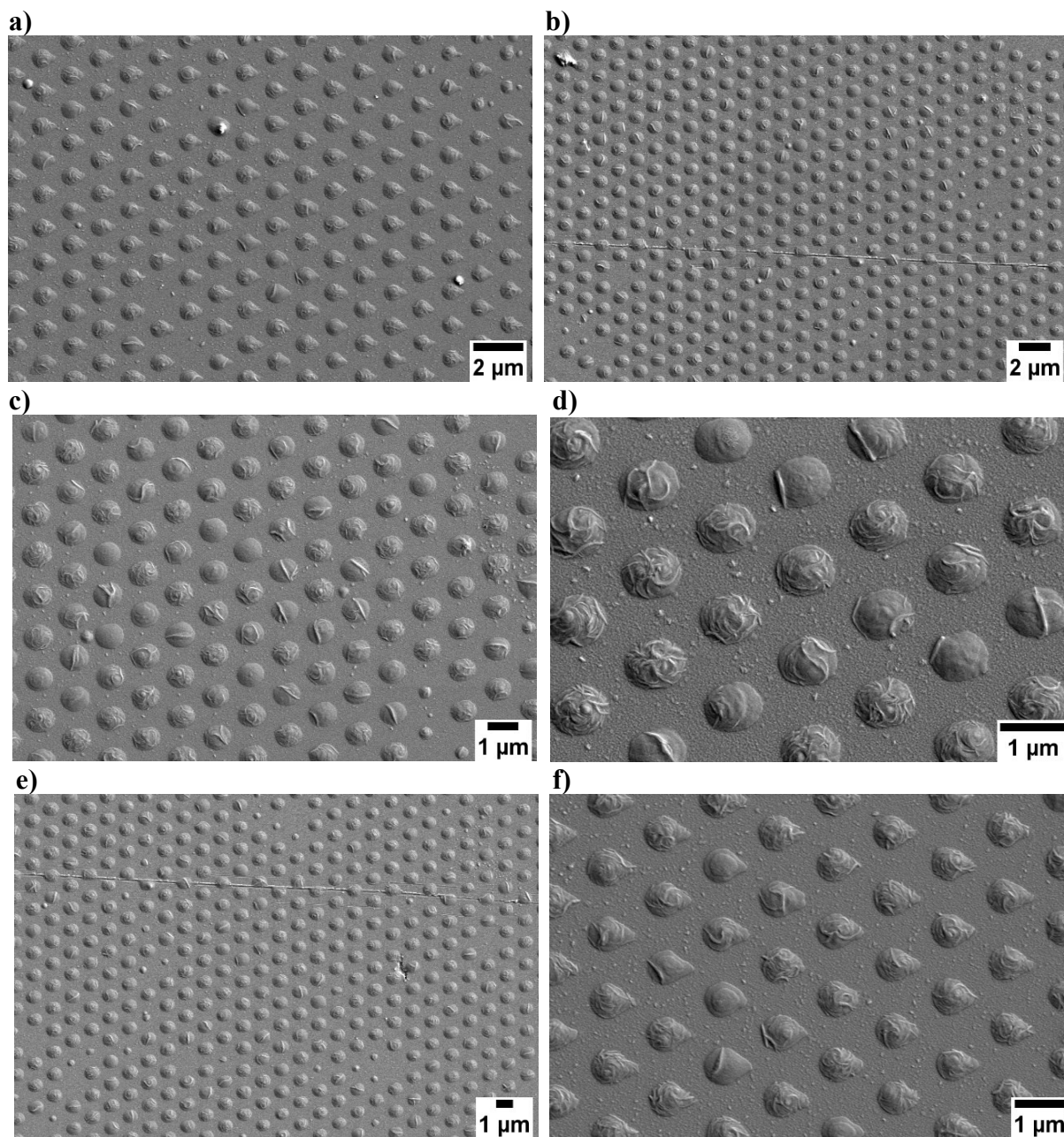
a)
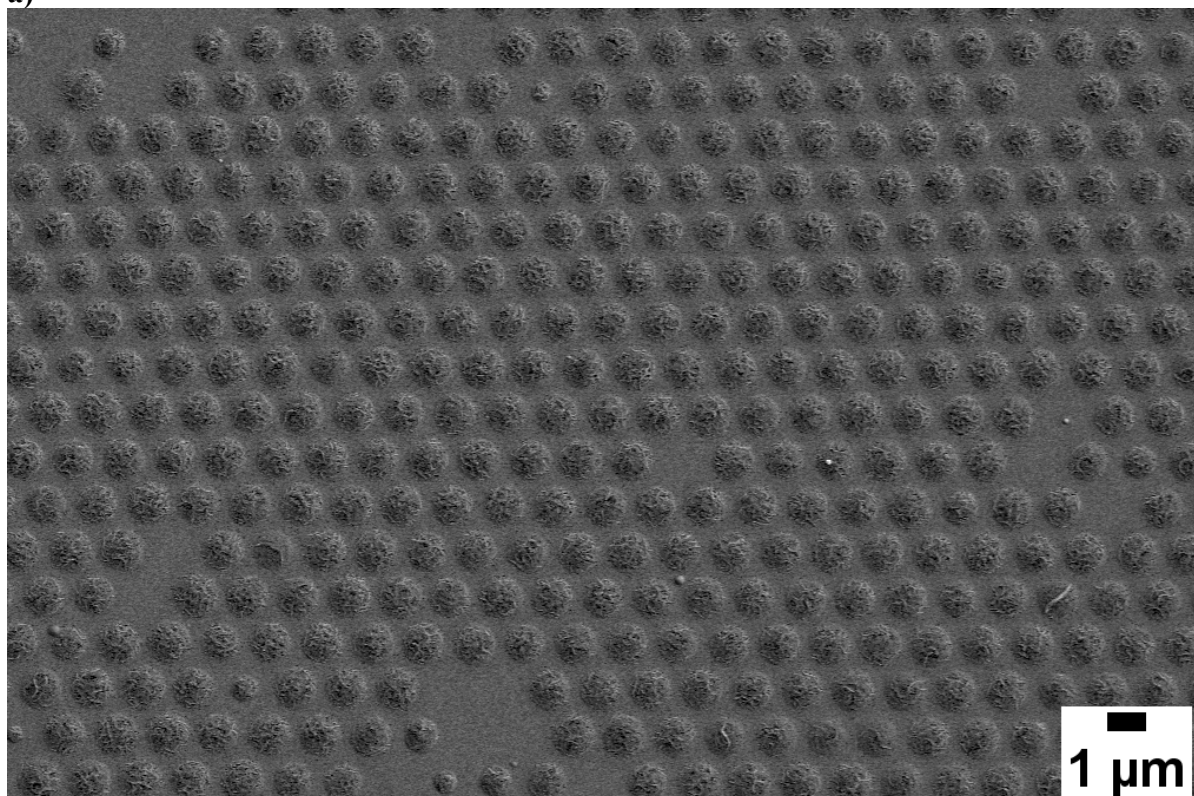
Figure 4.115 SEM images of P(VDF-TrFE) dots stamped on an aluminium (Al) coated silicon (Si) substrate with a composite np-Au stamp at 205 °C and with 6 min dwell time.
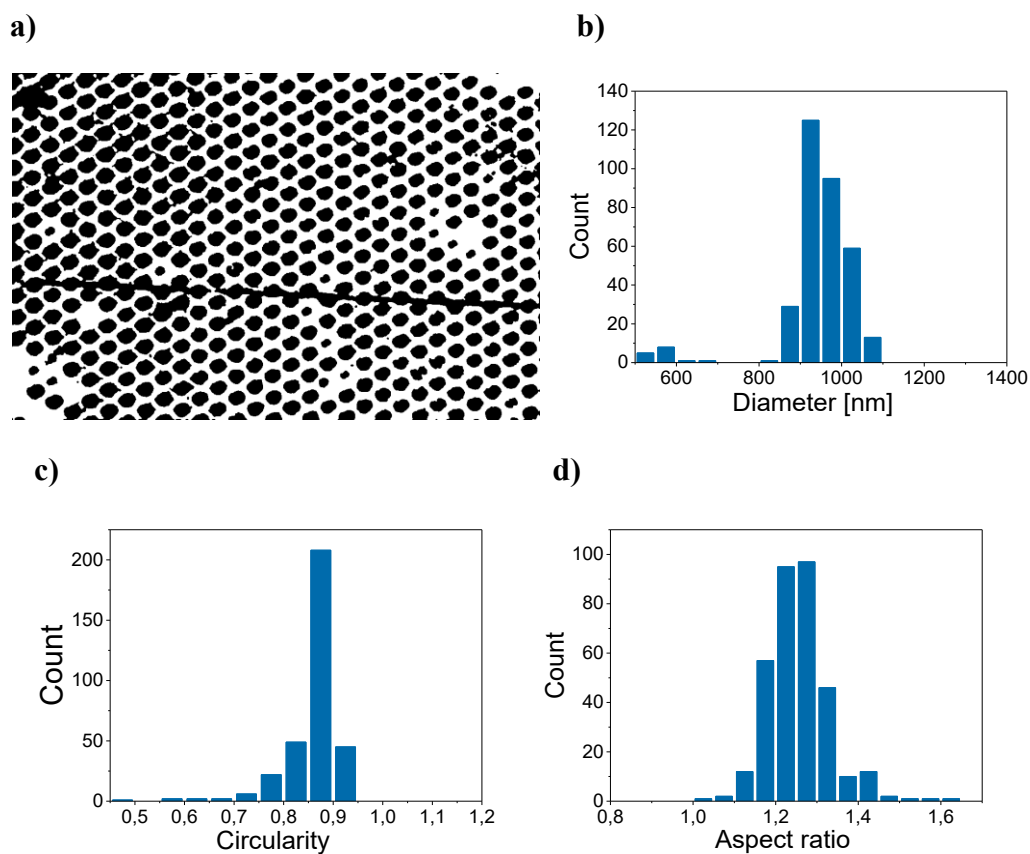

Figure 4.116 (a) Binarized SEM image (see original SEM image in Fig. 4.115a) of P(VDF-TrFE) dots stamped on an aluminium (Al) coated silicon (Si) substrate with 6 min dwell time at 205 °C (stamping method III - *with pressure*). Histograms of **(b)** diameters, **(c)** circularities, and **(d)** aspect ratios of 314 analyzed P(VDF-TrFE) dots.
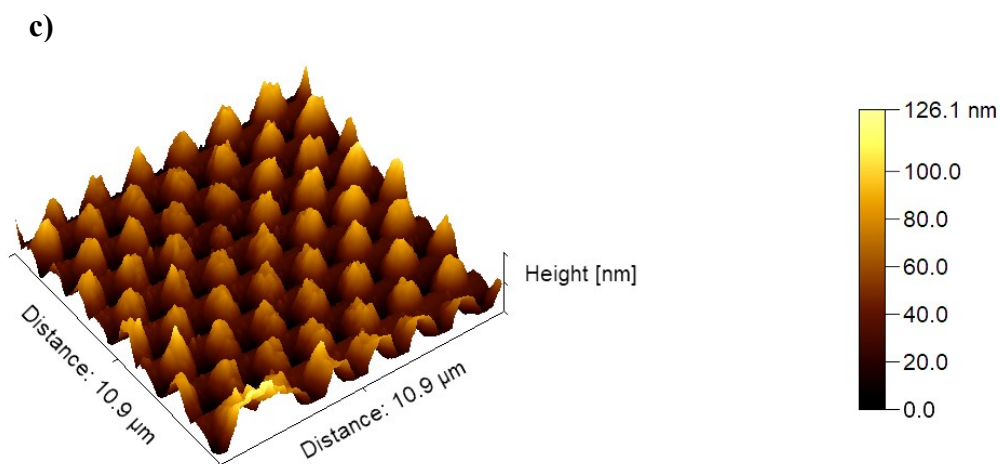
a)

b)

c)
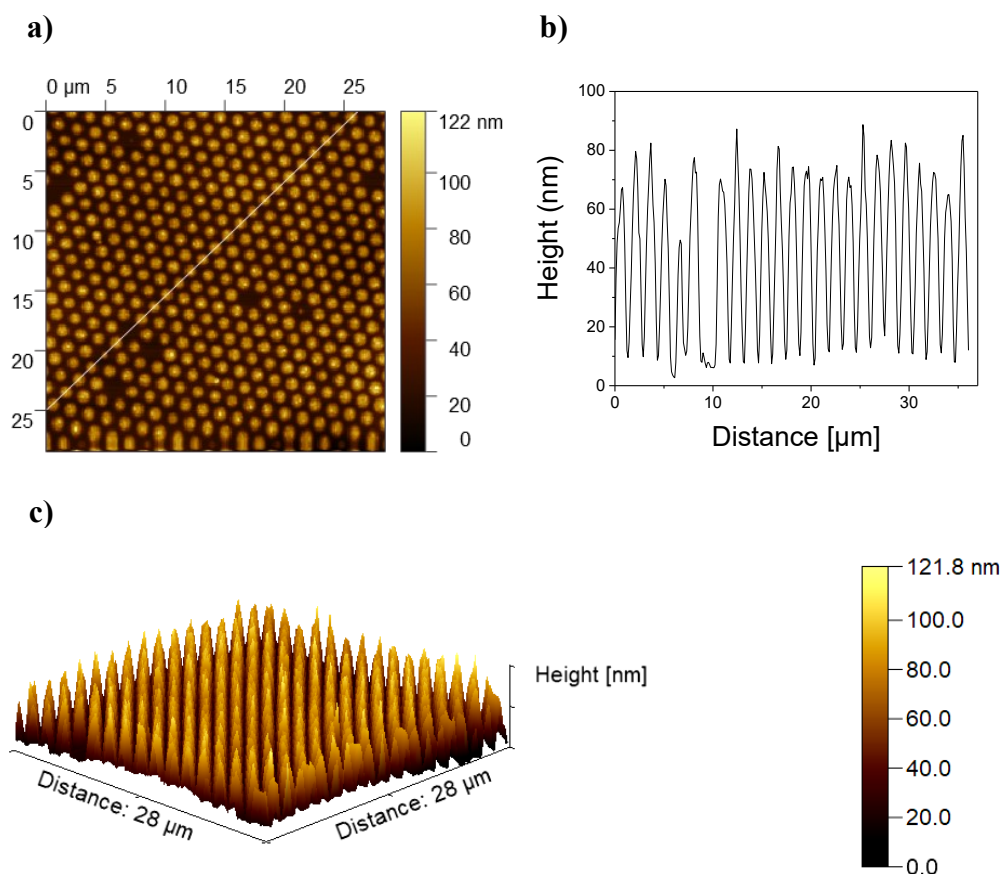
Figure 4.117 AFM image of P(VDF-TrFE) dots stamped on an aluminium (Al) coated silicon (Si) substrate at 205 °C with 6 min dwell time showing: **(a)** topographical AFM image, **(b)** topographical profile along the line in the panel (a) and **(c)** 3D AFM image.
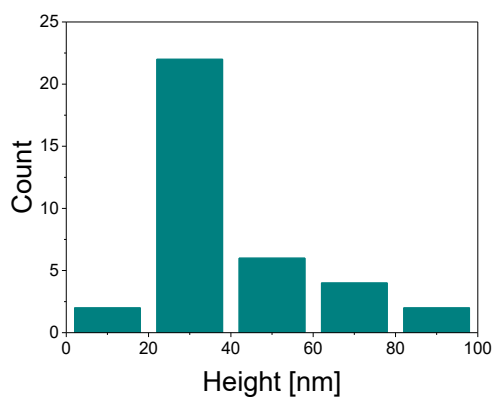

Figure 4.118 Height histogram of 391 analyzed P(VDF-TrFE) dots printed on an aluminium (Al) coated silicon (Si) substrate with 6 min dwell time. Heights were obtained from the analysis of the AFM image shown in the Figure 4.117a.

From the binarization of the SEM image (from Fig 4.119c) of the P(VDF-TrFE) dots stamped on an Al/Si substrate with 7 min dwell time an average diameter of 114 nm ± 31 nm, an average circularity of 0.79 ± 0.05 and an average aspect ratio of 1.17 ± 0.05 were obtained (Fig. 4.120)

considering 173 stamped dots. From the AFM measurement (Fig. 4.121) 640 stamped P(VDF-TrFE) dots on Al/Si after 7 min dwell time were analysed and a frequency distribution of the dot heights was obtained (Fig. 4.122). The average height of the stamped P(VDF-TrFE) dots was 49 nm ± 11 nm.
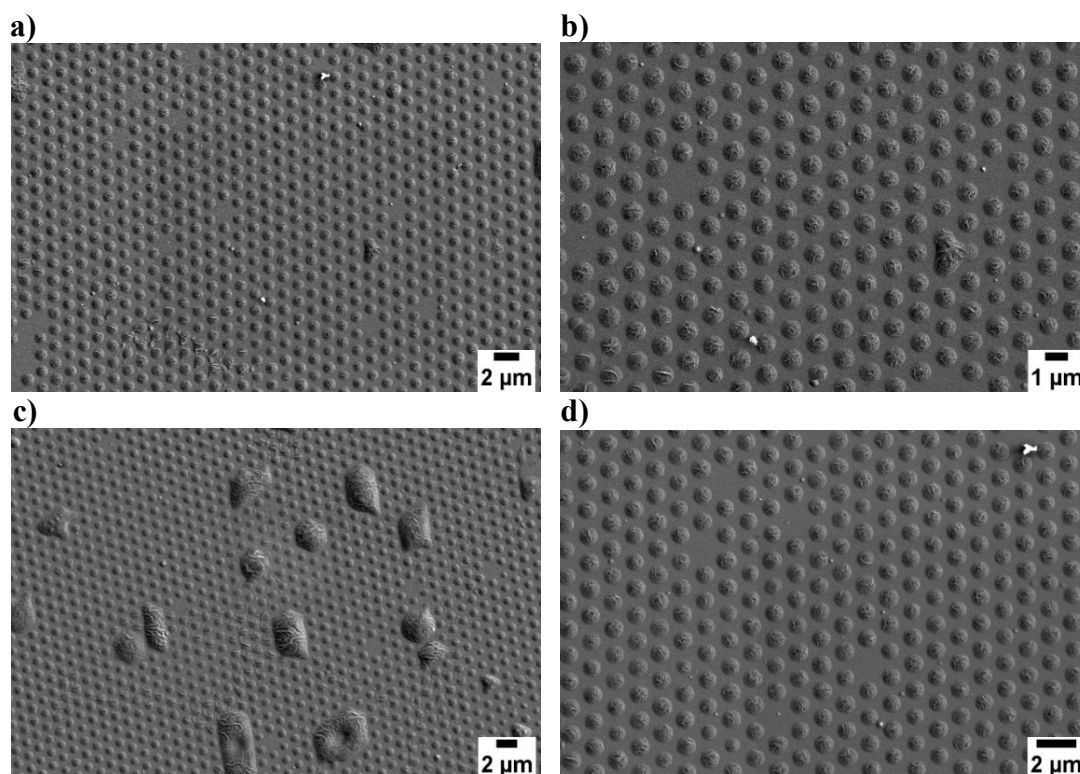
a)
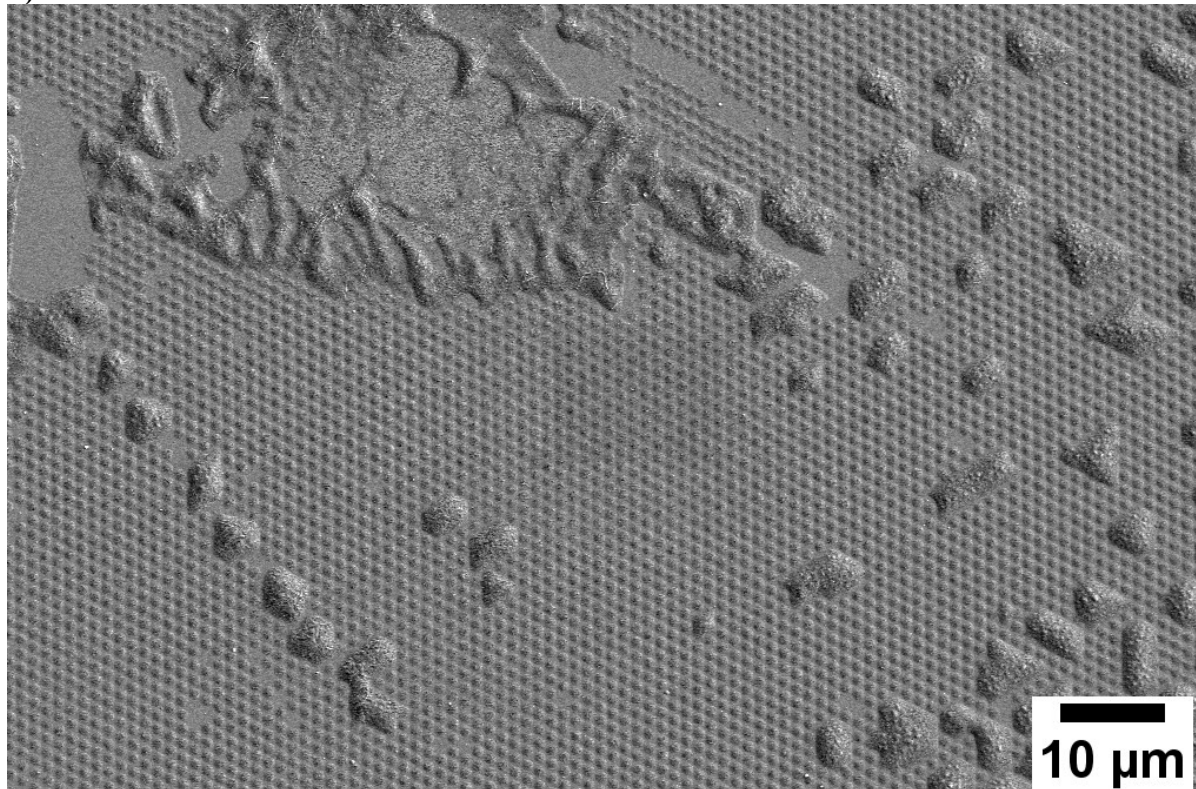
b)
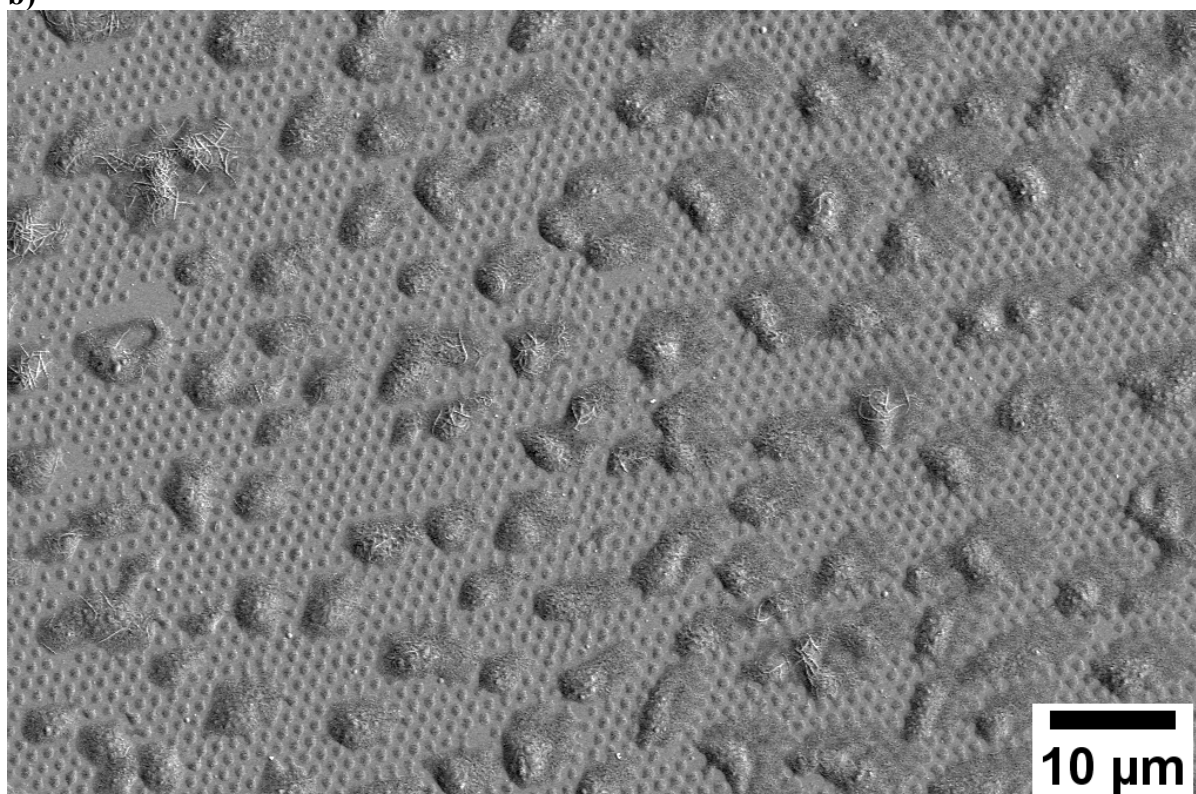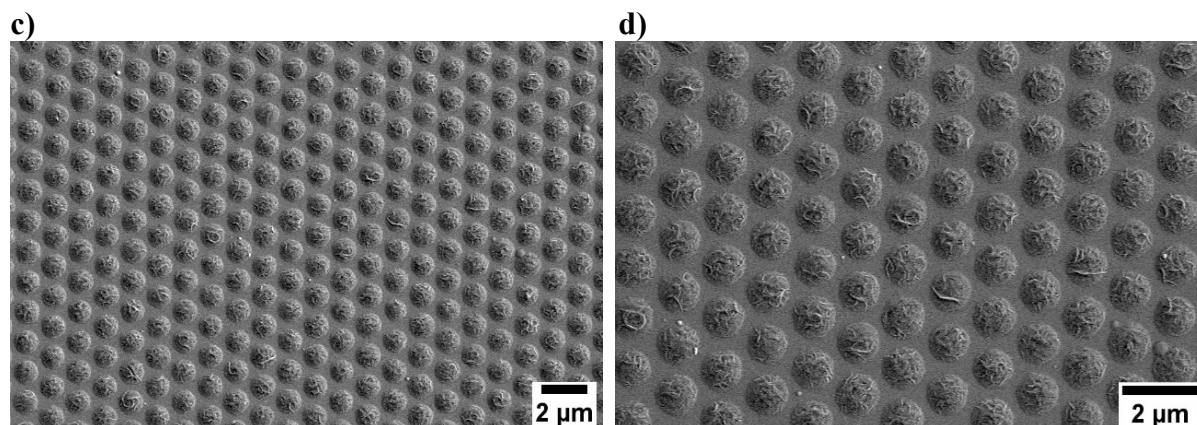
Figure 4.119 SEM images of P(VDF-TrFE) dots stamped on an aluminium (Al) coated silicon (Si) substrate with a composite np-Au stamp at 205 °C and with 7 min dwell time.
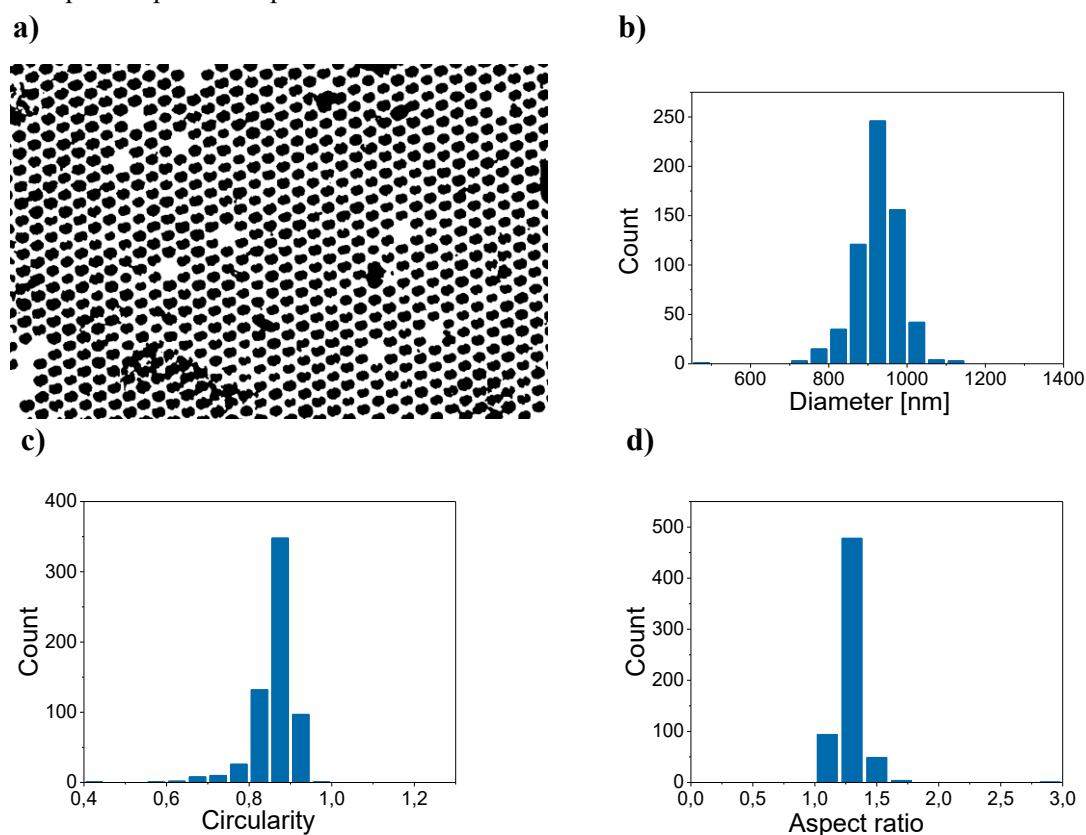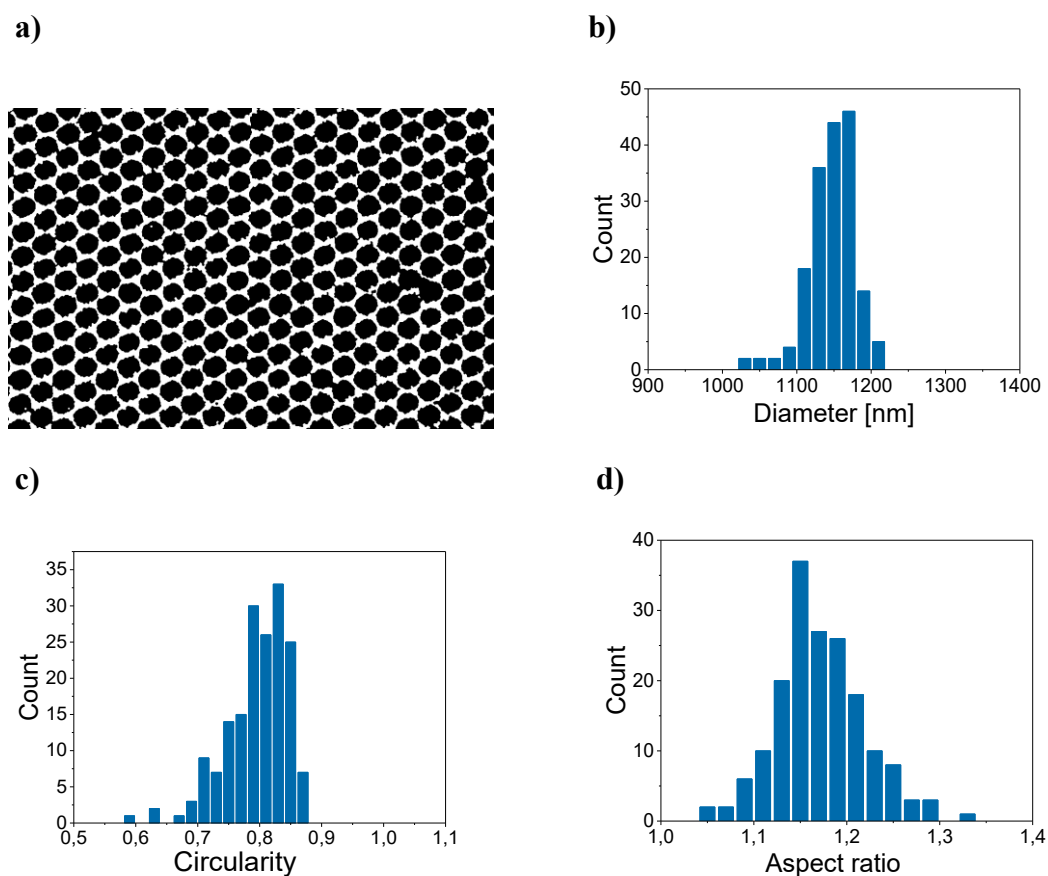

Figure 4.120 (a) Binarized SEM image (see original SEM image in Fig. 4.119c) of P(VDF-TrFE) dots stamped on an aluminium (Al) coated silicon (Si) substrate with 7 min dwell time at 205 °C (stamping method III - *with pressure*). Histograms of **(b)** diameters, **(c)** circularities, and **(d)** aspect ratios of 173 analyzed P(VDF-TrFE) dots.
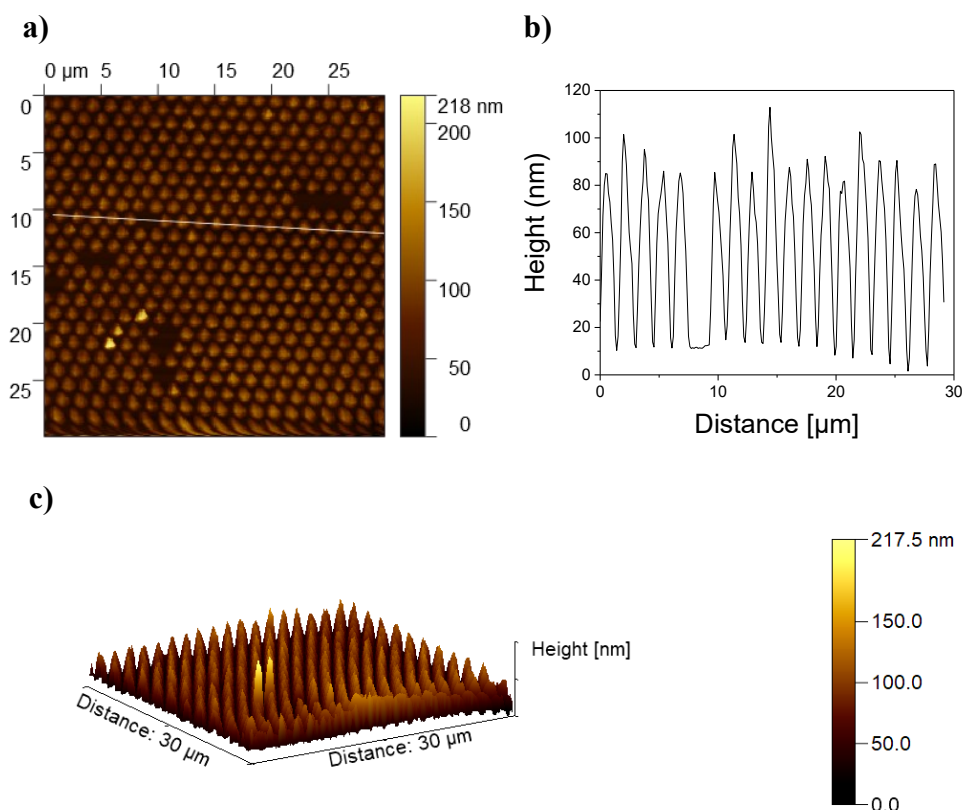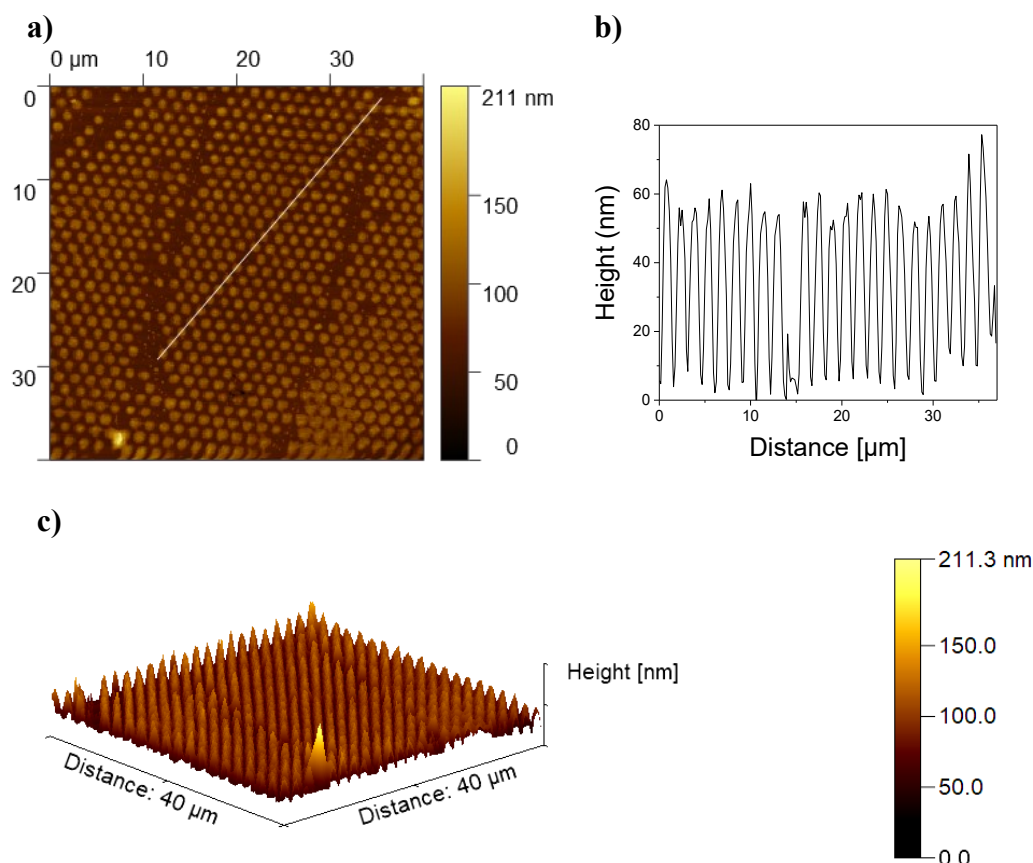
Figure 4.121 AFM image of P(VDF-TrFE) dots stamped on an aluminium (Al) coated silicon (Si) substrate at 205 °C after 7 min dwell time showing: **(a)** topographical AFM image, **(b)** topographical profile along the line in the panel (a) and **(c)** 3D AFM image.
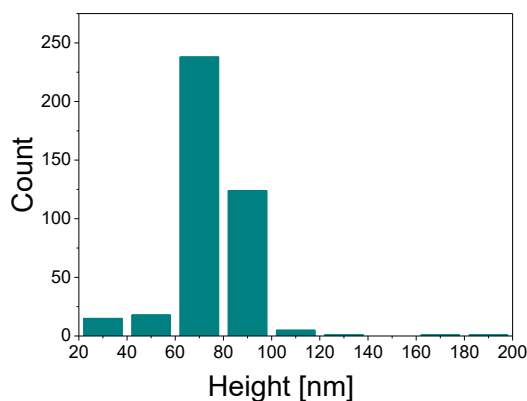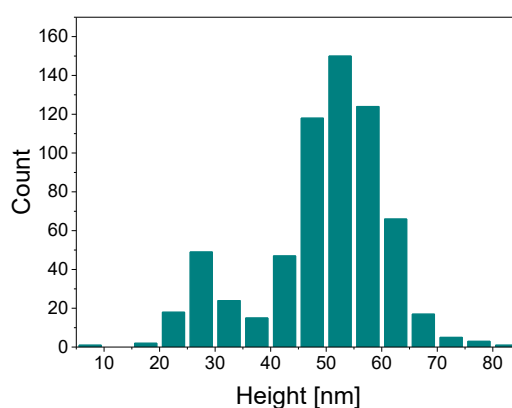

Figure 4.122 Height histogram of 640 analyzed P(VDF-TrFE) dots printed on an aluminium (Al) coated silicon (Si) substrate with 7 min dwell time. Heights were obtained from the analysis of the AFM image shown in the Figure 4.121a.

From the binarization of the SEM image (from Fig 4.123e) of P(VDF-TrFE) dots stamped on an Al/Si substrate with 10 min dwell time an average diameter of 959 nm ± 36 nm, an average circularity of 0.87 ± 0.04 and an average aspect ratio of 1.12 ± 0.04 were obtained (Fig. 4.124)

considering 158 stamped dots. From the AFM measurement (Fig. 4.125) 250 stamped P(VDF-TrFE) dots on Al/Si after 10 min dwell time were analysed and a frequency distribution of the dot heights was obtained (Fig. 4.126). The average height of the stamped P(VDF-TrFE) dots was 58 nm ± 16 nm.

a)
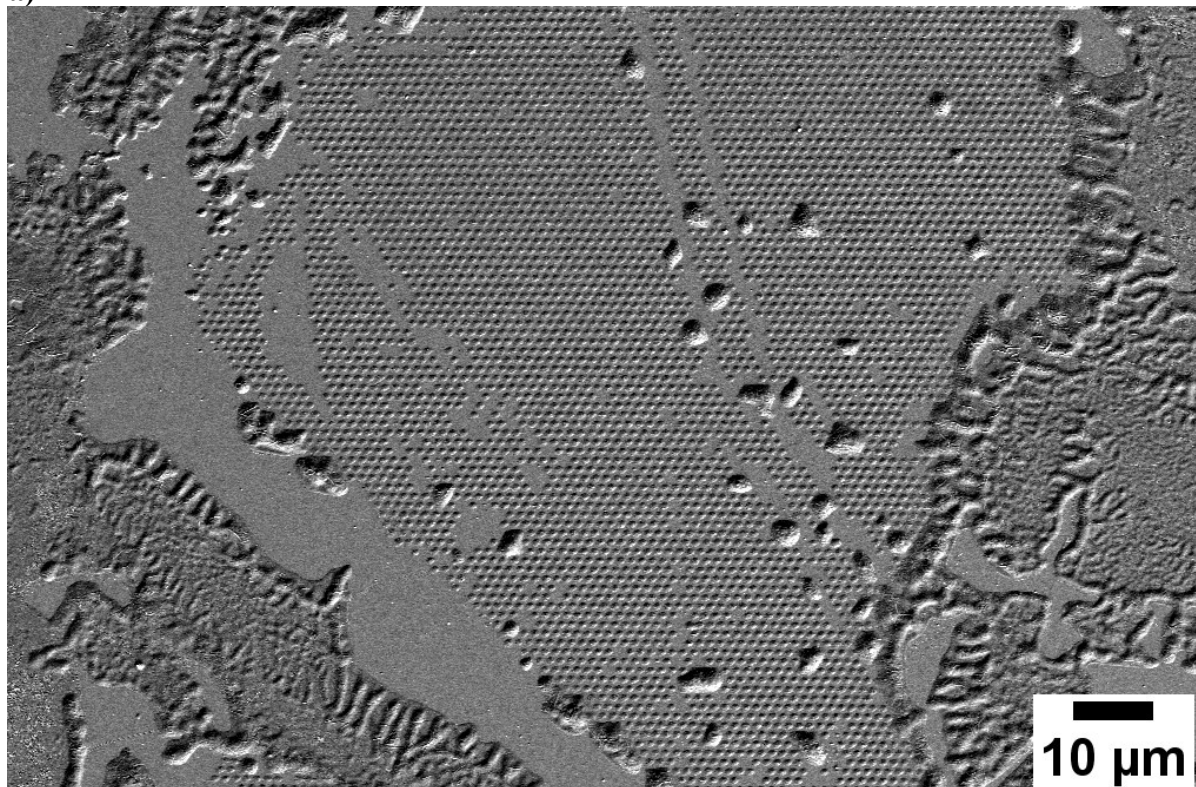
b)
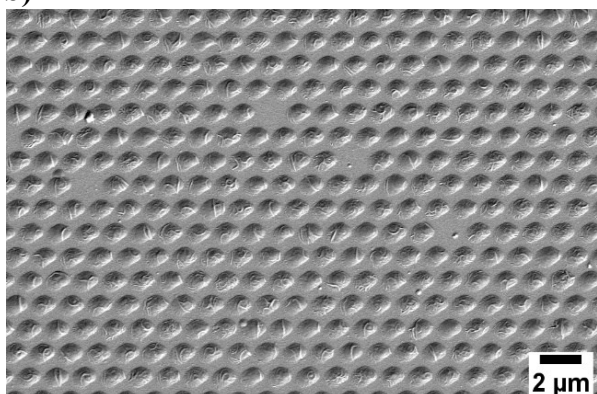
c)
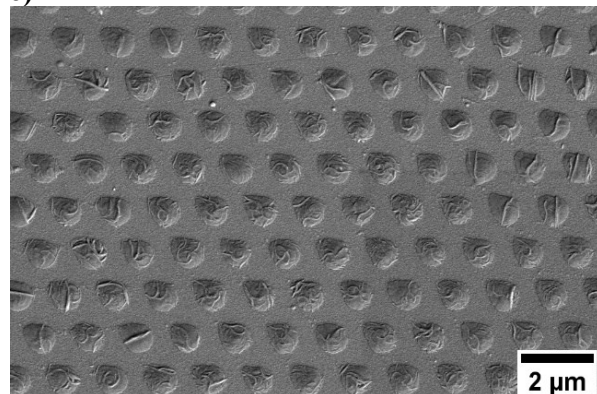
d)
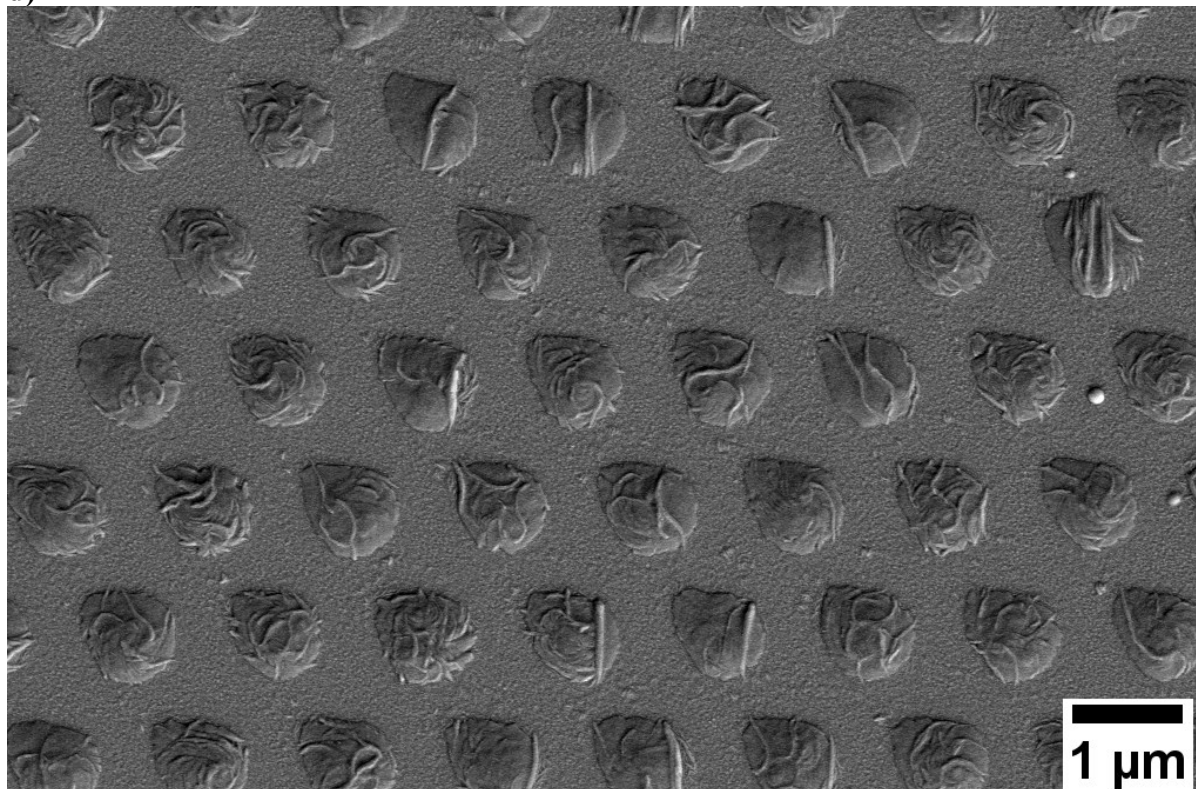
e)
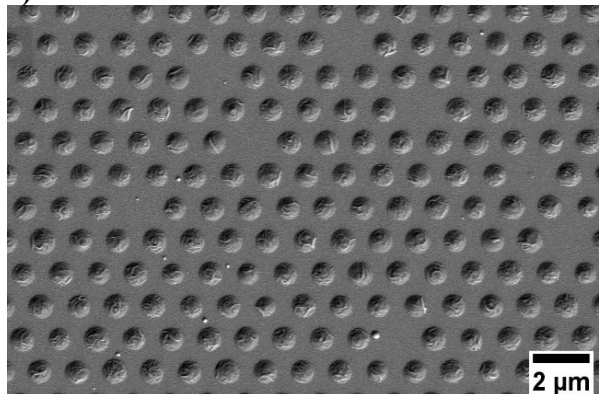
f)
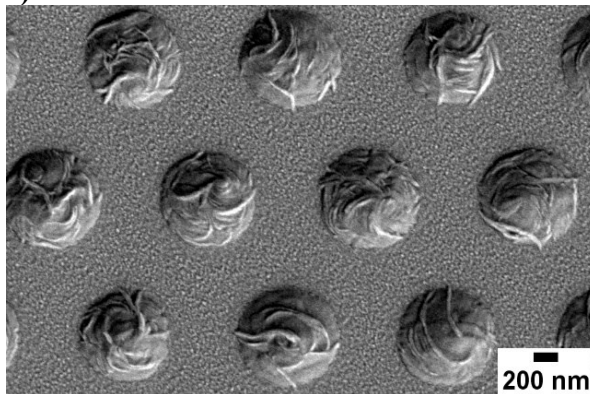
Figure 4.123 SEM images of P(VDF-TrFE) dots stamped on an aluminium (Al) coated silicon (Si) substrate with a composite np-Au stamp at 205 °C and with 10 min dwell time.

a)

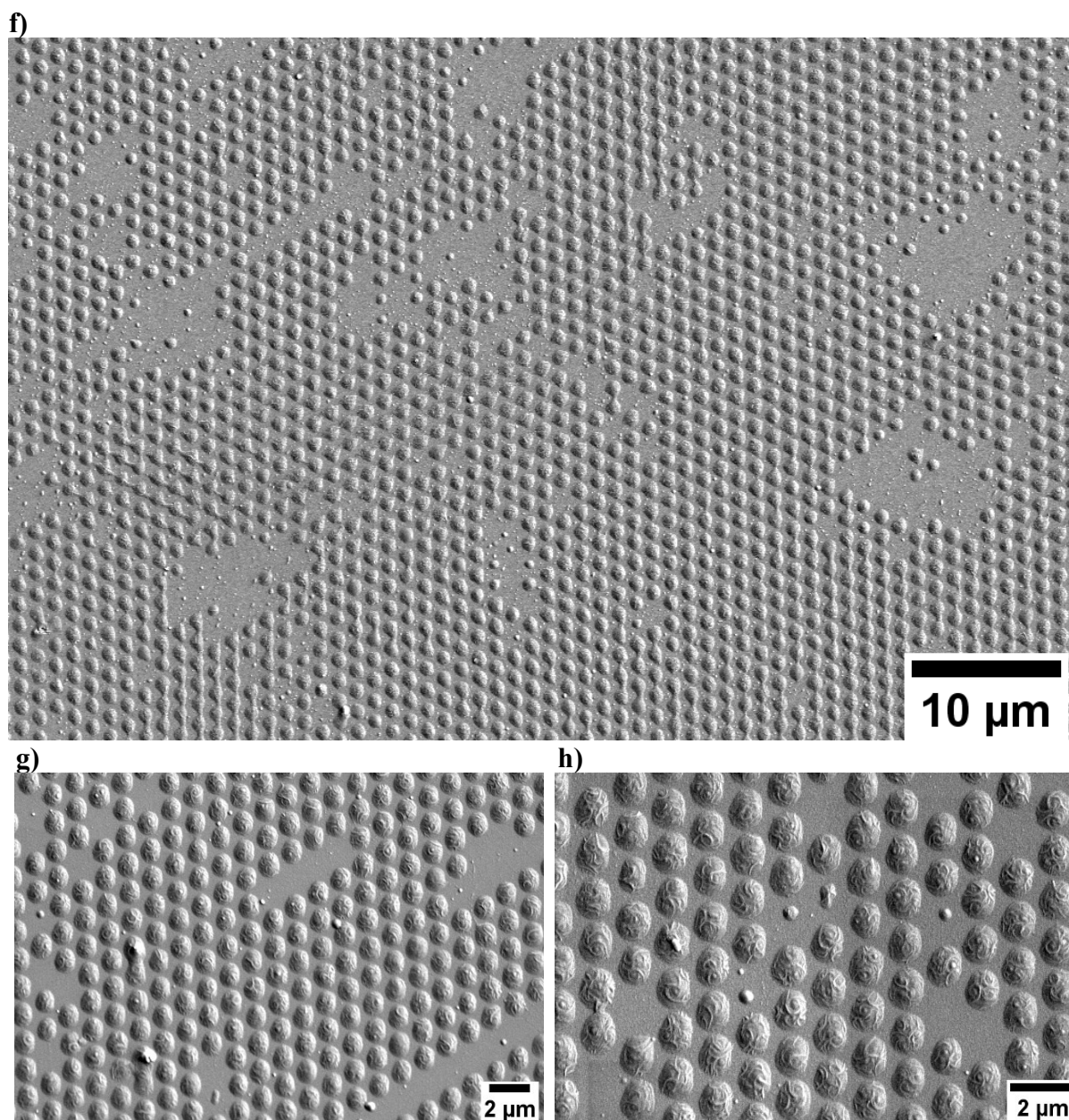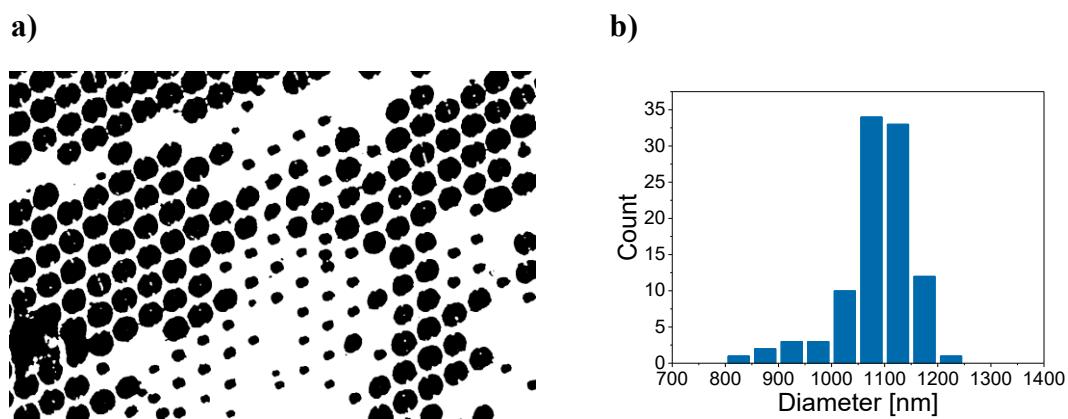**b)**

c)

d)
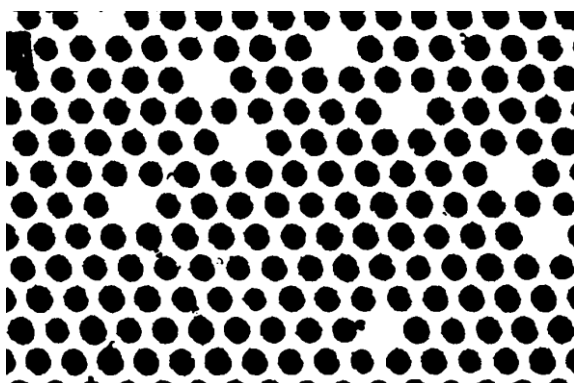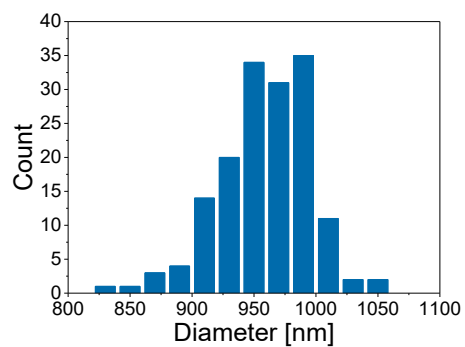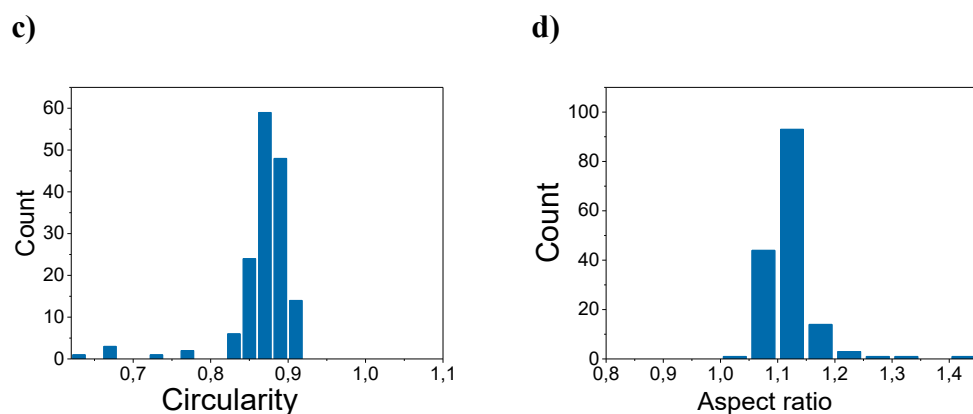
Figure 4.124 (a) Binarized SEM image (see original SEM image in Fig. 4.123e) of P(VDF-TrFE) dots stamped on an aluminium (Al) coated silicon (Si) substrate with 10 min dwell time at 205 °C (stamping method III - *with pressure*). Histograms of **(b)** diameters, **(c)** circularities, and **(d)** aspect ratios of 158 analyzed P(VDF-TrFE) dots.

a)

b)

c)
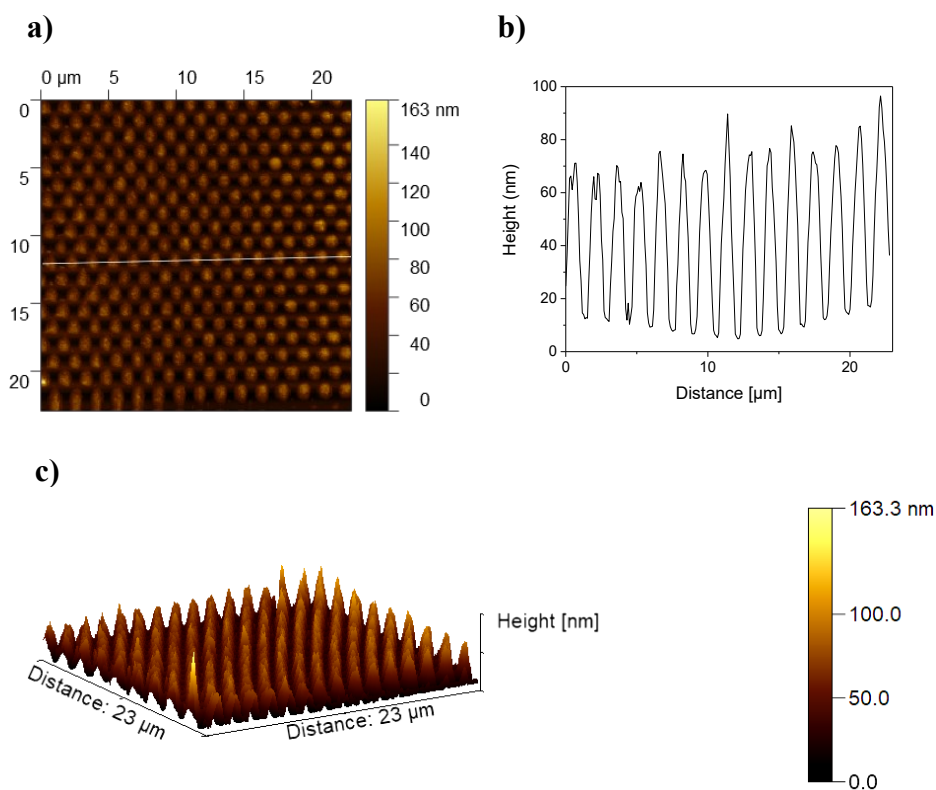
Figure 4.125 AFM image of P(VDF-TrFE) dots stamped on aluminium (Al) coated silicon (Si) substrate at 205 °C with 10 min dwell time showing: **(a)** topographical AFM image, **(b)** topographical profile along the line in the panel (a) and **(c)** 3D AFM image.
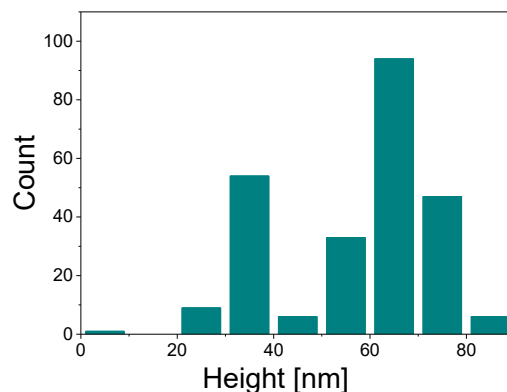
Figure 4.126 Height histogram of 250 analyzed P(VDF-TrFE) dots printed on an aluminium (Al) coated silicon (Si) substrate after 10 min dwell time. Heights were obtained from the analysis of the AFM image shown in the Figure 4.125a.

From the binarization of the SEM image (from Fig 4.127) of P(VDF-TrFE) dots stamped on an Al/Si substrate with 15 min dwell time an average diameter of 1095 nm ± 92 nm, an average circularity of 0.71 ± 0.11 and an average aspect ratio of 1.29 ± 0.42 were obtained (Fig. 4.128) considering 61 stamped dots. From the AFM measurement (Fig. 4.129) 70 stamped P(VDF-TrFE) dots on Al/Si after 15 min dwell time were analysed and a frequency distribution of the dot heights was obtained (Fig. 4.130). The average height of the stamped P(VDF-TrFE) dots was 56 nm ± 21 nm.

a)

b)

c)

d)

e)
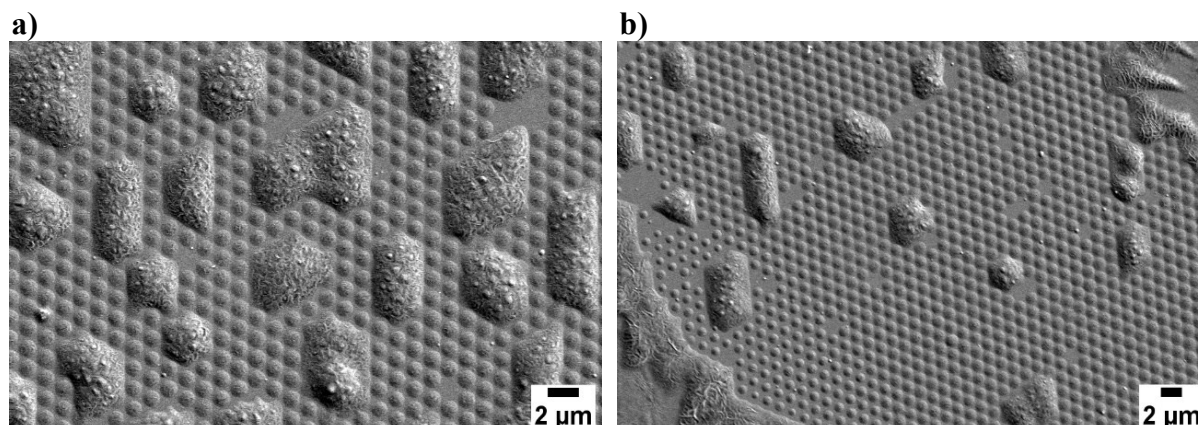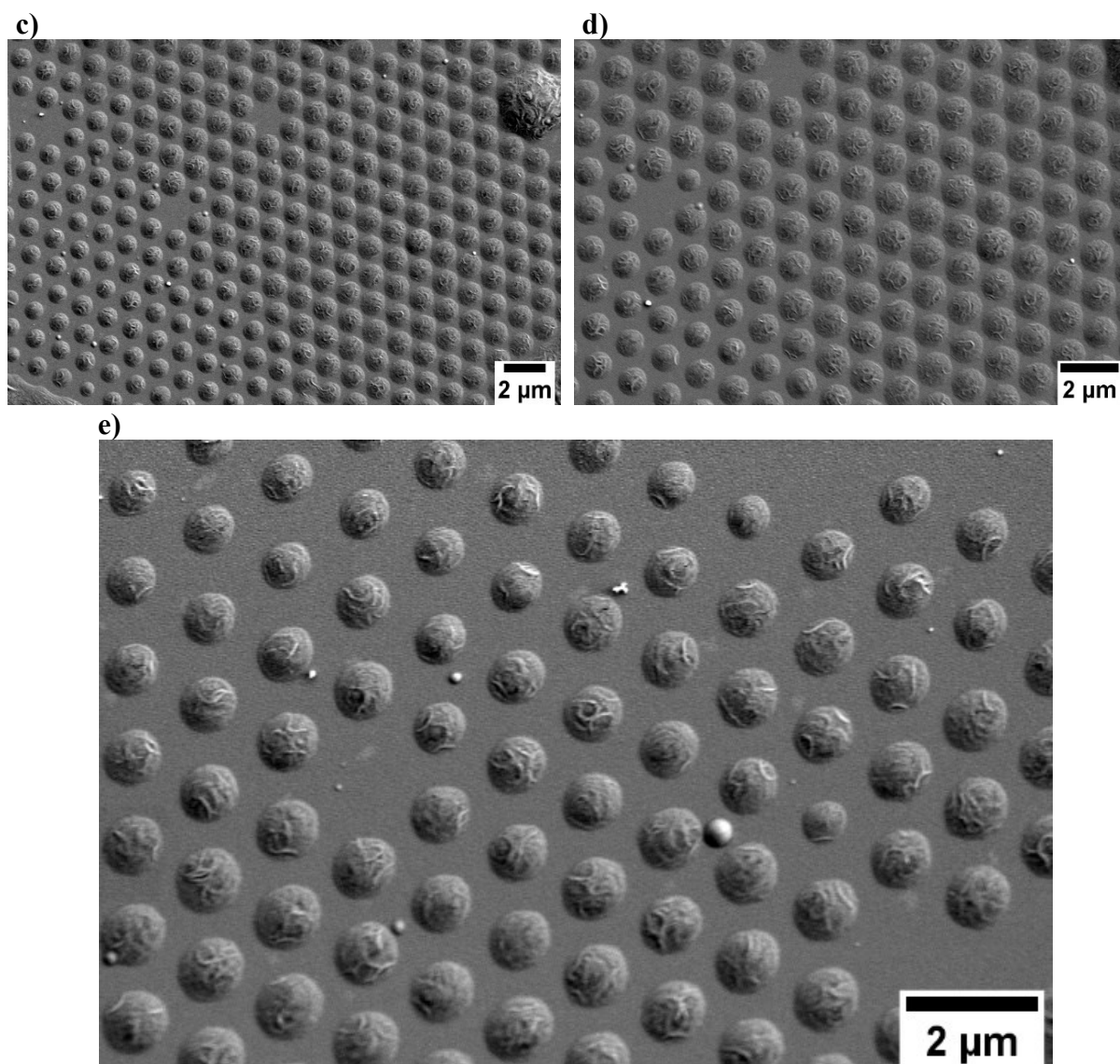
Figure 4.127 SEM images of P(VDF-TrFE) dots stamped on an aluminium (Al) coated silicon (Si) substrate with a composite np-Au stamp at 205 °C and with 15 min dwell time.
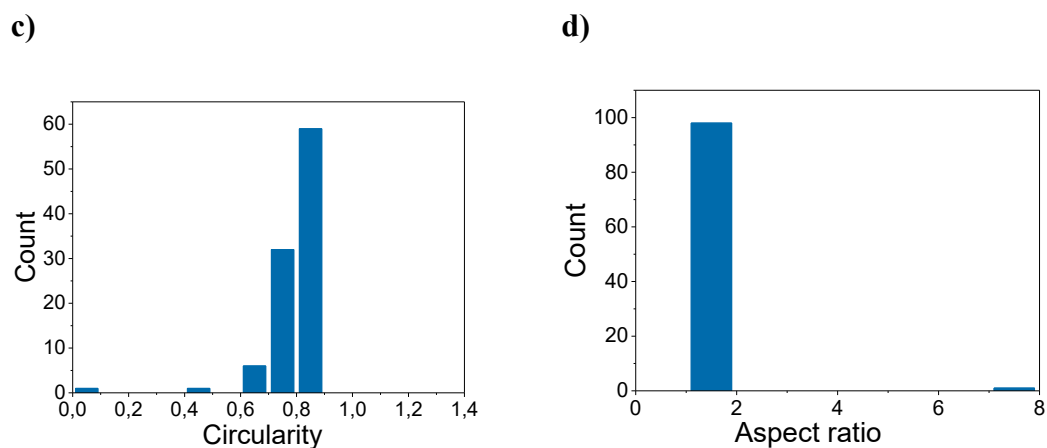
a)

b)

c)

d)
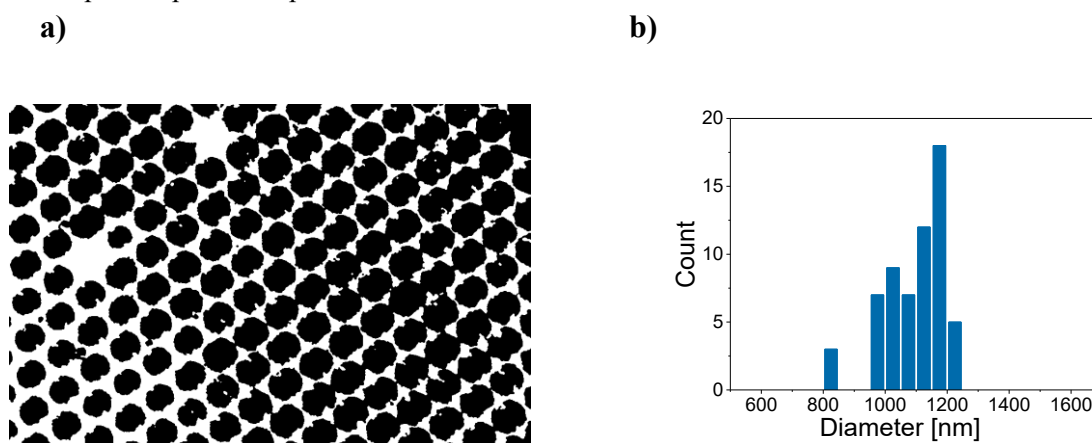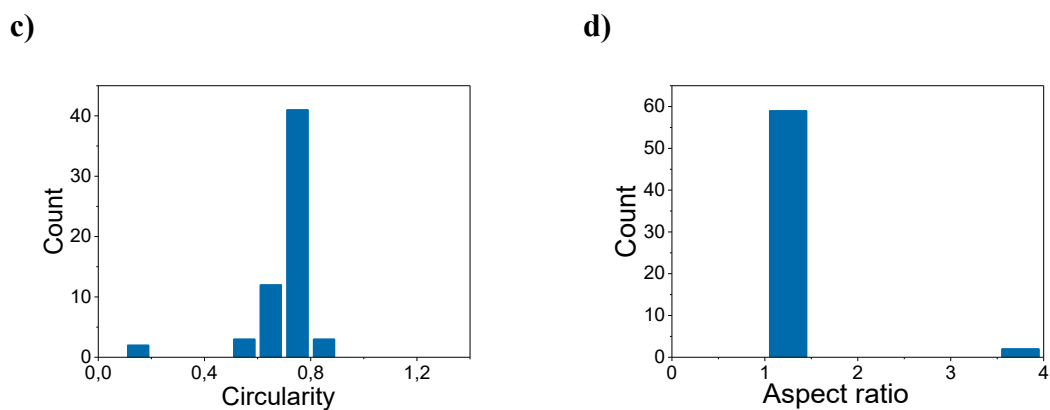
Figure 4.128 (a) Binarized SEM image (see original SEM image in Fig. 4.127d) of P(VDF-TrFE) dots stamped on an aluminium (Al) coated silicon (Si) substrate with 15 min dwell time at 205 °C (stamping method III - *with pressure*). Histograms of **(b)** diameters, **(c)** circularities, and **(d)** aspect ratios of 61 analyzed P(VDF-TrFE) dots.

a)

b)

c)
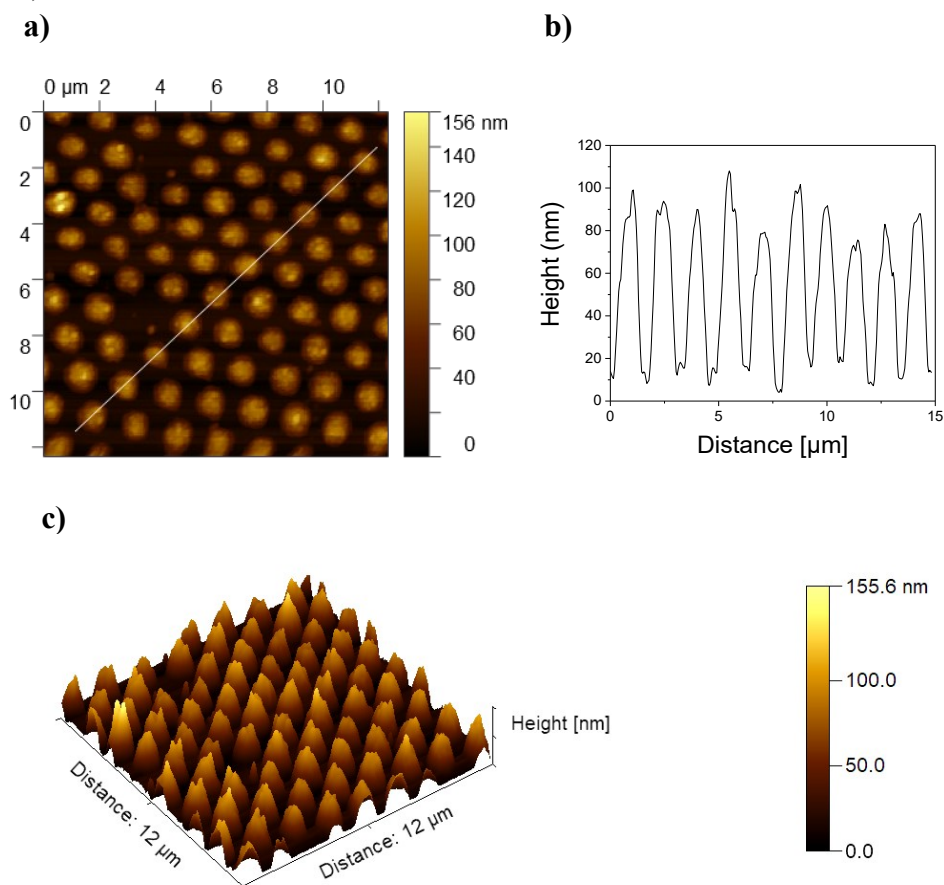
Figure 4.129 AFM image of P(VDF-TrFE) dots stamped on an aluminium (Al) coated silicon (Si) substrate at 205 °C with 15 min dwell time showing: **(a)** topographical AFM image, **(b)** topographical profile along the line in the panel (a) and **(c)** 3D AFM image.
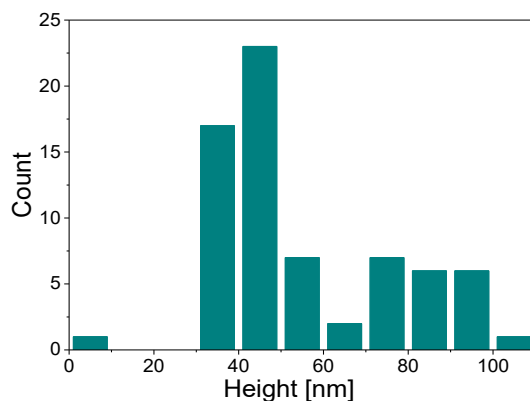
Figure 4.130 Height histogram of 70 analyzed P(VDF-TrFE) dots printed on an aluminium (Al) coated silicon (Si) substrate with 15 min dwell time. Heights were obtained from the analysis of the AFM image shown in the Figure 4.129a.

From the binarization of the SEM image (from Fig 4.131a) of the P(VDF-TrFE) dots stamped on an Al/Si substrate with 20 min dwell time an average diameter of 872 nm ± 40 nm, an average circularity of 0.93 ± 0.03 and an average aspect ratio of 1.09 ± 0.08 were obtained (Fig. 4.132) considering 877 stamped dots. From the AFM measurement (Fig. 4.133) 44 stamped P(VDF-TrFE) dots on an Al/Si after 20 min dwell time were analysed and a frequency distribution of the dot heights was obtained (Fig. 4.134). The average height of the stamped P(VDF-TrFE) dots was 71 nm ± 15 nm.

a)

b)

c)

d)

e)

f)

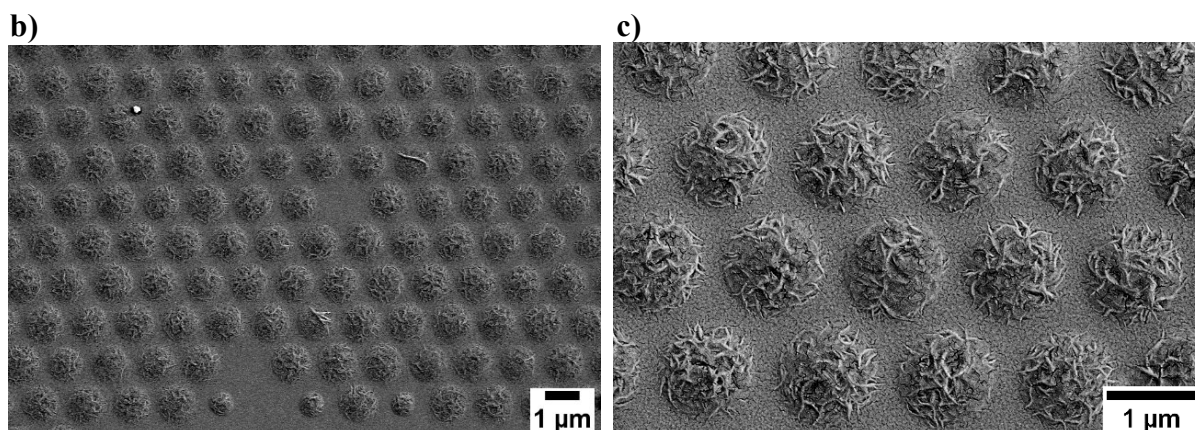
135

g) **h)**

2 µm   1 µm
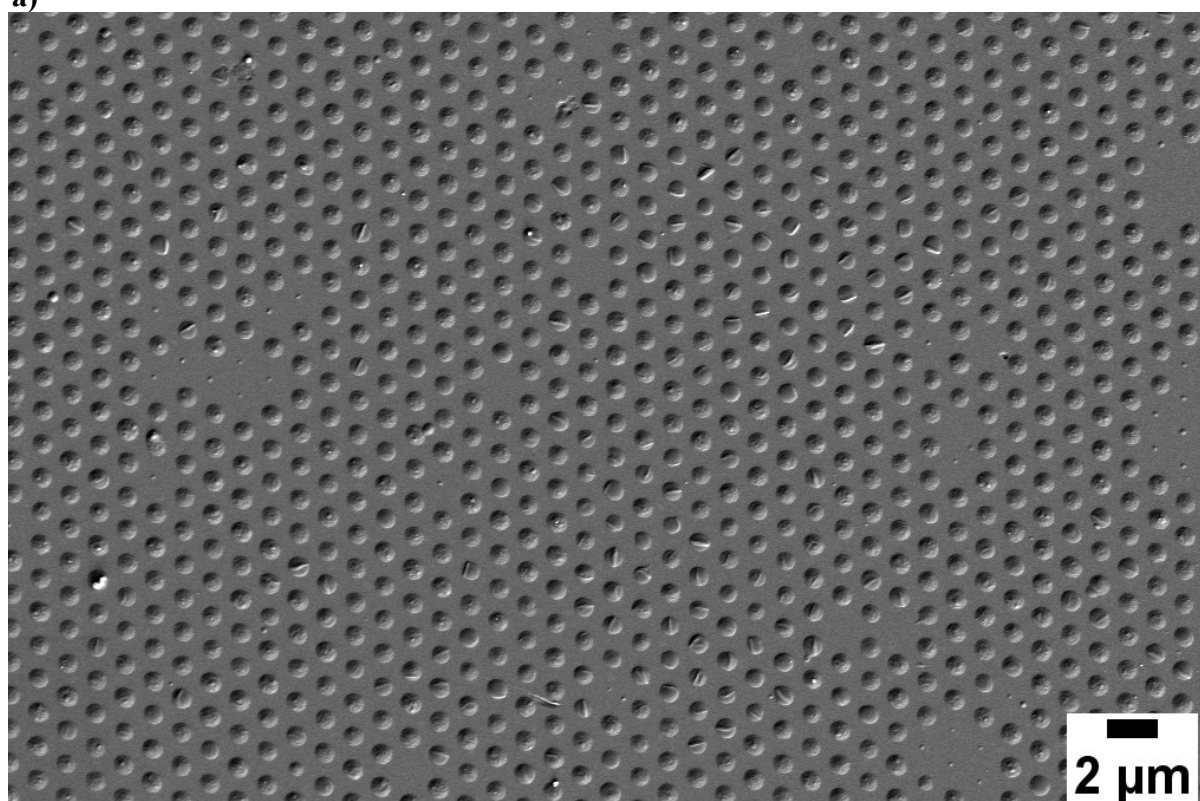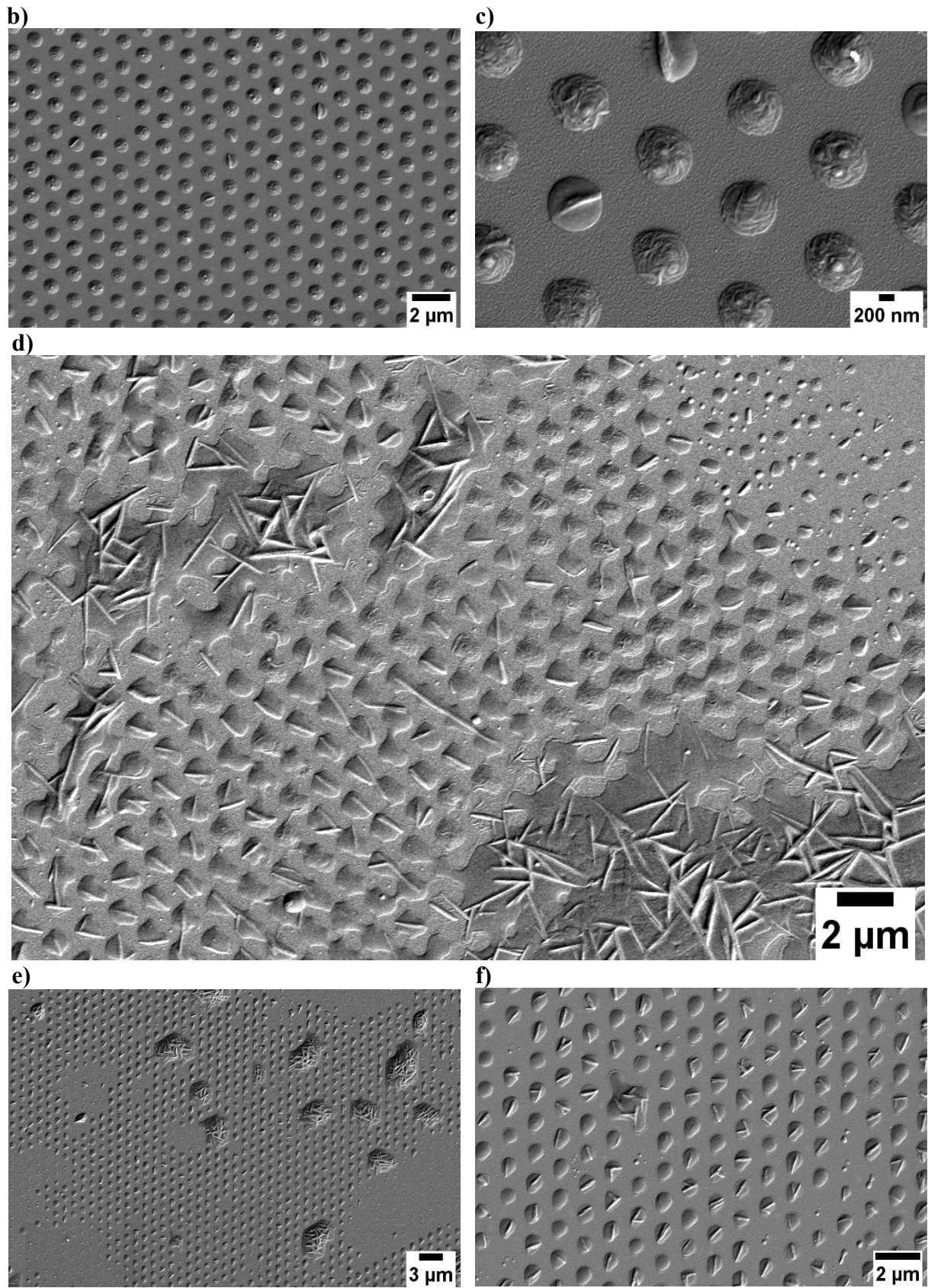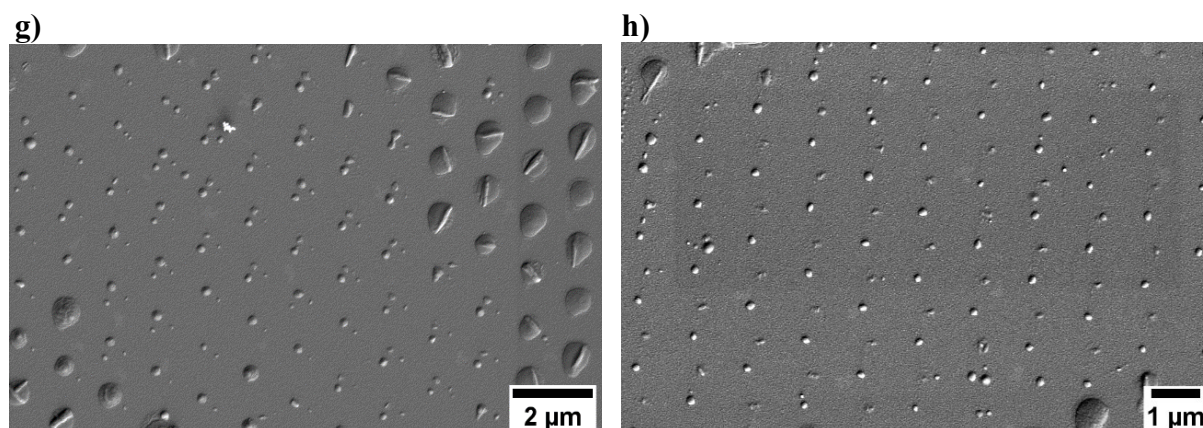
Figure 4.131 SEM images of P(VDF-TrFE) dots stamped on an aluminium (Al) coated silicon (Si) substrate with a composite np-Au stamp at 205 °C and with 20 min dwell time.
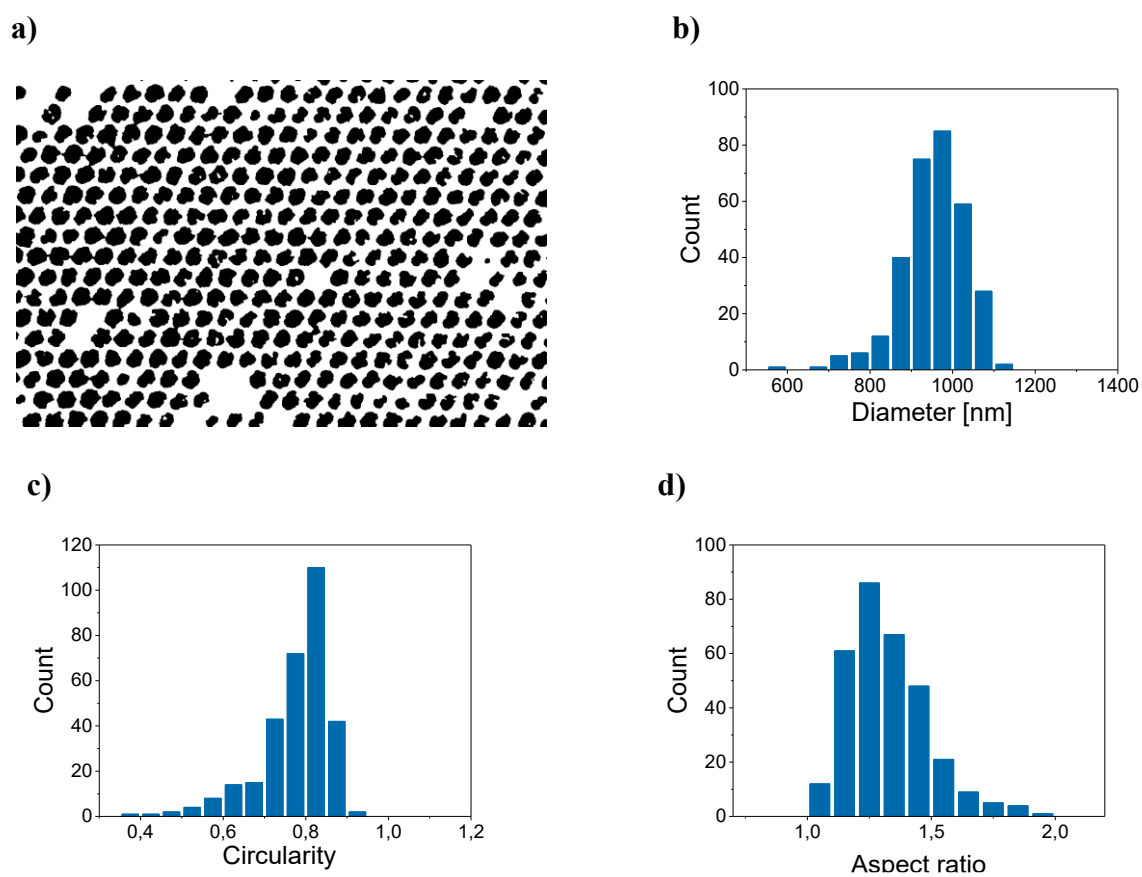

a) **b)**

c) **d)**
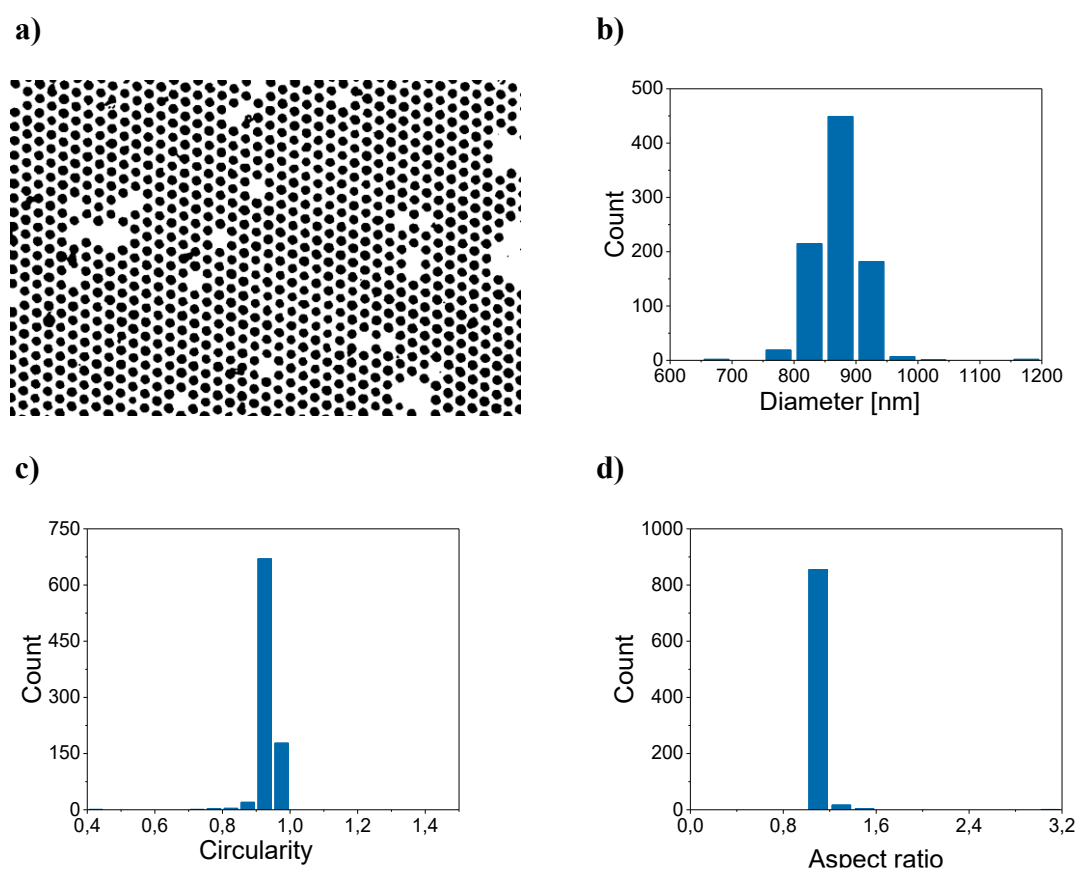
Figure 4.132 (a) Binarized SEM image (see original SEM image in Fig. 4.131a) of P(VDF-TrFE) dots stamped on an aluminium (Al) coated silicon (Si) substrate with 20 min dwell time at 205 °C (stamping method III - *with pressure*). Histograms of **(b)** diameters, **(c)** circularities, and **(d)** aspect ratios of 877 analyzed P(VDF-TrFE) dots.

a)

b)

c)
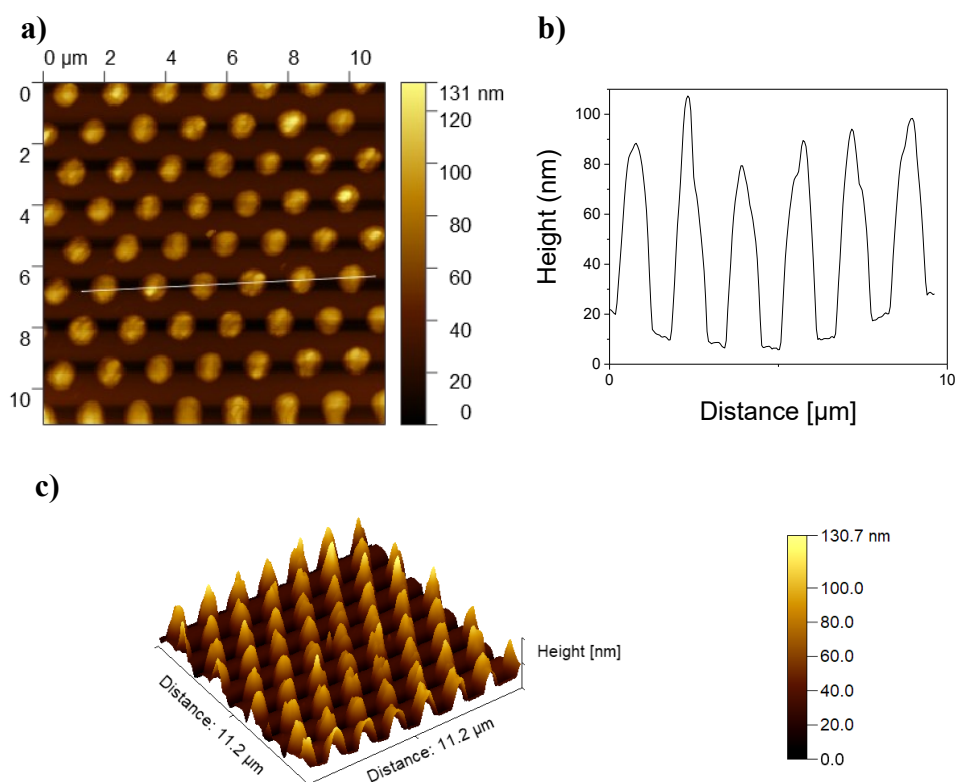
Figure 4.133 AFM image of P(VDF-TrFE) dots stamped on an aluminium (Al) coated silicon (Si) substrate at 205 °C with 20 min dwell time showing: **(a)** topographical AFM image, **(b)** topographical profile along the line in the panel (a) and **(c)** 3D AFM image.
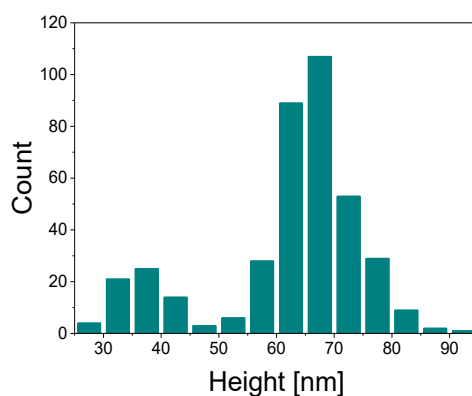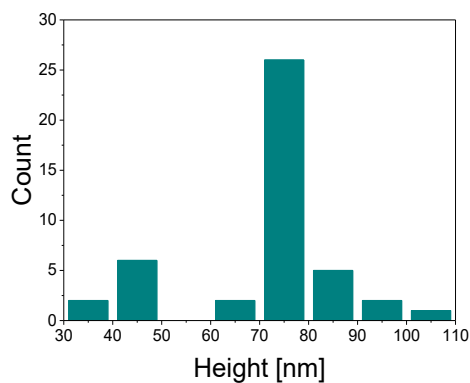

Figure 4.134 Height histogram of 44 analyzed P(VDF-TrFE) dots printed on an aluminium (Al) coated silicon (Si) substrate with 20 min dwell time. Heights were obtained from the analysis of the AFM image shown in the Figure 4.133a.
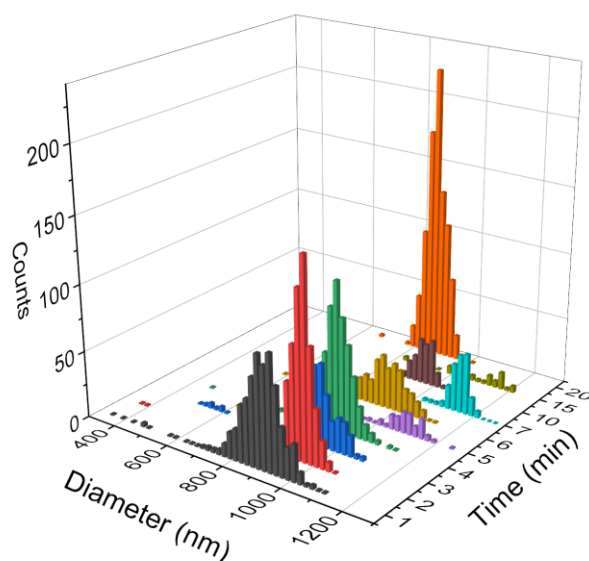
Figure 4.135 Summary histogram with diameter values of P(VDF-TrFE) dots stamped on aluminium coated Si with 1 min (black), 2 min (red), 3 min (blue), 4 min (green), 5 min (purple), 6 min (yellow), 7 min (turquoise), 10 min (brown), 15 min (navy green) and 20 min (orange) stamping time.
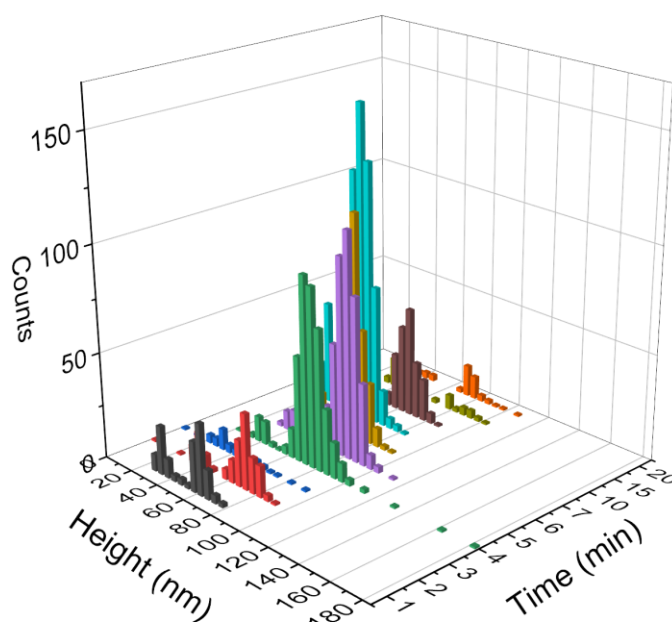
Figure 4.136 Summary histogram with height values of P(VDF-TrFE) dots stamped on aluminium coated Si after 1 min (black), 2 min (red), 3 min (blue), 4 min (green), 5 min (purple), 6 min (yellow), 7 min (turquoise), 10 min (brown), 15 min (navy green) and 20 min (orange) stamping time.

Distribution of the dot diameters for different stamping times are presented in Figure 4.135. In Table 4.6 aritmethic average values of diameters, circularities and aspect ratios are summerized. Average diameters are in the range from 872 nm to 1147 nm. Average dot circularities are in the range from 0.7 to 0.9 and average aspect ratios in the range from 1.2 to 1.3. There is no

apparent correlation between the stamping time and the size of the printed P(VDF-TrFE) dots. The shape of the printed dots remains uniform after multiple stamping cycles and after different stamping times.

Although no direct correlation between the diameter and the height of the printed dots and the stamping time exists, it was shown that with composite np-Au stamps stamping of polymer dots in the different sizes is possible. For this, further reaserch is necessary to determine which of the stamping parameters influence the deposition of the ink. This would enabled the deposition of various desired volumes of the ink on the substrates with composite np-Au stamp by controling the stamping parameters.

Table 4.6.

Stamping time [min]	Average diameter [nm]	Average circularity	Average aspect ratio
1	894 ± 83	0.85 ± 0.07	1.19 ± 0.13
2	957 ± 49	0.83 ± 0.07	1.26 ± 0.08
3	940 ± 93	0.86 ± 0.05	1.25 ± 0.07
4	925 ± 60	0.86 ± 0.05	1.28 ± 0.11
5	1085 ± 71	0.79 ± 0.10	1.29 ± 0.68
6	954 ± 78	0.77 ± 0.08	1.32 ± 0.16
7	1147 ± 31	0.79 ± 0.05	1.17 ± 0.05
10	959 ± 36	0.87 ± 0.04	1.12 ± 0.04
15	1095 ± 92	0.71 ± 0.11	1.29 ± 0.42
20	872 ± 40	0.93 ± 0.03	1.09 ± 0.08

Table 4.7.

Stamping time [min]	Average height [nm]
1	52 ± 14
2	64 ± 17
3	39 ± 19
4	75 ± 15
5	77 ± 13
6	62 ± 13
7	49 ± 11
10	58 ± 16
15	56 ± 21
20	71 ± 15

4.4   Local ferroelectric switching of printed P(VDF-TrFE) dots

The ferroelectric properties of printed P(VDF-TrFE) dots on aluminium coated Si substrate after 20 min dwell time with the composite np-Au stamp (stamping method III - *with pressure)* was investigated with PFM as described in Chapter 3.4.2. Preparation of the Al/Si substrate and the stamping process of P(VDF-TrFE) on the Al/Si substrate are described in detail in the experimental chapters 3.3.1 and 3.3.5, respectively.

The topography image, Figure. 4.137a, shows seven printed P(VDF-TrFE) dots in the hexagonal arrangement that corresponds to the pattern of the stamp and with diameters of 100-200 nm. Local polarization switching was performed by applying rectangular voltage pulses of ±15 V and pulse width of 300 ms after locating the Pt/Ir coated AFM tip on top of the dots. All dots show ferroelectric switching as indicated in characteristic 180 deg (dark/bright or vice versa) phase shifts in the PFM phase image (Fig. 4.137b,c). To rule imaging artifacts out, positive, and negative polarizations were performed within one group of dots (Fig. 4.138b,c) and imaged simultaneously, showing the same phase contrast as in Figure 4.137b,c. Ferroelectric domains cover the entire dot for dots as small ~ 100 nm the and the polarization contrast is fully reversed. While single pulse poling at voltages significantly higher than the coercive voltage prove ferroelectric switching, they do not provide further insight in the switching process itself, e.g the coercive voltage (field strength). Therefore, we recorded series of local PFM hysteresis loops for four P(VDF-TrFE) dots of the ensemble by applying voltage pulse trains (pulse width Δt =300 ms) with triangular shaped envelopes, starting with a -15 V swept to +15 V and returning to -15 V.

(a)   (b)   (c)
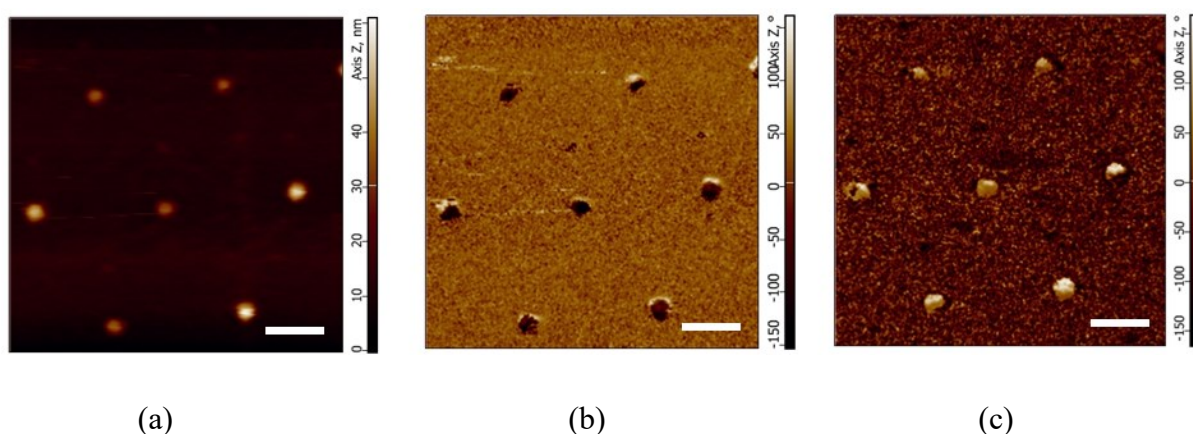
Figure 4.137 For all images A-C: image size 3 μm x 3 μm; scale bar 500 nm. **(a)** Topography image of P(VDF-TrFE) copolymer dots with the diameter of 100-200 nm before applying the voltage. **(b)** PFM topography OOP phase image of the same area after applying -15 V for 300 ms at all seven P(VDF-TrFE) dots with AFM tip as electrode and Al/Si substrate as a bottom electrode. **(c)** PFM topography OOP phase

image of the same area after applying +15 V for 300 ms at all seven P(VDF-TrFE) dots with AFM tip as electrode and Al/Si substrate as a bottom electrode.

(a)   (b)   (c)
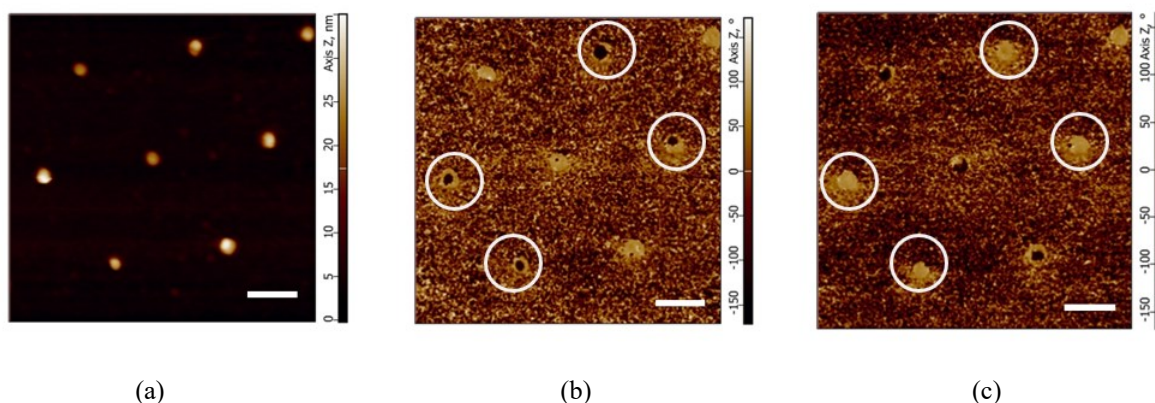
Figure 4.138 For all images a-c: image size 3 μm x 3 μm; scale bar 500 nm. **(a)** Topography image of P(VDF-TrFE) copolymer dots with the diameter of 100-200 nm before applying the voltage. **(b)** PFM topography OOP phase image of the same area after applying -15V for 300 ms at four P(VDF-TrFE) dots (marked dark dots) with AFM tip as electrode and Al/Si substrate as a bottom electrode. **(c)** PFM topography OOP phase image of the same area after applying +15V for 300 ms at four P(VDF-TrFE) dots (marked bright dots) with AFM tip as electrode and Al/Si substrate as a bottom electrode.

All four dots show hysteresis loops, characteristic for ferroelectric behavior (Fig. 4.139). However, they vary in coercive voltages $\pm V_c^+$ and shape. While for dot 1, $\pm V_c^+ \approx \pm 9V$, is almost symmetric, we also observe asymmetry in with $V_c \approx -7V, +5V$ and $V_c \approx -7.5V, +6V$ in dot 2 and 3, respectively. In dot 4 the asymmetry is vice versa with $V_c \approx -8V, +10V$. Furthermore, the switching behavior, is characterized for all four dots with an asymmetry in the piezoresponse magnitude, which is always lower for positive switching voltages than for the negative half cycles. We further observe rather slow switching indicated by less steeper slopes, making all four characteristic "butterfly loops" in the PFM magnitude signal broader.

(a)

(b)

(c)

(d)

(e)
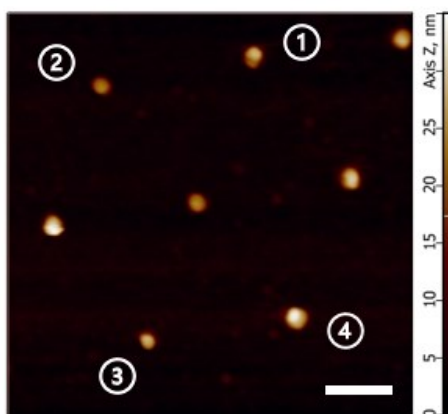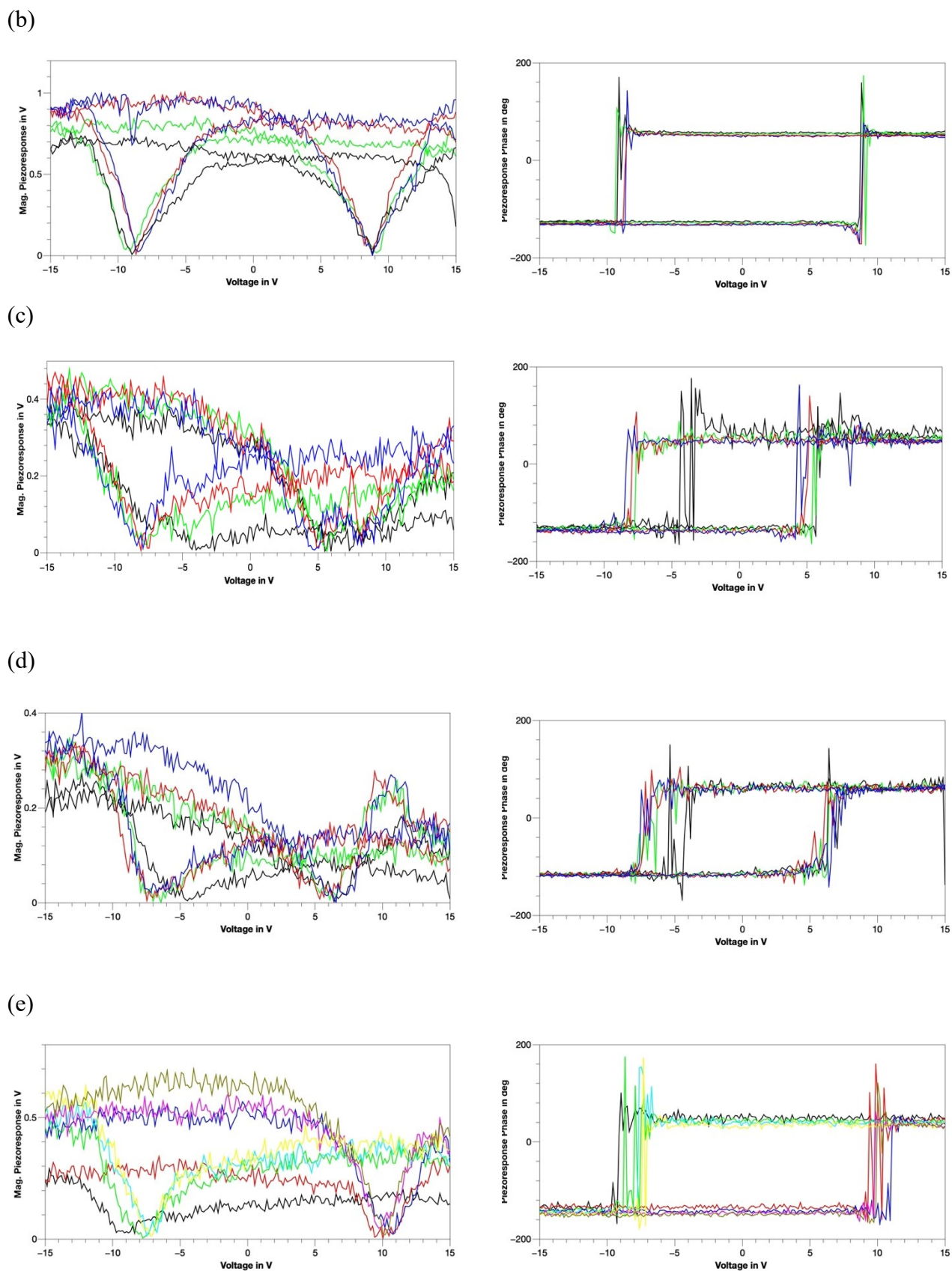
Figure 4.139 (a) Topography image of P(VDF-TrFE) dots with marked positions of the four investigated dots (image size 3 µm x 3 µm; scale bar 500 nm). **(b)** Dot 1, **(c)** dot 2, **(d)** dot 3 **(e)** dot 4 pulse OOP-PFM hysteresis loops for magnitude (left) phase (right) showing the 1st (black), 2nd (green), 3rd (red), 4th cycle (blue).

Poling of the larger P(VDF-TrFE) dots with diameters of ~ 400 nm shows similar behavior as smaller dots (Fig. 4.140). After applying +15 V for 300 ms the poled regions are visible in the PFM phase image as the dark domains (Fig. 4.140b) and reversal of the polarization state with -15 V for 300 ms as bright regions (Fig. 4.140c). Intriguingly, despite the same pulse length, we observe significant larger dark domains than bright domains in both dots.
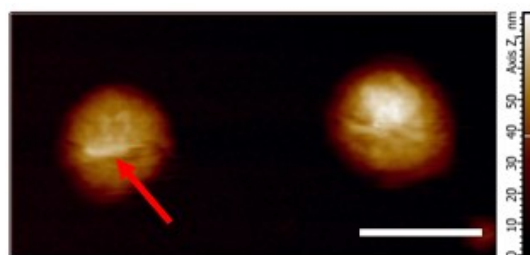
(a)
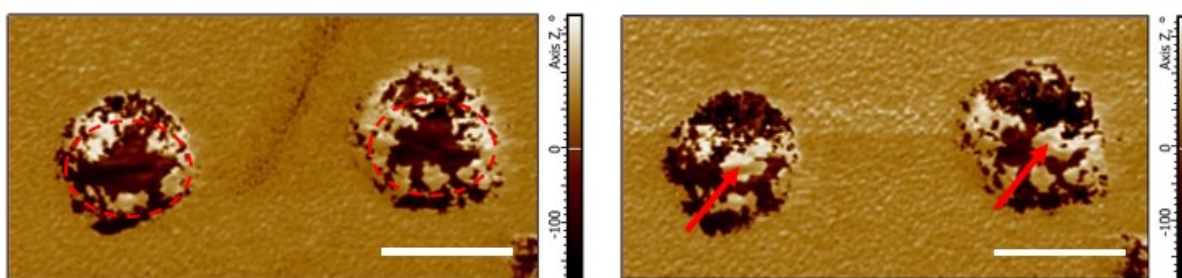
(b)   (c)

Figure 4.140 For all images a-c: image size 2 µm x 1 µm; scale bar: 500 nm. **(a)** Topography image of P(VDF-TrFE) copolymer dots with the diameter of ~ 400 nm of the investigated area. **(b)** OOP-PFM phase image of the same area after applying -15 V for 300 ms showing prepoled areas (dashed circles – dark domains). **(c)** OOP-PFM phase image of the same area after applying +15 V for 300 ms showing polarization reversal (red –rrows - bright domains).

PFM loop measurement of larger P(VDF-TrFE) dots with diameter of ~ 400 nm is shown in the Figure 1.141 where obtained hysteresis loops indicate high crystallinity in investigated dot.
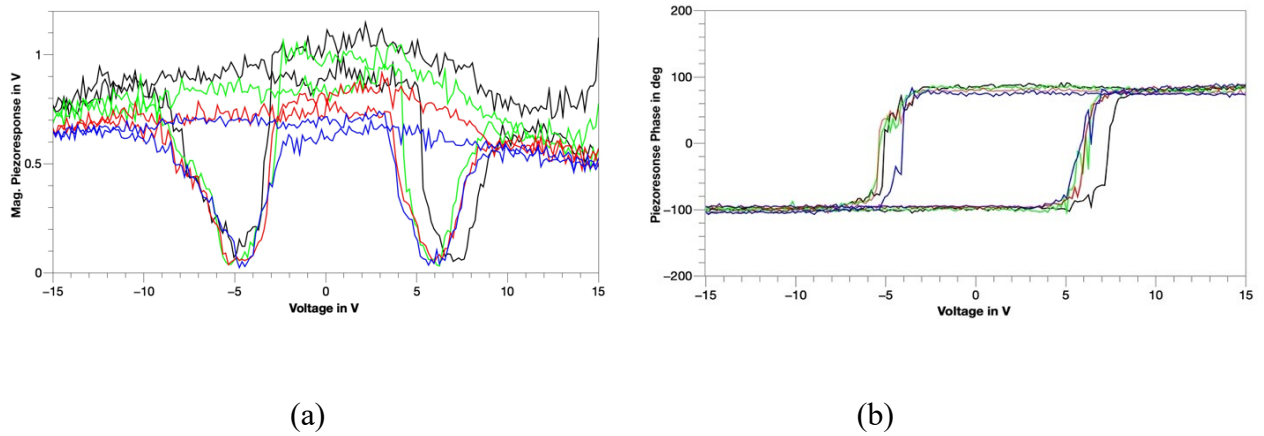
Figure 4.141 **(a)** Magnitude and **(b)** phase OOP-PFM hysteresis loops showing 1st (black), 2nd (green), 3rd (red), and 4th cycle (blue) (Analyzed P(VDF-TrFE) dot with a location of measurement (red arrow) is shown in Fig. 4.140a).

In contrast to the much smaller dots, here we observe almost symmetric switching in the PFM magnitude "butterfly". The coercive voltage is slightly asymmetric as for small dots with $V_c \approx -5V, +6V$. Furthermore, slopes are steeper in PFM magnitude, indicating faster switching.

5 Discussion

5.1 Composite nanoporous gold stamp

In this work, composite nanoporous gold stamp (np-Au) for capillary printing of polymer melts has been developed. The stamp consists of topographically patterned porous gold film with a thickness of ~ 2.7 µm and a layer of polymer film that serves as a support for the np-Au stamp as well as an ink reservoir. The surface of the nanoporous gold film has been patterned with arrays of hexagonally ordered contact elements with a pitch distance of ~ 1.5 µm. Continuous pore system of the stamp with pore sizes from ~ 40 nm to ~ 80 nm ensures that molten polymer flows to the tips of the contact elements during stamping which enables stamping in consecutive cycles. Stamps with two different polymer film inks were developed: (1) composite np-Au-PS stamps and (2) composite np-Au-P(VDF-TrFE) stamps.

5.1.1 Composite np-Au stamps after stamping

Composite np-Au stamps were typically used for 6 to 10 cycles for printing of polymer melts. In all stamping processes the composite np-Au stamps were heated to 200 °C or 205 °C, depending on the used ink. Here, the morphology of the composite np-Au stamps after multiple stamping cycles is discussed.

Figure 5.1 shows SEM top view of the composite np-Au stamp after the stamping of PS ink on glass substrates at 200 °C . In the Figure 5.1a and b, the dark areas show the overflow of the PS ink in between the pillars of the composite np-Au stamp. Ink overflow happens most likely because of the cleavages in the metallic film of the stamp and from the breaking of the contact elements of the stamp (Fig. 5.1c). However, large areas of the composite np-Au stamp remained intact after the stamping (Fig. 5.1g, h). Same defects are seen in the composite np-Au stamp after stamping of P(VDF-TrFE) ink on Al/Si substrates at 205 °C which is shown in SEM micrographs at the Figure 5.2. The composite np-Au stamps can be used typically from 6 to 10 stamping cycles after which the stamps can not be used again due to the large ink overflow between the pillars of the stamp.
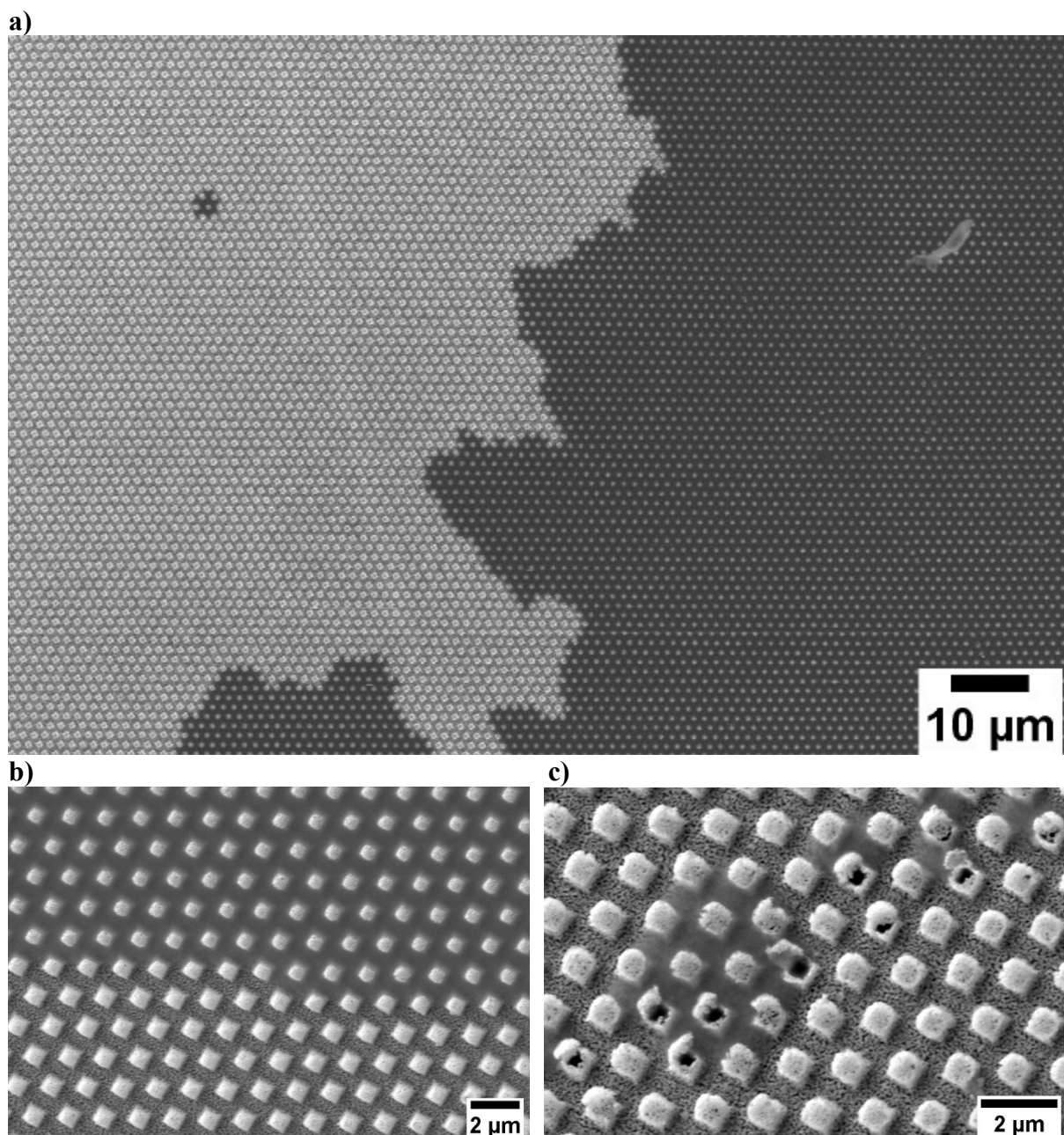
Figure 5.1 SEM images of composite np-Au stamp (top view) after stamping of PS ink on glass substrates with III stamping method, at 200 °C after 7 stamping cycles.

c)

d)
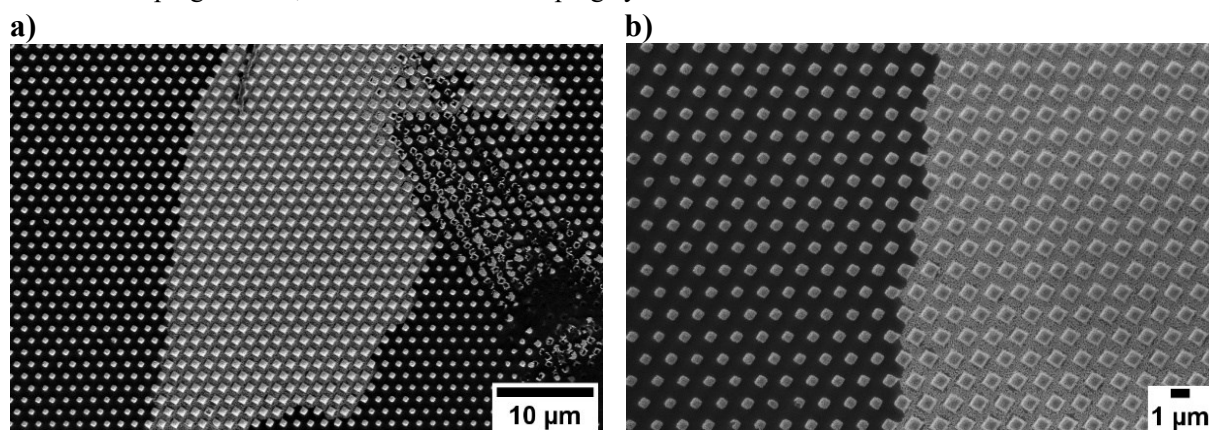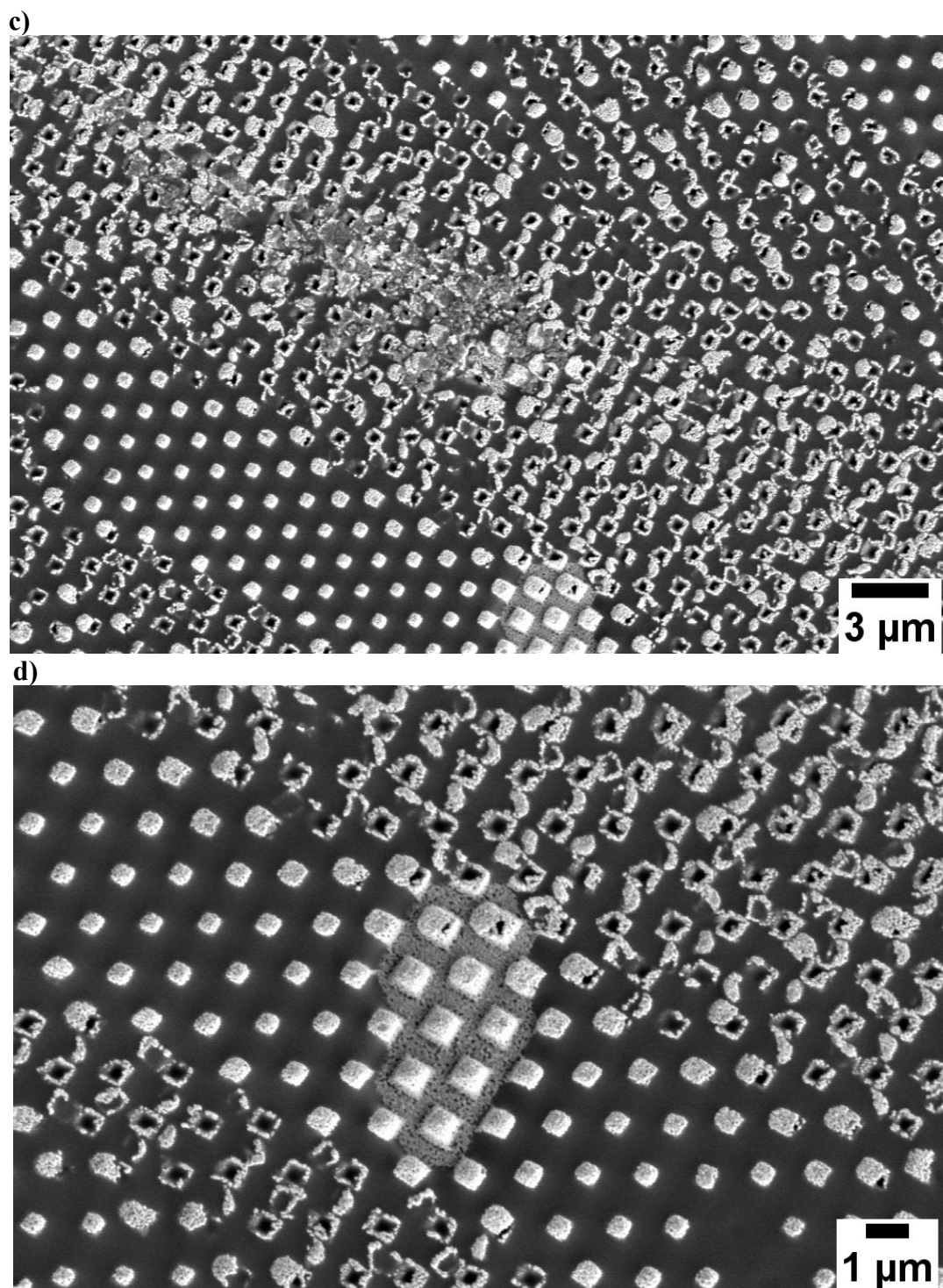
Figure 5.2 SEM images of composite np-Au stamp (top view) after stamping of P(VDF-TrFE) ink on Al/Si substrates with III stamping method, at 205 °C after 8 stamping cycles.

5.2   Printing of PS dots

In this work, polystyrene has been used as a proof-of-concept ink for the capillary stamping method of polymer melts with the porous np-Au stamps. To obtain the printed structures that have mechanical stability, PS with high molecular weight has been selected, because it has been shown that the increase of molecular weight leads to better physical properties of the polymer, due to the entanglements of the large chains[131]. On the other hand, considerable entanglements of polymer chains in high molecular weight polymer limit the motion of the chains at temperatures lower than the T_g, but at the temperatures that are 80 - 100 °C higher than the T_g, chains will get moving irrespective of the entanglements[147]. Hence, the stamping temperature of 200 °C has been selected for stamping of polystyrene melts, assuming T_g = 100 °C. Additionally, imbibition into nanopore channels of AAO with polystyrene of same molecular weight at 200 °C has been demonstrated[148]. Stamping of unmodified glass substrates (surface terminated with hydroxyl groups) was done with three different stamping approaches: methods I (*by hand*), II (*without pressure*) and III (*with pressure*) at 200 °C .

First, stamping of PS was done with the stamping method I – *by hand*, which resulted in the hexagonally ordered printed PS dots (corresponding to the pattern of the contact elements of the np-Au stamp) on the glass after 5 min dwell time. Although this method yielded in printed PS dots on glass substrates, there are two main disadvantages of this method: (1) the hand of the experimenter is near to the heating source during the stamping process which limits the possible dwell times to only short ones and (2) the influence of the experimenter on the stamping process in an uncontrolled way by pressing the stamp/substrate during the stamping process. Due to this, the stamping process needed to be optimized and the method II – *without pressure* was developed. In comparison to the method I no additional pressure was applied on the stamp/substrate during the stamping with method II. Stamping with this method was done with various stamping times (10 min, 13 min, 20 min, and 27 min). Lack of pressure on stamp/substrate led to the uneven surface contact between contact elements of the np-Au stamp and the substrate as the np-Au is not perfectly flat (not all contact elements are exact same hight) which resulted in the low quality of the stamped PS deposits. Because of this, the stamping method was again optimized and the stamping method III – *with pressure* has been developed. Stamping with method III was done with stamping times 5 min, 15 min, 16 min, 17 min, 18 min, 19 min, 20 min, 25 min and 30 min. Further, as stamping method III gave the best quality results it has been later used as the standard stamping method for the stamping of P(VDF-TrFE) polymer melts.

Printed PS dots on glass substrates with all three stamping methods resulted in the following observations (Figure 5.3):

- Large areas of glass substrates were patterned with hexagonally ordered PS dots that corresponded to the pattern of the contact elements of the np-Au stamp.

- There are two common shapes of PS droplets: dot shaped and ring shaped (ring shaped does not appear in the samples obtained by stamping method II)

- Distortion of the PS dots due to the tilting of the substrate after stamping.

- Sizes of the PS dots vary.

- Missing spots or 'empty' areas in between the deposited PS dots.

- Leaking of the PS ink in large amounts on the substrate due to the damages on the stamp that occurred during stamp preparation steps or stamping process.

- Difference in overall quality of the stamped PS dots as well as the difference in the size of the stamped areas.
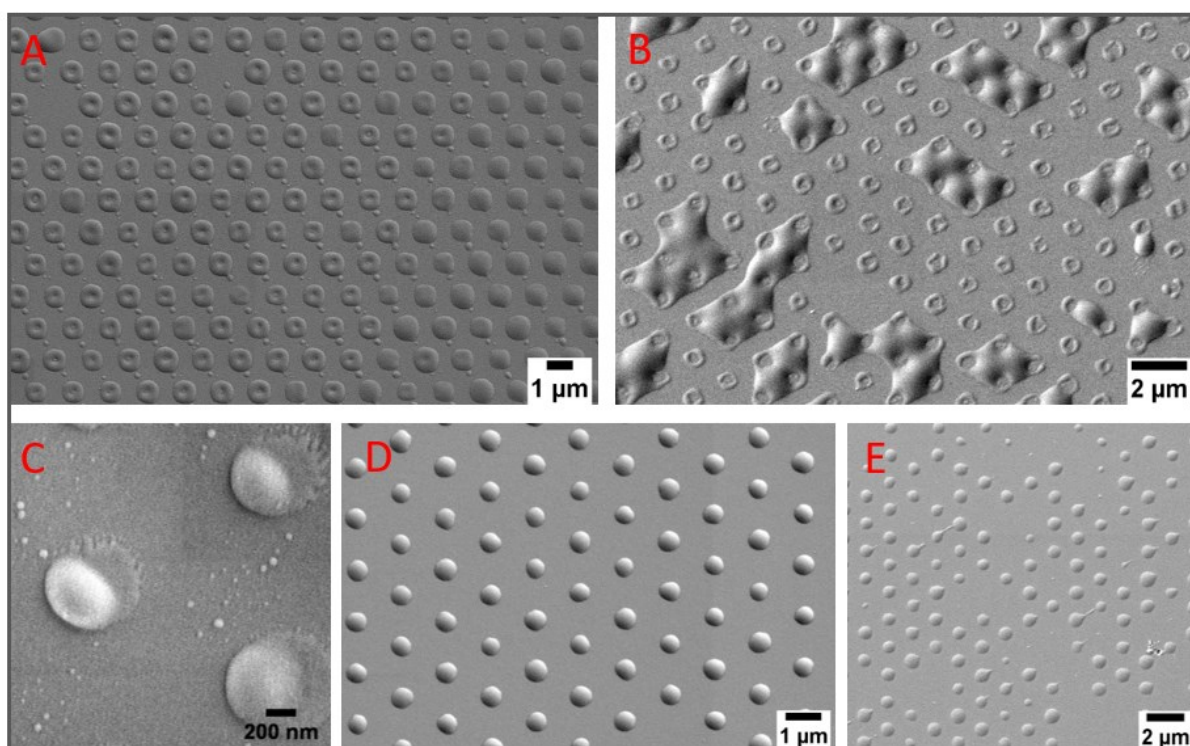
Figure 5.3 Printed PS droplets on glass showing: **(a)** different types of droplet shapes (dot and ring shape), **(b)** islands of PS ink due to the leakage on the substrate, **(c)** distortion of the PS droplets, **(d)** hexagonally ordered printed deposits and **(e)** missing spots in between the printed PS dots.

5.2.1 Influence of the dwell time on the diameter of the printed PS dots

The average diameter of the PS dots after 5 min stamping time was ~ 660 nm, for the stamping that was carried out with the stamping method I. Stamping with stamping method II for the different stamping times gave the diameters of the PS droplets in the range from ~ 600 nm to ~ 900 nm. Diameter sizes of dots after 10 min, 20 min and 27 min have values of ~ 900 nm. The dwell time of 13 min resulted in the smallest size of the droplets even smaller than the size of the PS dots after 10 min dwell time. Reason for this deviation is unclear. From the obtained data we can conclude that there is no direct correlation between the dwell time and the diameter size of the PS dots. Beside the deviation of diameter size after 13 min dwelling time, for the rest of the stamping time measurements it is evident that the stamping time does not influence the diameter size when stamping was done with the stamping method II.

Table 5.1

Stamping method	Stamping time [min]	Average diameter [nm]
I – by hand	5	659 ± 70
II – without pressure	10	895 ± 122
	13	622 ± 130
	20	891 ± 112
	27	909 ± 68
III – with pressure	5	813 ± 60
	15	901 ± 67
	16	800 ± 71
	17	883 ± 66
	18	819 ± 58
	19	865 ± 52
	20	827 ± 48
	25	879 ± 75
	30	967 ± 57

As seen from the Table 5.1 the average values of PS dots for different stamping times by stamping method III are in the range from 800 nm to ~ 970 nm. Diameter values after 5 min dwelling and 15 min dwelling time show jump of ~ 100 nm. Values for the dwell times from 15 min to 20 min which have difference in only 1 min in duration show almost constant value of diameters that lies in the range from 800 nm to 870 nm. Diameter value for 25 min dwell time is in that same range with the value of 880 nm. Second jump in the diameter values is observable from 25 min to 30 min of around ~ 100 nm. However, from the data there is no evidence of direct correlation between the stamping time and the diameter size of the printed PS dots for the stamping times until 30 min.
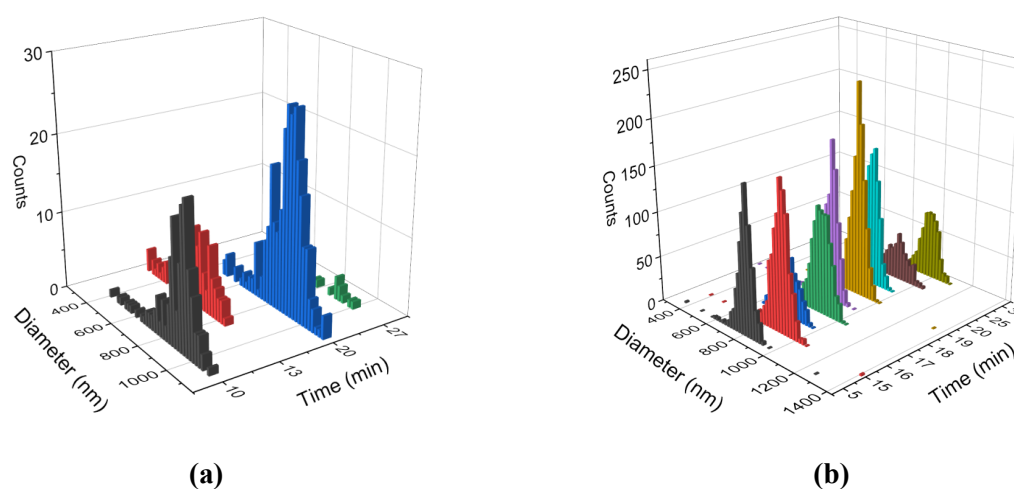
Figure 5.4 Histograms of diameters of printed PS dots on glass substrates for different stamping times by **(a)** II and **(b)** III stamping method.

The deviation of the diameter values after 13 min stamping time by stamping method II is visible at the distribution histogram at Figure 5.4a. The dot diameters are in the range from 200 nm to 1200 nm with most dots with the diameters from 500 nm to 1000 nm.
Distribution of diameter values by stamping method III shows values in the range from 200 nm to 1500 nm (Fig. 5.4b). The highest density of values is in the range from 600 nm to 1100 nm.

5.2.2   Influence of the dwell time on the height of the deposited PS droplets

Average height of the PS dots stamped by the method I is 64 nm. Samples of glass printed with PS dots with the stamping method II had a very large rim of leaked polymer on the rims of the surface that was stamped which made the AFM measurement not possible as it caused the breaking of the AFM tip while approaching to the surface of the sample. Therefore, only the

influence of the dwell time on the hight of the dots by stamping method III will be reviewed here as this stamping method was set as a standard stamping procedure for this work and has the highest relevance. Arithmetic average values of heights of the PS dots for different stamping times are in the range from 33 nm to 81 nm (Table 5.2). From this obtained data it is evident that there is no correlation between the stamping time and the height of the dots. Distribution of heights of PS dots (Fig. 5.5) for different stamping times are in the range from 10 nm to 110 nm.

Table 5.2

Stamping method	**Stamping time [min]**	**Average height [nm]**
I – by hand	5	64 ± 10
	5	81 ± 10
	15	60 ± 7
	16	68 ± 6
	17	68 ± 7
III – with pressure	18	33 ± 6
	19	43 ± 9
	20	46 ± 8
	25	49 ± 8
	30	69 ± 8

Figure 5.5 Height histograms of PS dots printed on the glass substrates.

5.3   Printing of P(VDF-TrFE) dots

As mentioned earlier in Section 5.2, stamping method III has been set as a standard stamping procedure in this work and as such has been used as the only stamping procedures for all stamping experiments of P(VDF-TrFE) that will be discussed here in this Section. Stamping of P(VDF-TrFE) was done with np-Au-P(VDF-TrFE) stamp on two different types of substrates: (1) glass and (2) Al/Si substrates. Infiltration of the same molecular weight P(VDF-TrFE) melts at temperatures at 200 °C and 523 K into AAO pores has been already demonstrated[144]. Based on this data, the stamping temperature of P(VDF-TrFE) melts in this work of 205 °C has been selected.

Printed P(VDF-TrFE) dots on both types of substrates showed following observations (Fig. 5.6):

- Large areas of glass substrates were patterned with hexagonally ordered P(VDF-TrFE) dots that corresponded to the pattern of the contact elements of the np-Au stamp.
- There are two shapes of P(VDF-TrFE) droplets: dot shaped and ring shaped (ring shaped dots were rarely present) .
- Variation in sizes of deposited P(VDF-TrFE) dots.
- Distortion of the P(VDF-TrFE) droplets.
- Crystal lamellae structures of P(VDF-TrFE) copolymer visible at the surface of the deposits.
- Missing spots or 'empty' areas in between the deposited P(VDF-TrFE) dots.
- Leaking of the PS ink in large amounts on the substrate due to the damages on the stamp that occurred during stamp preparation steps or stamping process.
- Different quality of the stamped P(VDF-TrFE) dots as well as the difference in the size of the stamped areas.
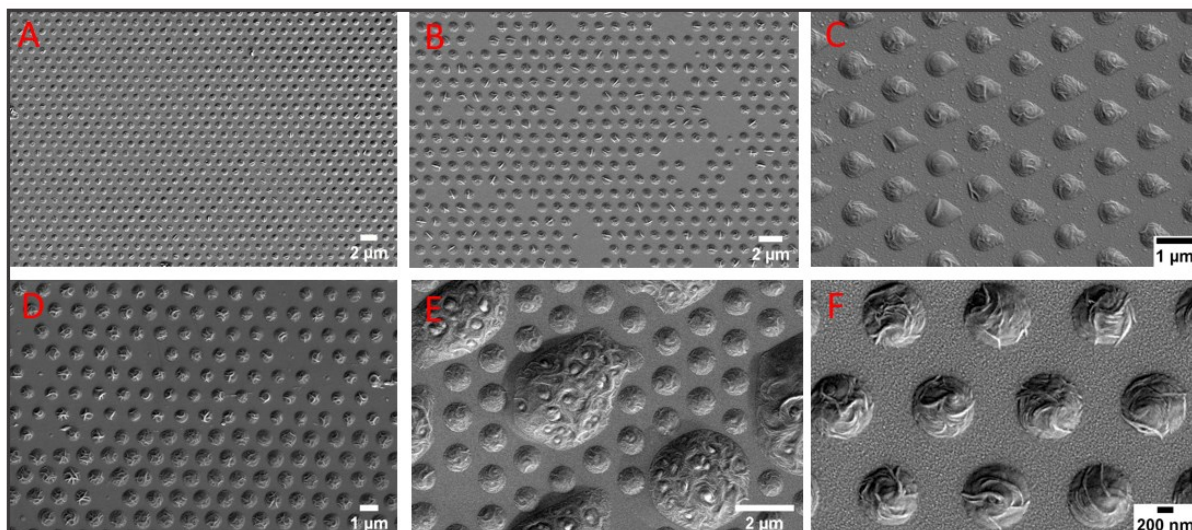
Figure 5.6 Printed P(VDF-TrFE) dots showing the **(a)** large area of hexagonally ordered printed P(VDF-TrFE) dots, **(b)** areas with missing dots in between the deposited droplets, **(c)** distortion of the printed P(VDF-TrFE) dots, **(d)** difference in the dot sizes in the printed area, **(e)** islands of P(VDF-TrFE) ink due to the excessive leakage of the ink and **(f)** lamellae structures in the printed dots.

5.3.1 Influence of the dwell time on the diameter of the printed P(VDF-TrFE) dots

Average values of diameters measured for the different stamping times are presented in the Table 5.3 below. The diameter values are in the range from 960 nm to ~ 1170 nm. Stamping times from 15 min to 18 min show a constant diameter value of ~ 1000 nm and there is an increase of ~ 100 nm in diameter for the stamping time of 19 min. For stamping times 25 min and 30 min the values remain above 1100 nm, with the observable deviation of the value for the stamping time of 20 min that is 960 nm. Distributions of the dot diameters for the stamping times 15 min, 16 min, 17 min and 18 min are in the same range of values whereas the shift towards the higher values is visible for the stamping times 19 min, 25 min and 30 min (Fig. 5.7a). Diameter values after 20 min stamping time show a deviation from the increase of the dot diameters with longer stamping time. Based on this data there is no clear indication that the longer stamping times will result in the larger diameters of deposited P(VDF-TrFE) dots for the stamping times under 30 min.

Table 5.3

Substrate	Stamping time [min]	Average diameter [nm]
Glass	15	1023 ± 72
	16	1002 ± 150
	17	1057 ± 31
	18	1052 ± 54
	19	1131 ± 36
	20	960 ± 40
	25	1169 ± 102
	30	1103 ± 117
Al/Si	1	894 ± 83
	2	957 ± 49
	3	940 ± 93
	4	925 ± 60
	5	1085 ± 71
	6	954 ± 78
	7	1147 ± 31
	10	959 ± 36
	15	1095 ± 92
	20	872 ± 40

Stamping of P(VDF-TrFE) dots on Al/Si substrates was carried out with the stamping times from 1 min to 7 min with an increment of 1 min and for the stamping times of 10 min, 15 min and 20 min. Average values of the dot diameters lie in the range from ~ 870 nm to ~ 1150 nm. Table 5.3 shows that the average diameter values are in no correlation to the duration of the stamping . Similar results have been already seen for the diameters values of P(VDF-TrFE) dots deposited on glass substrates. The histograms of P(VDF-TrFE) dots for various stamping times are shown in Figure 5.7b and show broad range of values up to 1400 nm.

By comparison of the two histogram shown in Figure 5.7 for the P(VDF-TrFE) dots printed on two different types of substrates and for different stamping times is that in both cases the first 4 cycles show constant values of dot diameters and the 5th stamping cycle is moved towards the higher diameter values. Further, 6th and 7th cycle show also similar behavior.

(a)   **(b)**
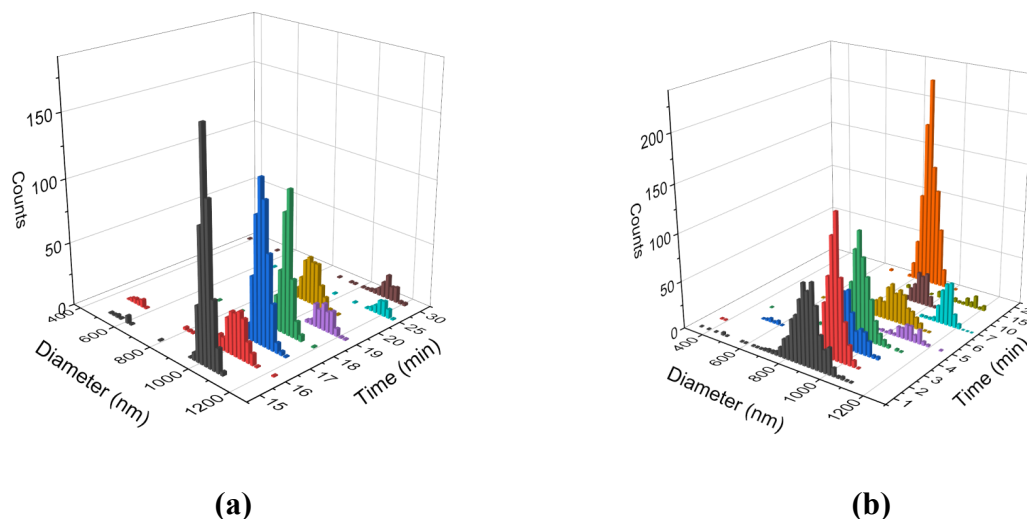
Figure 5.7 Diameter histograms of P(VDF-TrFE) dots printed on the **(a)** glass and **(b)** Al/Si substrates.

5.3.2   Influence of the dwell time on the height of the printed P(VDF-TrFE) dots

Average heights of the printed P(VDF-TrFE) dots for different stamping times are summerized in the Table 5.4 and are in the range from ~ 80 nm to ~ 120 nm. From the obtained data from the Table 5.4 for the P(VDF-TrFE) dots that were deposited on to the glass substrate there is no trend that shows correlation between the stamping time and the height of the dots. Histograms shown in the Figure 5.5a shows the height values up to 150 nm.

Similarily, the values of average heights of P(VDF-TrFE) dots that were printed on the Al/Si substrates are in no correlation to the stamping time. The height values for dots deposited on Al/Si are in the range from ~ 40 nm to ~ 80 nm (Table 5.4).

By comparison of height distribution histograms of dots printed on glass and on Al/Si the height of dots printed on Al/Si are flater that the ones printed on glass (Fig. 5.8).

Table 5.4

Substrate	Stamping time [min]	Average height [nm]
Glass	15	116 ± 14
	16	93 ± 18
	17	84 ± 19
	18	99 ± 21
	19	106 ± 19
	20	81 ± 14
	25	102 ± 23
	30	94 ± 29
Al/Si	1	52 ± 14
	2	64 ± 17
	3	39 ± 19
	4	75 ± 15
	5	77 ± 13
	6	62 ± 13
	7	49 ± 11
	10	58 ± 16
	15	56 ± 21
	20	71 ± 15
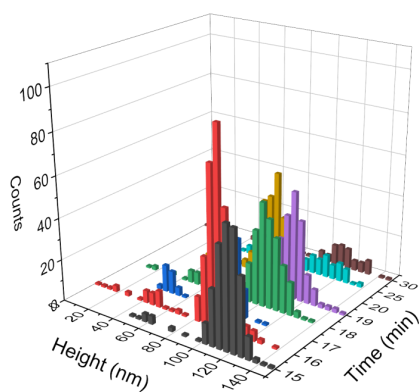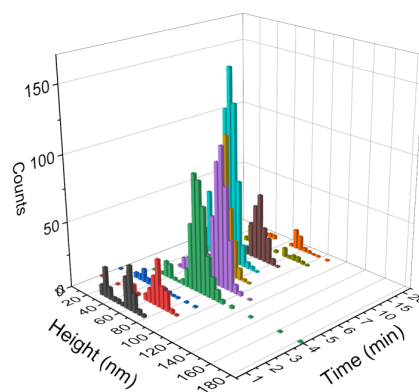
(a) (b)

Figure 5.8 Height histograms of P(VDF-TrFE) dots printed on the **(a)** glass and **(b)** Al/Si substrates.

5.3.3 Switching of P(VDF-TrFE) dots

Local switching of ferroelectric P(VDF-TrFE) ink was conducted on two different sizes of dots, smaller ones that had diameter of 100-200 nm and larger ones with diameter of ~ 400 nm. It has been shown with single pulse poling that all investigated P(VDF-TrFE) dots could be switched. As the switching follows a $1/E$ law according to Furukawa et.al[149], the selected voltage of ± 15 V and pulse length of 300 ms is in the polarization saturation. For the dots as small as ~ 100 nm, ferroelectric domains covered entire dot and the polarization contrast (dark/bright or vice versa) was fully reversed. While single pulse poling of the larger dots of ~ 400 nm showed domains that cover only a part of the dot. Bright/dark phase contrast at rim of dots cannot be interpreted, because of a deconvolution of dot and tip shape and a complex transfer of the piezoresponse.

Hysteresis loops investigation of four small dots (100-200 nm) showed characteristic ferroelectric behaviour that in between them vary in shape and coercive voltage V_c. While one of the investigated dots shows symmetrical voltage of $V_c \approx$ ± 9V, other three dots show asymmetry with the values of $V_c \approx$ - 7V, + 5V; $V_c \approx$ - 7.5V, + 6V; $V_c \approx$ - 8V, + 10V. Smaller dots show lower crystallinity. Larger investigated dot of ~ 400 nm shows almost symmetrical switching and high crystallinity. Deviations from the perfect infinitely steep switching can be attributed to lower degree of crystallinity and polycrystalline structure inside the dots[149]. There are more possible reasons for the asymmetries in the coercive voltages as: self-polarized region at the electrode/ferroelectric interface (different crystallization at interface than at air/ferroelectric boundary); built-in field at the interface related to Schottky barrier between semiconducting ferroelectric polymer and metallic electrode; difference in work function between Pt/Ir (tip) and Al (bottom) electrode that causes natural asymmetry in switching. Asymmetry in coercive voltage is followed by differences in nucleation and growth rates as observed by Furukawa et al[149]. and Kim et al[150].

6   Conclusion and outlook

Composite nanoporous gold stamp (np-Au) for capillary stamping has been developed in this work. This enabled printing of polymers directly from their melts which was not possible with the already existing stamps for capillary stamping. Developed composite gold stamps consist of continuous network of pores throughout the gold film and a layer of polymer ink that is attached to it and serves both as support and an ink reservoir that enables the stamping in multiple continues cycles without the need for reinking. Stamping procedures of polymer melts with composite np-Au was done at elevated temperatures (stamping temperature depends on the polymer ink) and are done in the atmospheric environment.

Optimization of the stamping procedure has also been developed in this work and the stamping method III – *with pressure* has been set as the standard procedure for the capillary stamping of polymer melts.

Polystyrene is available with narrow molecular mass distributions over a broad molecular mass range, and as such has been selected as the proof-of-concept ink for the capillary stamping with composite np-Au stamps. Additionally, it has also been used for the optimization of the stamping process. Polystyrene has been printed on the glass substrates with composite np-Au stamp at 200 °C with various stamping times and all three stamping methods. Printing of polystyrene with composite np-Au stamp resulted in hexagonally ordered array of droplets deposited on the glass substrates. Polystyrene droplets were deposited with the average diameter values from ~ 600 nm to 1000 nm and average heights from 30 nm to 80 nm depending on the stamping method and the dwell time.

P(VDF-TrFE) was the second ink that has been printed with the np-Au stamp at 205 °C on two different types of substrates, glass, and aluminium coated Si wafers. The printing of P(VDF-TrFE) has been carried out on both types of substrates with various stamping times and has resulted in hexagonally ordered arrays of deposited P(VDF-TrFE) droplets with the average diameters ranging from ~ 870 nm to 1170 nm and average heights from 40 nm to 120 nm, depending on the dwell time and the substrate.

As already known wetting behaviour of polymer melts on solid surfaces depends on the various parameters such as surface energy[151] roughness of the substrate[152], surface tension[153] of polymer melts and stamping temperature[154]. In this work, the influence of the stamping time on the

diameter and the height of the deposited polymer melts at constant selected temperatures (depending on the polymer ink) was studied. For both polymer inks it could not be determined the direct correlation between the duration of the dwelling and the size of the polymer deposits. However, it has been shown that with capillary stamping method with composite np-Au stamp it is possible to obtain the different sizes of printed deposits. With further understanding of all parameters that influence the stamping process opens the possibility to print polymer structures with predefined desired sizes.

It was demonstrated that stamped dots of P(VDF-TrFE) are of polycrystalline character and exhibit full ferroelectric switching behavior. For different dot sizes the domains are of different size where domains in smaller dots of ~100 nm covers the entire dot in larger dots of ~ 400 nm the domains cover only the prat of the dots. Smaller dots have shown low crystallinity in comparison to the larger dots that showed high crystallinity.

In this work, polymer melts were successfully printed with the novel composite nanoporous gold stamp in capillary stamping approach under elevated temperatures. This method offers advantages to solution printing because the evaporation of volatile organic solvents is avoided and results in more homogeneous structures due to their lower tendency to deform after printing. Stamping with composite np-Au stamp was possible in continues cycles without reinking. It has been shown that droplets of polymer melts can be printed with various sizes up to 1 μm by using composite np-Au stamp without changing any of the features of the stamp. It was also demonstrated that the ferroelectric polymer deposits have retained their ferroelectric properties after the stamping.

Further understanding of the stamping process with composite np-Au stamp should be carried out in the future to further improve the process. This would enable the printing of desired sizes of polymer deposits and open the possibility to print different sizes of polymer structures in consecutive cycles without changing the features of the stamp.

In future, different polymers could be printed with this method which would advance the development of different areas of applications such as sensing, energy storage and drug delivery systems.

7 Bibliography

1.   Zhao, X. *et al.* Enhancing the Intrinsic Stretchability of Micropatterned Gold Film by Covalent Linkage of Carbon Nanotubes for Wearable Electronics. *ACS Appl. Electron. Mater.* **1**, 1295–1303 (2019).
2.   Surmenev, R. A., Chernozem, R. V., Pariy, I. O. & Surmeneva, M. A. A review on piezo- and pyroelectric responses of flexible nano- and micropatterned polymer surfaces for biomedical sensing and energy harvesting applications. *Nano Energy* **79**, 105442 (2021).
3.   Martinez-Rivas, A., González-Quijano, G. K., Proa-Coronado, S., Séverac, C. & Dague, E. Methods of micropatterning and manipulation of cells for biomedical applications. *Micromachines* **8**, (2017).
4.   Guan, J., He, H., Lee, L. J. & Hansford, D. J. Fabrication of particulate reservoir-containing, capsulelike, and self-folding polymer microstructures for drug delivery. *Small* **3**, 412–418 (2007).
5.   Leclerc, E. *et al.* Fabrication of microstructures in photosensitive biodegradable polymers for tissue engineering applications. *Biomaterials* **25**, 4683–4690 (2004).
6.   Ferrell, N., Woodard, J. & Hansford, D. Fabrication of polymer microstructures for MEMS: Sacrificial layer micromolding and patterned substrate micromolding. *Biomed. Microdevices* **9**, 815–821 (2007).
7.   Revzin, A., Tompkins, R. G. & Toner, M. Surface Engineering with Poly(ethylene glycol) Photolithography to Create High-Density Cell Arrays on Glass. *Langmuir* **19**, 9855–9862 (2003).
8.   Tran, K. T. M. & Nguyen, T. D. Lithography-based methods to manufacture biomaterials at small scales. *J. Sci. Adv. Mater. Devices* **2**, 1–14 (2017).
9.   Piner, R. D., Zhu, J., Xu, F., Hong, S. & Mirkin, C. A. 'Dip-pen' nanolithography. *Science (80-.).* **283**, 661–663 (1999).
10. Alom Ruiz, S. & Chen, C. S. Microcontact printing: A tool to pattern. *Soft Matter* **3**, 168–177 (2007).
11. Shao, J. Y. *et al.* Nanoimprint lithography for the manufacturing of flexible electronics. *Sci. China Technol. Sci.* **62**, 175–198 (2019).
12. Kumar, A., Biebuyck, H. A. & Whitesides, G. M. Patterning Self-Assembled Monolayers: Applications in Materials Science. *Langmuir* **10**, 1498–1511 (1994).
13. Xu, H. *et al.* Microcontact printing of dendrimers, proteins, and nanoparticles by porous stamps. *J. Am. Chem. Soc.* **131**, 797–803 (2009).
14. Schmidt, M. *et al.* Capillary Nanostamping with Spongy Mesoporous Silica Stamps. *Adv. Funct. Mater.* **28**, 1–9 (2018).
15. Han, W. *et al.* Ordered Topographically Patterned Silicon by Insect-Inspired Capillary Submicron Stamping. *ACS Appl. Mater. Interfaces* **10**, 7451–7458 (2018).
16. Hou, P. *et al.* Scanner-Based Capillary Stamping. *Adv. Funct. Mater.* **30**, (2020).
17. Van De Witte, P., Dijkstra, P. J., Van Den Berg, J. W. A. & Feijen, J. Phase separation processes in polymer solutions in relation to membrane formation. *J. Memb. Sci.* **117**, 1–31 (1996).
18. Craster, R. V. & Matar, O. K. Dynamics and stability of thin liquid films. *Rev. Mod. Phys.* **81**, 1131–1198 (2009).
19. Li, J. *et al.* A stable solution-processed polymer semiconductor with record high-mobility for printed transistors. *Sci. Rep.* **2**, 1–9 (2012).
20. Kim, S. *et al.* Nanostructured multifunctional surface with antireflective and

antimicrobial characteristics. *ACS Appl. Mater. Interfaces* **7**, 326–331 (2015).

21. El-Schich, Z. *et al.* Molecularly imprinted polymers in biological applications. *Biotechniques* **69**, 407–420 (2020).

22. Aissou, K., Kogelschatz, M., Baron, T. & Gentile, P. Self-assembled block polymer templates as high resolution lithographic masks. *Surf. Sci.* **601**, 2611–2614 (2007).

23. Ren, H., Fan, Y.-H. & Wu, S.-T. Liquid-crystal microlens arrays using patterned polymer networks. *Opt. Lett.* **29**, 1608 (2004).

24. Al-Khayat, O., Hong, J. K., Beck, D. M., Minett, A. I. & Neto, C. Patterned Polymer Coatings Increase the Efficiency of Dew Harvesting. *ACS Appl. Mater. Interfaces* **9**, 13676–13684 (2017).

25. De Teresa, J. M. Introduction to nanolithography techniques and their applications. *Nanofabrication* (2020) doi:10.1088/978-0-7503-2608-7ch1.

26. Acikgoz, C., Hempenius, M. A., Huskens, J. & Vancso, G. J. Polymers in conventional and alternative lithography for the fabrication of nanostructures. *Eur. Polym. J.* **47**, 2033–2052 (2011).

27. Chen, Y. Nanofabrication by electron beam lithography and its applications: A review. *Microelectron. Eng.* **135**, 57–72 (2015).

28. Namatsu, H., Yamaguchi, T. & Kurihara, K. *Resist materials providing small line-edge roughness. Materials Research Society Symposium - Proceedings* vol. 584 (2000).

29. Gangnaik, A. S., Georgiev, Y. M., Collins, G. & Holmes, J. D. Novel germanium surface modification for sub-10 nm patterning with electron beam lithography and hydrogen silsesquioxane resist. *J. Vac. Sci. Technol. B, Nanotechnol. Microelectron. Mater. Process. Meas. Phenom.* **34**, 041603 (2016).

30. Sun, J., Wang, Y. & Liao, J. Tailoring two-dimensional nanoparticle arrays into various patterns. *Nanotechnology* **29**, 44003 (2017).

31. Reyntjens, S. & Puers, R. A review of focused ion beam applications in microsystem technology INSTITUTE OF PHYSICS PUBLISHING JOURNAL OF MICROMECHANICS AND MICROENGINEERING A review of focused ion beam applications in microsystem technology. *J. Micromech. Microeng* **11**, 287–300 (2001).

32. Arshak, K., Mihov, M., Arshak, A., McDonagh, D. & Sutton, D. Focused ion beam lithography- Overview and new approaches. *Proc. Int. Conf. Microelectron.* **24 II**, 459–462 (2004).

33. Gamo, K. Focused ion beam lithography. *Nucl. Inst. Methods Phys. Res. B* **65**, 40–49 (1992).

34. Menard, L. D. & Ramsey, J. M. Fabrication of sub-5 nm nanochannels in insulating substrates using focused ion beam milling. *Nano Lett.* **11**, 512–517 (2011).

35. V. Grayli, S. *et al.* Scalable, Green Fabrication of Single-Crystal Noble Metal Films and Nanostructures for Low-Loss Nanotechnology Applications. *ACS Nano* **14**, 7581–7592 (2020).

36. Wang, W., Pfeiffer, P. & Schmidt-Mende, L. Direct Patterning of Metal Chalcogenide Semiconductor Materials. *Adv. Funct. Mater.* **30**, 1–8 (2020).

37. Askew, H. J., Jarvis, K. L., Jones, R. T. & McArthur, S. L. Electron Beam Lithography Nanopatterning of Plasma Polymers. *Macromol. Chem. Phys.* **222**, 1–9 (2021).

38. Moon, M. W. *et al.* Controlled formation of nanoscale wrinkling patterns on polymers using focused ion beam. *Scr. Mater.* **57**, 747–750 (2007).

39. Clendenning, S. B. *et al.* Direct writing of patterned ceramics using electron-beam lithography and metallopolymer resists. *Adv. Mater.* **16**, 215–219 (2004).

40. Fan, P. *et al.* Scanning Probe Lithography: State-of-the-Art and Future Perspectives. *Micromachines* **13**, 1–32 (2022).

41. Nassiopoulou, A. G. *et al.* Laterally ordered 2-D arrays of Si and Ge nanocrystals within SiO 2 thin layers for application in non-volatile memories. **6**, 18–34 (2009).

42. Garcia, R., Knoll, A. W. & Riedo, E. Advanced scanning probe lithography. *Nat. Nanotechnol.* **9**, 577–587 (2014).

43. Paul, P. C. *Thermal scanning probe lithography*. *Frontiers of Nanoscience* vol. 11 (Elsevier, 2016).

44. Wang, J. *et al.* Processing outcomes of atomic force microscope tip-based nanomilling with different trajectories on single-crystal silicon. *Precis. Eng.* **72**, 480–490 (2021).

45. Liu, G., Petrosko, S. H., Zheng, Z. & Mirkin, C. A. Evolution of Dip-Pen Nanolithography (DPN): From Molecular Patterning to Materials Discovery. *Chem. Rev.* **120**, 6009–6047 (2020).

46. Nelson, B. A., King, W. P., Laracuente, A. R., Sheehan, P. E. & Whitman, L. J. Direct deposition of continuous metal nanostructures by thermal dip-pen nanolithography. *Appl. Phys. Lett.* **88**, 1–3 (2006).

47. Dagata, J. A. SPM-based lithography for electronics device fabrication: new strategies and directions. *Mater. Res. Soc. Symp. - Proc.* **380**, 153–162 (1995).

48. Hu, H., Cho, H., Somnath, S., Vakakis, A. F. & King, W. P. Silicon nano-mechanical resonators fabricated by using tip-based nanofabrication. *Nanotechnology* **25**, (2014).

49. Nie, Z. & Kumacheva, E. Patterning surfaces with functional polymers. *Nat. Mater.* **7**, 277–290 (2008).

50. Baba, A., Sato, F., Fukuda, N., Ushijima, H. & Yase, K. Micro/nanopatterning of single-walled carbon nanotube-organic semiconductor composites. *Nanotechnology* **20**, (2009).

51. O'Connell, C. D., Higgins, M. J., Marusic, D., Moulton, S. E. & Wallace, G. G. Liquid ink deposition from an atomic force microscope tip: Deposition monitoring and control of feature size. *Langmuir* **30**, 2712–2721 (2014).

52. Maynor, B. W., Filocamo, S. F., Grinstaff, M. W. & Liu, J. Direct-writing of polymer nanostructures: Poly(thiophene) nanowires on semiconducting and insulating surfaces. *J. Am. Chem. Soc.* **124**, 522–523 (2002).

53. Ru, C., Luo, J., Xie, S. & Sun, Y. A review of non-contact micro- and nano-printing technologies. *J. Micromechanics Microengineering* **24**, (2014).

54. O'Connell, C. D., Higgins, M. J., Sullivan, R. P., Moulton, S. E. & Wallace, G. G. Ink-on-probe hydrodynamics in atomic force microscope deposition of liquid inks. *Small* **10**, 3717–3728 (2014).

55. Sheehan, P. E., Whitman, L. J., King, W. P. & Nelson, B. A. Nanoscale deposition of solid inks via thermal dip pen nanolithography. *Appl. Phys. Lett.* **85**, 1589–1591 (2004).

56. Lee, W. K., Whitman, L. J., Lee, J., King, W. P. & Sheehan, P. E. The nanopatterning of a stimulus-responsive polymer by thermal dip-pen nanolithography. *Soft Matter* **4**, 1844–1847 (2008).

57. Howell, S. T., Grushina, A., Holzner, F. & Brugger, J. Thermal scanning probe lithography—a review. *Microsystems Nanoeng.* **6**, 1–24 (2020).

58. Felts, J. R., Somnath, S., Ewoldt, R. H. & King, W. P. Nanometer-scale flow of molten polyethylene from a heated atomic force microscope tip. *Nanotechnology* **23**, (2012).

59. Calvert, P. Inkjet printing for materials and devices. *Chem. Mater.* **13**, 3299–3305 (2001).

60. Dijksman, J. F. *et al.* Precision ink jet printing of polymer light emitting displays. *J. Mater. Chem.* **17**, 511–522 (2007).

61. Mikkonen, R., Puistola, P., Jönkkäri, I. & Mäntysalo, M. Inkjet Printable Polydimethylsiloxane for All-Inkjet-Printed Multilayered Soft Electrical Applications. *ACS Appl. Mater. Interfaces* **12**, 11990–11997 (2020).

62. Tien, C. H., Hung, C. H. & Yu, T. H. Microlens arrays by direct-writing inkjet print for LCD backlighting applications. *IEEE/OSA J. Disp. Technol.* **5**, 147–151 (2009).

63. Salim, A. & Lim, S. Review of recent inkjet-printed capacitive tactile sensors. *Sensors (Switzerland)* **17**, (2017).

64. Montenegro-Nicolini, M., Miranda, V. & Morales, J. O. Inkjet Printing of Proteins: an Experimental Approach. *AAPS J.* **19**, 234–243 (2017).

65. Maleki, H. & Bertola, V. Recent advances and prospects of inkjet printing in heterogeneous catalysis. *Catal. Sci. Technol.* **10**, 3140–3159 (2020).

66. De Gans, B. J. & Schubert, U. S. Inkjet printing of well-defined polymer dots and arrays. *Langmuir* **20**, 7789–7793 (2004).

67. Bonaccurso, E., Butt, H. J., Hankeln, B., Niesenhaus, B. & Graf, K. Fabrication of microvessels and microlenses from polymers by solvent droplets. *Appl. Phys. Lett.* **86**, 1–3 (2005).

68. Sowade, E., Blaudeck, T. & Baumann, R. R. Inkjet Printing of Colloidal Nanospheres: Engineering the Evaporation-Driven Self-Assembly Process to Form Defined Layer Morphologies. *Nanoscale Res. Lett.* **10**, 0–8 (2015).

69. Dong, J., Liu, J., Kang, G., Xie, J. & Wang, Y. Pushing the resolution of photolithography down to 15nm by surface plasmon interference. *Sci. Rep.* **4**, 1–6 (2014).

70. KING, M. C. *Principles of Optical Lithography*. (1981). doi:10.1016/b978-0-12-234101-4.50009-6.

71. Liaros, N. & Fourkas, J. Ten years of two-color photolithography [Invited]. *Opt. Mater. Express* **9**, 3006 (2019).

72. Nanocenter, M. Ten years of two-color photolithography [Invited]. **9**, 3006–3020 (2019).

73. Schock, M. & Bräse, S. Reactive & efficient: Organic azides as cross-linkers in material sciences. *Molecules* **25**, (2020).

74. Nie, Z. & Kumacheva, E. Nmat2109.

75. Gordon, T. J., Yu, J., Yang, C. & Holdcroft, S. Direct thermal patterning of a π-conjugated polymer. *Chem. Mater.* **19**, 2155–2161 (2007).

76. Chang, J. F., Gwinner, M. C., Caironi, M., Sakanoue, T. & Sirringhaus, H. Conjugated-polymer-based lateral heterostructures defined by high-resolution photolithography. *Adv. Funct. Mater.* **20**, 2825–2832 (2010).

77. Perl, A., Reinhoudt, D. N. & Huskens, J. Microcontact printing: Limitations and achievements. *Adv. Mater.* **21**, 2257–2268 (2009).

78. Geissler, M. *et al.* Fabrication of metal nanowires using microcontact printing. *Langmuir* **19**, 6301–6311 (2003).

79. Schmalenberg, K. E., Buettner, H. M. & Uhrich, K. E. Microcontact printing of proteins on oxygen plasma-activated poly(methyl methacrylate). *Biomaterials* **25**, 1851–1857 (2004).

80. Kaufmann, T. & Ravoo, B. J. Stamps, inks and substrates: Polymers in microcontact printing. *Polym. Chem.* **1**, 371–387 (2010).

81. Xu, C., Taylor, P., Ersoz, M., Fletcher, P. D. I. & Paunov, V. N. Microcontact printing of DNA-surfactant arrays on solid substrates. *J. Mater. Chem.* **13**, 3044–3048 (2003).

82. Singh, P. K., Sharma, V., Tanwar, V. K. & Jain, S. C. Soft-lithography: Its application in solar cells, microelectronics and life sciences. *J. Optoelectron. Adv. Mater.* **9**, 127–133 (2007).

83. Qin, D., Xia, Y. & Whitesides, G. M. Soft lithography for micro- and nanoscale patterning. *Nat. Protoc.* **5**, 491–502 (2010).

84. von Philipsborn, A. C. *et al.* Microcontact printing of axon guidance molecules for generation of graded patterns. *Nat. Protoc.* **1**, 1322–1328 (2006).

85. Guo, L. *et al.* Phenolic Resin Dual-Use Stamps for Capillary Stamping and Decal Transfer Printing. *ACS Appl. Mater. Interfaces* **13**, 49567–49579 (2021).

86.   Alarslan, F. *et al.* Thin Patterned Lithium Niobate Films by Parallel Additive Capillary Stamping of Aqueous Precursor Solutions. *Adv. Eng. Mater.* **24**, (2022).

87.   Alarslan, F. *et al.* Reactive Additive Capillary Stamping with Double Network Hydrogel-Derived Aerogel Stamps under Solvothermal Conditions. *ACS Appl. Mater. Interfaces* **14**, 44992–45004 (2022).

88.   Guo, L. J. Nanoimprint lithography: Methods and material requirements. *Adv. Mater.* **19**, 495–513 (2007).

89.   Kwon, B. & Kim, J. H. Importance of Molds for Nanoimprint Lithography: Hard, Soft, and Hybrid Molds. *J. Nanosci.* **2016**, 1–12 (2016).

90.   Mancini, D. P. *et al.* Hydrogen silsesquioxane for direct electron-beam patterning of step and flash imprint lithography templates. *J. Vac. Sci. Technol. B Microelectron. Nanom. Struct.* **20**, 2896–2901 (2002).

91.   Dauksher, W. J. *et al.* Characterization of and imprint results using indium tin oxide-based step and flash imprint lithography templates. *J. Vac. Sci. Technol. B Microelectron. Nanom. Struct.* **20**, 2857–2861 (2002).

92.   Stewart, M. D. & Willson, C. G. Imprint materials for nanoscale devices. *MRS Bull.* **30**, 947–951 (2005).

93.   Hagberg, E. C., Malkoch, M., Ling, Y., Hawker, C. J. & Carter, K. R. Effects of modulus and surface chemistry of thiol-ene photopolymers in nanoimprinting. *Nano Lett.* **7**, 233–237 (2007).

94.   Thanner, C. & Eibelhuber, M. UV nanoimprint lithography: Geometrical impact on filling properties of nanoscale patterns. *Nanomaterials* **11**, (2021).

95.   Malloy, M. Technology review and assessment of nanoimprint lithography for semiconductor and patterned media manufacturing. *J. Micro/Nanolithography, MEMS, MOEMS* **10**, 032001 (2011).

96.   Wu, W. *et al.* Optical metamaterials at near and mid-IR range fabricated by nanoimprint lithography. *Appl. Phys. A Mater. Sci. Process.* **87**, 143–150 (2007).

97.   Vigneswaran, N., Samsuri, F., Ranganathan, B. & Padmapriya, P. Recent advances in nano patterning and nano imprint lithography for biological applications. *Procedia Eng.* **97**, 1387–1398 (2014).

98.   Kooy, N., Rahman, N. & Mohamed, K. Patterning of multi-leveled microstructures on flexible polymer substrate using roll-to-roll ultraviolet nanoimprint lithography. *Proc. IEEE/CPMT Int. Electron. Manuf. Technol. Symp.* (2012) doi:10.1109/IEMT.2012.6521804.

99.   Forty, A. J. Corrosion micromorphology of noble metal alloys and depletion gilding [5]. *Nature* vol. 282 597–598 (1979).

100.   Biener, J., Biener, M. M., Madix, R. J. & Friend, C. M. Nanoporous Gold: Understanding the Origin of the Reactivity of a 21st Century Catalyst Made by Pre-Columbian Technology. *ACS Catal.* **5**, 6263–6270 (2015).

101.   Erlebacher, J., Aziz, M. J., Karma, A., Dimitrov, N. & Sieradzki, K. Evolution of nanoporosity in dealloying. *Nature* **410**, 450–453 (2001).

102.   Wittstock, A., Biener, J. & Bäumer, M. Nanoporous gold: A new material for catalytic and sensor applications. *Phys. Chem. Chem. Phys.* **12**, 12919–12930 (2010).

103.   Li, J., Markmann, J., Weissmüller, J. & Mameka, N. Nanoporous gold-polypyrrole hybrid electrochemical actuators with tunable elasticity. *Acta Mater.* **212**, 116852 (2021).

104.   Hengge, E. *et al.* Nanoporous gold electrodes modified with self-assembled monolayers for electrochemical control of the surface charge. *Phys. Chem. Chem. Phys.* **23**, 14457–14464 (2021).

105.   Koifman Khristosov, M., Dishon, S., Noi, I., Katsman, A. & Pokroy, B. Pore and ligament size control, thermal stability and mechanical properties of nanoporous single

crystals of gold. *Nanoscale* **9**, 14458–14466 (2017).

106. Zhang, C. *et al.* Formation and microstructure of nanoporous silver by dealloying rapidly solidified Zn-Ag alloys. *Electrochim. Acta* **63**, 302–311 (2012).

107. Sun, L., Chien, C. L. & Searson, P. C. Fabrication of nanoporous nickel by electrochemical dealloying. *Chem. Mater.* **16**, 3125–3129 (2004).

108. Hayes, J. R., Hodge, A. M., Biener, J., Hamza, A. V. & Sieradzki, K. Monolithic nanoporous copper by dealloying Mn-Cu. *J. Mater. Res.* **21**, 2611–2616 (2006).

109. Xu, Q., Yin, L., Hou, C., Liu, X. & Hu, X. Facile fabrication of nanoporous platinum by alloying-dealloying process and its application in glucose sensing. *Sensors Actuators, B Chem.* **173**, 716–723 (2012).

110. Guisbiers, G. *et al.* Electrum, the gold-silver alloy, from the bulk scale to the nanoscale: Synthesis, properties, and segregation rules. *ACS Nano* **10**, 188–198 (2016).

111. Seker, E., Reed, M. L. & Begley, M. R. Nanoporous gold: Fabrication, characterization, and applications. *Materials (Basel).* **2**, 2188–2215 (2009).

112. Artymowicz, D., Newman, R. & Erlebacher, J. Insights into the Parting Limit for De-Alloying from Reconsideration of Atomistic Considerations. *ECS Trans.* **3**, 499–506 (2007).

113. McCue, I., Benn, E., Gaskey, B. & Erlebacher, J. Dealloying and Dealloyed Materials. *Annu. Rev. Mater. Res.* **46**, 263–286 (2016).

114. Eilks, C. & Elliott, C. M. Numerical simulation of dealloying by surface dissolution via the evolving surface finite element method. *J. Comput. Phys.* **227**, 9727–9741 (2008).

115. Erlebacher, J. & Seshadri, R. Hard materials with tunable porosity. *MRS Bull.* **34**, 561–568 (2009).

116. Dursun, A., Pugh, D. V. & Corcoran, S. G. Dealloying of Ag-Au Alloys in Halide-Containing Electrolytes. *J. Electrochem. Soc.* **150**, B355 (2003).

117. Luo, X., Li, R., Huang, L. & Zhang, T. Nucleation and growth of nanoporous copper ligaments during electrochemical dealloying of Mg-based metallic glasses. *Corros. Sci.* **67**, 100–108 (2013).

118. Dursun, A., Pugh, D. V. & Corcoran, S. G. A steady-state method for determining the dealloying critical potential. *Electrochem. Solid-State Lett.* **6**, 34–36 (2003).

119. Lerman, M. J., Lembong, J., Muramoto, S., Gillen, G. & Fisher, J. P. The Evolution of Polystyrene as a Cell Culture Material. *Tissue Eng. - Part B Rev.* **24**, 359–372 (2018).

120. Cai, S., Zhang, B. & Cremaschi, L. Review of moisture behavior and thermal performance of polystyrene insulation in building applications. *Build. Environ.* **123**, 50–65 (2017).

121. Wang, J. & Mao, Q. Methodology Based on the PVT Behavior of Polymer for Injection Molding. *Adv. Polym. Technol.* **32**, 474–485 (2012).

122. Brun, N., Bourson, P., Margueron, S. & Duc, M. Study of the Thermal Behavior of Syndiotactic and Atactic Polystyrene By Raman Spectroscopy. *AIP Conf. Proc.* **1353**, 856–861 (2011).

123. Zhao, J. & Fan, Q. Amorphous phase in atactic polystyrene. *Polym. Bull.* **47**, 91–97 (2001).

124. McKeen, L. W. 1 - Introduction to Plastics and Polymers Compositions. in *The Effect of UV Light and Weather on Plastics and Elastomers (Third Edition)* (ed. McKeen, L. W.) 1–16 (William Andrew Publishing, 2013). doi:https://doi.org/10.1016/B978-1-4557-2851-0.00001-3.

125. Gautier, E., Fuertes, P., Cassagnau, P., Pascault, J. P. & Fleury, E. Synthesis and rheology of biodegradable poly(glycolic acid) prepared by melt ring-opening polymerization of glycolide. *J. Polym. Sci. Part A Polym. Chem.* **47**, 1440–1449 (2009).

126. Singh, M. K. *et al.* Glass Transition of Disentangled and Entangled Polymer Melts:

Single-Chain-Nanoparticles Approach. *Macromolecules* **53**, 7312–7321 (2020).

127. Santangelo, P. G. & Roland, C. M. Molecular Weight Dependence of Fragility in Polystyrene. *Macromolecules* **31**, 4581–4585 (1998).

128. Kuo, C. J. & Lan, W. L. 5 - Gel spinning of synthetic polymer fibres. in *Advances in Filament Yarn Spinning of Textiles and Polymers* (ed. Zhang, D.) 100–112 (Woodhead Publishing, 2014). doi:https://doi.org/10.1533/9780857099174.2.100.

129. Dobkowski, Z. Determination of critical molecular weight for entangled macromolecules using the tensile strength data. *Rheol. Acta* **34**, 578–585 (1995).

130. Kong, D. C. *et al.* Control of Polymer Properties by Entanglement: A Review. *Macromol. Mater. Eng.* **306**, 1–20 (2021).

131. Mccormick, H. W., Brower, F. R. T. & Kik, L. E. O. The Effect of Molecular Weight Distribution on the. **X**, 87–100 (1959).

132. Feldman, D. The theory of polymer dynamics, by M. Doi and S. F. Edwards, the Clarendon Press, Oxford University Press, New York, 1986, 391 pp. Price: $78.50. *J. Polym. Sci. Part C Polym. Lett.* **27**, 239–240 (1989).

133. Fetters, L. J., Lohse, D. J., Milner, S. T. & Graessley, W. W. Packing length influence in linear polymer melts on the entanglement, critical, and reptation molecular weights. *Macromolecules* **32**, 6847–6851 (1999).

134. Soulestin, T., Ladmiral, V., Dos Santos, F. D. & Améduri, B. Vinylidene fluoride- and trifluoroethylene-containing fluorinated electroactive copolymers. How does chemistry impact properties? *Prog. Polym. Sci.* **72**, 16–60 (2017).

135. Toshiharu, Y., Masayoshi, T. & Jun-Ichi, S. Transition behavior and dielectric properties in trifluoroethylene and vinylidene fluoride copolymers. *Polym. J.* **12**, 209–223 (1980).

136. Lakbita, I. & El-Hami, K. P(VDF/TrFE) morphologies and crystalline lamellae orientations dependence on substrates characterized by scanning probe microscopy. *AIP Conf. Proc.* **1932**, 1–6 (2018).

137. Bharti, V. & Zhang, Q. M. Dielectric study of the relaxor ferroelectric poly(vinylidene fluoride-trifluoroethylene) copolymer system. *Phys. Rev. B - Condens. Matter Mater. Phys.* **63**, 1–6 (2001).

138. Haque, R. I. *et al.* Inkjet printing of high molecular weight PVDF-TrFE for flexible electronics. *Flex. Print. Electron.* **1**, (2016).

139. Jia, N., He, Q., Sun, J., Xia, G. & Song, R. Crystallization behavior and electroactive properties of PVDF, P(VDF-TrFE) and their blend films. *Polym. Test.* **57**, 302–306 (2017).

140. Arrigoni, A. *et al.* P(VDF-TrFE) nanofibers: Structure of the ferroelectric and paraelectric phases through IR and Raman spectroscopies. *RSC Adv.* **10**, 37779–37796 (2020).

141. Wang, S. & Li, Q. Design, synthesis and processing of PVDF-based dielectric polymers. *IET Nanodielectrics* **1**, 80–91 (2018).

142. Tashiro, K. & Tanaka, R. Structural correlation between crystal lattice and lamellar morphology in the ferroelectric phase transition of vinylidene fluoride-trifluoroethylene copolymers as revealed by the simultaneous measurements of wide-angle and small-angle X-ray scatterings. *Polymer (Guildf).* **47**, 5433–5444 (2006).

143. Ohigashi, H., Akama, S. & Koga, K. Lamellar and Bulk Single Crystals Grown in Annealed Films of Vinylidene Fluoride and Trifluoroethylene Copolymers. *Jpn. J. Appl. Phys.* **27**, 2144 (1988).

144. Shingne, N., Geuss, M., Hartmann-Azanza, B., Steinhart, M. & Thurn-Albrecht, T. Formation, morphology and internal structure of one-dimensional nanostructures of the ferroelectric polymer P(VDF-TrFE). *Polymer (Guildf).* **54**, 2737–2744 (2013).

145. Kholkin, A. L., Kiselev, D. A. & Heredia, A. Piezoresponse Force Microscopy. *Encycl.*

Mater. Sci. Technol. 1–8 (2011) doi:10.1016/B978-0-08-043152-9.02281-8.

146. Soergel, E. Piezoresponse force microscopy (PFM). *J. Phys. D. Appl. Phys.* **44**, 464003 (2011).

147. Thomas, J., Gangopadhyay, P., Araci, E., Norwood, R. A. & Peyghambarian, N. Nanoimprinting by melt processing: An easy technique to fabricate versatile nanostructures. *Adv. Mater.* **23**, 4782–4787 (2011).

148. Kim, Y. *et al.* Non-Kolmogorov−Avrami−Ishibashi Switching Dynamics in Nanoscale Ferroelectric Capacitors. *Nano Lett.* **10**, 1266–1270 (2010).

149. Furukawa, T., Nakajima, T. & Takahashi, Y. Factors governing ferroelectric switching characteristics of thin VDF/TrFE copolymer films. *IEEE Trans. Dielectr. Electr. Insul.* **13**, 1120–1131 (2006).

150. Kim, Y. *et al.* Non-kolmogorov-avrami-ishibashi switching dynamics in nanoscale ferroelectric capacitors. *Nano Lett.* **10**, 1266–1270 (2010).

151. Schonhorn, H., Frisch, H. L. & Kwei, T. K. Kinetics of wetting of surfaces by polymer melts. *J. Appl. Phys.* **37**, 4967–4973 (1966).

152. Packham, D. E. Surface energy, surface topography and adhesion. *Int. J. Adhes. Adhes.* **23**, 437–448 (2003).

153. Zitzenbacher, G., Dirnberger, H., Längauer, M. & Holzer, C. Calculation of the contact angle of polymer melts on tool surfaces from viscosity parameters. *Polymers (Basel).* **10**, (2018).

154. M. Wulf, S. Michel, K. Grundkea, O.I. del Rio, D.Y. Kwok, A. W. N. Simultaneous Determination of Surface Tension and Density.pdf. *J. Colloid Interface Sci.* **210**, 172–181 (1999).

8 Appendix

8.1 List of abbreviations

3D	three-dimensional
AFM	Atomic force microscopy
DMDCS	Dimethyldichlorosilane
DPN	Dip pen lithography
EBL	Electron beam lithography
ETFE	Ethylen-tetrafluorethylen-copolymer
FIB	Focused ion beam lithogryphy
IBM	International Business Machines
mSi	Macroporous silicon
μCP	Microcontact printing
NIL	Nanoimprint lithography
np-Au	Nanoporous gold
PDMS	Polydimethylsiloxane
PFM	Piezoelectric force microscopy
PS	Polystyrene
P(VDF-TrFE)	Poly(vinylidenefluoride)-trifluoroethylene
RIE	Reactive ion etching
SEM	Scanning electron microscopy
SPL	Scanning probe lithography
t-DPN	Thermal dip pen lithography
t-NIL	Thermal nanoimprint lithography
UV	Ultraviolet

8.2   Curriculum vitae

05/2021 – present   Lecturer

Swiss Distance University of Applied Sciences, Brig

10/2016 – 05/2021   University of Osnabrück

Research Assistant – PhD student

Doctoral thesis: Development of composite nanoporous gold stamps

and their application in capillary microprinting of polymer melts

03/2014 – 04/2015   **M.Sc. in Physical Chemistry**

University of Belgrade

Master thesis: Detection of free radicals in the homogeneous brain

tissue G93A-SOD1 of transgenic rat models of ALS (Amyotrophic

Lateral Sclerosis)

10/2004 – 02/2014   **Diplom in Physical Chemistry**

University of Belgrade

Diplom thesis: Synthesis and testing of Mn^{+2}/MgO reference standard

using EPR spectroscopy method

09/2000 – 06/2004   Gymnasium "Mihajlo Petrović Alas", Belgrade

Orientation: Mathematics and Natural Sciences

8.3 Declaration of authorship

I hereby declare that the presented thesis:

Development of composite nanoporous gold stamps and their application in capillary microprinting of polymer melts

describes my own work unless otherwise acknowledged in the text. All the sources are cited as a list of references. The thesis research was carried out at the School of Biology/Chemistry at the University of Osnabrück, Germany under the supervision of Prof. Dr. Martin Steinhart. Following persons attributed to this work as a collaboration partner or a student under my supervision:

- Markus Geuss conducted the PFM measurements.
- Leon-Calvin Segelken conducted the stamping of polystyrene on glass substrates with stamping method II (without pressure) and stamping of P(VDF-TrFE) on glass substrates for the dwell times of 17 min, 19 min and 20 min.
- Dr. Jürgen Markmann sputtered the mSi samples with AgAu films.
- Dr. Nadiia Mameka conducted the electrochemical dealloying of AgAu films.

I have not attempted a promotion before, and this work was not presented to any other institution before.

Osnabrück (April 2023)   Ruža Periz